

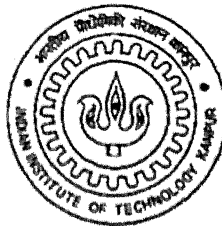
INFLUENCE OF THERMOSOLUTAL CONVECTION ON MACROSEGREGATION DURING SOLIDIFICATION OF BINARY ALLOYS

A Thesis Submitted
in Partial Fulfillment of the Requirements for the Degree of
Doctor of Philosophy

by

AMARENDRA KUMAR SINGH

Roll no. 9420661



to the

DEPARTMENT OF MATERIALS AND METALLURGICAL ENGINEERING

Indian Institute of Technology, Kanpur

December 2002

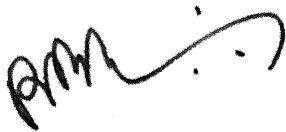
CERTIFICATE

It is certified that the work on "INFLUENCE OF THERMOSOLUTAL CONVECTION ON MACROSEGREGATION DURING SOLIDIFICATION OF BINARY ALLOYS" by **Amarendra Kumar Singh** has been carried out under our supervision and that this work has not been submitted elsewhere for a degree.



(B. Basu)
Scientist

Tata Research Development and Design Centre
Pune



(R. Balasubramaniam)
Professor



(A. Ghosh)
Formerly Professor

Department of Materials and Metallurgical Engineering
Indian Institute of Technology
Kanpur

TH
MME/2002/D
Si 64i

26 OCT 2004

गुरुचोत्तम काशीनाथ केलकर पुस्तकालय
भारतीय प्रौद्योगिकी संस्थान, कानपुर
अवधि क्र० A-149344



A149344

Acknowledgements

I wish to express my deep sense of gratitude to Prof. Ahindra Ghosh and Dr. B. Basu for their inspiring guidance and constant encouragement throughout the course of this work. I am grateful to Prof. R. Balasubramaniam for his helpful advice and constant encouragement.

I am grateful to Prof. E. C. Subbarao for his valuable suggestions and constant encouragement during the course of my thesis.

I am grateful to Prof. Mathai Joseph, Executive Director, TRDDC for helpful advice and constant encouragement.

I am indebted to my organization, Tata Research Development and Design Center, Pune, for providing me this opportunity and facilities for completion of this work.

I wish to thank Prof. D. Gobin for many useful discussions and suggestions on the work. I wish to thank Prof. D. Stefanescu, Prof. H. Fredriksson and Prof. J. A. Sekhar for review of the work at various stages of my thesis.

I would like to thank Mr. Ravindra Pardeshi, Mr. Sankar Basak, Mr. K. Mallikarjun, Mr. Amit Moandal, Mr. Mandhar Pandit, Mr. Jayant Joshi, Mr. Mahavir, Mr. Anand Vaidya and Mr. Satish Gupta for their direct and indirect help.

I wish to thank Ms. Sandhya Kokil for her help in spectroscopy. I wish to thank Dr. Satyam Sahay and Dr. Sudipto Ghosh for many useful discussions.

I would like to thank all my colleagues at TRDDC for their direct and indirect help in the completion of this work.

I would like to thank Col. A. A. Irani, Mr. Nitin Purandhare, and other members of administrative staff for their assistance in procurement of laboratory chemicals, consumables and equipments.

I wish to thank all the laboratory staff at TRDDC for their help during the course of experimental work.

I am very much grateful to Dr. (Mrs.) Radha Ghosh and other family members for their kindness and affection.

I wish to thank Mr. A. Sharma, IIT Kanpur for his assistance during the trial experiments. I wish to thank Dr. M. N. Mungole and Mr. Tapas Laha, IIT Kanpur, for their help during the closing stages of my thesis.

I am indebted to my wife, Seema, for her understanding and patience.

Finally, I wish to thank Indo-French Center for Promotion of Advanced Research, New Delhi and Department of Science and Technology, New Delhi for their financial support to carry out this work.

Pune
December, 2002

A. K. Singh

Contents

LIST OF FIGURES.....	VI
LIST OF TABLES.....	XIII
LIST OF SYMBOLS.....	XIV
SYNOPSIS.....	XVII
1 INTRODUCTION	1
1.1 FUNDAMENTALS.....	1
1.1.1 <i>Heat transfer during solidification.....</i>	<i>1</i>
1.1.2 <i>Solute redistribution and microsegregation.....</i>	<i>5</i>
1.1.3 <i>Nucleation, growth, and solidification morphology.....</i>	<i>7</i>
1.2 FLUID FLOW, SOLID MOVEMENT AND MACROSEGREGATION.....	9
1.3 OBJECTIVES OF THE PRESENT INVESTIGATION.....	12
1.4 PLAN OF WORK	13
2 LITERATURE REVIEW	14
2.1 MATHEMATICAL MODELING OF MACROSEGREGATION: HISTORICAL PERSPECTIVE.....	14
2.2 SINGLE DOMAIN MODEL.....	19
2.2.1 <i>Modeling of permeability through the mushy region</i>	<i>21</i>
2.2.2 <i>Thermophysical properties and thermodynamic data.....</i>	<i>24</i>
2.3 LITERATURE REVIEW ON SOLIDIFICATION STUDIES IN LEAD-TIN SYSTEM.....	27
2.3.1 <i>Horizontal solidification of lead-tin alloys</i>	<i>27</i>
2.3.2 <i>Unidirectional cooling from bottom.....</i>	<i>32</i>
2.4 CONCLUSIONS	35
3 MATHEMATICAL MODEL DEVELOPMENT	36
3.1 ASSUMPTIONS FOR MODEL DEVELOPMENT.....	36
3.2 THE GOVERNING EQUATIONS.....	36
3.2.1 <i>Auxiliary relationships employed in the model.....</i>	<i>38</i>
3.2.2 <i>Initial and boundary conditions.....</i>	<i>40</i>
3.3 SOLUTION PROCEDURE.....	41
3.3.1 <i>Finite difference formulation</i>	<i>42</i>
3.3.2 <i>Numerical details</i>	<i>43</i>
3.4 GRID SENSITIVITY TESTS.....	43

3.4 MODEL VALIDATION	45
3.4.1 Test problem I	45
3.4.2 Test problem II	47
3.4.3 Test problem III	47
4 MACROSEGREGATION: CASE STUDIES	51
4.1 INTRODUCTION	51
4.2 ROLE OF MATERIAL PROPERTIES ON THERMOSOLUTAL CONVECTION AND MACROSEGREGATION	52
4.2.1 Problem definition	52
4.2.2 Initial and boundary conditions	52
4.2.3 Selection of Material and Process Parameters	55
4.2.4 Results and discussions	58
4.2.5 Conclusion	67
4.3 ROLE OF PERMEABILITY ON MACROSEGREGATION	71
4.3.1 Introduction	71
4.3.2 Permeability models	72
4.3.3 Problem definition	73
4.3.4 Results and discussions	74
4.3.5 Conclusions	83
4.4 EFFECT OF COOLING RATE ON THERMOSOLUTAL CONVECTION AND MACROSEGREGATION IN IRON- CARBON SYSTEM	83
4.4.1 Problem Definition	84
4.4.2 Results and discussion	84
4.4.3 Conclusions	94
5 VERTICAL SOLIDIFICATION: EXPERIMENTAL	95
5.1 INTRODUCTION	95
5.2 EXPERIMENTAL SETUP	95
5.2.1 The vertical tubular furnace	99
5.2.2 The solidification cell and cooling jacket	99
5.2.3 Melting furnace	102
5.3 ACCESSORIES FOR TEMPERATURE MEASUREMENTS	102
5.4 EQUIPMENT FOR DETERMINATION OF MACROSEGREGATION AND MICROSTRUCTURE	104
5.5 EXPERIMENTAL PROCEDURES	106
5.5.1 Alloy preparation	106
5.5.2 Directional solidification experiments	109
5.5.3 Temperature measurement	110
5.5.4 Microstructural examination and metallography	111

5.5.5 Macrosegregation.....	112
5.6 MEASUREMENTS ERRORS, CALIBRATIONS AND REPRODUCIBILITY CHECKS.....	113
5.6.1 Temperature.....	113
5.6.2 Concentration.....	114
5.7 EXPERIMENTAL RESULTS OF A TYPICAL RUN.....	114
5.7.1 Time-temperature curve.....	115
5.7.2 Macrosegregation and microstructure.....	115
6 RESULTS AND DISCUSSIONS OF RESULTS	120
6.1 EXPERIMENTAL CONDITIONS.....	120
6.2 EXPERIMENTAL RESULTS	120
6.2.1 Thermal data in the melt	120
6.2.2 Macrosegregation data.....	124
6.2.3 Microstructure	128
6.2.4 Other observations.....	128
6.3 ANALYSES OF EXPERIMENTAL DATA	128
6.3.1 Dendrite arm spacing.....	128
6.3.2 Procedure for obtaining heat flux values for various experiments	139
6.4 ANALYSIS OF MACROSEGREGATION WITH MATHEMATICAL MODEL.....	143
6.4.1 Experiment E6 (Fast cooling rate).....	146
6.4.2 Experiment E1 (Intermediate cooling rate).....	152
6.4.3 Experiment E17 (Slow cooling rate)	158
6.4.3 Simulation of Sazarin and Hellawell experiment [107].....	164
6.5 CONCLUSIONS	178
7 SUMMARY AND CONCLUSIONS	183
8 SUGGESTIONS FOR FURTHER WORK	187
BIBLIOGRAPHY	188
APPENDIX I: TEMPERATURE-TIME CURVES FOR SOLIDIFICATION CELL	
THERMOCOUPLES	194
APPENDIX II: MACROSEGREGATION EXPERIMENTAL DATA TABLES	215

List of Figures

No.	Title	Pg. No.
1.1	The schematic of a solidifying casting; the modes of heat transfer are indicated within brackets	2
1.2	A typical mushy zone (schematic) showing primary , secondary and tertiary dendrites	4
2.1	Phase diagram of Pb-Sn binary alloy	25
2.2	Schematic of (a) horizontal solidification and (b) vertical solidification	29
2.3	Thermosolutal solutal convection pattern in the melt and mushy zone of a solidifying alloy (a) solutal buoyancy augmenting thermal buoyancy force, (b) solutal buoyancy forces opposing thermal buoyancy forces, with thermal buoyancy dominating in the mushy zone, and (c) solutal buoyancy forces opposing and dominating thermal buoyancy forces in the mushy region [18]	31
2.4	Schematic of flow conditions during bottom cooled solidification (a) heavier solute, (b) lighter solute	33
3.1	Comparison of streamlines, isotherms, liquid fraction profile and iso-composition for (a) 50x50 and (b) 30x30 grids	44
3.2	Predicted axial macrosegregation with different grids obtained from simulation of Sazarin et al's experiment[107].	46
3.3	Comparison with Yoo et al's [86] experimental results and numerical predictions; (a) predictions of present model, (b) Yoo et al's predictions, and (c) Yoo et al's experimental results	48
3.4	Comparison of numerical predictions: (a) streamlines (present model), (b) streamlines[60], (c) fraction solid (present model) and (d) fraction solid [60].	49
3.5	Comparison of predicted results from present model with the numerical results of Prescott, et al [117] for solidification of Pb-19 wt % Sn alloy in a cylindrical mould.	50
4.1	Geometry of the cavity, initial and boundary conditions.	53
4.2	Permeability functions used in literature	54
4.3	Progress of solidification.	60

4.4	Model predictions for solidification of Fe-1 wt % C alloy, solidification time (t) = 250 sec showing (a) streamlines, (b) isotherms, (c) solid fraction lines, and (d) iso-composition lines (wt % of carbon).	61
4.5	Model predictions for solidification of Fe-1 wt % C alloy, solidification time (t) = 2000 sec showing (a) streamlines, (b) isotherms, (c) solid fraction lines, and (d) iso-composition lines (wt % of carbon).	62
4.6	Model predictions for solidification of Pb-15 wt % Sn alloy, solidification time (t) = 250 sec showing (a) streamlines, (b) isotherms, (c) solid fraction lines, and (d) iso-composition lines (wt % of tin).	64
4.7	Model predictions for solidification of Pb-15 wt % Sn alloy, solidification time (t) = 1000 sec showing (a) streamlines, (b) isotherms, (c) solid fraction lines, and (d) iso-composition lines (wt % of tin).	65
4.8	Model predictions for solidification of Pb-15 wt % Sn alloy, solidification time (t) = 2000 sec showing (a) streamlines, (b) isotherms, (c) solid fraction lines, and (d) iso-composition lines (wt % of tin).	66
4.9	Model predictions for solidification of NH ₄ Cl-18 wt % H ₂ O solution, solidification time (t) = 250 sec showing (a) streamlines, (b) isotherms, (c) solid fraction lines, and (d) iso-composition lines (wt % of H ₂ O).	68
4.10	Model predictions for solidification of NH ₄ Cl-18 wt % H ₂ O solution, solidification time (t) = 500 sec showing (a) streamlines, (b) isotherms, (c) solid fraction lines, and (d) iso-composition lines (wt % of H ₂ O).	69
4.11	Model predictions for solidification of NH ₄ Cl-18 wt % H ₂ O solution, solidification time (t) = 2000 sec showing (a) streamlines, (b) isotherms, (c) solid fraction lines, and (d) iso-composition lines (wt % of H ₂ O).	70
4.12	(a) Geometry of the casting, initial and boundary conditions and (b) macrosegregation profile at the end of solidification.	75
4.13	Comparison of composition profiles from various permeability models with experimental data [42] at (a) Y = 15 mm and (b) Y = 39 mm.	76
4.14	Comparison of composition profiles from various permeability models with experimental data [42] at (a) Y = 15 mm and (b) Y = 39 mm.	77
4.15	Comparison of permeability model (this work) with experimental data [90] for flow (a) parallel and (b) perpendicular to primary dendrite arms spacing.	80

4.16	Comparison of composition profiles (using present permeability model) with experimental data [42] at (a) $Y = 15$ mm and (b) $Y = 39$ mm.	81
4.17	Comparison of composition profiles (using present permeability model) with experimental data [42] at (a) $Y = 69$ mm and (b) $X = 19$ mm.	82
4.18	Streamlines, isotherms, mush profile and macrosegregation pattern for 20, 50 and 80 % solidification for heat flux of 10 kW/m^2 : ψ_{\max} & ψ_{\min} : Table II, $\Delta\psi = 0.25$ for (a), 0.05 for (e), and 1.5×10^{-3} for (i); (b), (f) & (j) T_{\max} & T_{\min} : Table II, $\Delta T = 5^\circ\text{C}$; (c), (g) & (k) f_{\max} & f_{\min} : Table II, $\Delta f = 0.1$; (d), (h) & (l) C_{\max} & C_{\min} : Table II, $\Delta C = 0.1$.	86
4.19	Streamlines, isotherms, mush profile and macrosegregation pattern for 20, 50 and 80 % solidification for heat flux of 60 kW/m^2 : ψ_{\max} & ψ_{\min} : Table II, $\Delta\psi = 1$ for (a), 0.55 for (e) and 0.02 for (i); (b), (f) & (j) T_{\max} & T_{\min} : Table II, $\Delta T = 5^\circ\text{C}$; (c), (g) & (k) f_{\max} & f_{\min} : Table II, $\Delta f = 0.1$; (d), (h) & (l) C_{\max} & C_{\min} : Table II, $\Delta C = 0.1$.	87
4.20	Streamlines, isotherms, mush profile and macrosegregation pattern for 20, 50 and 80 % solidification for heat flux of 360 kW/m^2 (a), (e) & (i) ψ_{\max} & ψ_{\min} : Table II, $\Delta\psi = 2.5$ for major vortex and 0.2 for minor vortex; (b), (f) & (j) T_{\max} & T_{\min} : Table II, $\Delta T = 5^\circ\text{C}$; (c), (g) & (k) f_{\max} & f_{\min} : Table II, $\Delta f = 0.1$; (d), (h) & (l) C_{\max} & C_{\min} : Table II, $\Delta C = 0.1$.	88
4.21	Macrosegregation pattern upon complete solidification.	91
4.22	Variation of global extent of segregation with heat flux.	93
5.1	Furnace, solidification unit and various accessories (schematic).	96
5.2	The melting unit (schematic).	97
5.3	Photograph of experimental setup: two views.	98
5.4	Design of instrumented mould; dimensions in millimeter.	100
5.5	Design of cooling jacket; dimensions in millimeter.	101
5.6	Thermocouple placements inside the mould and the cooling jacket.	103
5.7	Schematic of thermocouple circuitry.	105
5.8	(a) Locations of samples taken for AAS examination; (b) Locations of samples taken for metallographic examination; dimensions in	107

millimeter.

5.9	Outline of experimental procedure	108
5.10	Transient temperature response of thermocouples TC1 to TC8 in the melt and other locations.	116
5.11	Transient temperature response of thermocouples in chill block and water inlet/outlet.	117
5.12	Composition of solute at various locations and averaged value at various heights.	118
5.13	Microstructure of Pb-35 wt % Sn alloy.	119
6.1	Transient temperature response (experiment E1) in the solidification cell for TC1 to TC8 of Fig. 5.6; vertical distances of thermocouples from the base of the mould are indicated.	123
6.2	Transient temperature response (experiment E1) in the solidification cell for TC9 to TC12 of Fig. 5.6.	127
6.3	Longitudinal macrosegregation for experiment E17 (Pb-35 wt % Sn).	129
6.4	Longitudinal macrosegregation for experiment E8 (Pb-19 wt % Sn).	130
6.5	Longitudinal macrosegregation for experiment E14 (Sn-15 wt % Pb).	131
6.6	Microphotographs of experiments E5 and E6 from different locations of casting (bottom, middle and top).	132
6.7	Microphotographs of experiments E9 and E10 from different locations of casting (bottom, middle and top).	133
6.8	Microphotographs of experiments E13 and E14 from different locations of casting (bottom, middle and top).	134
6.9	Predicted vs. measured primary dendrite arm spacing (μm).	138
6.10	Comparison of computed secondary dendrite arm spacing with experimental data (a) E3 and (b) E4.	140
6.11	Predicted vs. measured secondary dendrite arm spacing (μm).	141
6.12	Schematic of the calculation domain and grid locations.	145
6.13	Comparison of predicted temperatures with experimental data for experiment E6.	147

6.14	Simulated results for E6 at 25 % solidification (a) Streamlines (ψ_{\min} : -0.557, ψ_{\max} : 1.1, equal increment, (b) isotherms, (c) iso-liquid fraction, and (d) iso-composition profiles.	148
6.15	Simulated results for E6 at 50 % solidification (a) Streamlines (ψ_{\min} : -0.088, ψ_{\max} : 0.33, equal increment, (b) isotherms, (c) iso-liquid fraction, and (d) iso-composition profiles.	149
6.16	Calculated results for E6 at the end of solidification (a) Final solute distribution (initial composition 35 wt % Sn) and (b) Secondary dendrite arms spacing (μm).	150
6.17	Comparison of experimental and computed average macrosegregation along vertical direction for experiment E6.	151
6.18	Comparison of predicted temperatures with experimental data for experiment E1.	152
6.19	Simulated results for E1 at 25 % solidification (a) Streamlines (ψ_{\min} : -0.495, ψ_{\max} : 0.772, equal increment, (b) isotherms, (c) iso-liquid fraction, and (d) iso-composition profiles.	153
6.20	Simulated results for E1 at 50 % solidification (a) Streamlines (ψ_{\min} : -0.121, ψ_{\max} : 0.535, equal increment, (b) isotherms, (c) iso-liquid fraction, and (d) iso-composition profiles.	145
6.21	Calculated results for E1 at the end of solidification (a) Final solute distribution (initial composition 35 wt % Sn) and (b) Secondary dendrite arms spacing (μm).	146
6.22	Comparison of experimental and computed average macrosegregation along vertical direction for experiment E1.	147
6.23	Comparison of predicted temperatures with experimental data for experiment E17.	155
6.24	Simulated results for E17 at 25 % solidification (a) Streamlines (ψ_{\min} : -0.195, ψ_{\max} : 0.90, equal increment, (b) isotherms, (c) iso-liquid fraction, and (d) iso-composition profiles.	156
6.25	Simulated results for E17 at 50 % solidification (a) Streamlines (ψ_{\min} : -0.027, ψ_{\max} : 0.126, equal increment, (b) isotherms, (c) iso-liquid fraction, and (d) iso-composition profiles.	157
6.26	Calculated results for E17 at the end of solidification (a) Final solute distribution (initial composition 35 wt % Sn) and (b) Secondary	158

dendrite arms spacing (μm).

6.27	Comparison of experimental and computed average macrosegregation along vertical direction for experiment E17.	159
6.28	Comparison of final solute distribution for three cases (E1, E6 and E17).	162
6.29	Comparison of experimental and computed average macrosegregation along vertical direction for experiment E2.	163
6.30	Comparison of experimental and computed average macrosegregation along vertical direction for experiment E3.	164
6.31	Comparison of experimental and computed average macrosegregation along vertical direction for experiment E4.	165
6.32	Comparison of experimental and computed average macrosegregation along vertical direction for experiment E5.	166
6.33	Comparison of experimental and computed average macrosegregation along vertical direction for experiment E15.	167
6.34	Comparison of experimental and computed average macrosegregation along vertical direction for experiment E16.	168
6.35	Comparison of experimental and computed average macrosegregation along vertical direction for experiment E7.	169
6.36	Comparison of experimental and computed average macrosegregation along vertical direction for experiment E8.	170
6.37	Comparison of experimental and computed average macrosegregation along vertical direction for experiment E9.	171
6.38	Comparison of experimental and computed average macrosegregation along vertical direction for experiment E10.	172
6.39	Comparison of experimental and computed average macrosegregation along vertical direction for experiment E18.	173
6.40	Comparison of experimental and computed average macrosegregation along vertical direction for experiment E19.	174
6.41	Simulated results for experiments of Sazarin, et al [107] at 25 % solidification (a) Streamlines (ψ_{\min} : -0.132, ψ_{\max} : 1.3×10^{-3} , equal increment, (b) isotherms, (c) iso-liquid fraction, and (d) iso-composition profiles.	176

- 6.42 Simulated results for experiments of Sazarin, et al [107] at 50 % solidification (a) Streamlines (ψ_{\min} : -2.3×10^{-7} , ψ_{\max} : 1.8×10^{-6} , equal increment. (b) isotherms. (c) iso-liquid fraction, and (d) iso-composition profiles. 177
- 6.43 Comparison of experimental and computed average macrosegregation along the vertical direction for experiment of Sazarin, et al [107]. 178

List of Tables

No.	Title	Pg. No.
2.1	Various permeability models	22
2.2	Thermophysical properties of lead-tin alloys	26
4.1	Thermo-physical properties of $\text{NH}_4\text{Cl-H}_2\text{O}$, Fe-C and Pb-Sn alloy system	56
4.2	Dimensionless parameters	57
4.3	Maximum and minimum values of stream function, temperature and average composition for various systems	59
4.4	Maximum and minimum values of stream function, temperature and average composition for various heat fluxes for solidification of Fe-1 wt % C alloy	89
5.1	Summary of bias, precision and uncertainty for a typical thermocouple	113
6.1	Experiments of Set 1	121
6.2	Experiments of Set 2	122
6.3	Solidification condition at TC3 for various experiments	125
6.4	Local solidification time (seconds) at various thermocouple locations	126
6.5	Dendrite arms spacing from selected experiment	135
6.6	Comparison of calculated primary dendrite arms with experimental data	137
6.7	Comparison of calculated secondary dendrite arms spacing from selected experiments (μm)	142

List of Symbols

A	area (m^2)
B	constant
B	body force (Kg m /s^2)
C	composition (wt %)
D	diffusivity (m^2/s)
Da	Darcy number, K_0/L^2
F	drag offered by mushy region
G	thermal gradient (K/m)
H	height of the cavity (m)
K_{NR}	permeability normal to primary dendrite arm (m^2)
K_{PR}	permeability parallel to primary dendrite arm (m^2)
K_p	equilibrium partition coefficient
K_{eff}	effective partition coefficient
K_o	permeability coefficient (m^2)
K⁽²⁾	permeability tensor (m^2)
L	length of the cavity (m)
Le	Lewis number, α/D_1
N	relative strength of solutal buoyancy over thermal buoyancy
Pr	Prandtl number, ν_1/α_1
R	linear rate of advancement of solidification front (m/s)
Ra_{th}	thermal Rayleigh number, $g\beta_T q_{\text{ref}} L^4 / (k\mu\alpha)$
Ra_s	solutal Rayleigh number, $g\beta_s C_{\text{eut}} L^3 \rho / (\mu\alpha)$
R_r	Darcian resistance term in r/x direction
R_z	Darcian resistance term in z/y direction
S_e	source term of energy equation
Ste	Stefan number, $c_l q L / (k_l \Delta H)$
T	temperature ($^{\circ}\text{C}$ or K)
U	velocity vector (m/s)
a_i	coefficient of finite volume based discretization equation (Eq. 3.30)

C_v	coefficient of finite volume based discretization equation (Eq. 3.30)
c	specific heat (J/Kg/K)
d	dendrite arm spacing (micrometer)
d_1	primary dendrite arm spacing (micrometer)
d_2	secondary dendrite arm spacing (micrometer)
f	fraction
g	acceleration due to gravity (m/s^2)
h	enthalpy (J/kg)
ΔH	latent heat of fusion (J/kg)
k	conductivity (W/m/K)
k_m	mass transfer coefficient (1/s)
m	slope of liquidus line ($^{\circ}K/wt\%$)
p	pressure (N/m^2)
q	heat flux (W/m^2)
t	time (s)
r, z	spatial coordinates in cylindrical coordinate system (m)
u	velocity in x direction (m/s)
v	velocity in y direction (m/s)
x, y	spatial co-ordinates in rectangular coordinate system (m)

Greek Symbols

α	thermal diffusivity (m^2/s)
β_T	co-efficient of thermal expansion (1/K)
β_S	co-efficient of solutal expansion (1/wt %)
δ_c	effective boundary layer thickness (m)
Γ	Gibbs-Thomson coefficient (J/m^2)
ν	kinematic viscosity (m^2/s)
λ	under-relaxation parameter
μ	dynamic viscosity ($N/m^2/s$)
ϕ	general variable
ρ	density (kg/m^3)

Subscript

l	liquid
s	solid
eut	eutectic
mush	mushy phase
int	initial
ref	reference value

Superscripts

*	dimensional value
---	-------------------

SYNOPSIS

Solidification is an integral part of many important manufacturing processes such as casting, welding, crystal growth, and varieties of near net shape processing. Solidification process is governed by a large number of interacting phenomena like heat transfer, solute redistribution and segregation, fluid flow, nucleation and grain growth, morphological transition etc. Structure and properties of solidified components are controlled by some of these phenomena.

Macroseggregation, which is the subject of present study, is one of the most common casting defects. Macroseggregation refers to variations in composition that occur in alloy castings or ingots during solidification at the length scale of casting. It is caused by the movement of solid crystals (purer in solute), or solute enriched liquid. It cannot be eliminated by subsequent treatments, such as annealing. It is detrimental to the properties of the cast product. Therefore, major efforts are directed towards minimizing this defect through control of fluid flow and movement of free crystals.

There are various causes of fluid flow. The present study is concerned with influence of thermosolutal convection on macroseggregation. *Thermosolutal convection* results from buoyancy forces, arising from temperature and composition gradients in the liquid as a consequence of the solidification process. The present day understanding of macroseggregation is the result of extensive research of last four decades, which clearly show the importance of thermosolutal convection on evolution of macroseggregation. This thesis is aimed at throwing more light on role of thermosolutal convection on macroseggregation during solidification of binary alloys.

The thesis consists of eight chapters. Chapter 1 briefly reviews the fundamentals of solidification with specific emphasis on macroseggregation. It also outlines the objectives of the present work and plan of work. Chapter 2 contains literature review on (i) mathematical modeling of macroseggregation, (ii) modeling of permeability through the mushy region, thermophysical properties and thermodynamic data, and (iv) literature review on solidification studies in lead-tin system.

The findings of the review reveal that uncertainty in permeability functions of mush is one of the main reasons for quantitative mismatch between numerical predictions and

experimental data on macrosegregation. Other than permeability, thermophysical properties of material and cooling rate seem to have major influence on macrosegregation. Experimental data are limited, and these are generally not complete in all respects for usage in mathematical models. In the present investigation, a combined modeling and experimental approach was taken to focus on these issues, and to throw further light on understanding of evolution of macrosegregation during solidification.

Chapter 3 deals with development of the mathematical model. In the present investigation, a model based on continuum formulation was developed in two dimensional rectangular and cylindrical co-ordinate systems. The governing equations for the model were for conservation of mass, momentum, energy and species. The following auxiliary relationships were used in the model (i) Darcy Law for representation of flow through the mushy region, (ii) Boussinesq approximation to account for thermosolutal buoyancy, and (iii) Lever rule to account for the relation between temperature, composition and fraction liquid, f_l , in the mushy region. The solution procedure, numerical details and validation of the model are outlined in this chapter.

Chapter 4 presents case studies of some important aspects of thermosolutal convection. Using the mathematical model developed in Chapter 3, computer simulations were performed to study the influence of (i) material properties, (ii) choice of permeability function for mushy region, and (iii) cooling rate on evolution of thermosolutal convection and consequent macrosegregation during horizontal solidification of binary alloys. To show the role of material, three alloy systems, namely, Pb-Sn alloy, Fe-C alloy and $\text{NH}_4\text{Cl-H}_2\text{O}$ system, all with lighter solute, were chosen in present study. Initial conditions were set through considerations of superheat and mushy zone length. Boundary conditions for simulations were arrived at through considerations of equality in rate of solidification. Difference in stability number (N), which is a function of the coefficient of solutal buoyancy to the coefficient of thermal buoyancy, appeared to govern the evolution of thermosolutal convection and subsequent macrosegregation. It was shown that the differences in material properties led to entirely different thermosolutal convection and macrosegregation pattern. Thus, it was concluded that extrapolation of results from one material to other needs to be done with utmost care.

To show the inadequacies of various permeability functions, experimental data on solidification of Pb-Sn alloy, reported in literature, was utilized. The reason for discrepancy has been attributed in the past to inadequacy of permeability function in thin mushy region. To address this, an appropriate function for thin mushy region ($f_l > 0.5$) was selected and generalized in terms of secondary dendrite arm spacing. The resultant function was tested with limited experimental data on permeability on Pb-Sn alloy. Using this permeability function in the model, the experiment reported in literature was simulated. Predicted macrosegregation profiles were compared with experimental data, which were reported at four different planes of the casting. There were reasonable matches for two planes, whereas the matches for two other planes were poor. It was concluded from this study that selection of better function for thin mushy region and use of secondary dendrite arm spacing in it resulted in better correspondence between predicted and experimental values of macrosegregation. It was also concluded that further research was needed in this area.

The effect of cooling rate on macrosegregation was investigated for solidification of Fe-1 wt % C alloy. Variation of global extent of segregation with variation of heat flux from 5 to 6000 kW/m² was studied. Factors controlling extent of segregation at various cooling rates were identified. It was shown how thermal and solutal buoyancy forces control the extent of segregation at various rates of cooling and the variation in global extent of segregation with cooling rate was explained.

Chapter 5 outlines the experimental procedure and apparatus of the present investigation. Molten lead-tin alloy was contained in a cylindrical mould, and it was subjected to unidirectional solidification vertically downward by water cooling from the bottom. The apparatus was designed and fabricated in the laboratory. The setup and experimental procedure were finalized through a series of trials. This chapter provides details of (i) experimental setup, (ii) accessories for temperature measurements, (iii) equipments for determination of macrosegregation and macrostructure, (iv) experimental procedure, (v) experimental error, calibrations and reproducibility checks and, (vi) experimental results of a typical run.

Chapter 6 presents results of experiments and discussions of results. Experiments were conducted on Pb-19 wt % Sn, Pb-35 wt % Sn, and Sn-15 wt % Pb alloys. For each alloy,

experiments were carried out for two superheats and at least two different cooling rates. The data from the experiments were obtained in terms of temperature-time curves, macrosegregation and microstructural details in terms of primary and secondary dendrite arm spacing. The data from the experiments were analyzed to obtain heat transfer coefficients. Experimental data on primary and secondary dendrite arm spacings were used to fine-tune microstructural modules of the model.

The mathematical model was then used to analyze evolution of thermosolutal convection, isotherms, liquid fraction profiles and macrosegregation profiles during vertical solidification of lead-rich binary lead-tin alloys for conditions of experiments of present investigation. It was shown that the evolution of segregation in vertical solidification was very sensitive to the nature of permeability function near mush/liquid interface. Generalized West permeability function, which differs with Kozeny-Carman equation near mush/liquid interface only, appeared to suppress the flow and consequent macrosegregation. It was observed that the flow field did not show significant effect on thermal field but it affected macrosegregation substantially.

The model was also used to simulate an experiment cited in literature for extremely slow solidification condition (solidification time for this case was 8 hours as opposed to 0.5-1 hours in experiments of present investigation). A reasonable prediction of macrosegregation profile for this case as well demonstrated the capability of the mathematical model to simulate solidification processes with variety of cooling rates.

Chapter 7 presents summary and conclusions from this work and Chapter 8 provides suggestions for future work.

In this work, a new procedure was established where by large number of experimental inputs were incorporated into the model.

- Temperature profiles of the melt prior to initiation of cooling was used as initial condition for the model.
- Boundary heat fluxes were derived from experimental temperature-time curves in chill block.
- Microstructural module of the model was fine-tuned based on the data of dendrite arm spacing from post solidification analysis.

- Using the model in conduction mode average dendrite arms spacing for usage in permeability model was obtained.
- Finally, experimental data on macrosegregation were used for validation of the mathematical model.

Additionally, the following are the major finding of this work:

- The critical role of stability number (N) on evolution of double-diffusive convection and consequent macrosegregation was demonstrated through a comparative study of solidification of Fe-C, Pb-Sn and $\text{NH}_4\text{Cl-H}_2\text{O}$ system.
- Factors controlling the extent of segregation at various cooling rates were identified. Using the proposed mechanism, the variation in extent of segregation for wide range of cooling rates was explained.
- A modified permeability model was proposed. Its suitability to explain segregation in horizontal solidification was demonstrated.
- It was shown that the permeability model required further modification to explain experimental observation on macrosegregation during vertical solidification. The role of permeability near the mush/liquid interface was considered crucial in determining the evolution of macrosegregation during vertical solidification. This factor was not so apparent in case of horizontal solidification due to higher convection and unstably stratified liquid.

Chapter 1

INTRODUCTION

Solidification is an integral part of many important manufacturing processes such as casting, welding, crystal growth and varieties of near net shape processing. Its importance can be gauged from the fact that a large number of textbooks and recent conference proceedings [1-7] deal with the subject. Solidification process is governed by a large number of interacting phenomena like heat transfer, solute redistribution and segregation, fluid flow, nucleation and grain growth, morphological transition, etc. Structure and properties of solidified components are finally controlled by some of these phenomena.

Macrosegregation, which is the subject of present study, is one of the most common casting defects. Macrosegregation refers to variations in composition that occur in alloy castings or ingots at the length scale of casting. It is caused by the movement of solid crystal (purer in solute) or solute enriched liquid. It cannot be eliminated completely by subsequent treatments, such as annealing. Macrosegregation is detrimental to the properties of the cast product, and when composition variation is beyond acceptable range, it can lead to the rejection of the casting or the products made from the castings. Therefore, major efforts are directed towards controlling this defect. The movements of solid and liquid during the progress of solidification are closely related to other aspects of solidification such as heat transfer, solute redistribution, evolution of micro- and macrostructure. The fundamentals of some of the above phenomena are briefly discussed.

1.1 Fundamentals

1.1.1 Heat transfer during solidification

Solidification is accompanied by the *removal of the latent heat of fusion from the melt*. This aspect has been dealt with in great detail in many textbooks[1-4], and only a brief account is presented here with respect to ingot casting. A common method of latent heat removal is static casting where the melt is poured into a static mould (Fig. 1.1). So far as metallic melts are concerned it can be either a pure metal or an alloy. Pure metal

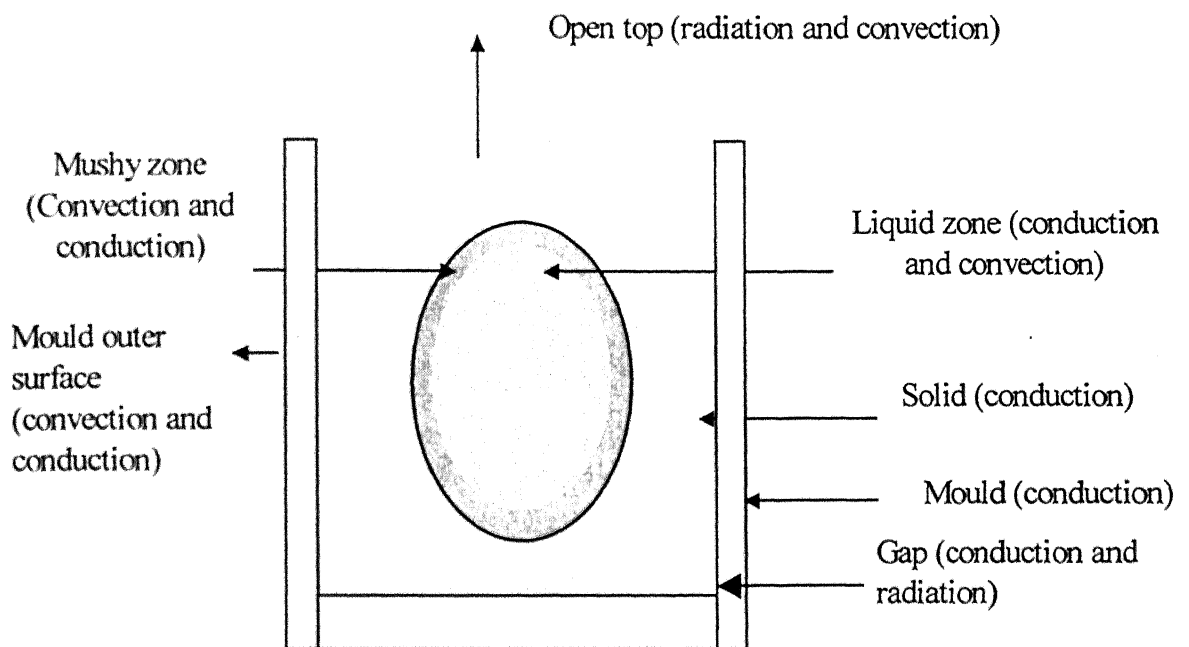


Fig. 1.1: The schematic of a solidifying casting; the modes of heat transfer are indicated within brackets.

solidifies at a single temperature during the progress of solidification. On the other hand, the solidification of alloy takes place over a range of temperatures, bounded by *liquidus* and *solidus*. This bounded region is normally referred to as *mushy zone*, where solid and liquid co-exists. An exception is the eutectic composition of an alloy, where transformation occurs at a single temperature. The three zones during progress of alloy solidification are also shown in Fig. 1.1.

Fig. 1.1 indicates the modes of heat transfer in various parts of ingot-mould assembly during solidification. Typically, the initial melt poured in the mould has temperature in excess of the liquidus. As cooling proceeds due to heat losses from open top and through mould walls, the melt temperature comes down. Fig. 1.1 depicts an intermediate stage of solidification where all three zones, viz. pure solid, mushy, and pure liquid zones, are present. A typical mushy zone [8] is shown in Fig. 1.2. Conduction is primarily responsible for the transport of heat through the solid to the mould surface and open top. However, in liquid and mushy zones, convection plays an important role in transport of heat. Convection in the melt, in turn, is the result of several factors including thermal gradient in the melt which gives rise to the thermal buoyancy driven flow.

Thermal gradient in the melt is related to the rate of heat removal through the mould and to the surroundings (outer surface of the mould and top). The heat transfer at the metal/mould interface is primarily by conduction in the beginning. However, as solidification progresses, a gap forms between the casting and mould due to solidification shrinkage and mould expansion. This offers large resistance to heat flow in later stages of solidification. In the gap, radiation also can be a mode of heat transfer depending upon the surface temperature. From the outer surface of the mould and top surface of the casting, cooling occurs by convection as well as radiation.

Heat transfer during solidification has profound effect on macrosegregation, microstructure etc., and in turn, on the properties of the solidified product. Apart from its influence on flow of liquid through thermosolutal convection, heat transfer affects liquid flow in the mushy region through its influence on the mush structure, since length of the

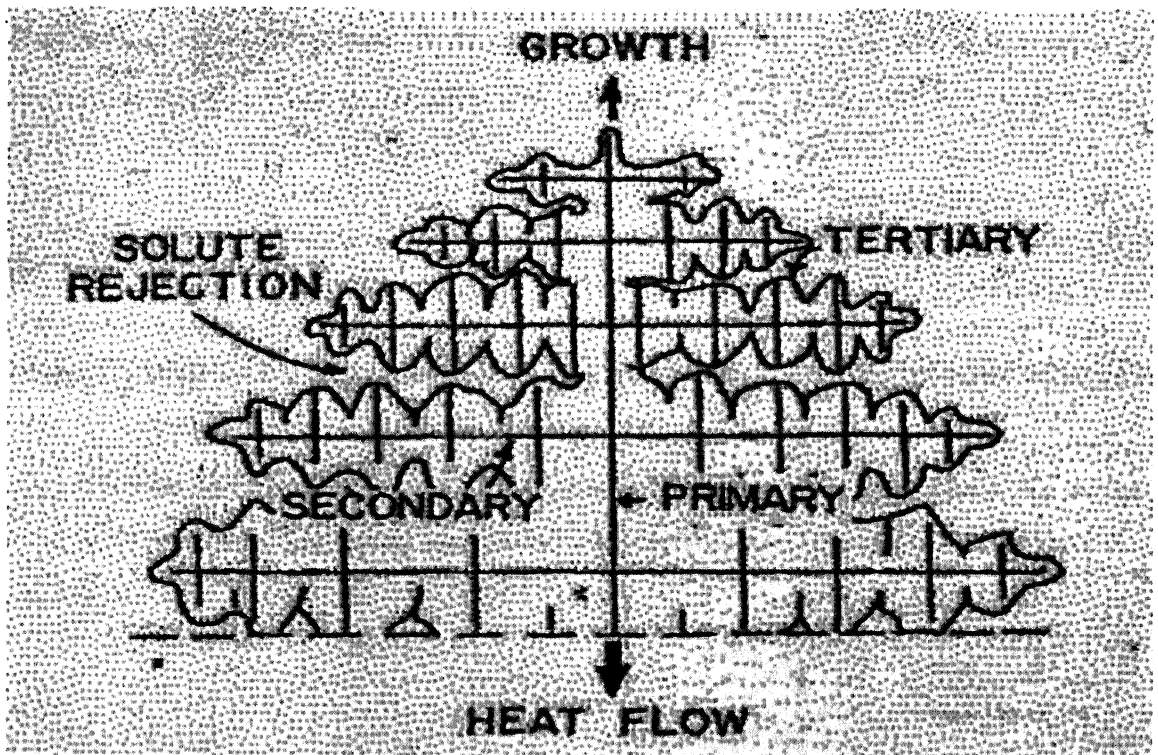


Fig. 1.2: A typical mushy zone (schematic) showing primary, secondary and tertiary dendrites[8].

mushy zone as well as primary and secondary dendrite arms spacing are all strong functions of cooling rate.

1.1.2 Solute redistribution and microsegregation

Owing to the difference in solubility of a solute in liquid and solid phases, solidification results in rejection of the solute at the solid-liquid interface. In normal solidification conditions, local equilibrium is assumed to exist at the solid/liquid interface. The concentrations of a solute in the solid and liquid are related at the interface as follows [1-4]:

$$C_s = K_p C_l \quad \dots 1.1$$

Where, K_p is the *equilibrium partition coefficient*, and C_s and C_l are concentration of the solute in solid and liquid respectively at the solid/liquid interface.

In equilibrium solidification, the compositions in both liquid and solid phase are assumed to be uniform. Then, the liquid and solid compositions are related by the *Lever rule* as follows:

$$C_l = \frac{C_0}{[1 - (1 - K_p)f_s]} \quad \dots 1.2$$

where, C_0 is the initial concentration of the solute in the liquid at the start of freezing, and f_s is the solid fraction at any instant during progress of solidification.

In actuality, however, equilibrium solidification is difficult to attain due to low diffusivity of solute causing concentration gradient build up in the solid, and often, incomplete mixing in the liquid as well. In non-equilibrium solidification, the local equilibrium between solid and liquid can, at best, be assumed to hold good at the interface. With respect to the non-equilibrium situation, there lies a host of possibilities. Few non-equilibrium models are briefly presented below.

No Diffusion in Solid, Complete Mixing in Liquid (Scheil's equation[9]):

The following assumptions are invoked in derivation of Scheil's equation: (i) equilibrium at solid/liquid interface, (ii) negligible diffusion in solid, and (iii) complete mixing in liquid. The concentration of a solute in the liquid as a function of fraction solid is given by Scheil's equation as follows:

$$C_l = C_o [1-f_s]^{(K_p - 1)} \quad \dots 1.3$$

Incomplete Mixing in Solid, Complete Mixing in Liquid (Brody-Flemings equation[10]):

This has all assumptions of Scheil's equation except that diffusion in solid is also considered. Upon derivation, the final equation is:

$$C_l = C_o [1-f_s/(1+BK_p)]^{(K_p - 1)} \quad \dots 1.4$$

B in Eq. 1.4 is defined as

$$B = 4D_s t_f / d^2 \quad \dots 1.5$$

where, D_s is diffusion coefficient in the solid phase, t_f is the local solidification time, and d is the dendrite arm spacing.

No Diffusion in Solid, Incomplete Mixing in Liquid[11]:

In cases where diffusion in solid is negligible (i.e., D_s is assumed as zero) and a solute boundary layer controls the solute transfer in the liquid, then for a semi-infinite volume-element and steady-state conditions, it has been derived that:

$$C_l = C_o [1-f_s]^{K_{eff} - 1} \quad \dots 1.6$$

K_{eff} is the *effective partition coefficient* and is defined as follows:

$$K_{\text{eff}} = \frac{C_s^*}{C_o} = \frac{K_p}{K_p + (1 - K_p) \exp(-R/k_m)} \quad \dots 1.7$$

where, R is the *linear rate of advancement of the solidification front* (a measure of rate of solidification), k_m is the *mass transfer coefficient* for the solute in the liquid, and is given by $k_m = D_l/\delta_c$, where δ_c is the *effective boundary layer thickness* in liquid at the interface and D_l is the diffusion coefficient of the solute in liquid. For more general cases, numerical solution is the only option available.

Microsegregation results from freezing of solute-enriched liquid in the interdendritic region. Maximum solute concentration would be in the solidified interdendritic liquid, and the minimum would be inside the grain. Microsegregation is usually evaluated by the '*Microsegregation Ratio*', which is the ratio of the maximum solute concentration to the minimum solute concentration after solidification. However, the estimation of microsegregation in real casting is made difficult due to various complexities including the movement of interdendritic liquid resulting from thermosolutal convection or solidification contraction. Again, solute distribution and microsegregation at microscopic level influence macroscopic convection and consequent macrosegregation, through its influence on solutal gradient and microstructure.

1.1.3 Nucleation, growth, and solidification morphology

Upon cooling, liquid transforms to solid through nucleation and growth of new phase. Nucleation is classified as homogeneous and heterogeneous. Heterogeneous nucleation is more prevalent due to presence of impurities in the melt. A detailed review on sources of nuclei, modes of grain growth and morphological transition is presented by Flood and Hunt[12]. For origin of nuclei, three principal mechanisms have been suggested, viz., (i) *Constitutional Supercooling* driven heterogeneous nucleation; (ii) *Big Bang Mechanism*; and (iii) *Dendrite Detachment Mechanism*. In constitutional supercooling driven mechanism, it is assumed that the heterogeneous nuclei form at the solidification front when sufficient constitutional supercooling is available. The big bang mechanism assumes that the pre-dendritic nuclei are formed in the chill zone, and are carried away elsewhere by convection. These grains survive at moderate superheat and act as nuclei.

Dendrite detachment mechanism assumes that the nuclei are formed due to fluctuations in growth rate and dendrite arm detachments. It is to be noted that the big bang and dendrite detachment together account for most of the observations.

Once a nuclei is formed it grows. In the beginning, the solid-liquid interface is of *plane-front* type. However, the nature of solid-liquid interface during the growth depends on solidification conditions and melt under consideration. It can remain plane-front or change to *cellular* or *dendritic* type. The final microstructure is largely governed by the interface morphology and various models are reviewed in literature [13-16]. Solid-liquid interface during dendritic growth can grow further instabilities to give rise to secondary and tertiary side branching. For example, recent model of Sekhar[17] provides the position of first secondary perturbation behind the dendrite tip. Evolving microstructure determines the permeability of the mushy region and plays an important role in evolution of macrosegregation.

At the level of macrostructure, there are basically two solidification growth morphologies, namely, *columnar* and *equiaxed*. In columnar solidification, dendrites grow along preferred crystallographic directions opposite to the direction of the heat flux. This results into what is known as the columnar zone. Columnar dendrites are stationary in space, and the network of columnar dendrites acts as a porous medium for interdendritic fluid flow. In addition to this, there is an equiaxed mode of solidification. Equiaxed grains grow in front of columnar grains and have no preferred orientation. They form a solid-liquid slurry and are free to move. Columnar-to-equiaxed transition (CET) occurs when equiaxed grains are sufficient in size and number to impede the advancing columnar front.

From the point of view of the present study, it is important to note that the flow in the mushy region is strongly dependent on solidification morphology. As noted earlier, in columnar solidification, the mushy region can be viewed as a porous medium. On the other hand, in the equiaxed mode of solidification, the solid and liquid can be treated as slurry. Thus, in columnar solidification, the porous network offers resistance to the flow whereas in equiaxed solidification, the flow in the mushy region is modified through the increased viscosity of the slurry. Clearly, solidification morphologies play an important role in governing of fluid flow and, in turn, on macrosegregation. Although, there is a

strong linkage between the flow and growth morphologies, the present study focuses on the flow only during columnar solidification.

1.2 Fluid Flow, Solid Movement and Macrosegregation

Macrosegregation is a complex phenomenon. At the same time, the control of macrosegregation is one of the most important quality issues in any solidification processing. Any attempt to control macrosegregation is aimed at control of fluid flow and solid movement.

There are various causes of fluid flow and solid movement during solidification and these are highlighted below. The movement of fluid during solidification results from the buoyancy forces caused by the density gradients in the liquid. The foremost cause of density gradient is the cooling process, which causes thermal gradient in the liquid and leads to thermal buoyancy. The resultant flow is called *thermal convection*. In addition to this, alloy solidification is accompanied by solute rejection at the solid/liquid interface, setting up composition gradient, and thus, density gradient in the liquid. This results in solutal buoyancy; the resultant convective flow is called *solutal convection*. In most situations, both are significant and the resulting convection has been termed *thermosolutal convection* or *double-diffusive convection* [18].

During dendritic solidification, density of the interdendritic liquid varies spatially as well as temporally due to constitutional and thermal effects, which leads to double-diffusive convection in the interdendritic region. The double-diffusive convection affects the transport of energy and solute in the mushy phase and, in turn, dictates the morphology of the mush in terms of orientation and growth of the primary as well as secondary dendrites. An important manifestation of significant double-diffusive convection in the interdendritic space is the formation of *freckles* or *channel segregates* [19]. Freckles are shown to form when the solidification rate is relatively slow and the interdendritic liquid flows in the same direction at more than the rate of solidification. Apart from the freckles, double-diffusive convection at both micro and macro scales also leads to macrosegregation due to long range solute transport from the mush to the bulk melt, as well as sedimentation and flotation of equiaxed grains.

Convection can also arise from suction caused by solidification shrinkage and contraction of solid and liquid during cooling. Besides these, surface shear stresses at free surfaces, which result from surface tension gradients (Marangoni effect), can also create significant fluid flow. Apart from the natural convection generated flow, external forces such as electromagnetic stirring or centrifugal acceleration may also be imposed to control the nature of flow. Forced convection are also caused by motion of gas bubbles, stirring, rotation, vibration, etc. in many casting situations.

There are various sources through which free moving crystals originate during the progress of solidification. Fine crystals formed due to chill action of mould is washed away with the fluid to the bulk liquid regime. These form the nuclei of equiaxed crystals. Free crystals also originate due to fragmentation of dendrites and through heterogeneous nucleation and growth ahead of growing dendrites[12]. These crystals can float or settle depending on the density difference with bulk liquid. This is believed to be the mechanism of formation of bottom cone of negative segregation in steel ingots[18].

Considering its commercial importance, solidification has been a topic of active research for more than a century. With the advent of digital computer and mathematical modeling techniques from the decades of 1960s and 1970s, numerical modeling of solidification phenomena has grown in popularity by leaps and bounds. Excellent reviews on numerical models of melting and solidification are available in literature [20, 21]. The purposes of these models are manifold viz., prediction of microstructure, macrostructure, microsegregation, macrosegregation, temperature profile, rate of solidification, etc. Numerical models have been developed to study variety of processes and typical examples of these can be found in reference cited below: laser melting and solidification [22-25], electron beam melting [26], permanent mould casting[27,28], continuous casting of steel [29], thin strip casting[30-32], crystal growth [33-35] and die casting[36]. The above list shows that numerical models have emerged as a powerful tool for understanding complex transport processes in large number of manufacturing processes involving solidification. Macrosegregation is a defect, which is present in many of the above processes.

The present day understanding of macrosegregation is the result of extensive research of last four decades starting with the pioneering work of Flemings and co-workers, and

these are summarized in various review articles [18-19, 37-40]. Flemings [40] has summed up our current understanding on macrosegregation as follows:

“ All types of macrosegregation in castings and ingots form within the solid-liquid zone. In most cases, it is the result of slow interdendritic flow, driven by shrinkage, geometry, solid deformation or gravity. In some cases, it may be the result of solid movement in early stages of solidification. (i.e., settling).”

Models of macrosegregation have generally aimed at understanding the basic mechanisms involved, quantitatively predicting the occurrence and severity of macrosegregation, and for obtaining the effect of various process parameters on macrosegregation. Key literatures on recent theoretical analyses as well as experimental works on macrosegregation are presented in detail in Chapter 2. As may be noted from these studies, mathematical models have provided good insight into the formation of macrosegregation during the progress of solidification. Sophisticated models have been developed which account for convection in presence of simultaneous columnar and equiaxed solidification with the help of multiphase-multiscale models[37]. These state of the arts models attempt to capture the physics of the process comprehensively. However, unavailability of a large number of thermophysical data required in these models as well as incomplete understanding of phenomena at the microscopic level, do not allow their satisfactory usage at present. As compared to that, single domain models require fewer thermophysical data and have been widely employed[37] for study of macrosegregation. For example, the exact reproduction of double-diffusive convection cell in a transparent system[41] as well as good qualitative match with experimental data on macrosegregation pattern in a lead-tin system[42] are some of the highlights of the capability of the single-domain model for prediction of macrosegregation.

However, as noted in various reviews [18,37-38], quantitative match between model prediction and experimental data are far from satisfactory. There are several reasons cited in literature for this mismatch, as noted below:

- (i) Permeability functions for the entire solidification range are not known. Moreover, permeability is anisotropic, whereas most of the modeling work is based on isotropic permeability model.

- (ii) Thermophysical data are often not available for mixtures of solid and liquid. A better mixture or averaging model is required.
- (iii) Experimental data are limited and these are generally not complete in all respects for usage in mathematical models. Heat transfer coefficients, which form the boundary conditions for the energy equations of macrosegregation models, are not known precisely.

1.3 Objectives of the Present Investigation

Based on the literature review, it was decided to undertake combined mathematical modeling and experimental studies on macrosegregation. It was decided to perform experiments on as simple a situation as possible for attempting meaningful correlation. Hence the following were decided as the objectives of the present investigation.

- (i) Experimental measurements are to be carried out using unidirectional cooling. Pb-Sn system was chosen, as it is best-characterized system in fundamental solidification studies. Hence theoretical calculations will be more reliable. It was also decided that comparison would be made of two types of experiments without convection and with solutal convection.
- (ii) Mathematical modeling will be only macro-modeling which is a continuum model and does not require experimental microstructural details except dendrite arms spacing (DAS). The model will be used to predict macrosegregation for conditions prevailing during experiments and calculated values will be compared with experimental data.
- (iii) Existing experimental data available in literature on horizontal solidification on metallic and transparent systems will be employed to investigate the role of uncertain parameters namely, permeability, thermophysical properties and heat transfer coefficient, on macrosegregation.
- (iv) Influence of materials and cooling rate on macrosegregation will be studied using the numerical model of the present investigation.

1.4 Plan of Work

- (i) Development of a mathematical model for 2-dimensional rectangular coordinate system and 2-dimensional cylindrical polar coordinate systems based on continuum formulation
- (ii) Validation of the mathematical model with existing numerical and experimental results from literature
- (iii) Simulations of key horizontal solidification experiments reported in literature with the help of mathematical model to study the role of permeability and simulation studies on role of materials, cooling rate and thermosolutal coupling on macrosegregation
- (iv) Design and development of experimental setup for performing vertical solidification of lead-tin alloys
- (v) Preparation of alloys and trials, standardization and calibration of measurements involved, i.e., temperature, composition and metallography
- (vi) Performing experiments with hypo-eutectic and hyper-eutectic lead-tin alloys for various cooling rates and superheats
- (vii) Measurement of transient temperatures: (a) at five vertical locations inside casting, (b) at two locations in chill block, (c) at the top of the casting and (d) of water at the inlet and the outlet of water cooling jacket. The temperatures inside the casting are to be used for validation and evaluation of model performance. Other temperature readings are for determining the correct heat flux from the bottom of the casting to be used by the model
- (viii) Post solidification measurements of (a) dendrite arms spacing for usage in permeability correlation of macrosegregation model and (b) macrosegregation at various locations through atomic absorption spectroscopy
- (ix) Numerical simulations of vertical solidification of the present investigation experiments with the help of the mathematical model developed, and comparison of computed and experimental macrosegregation values.

Chapter 2

LITERATURE REVIEW

As stated in Ch.1, macrosegregation is a complex phenomenon. At the same time, the control of macrosegregation is one of the most important quality issues in any solidification processing. Any attempt to control macrosegregation is aimed at control of fluid flow and solid movement. Fundamentals of solidification phenomena such as heat transfer during solidification, solute redistribution and microsegregation, nucleation, growth, and solidification morphology, and fluid flow, solid movement and macrosegregation have been briefly reviewed in Ch.1. Hence, the same shall not be repeated here.

This chapter contains more detailed reviews of the following topics, which are of direct relevance to the present study. These are as follows:

- (i) Mathematical modelling of macrosegregation
- (ii) Modeling of permeability through the mushy region
- (iii) Thermophysical properties and thermodynamic data
- (iv) Literature review on solidification studies in lead-tin system

2.1 Mathematical Modeling of Macrosegregation: Historical Perspective

The present day understanding of quantitative aspect of macrosegregation is the result of extensive research of last four decades starting with the pioneering work of Flemings and co-workers and these are summarized in various review articles [18-19,37-40]. Early macroscopic models that included convection effects were highly simplified and neglected the coupling that exists between flows in the solid, mushy, and liquid zones. Amongst the earliest models that link macrosegregation to interdendritic fluid flow are those of Flemings and co-workers[43-45]. They developed a differential solute redistribution equation for application in the mushy phase. The flow in the bulk liquid region was not treated explicitly. Interdendritic flow was assumed to be induced by solidification shrinkage, and solute was transported by fluid advection. However, the

analysis required prescription of the temperature and fluid velocity fields. Although the model had limited utility, it did demonstrate how interdendritic flow is responsible for macrosegregation. Later, Mehrabian et al. [46], extended the solute redistribution model by incorporating an equation for buoyancy driven flow in the mushy zone. Using Darcy's Law, the mushy zone was treated as a porous medium, and its permeability was a prescribed function of the liquid volume fraction.

However, a shortcoming of the solute redistribution model is that it does not account for coupling, which exists between the mushy and fully melted zones. The first model to incorporate coupling between mushy and bulk liquid zones was reported by Szekely and Jassal[47], who predicted thermal convection both in the melt and the mushy regions. Transport equations were developed for a solid-liquid mixture in the mushy zone, and traditional single-phase equations were used for the melt. However, the effects of solutal buoyancy were ignored, and macrosegregation was not predicted. These models[47] and other similar models have been classified as *multi-domain models*, because the mathematical solution domain is distinctly divided according to the physical domains (solid, mushy, and melted zones). Because of practical considerations related to their numerical solution algorithms, multi-domain models are not well suited for predicting irregular interface shapes.

Single domain models, which overcame many of the limitations of the multi-domain models, emerged in the eighties. Bennon and Incropera[48-49] and Voller et al [50] presented a set of equations for momentum, energy, and species transport in binary, solid-liquid phase change systems based on mixture-theory. The single-domain equations obtained through application of mixture theory concurrently applied in all regions(solid, mushy, and liquid). It required only a single, fixed numerical grid and a single set of boundary conditions to effect a solution. The mushy zone in these was viewed as solid-liquid mixture with averaged macroscopic properties. Equations for solid and liquid phases, which were valid in the respective single-phase regions, were averaged to form a set of conservation equations for solid-liquid mixtures in mushy zone. Limiting assumptions were invoked (a non-deforming solid phase, $T_s = T_l$, and no diffusion through the solid phase) to reduce the number of dependent variables. The solidus and liquidus interfaces, as well as individual phase variables, were implicitly determined by

solving the mixture equations. Diao and Tsai[51] also developed single-domain model based on this concept.

Single-domain models were also developed employing technique of volume averaging as the basis for deriving macroscopic conservation equations for individual phases. As opposed to summations employed in mixture theory, integration of microscopic equations over finite volume is applied in volume-averaging technique. Models presented by Beckermann and Viskanta[41], Rappaz and Voller[52] and Ganesan and Poirier[53-54] were based on this technique.

Chang and Stefanescu[55] developed a continuum formulation based macrosegregation model which considered liquid flow and solid grain transport by thermosolutal convection as well as solidification contraction. A more elaborate treatment of fluid flow at free surface was incorporated. A hybrid mush model combining Kozeny-Carman model and variable viscosity function was used to account for the resistance to flow in the mushy region.

Goyeau et al [56] presented an alternative method for the assessment of macroscopic conservation equations in solidification processes to consider the two-phase, solid-liquid system as an equivalent continuum. The technique consisted in averaging the local conservation equations on an elementary representative volume and led to averaged equations where the coefficients were effective properties of the solid-liquid mixture. The study considered in detail the specific structure of dendritic mushy zones, characterized by a strong anisotropy, by the presence of porosity gradients along the dendrite arms and by a velocity of the solid-liquid interface. This approach allowed to determine the permeability tensor over a wider range of porosity and in a much less empirical way than the usual Kozeny-Carman relation used in most solidification models[57].

Ni and Incropera [58-59] developed a new model which combines the convenience of mixture theory based continuum model with inclusion of important features volume-average two-phase model. Several assumptions of the two-phase model were relaxed to make it possible to account for the effects of solutal undercooling, solidification contraction and solid movement.

Ahmed et al [60] performed macrosegregation calculations using volume-averaged model [52] and employing numerical techniques of finite-volume based and finite-element

methods to provide benchmark solutions. Although same parameters were used in both numerical methods, some differences were observed in results. Model was also used to simulate experiments on Pb-48 wt % Sn alloy and Sn-5 wt % alloy and reasonable agreements were reported.

Krane et al [61-63] developed the continuum formulation based model for solidification of ternary alloy and studied solidification of Pb-Sb-Sn ternary alloy. Yang et al [64] presented a continuum formulation based model for simulation of microstructure in multi-component alloys with equiaxed dendritic and eutectic morphology and implemented the model to study solidification of Al-Si-Mg alloy. The model accounted for the effects of natural convection, solidification contraction, solidification kinetics and grain movement during solidification. Chakraborty and Dutta[65] incorporated effect of solutal undercooling on thermosolutal convection and macrosegregation. The effect of non-equilibrium solidification was incorporated through modified partition coefficient, which, in turn, was based on parameters predicted by macroscopic model. The model predictions showed excellent agreement with the experimental data. In a separate study, Chakraborty and Dutta[66], et al incorporated the effect of dendrite arm coarsening into the macroscopic framework. Simulation results were compared with experimental results on Al-Cu and showed better match with macrosegregation data compared to model, which were based on shrinkage-induced flow alone. It was explained that due to inaccuracy in both the model, Kozeny-Carman model was used in conjunction with variable viscosity model due to its inaccuracy of permeability model above $f_l > 0.5$.

Xu [67-68] used single-domain volume averaged approach to incorporate micro-scale model in macrosegregation calculations. By doing so, the macro-micro model relaxed the need for assumptions of Scheil equation or lever-rule based micro-scale solidification models. The micro-macro model was applied to Al-Cu and Fe-C alloy solidification.

As discussed earlier, modelling of transport of species is important in large number of manufacturing processes and for large number of alloy systems. Few such studies are reviewed below. Simpson and Garimella[69] studied horizontal solidification of Sn-Bi alloy in a rectangular mould (length = 35 mm, height 50 mm) under terrestrial conditions and concluded that significant macrosegregation results due to large level of thermal convection. Simpson et al [70] also studied the effect of thermosolutal convection on

Bridgeman crystal growth of Bi—Sn alloy under micro-gravity. It was observed that thermosolutal convection resulted in measurable levels of radial segregation despite the reduced level of gravity. Kuppurao et al [71-72] studied Bridgeman growth of Cd-Zn-Te. They carried out a quasi-steady state analysis of heat transfer and convection in the ampoule and concluded that the shape of the solid/liquid interface was sensitive to the growth rate due to importance of latent heat release[71]. Subsequently, they studied segregation of zinc during crystal growth with the help of the model by carrying out transient calculations[72]. It was shown that significant segregation resulted due to convective mixing in the melt.

Zou et al[73] studied the mechanisms of thermosolutal transport and segregation in Czochralski crystal growth of III-IV compound (GaAs, InP, etc.). Flow and temperature solutions were obtained from quasi-steady state analysis whereas dopant transport and growth were considered at a finer time scale. It was shown that the combined effect of crystal rotation and natural convection resulted in strong radial segregation.

G. Phanikumar et al [74] developed a numerical model for the case of laser welding of dissimilar couples of Cu-Ni. The model was based on transport of energy, momentum and species. It was observed that weld-pool became asymmetric when the heat source was applied symmetrically on two metals forming the couple. Predicted weld pool shapes showed good qualitative match with experimental data.

Macrosegregation is an important issue in both ingot as well as continuous casting of steel and excellent reviews on the subject are presented elsewhere[18]. Steel is a multi-component alloy and segregation in steel is dependent on large number of factors such as turbulent flow, morphological transition, bulging, gas evolution and so on. Considering the complexity of the process, numerical models of continuous casting are gradually evolving. For example, in combined experimental and numerical study on macrosegregation and morphological transition in billet casting [75,76]. Choudhary and Ghosh [75] collected continuously cast billets and determined carbon, sulfur and positions of CET. This allowed calculations of liquidus temperature at CET location. Conjugate heat transfer-fluid flow model was used to compute temperature fields. The points, which gave the liquidus of CET boundaries were determined and compared with experimentally observed locations of CET. A good agreement was obtained.

Modeling of macrosegregation in iron-carbon and iron-carbon based steel ingots has been carried out by several researchers in the past. Amberg [77] reported a numerical study on Fe-C alloy by using a continuum formulation based model. Singh and Basu [78] carried out simulations to study the role of thermosolutal convection on macrosegregation during solidification of binary Fe-1 wt % C alloy. The effect of thermosolutal convection on extent of segregation and segregation profile were critically examined. In a separate study, Singh and Basu[79] investigated the importance of thermosolutal coupling on evolution of macrosegregation in Fe-C alloy. It was shown that in evolution of macrosegregation, the role of solutal field in defining mush profile through thermosolutal coupling was more important compared to its effect through buoyancy forces.

Lesoult, Combeau and co-workers [80-81] have reported the significant effects of permeability and carbon partition coefficient on axial segregation during solidification of multi-component steel. A significant conclusion of this work is that the axial segregation increases with an increase in permeability or a decrease in carbon partition coefficient. Schneider and Beckermann [82], using a fully coupled multi-component model, have shown that segregation profiles of carbon in multi-component steel show the same trend as in binary Fe-C alloy owing to dominant role of carbon in solutal buoyancy and thermodynamic equilibrium. Gu and Beckermann [27] have reported combined experimental and numerical study of solidification of industrial steel (micro-alloy medium carbon steel) ingot. Predicted segregation profile along the vertical centerline showed good qualitative match with experimental observations at the top of the ingot.

2.2 Single domain model

Typical single-domain model for columnar solidification [50] results in following set of equations for the transport of mass, momentum, energy and solute in two-dimensional, rectangular co-ordinate system.

Continuity

$$\frac{\partial \rho}{\partial t} + \nabla \cdot (\rho \mathbf{U}) = 0 \quad \dots 2.1$$

Momentum

$$\frac{\partial(\rho \mathbf{U})}{\partial t} + \rho \nabla \cdot (\mathbf{v} \mathbf{U}) = -\nabla p + \nabla \cdot (\mu \nabla \mathbf{U}) + \mathbf{F} - \mathbf{B} \quad \dots 2.2$$

Energy

$$\frac{\partial(\rho h)}{\partial t} + \nabla \cdot (\rho \mathbf{U} h) = \nabla \cdot \left(\frac{\kappa}{c_l} \nabla h \right) + S_e \quad \dots 2.3$$

Solute

$$\frac{\partial(\rho C)}{\partial t} + \nabla \cdot (\rho \mathbf{U} C) = \nabla \cdot [f_l D_l \nabla C_l + f_s D_s \nabla C_s] \quad \dots 2.4$$

In the above equations, \mathbf{U} is the velocity vector, h is the enthalpy, C is the mixture composition, t is the time, ρ is the density, μ is the viscosity, p is the pressure, \mathbf{F} is the source term representing resistance to flow in the mushy region, \mathbf{B} is the body force, k is the conductivity, f_s and f_l are the fraction solid and liquid, respectively, S_e is the source term of energy equation, and D is the diffusivity of solute. Subscripts s and l stand for the solid and the liquid phases, respectively.

In the above governing equations, transport variables, such as \mathbf{U} , h , C , etc. are volumetric mixture averages. Transport properties, such as thermal conductivity and solute diffusivity in the mushy region were obtained through mass averaging of solid and liquid properties. In order to complete the above set of governing equations, few supplementary equations are needed. For example, using *Boussinesq approximation*, the body force, \mathbf{B} , in the momentum equation can be expressed as:

$$\mathbf{B} = \rho_{\text{ref}} \mathbf{g} [\beta_T (T - T_{\text{ref}}) + \beta_C (C - C_{\text{ref}})] \quad \dots 2.5$$

where, \mathbf{g} is the acceleration due to gravity, β_T is the coefficient of thermal expansion, β_C is the coefficient of solutal expansion, and subscript 'ref' denotes reference value.

For columnar solidification, the resistance of flow through the mushy region is generally modeled using *Darcy Law*.

$$\mathbf{F} = \frac{\mu}{\mathbf{K}^{(2)}} \mathbf{U} \quad \dots 2.6$$

where, $\mathbf{K}^{(2)}$ is the permeability tensor. As outlined in the section below, permeability of the interdendritic region essentially largely determines the macrosegregation.

2.2.1 Modeling of permeability through the mushy region

In models of alloy solidification, modeling of mushy region is the key. For columnar solidification, mushy region is treated as porous media and Darcy's Law is applied. Darcy proposed that the pressure drop through the medium is directly proportional to the flow rate and viscosity of the liquid and inversely proportional to the permeability. Subsequently, Darcy's Law was modified to include the effect of viscous stress to the pressure gradient in the flow field [83]. For equiaxed solidification, the mushy zone is treated as a slurry of liquid and solid, and variable viscosity model has been used to model flow [84].

The permeability of a dendritic array depends on several factors, including the local volume fraction solid and its structure. In most of the solidification models, Kozeny-Carman equation [85] is employed to represent this relationship (see Table 2.1). Although, isotropic permeability has been widely used in the past, it has failed to provide close quantitative agreement with experimentally observed data [42]. One of the areas of improvement is the use of anisotropic nature to model the mushy region. Since the permeability is responsible for flow, heat and solute transport in the mushy region, a realistic representation of the mushy region can bring about better quantitative prediction. The effect of anisotropic permeability on thermosolutal convection and other solidification parameters has been demonstrated by Yoo et al [86] and Sinha et al [87]. Through a parametric study on $\text{NH}_4\text{Cl-H}_2\text{O}$, Yoo et al [86] has shown the important effect of use of anisotropic permeability on thermosolutal convection. However, the main difficulty lies in obtaining reliable isotropic/anisotropic models of permeability for the entire mushy region.

Table 2.1: Various permeability models

Model	Expression	Range of validity
Kozeny-Carman [85]	$\frac{K}{d^2} = 5.67 \cdot 10^{-3} f_1^3 / (1 - f_1^2)$	$f_1: 0.0-1.0$
Closure [57]	$\frac{K_{PR}}{d^2} = 10^{4.7248 \cdot \log(f_1/f_s) - 6.0218}$	$f_1: 0.365 - 0.89$
	$\frac{K_{NR}}{d^2} = 10^{2.5791 \cdot \log(f_1/f_s) - 4.33638}$	$f_1: 0.365 - 0.89$
Poirier [90]	$\frac{K_{PR}}{d^2} = 3.75 \times 10^{-4} f_1^2$	$f_1: 0.17 - 0.61$
	$\frac{K_{NR}}{d^2} = 0.001 \cdot f_1^{3.32} d^{0.08}$	$f_1: 0.19 - 0.66$
West [89]	$K = (6.4 \times 10^{-13}) \cdot f_1^2$	$f_1 < 1/3$
	$K = (6.4 \times 10^{-13}) \cdot f_1^2 + (8.8 \times 10^{-11}) \cdot f_s^{2/3} \cdot [3 + 4/f_s - 3 \cdot (8/f_s - 3)^{1/2}]$	$f_1 > 1/3$

Piwonka and Flemings [88] carried out experiments in which molten lead was forced through the semi-solid aluminum-copper alloy, and flow rates were measured for various pressures and fractions solid. At higher fractions of liquid, data were obtained by passing nitrogen directly through the semi-solid network for forced flow of the interdendritic liquid. Experimental data were found to follow Darcy Law. These data were employed by West [89] to fit a piecewise linear model (Table 2.1). However, it does not provide for the variation of permeability with dendrite arms spacing. Using experimental data on lead-tin and borneol-paraffin, Poirier [90] has tested several analytical models for flow parallel to the primary dendrite and flow perpendicular to the primary dendrite and recommended variety of models including regression based permeability models for both directions (Table 2.1). These expressions provide data up to 66 % liquid fraction only.

Despite the fact that the macrosegregation is greatly influenced by permeability in high liquid fraction zone[40], permeability data for high liquid fraction are not available due to fragile nature of dendrite at high liquid fractions. To overcome these difficulties, numerical simulations of flow through tortuous paths have been performed to provide permeability data for high liquid fractions of the mushy region[91-92]. Recently, Goyeau et al. [57] numerically estimated permeability of the mush by solving the closure problem resulting from averaging procedure. This procedure employed data on mush structure (digitized image of dendritic structure) and has given permeability expression for a wider range (Table 2.1). It allowed the determination of permeability tensor over a wider range of porosity and in a much less empirical way than the usual Kozeny-Carman relation.

As may be noted from the above table, except for West [89] model, permeability is a function of dendrite arms spacing (d). Ahmed et al [60] has studied the effect of variation of DAS on macrosegregation. Krane et al. has varied permeability coefficient of Kozeny-Carman equation [85] to obtain better match with the experimental data [42]. They also used permeability expression of West [89] in macrosegregation model, and obtained better match with the experimental data. Schneider and Beckermann [93] have carried out numerical study of Pb-Sn system using anisotropic permeability model [90]. Singh et al [94] carried a numerical study on solidification of $\text{NH}_4\text{Cl-H}_2\text{O}$ in a rectangular cavity using three permeability models, namely, Kozeny-Carman[85], Closure [57] and Poirier[90] models. It was observed that Poirier and Closure models provided nearly

identical results despite the fact that permeability data used in these models were obtained from different sources. Also, the level of segregation, predicted by these models, were lower than the Kozeny-Carman model. Thus, it is seen that a large number of permeability models have been proposed in the past and many of these have been employed in macrosegregation calculations. It is concluded in many studies (for example[42]) that discrepancy in permeability function is one of the key reasons for poor predictive power of macrosegregation models.

2.2.2 Thermophysical properties and thermodynamic data

In order to solve Eqs. 2.1 through 2.5, a large number of thermophysical properties and phase diagram-related inputs are required. Thermophysical properties required by the model include density, thermal conductivity, mass diffusivity, specific heat, latent heat of fusion, coefficients of thermal and solutal expansion, viscosity, etc. Additionally, auxiliary models require data from relevant phase diagram such as partition coefficient, slope of the liquidus, composition and temperature of eutectic point, and so on. It is clear that the performance of the model is largely governed by the accuracy of these data. In the present study, experimental investigations were carried out in lead-tin alloys. This system has a simple and well-established phase diagram (Fig. 2.1). In addition to this, precise thermodynamic and thermophysical data of this system are available. Other reasons for selection of this alloys are: (i) lead-tin alloys have low melting point, which makes the processing easier, and (ii) solidification of Pb-Sn system has been extensively studied and some of the literature can be used for comparison. Here it is worthwhile to note that lead-tin is a popular alloy for solidification studies from early days [1].

Thermophysical properties relevant for the model are compiled in Table 2.2. The compilation is mainly done from few standard sources[95-99]. In most of the references [95,96], properties are provided for pure components only. In case of viscosity, data on individual components are provided at large number of temperature[98] but for alloys, these are at fewer temperatures (liquidus, 300°C and 550 °C). Properties of alloys are obtained through averaging over component and phase fraction. As noted by Prescott[100-101], this is not true for many alloys which exhibit extreme in there

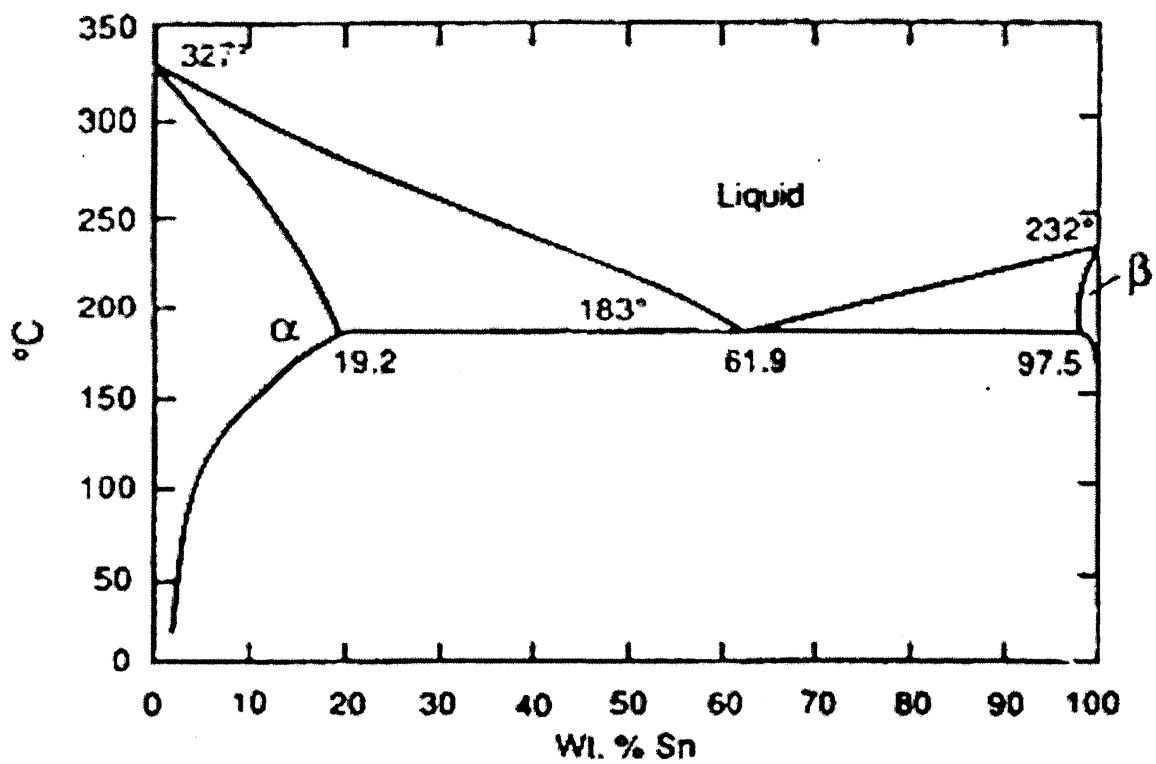


Fig. 2.1: Phase diagram of Pb-Sn binary alloy

Table 2.1: Thermophysical properties of lead-tin alloys

Properties	Value	Ref.
Density (kg/m ³)	$\rho_{\text{Pb}} = 11077 - 12800 \times 10^{-4} T$ $\rho_{\text{Sn}} = 7147 - 6895 \times 10^{-4} T$ $\rho_{\text{Pb-Sn}} = c_1 + c_2 T$ $c_1 = 11071 - 3184 X_{\text{Sn}} - 1481 (X_{\text{Sn}})^2 + 751 (X_{\text{Sn}})^2$ $c_2 = (-12777 + 2675 X_{\text{Sn}} + 8025 (X_{\text{Sn}})^2 - 751 (X_{\text{Sn}})^2) \times 10^{-4}$ T is in °C, X _n is atom fraction	97
Viscosity (kg/m/s)	$\mu_1^{\text{Sn}} = 2.75 \times 10^{-5} (\rho_1^{\text{Sn}})^{1/3} \exp(0.0885 \rho_1^{\text{Sn}}/T)$ $\mu_1^{\text{Pb}} = 2.54 \times 10^{-5} (\rho_1^{\text{Pb}})^{1/3} \exp(0.0863 \rho_1^{\text{Pb}}/T)$ ρ is in kg/m ³ and T is in K	93, 99
Thermal conductivity (W/m/K)	$\ln k_l^{\text{Sn}} = 0.85337 + 0.4109 \ln(T)$ $\ln k_l^{\text{Pb}} = -2.0725 + 0.7521 \ln(T)$ $\ln k_s^{\text{Sn}} = 4.5422 - 0.1708 \ln(T)$ $\ln k_s^{\text{Pb}} = 3.7507 - 0.2087 \ln(T)$ T is in K	54, 98
Specific heat (J/kg/K)	$c_1^{\text{Sn}} = 257; c_1^{\text{Pb}} = 147.9$ $c_s^{\text{Sn}} = 155 + 0.22 T; c_s^{\text{Pb}} = 114.8 + 0.0447 T$ T is in K	95
Latent heat (J/kg)	$(\Delta H)_{\text{Pb}} = 22980 \text{ to } 23380 \text{ J/kg}$ $(\Delta H)_{\text{Sn}} = 59500 \text{ J/kg}$	95
Diffusivity (m ² /s)	3.0×10^{-9}	93
Coefficient of thermal expansion (1/K)	-1.23×10^{-4}	95
Coefficient of solutal expansion (1/wt frac.)	0.525 (Sn-Pb) -0.339 (Pb-Sn)	95

transport properties at intermediate values of composition. For lead-tin systems, Touloukian et al [98] and Thresh et al[99] showed monotonic in transport properties with composition, Toyas et al [102] observed anomaly in viscosity data in middle composition range of Pb-Sn binary alloys.

Viscosity as well as other transport properties affects macrosegregation calculations significantly. It is worthwhile to note that measured viscosity data are up to liquidus temperature and in macrosegregation calculations the same value is used between liquidus and solidus/eutectic temperatures. Therefore, it is desirable to carry out some sensitivity analysis in mathematical modeling exercise. As Ahmed et al[60] have reported, viscosity and other thermophysical properties need to be calibrated substantially to obtain best mean fit with experimental data on macrosegregation and solid-liquid front[103].

2.3 Literature Review on Solidification Studies in Lead-Tin System

There have been large numbers of investigations on solidification of Pb-Sn alloys. In this section, only a few, especially recent studies, which are of direct relevance the present investigation, have been reviewed.

2.3.1 Horizontal solidification of lead-tin alloys

In the present investigation, we are concerned with influence of thermosolutal convection on macrosegregation. The studies reported in literature can be classified under two categories: (i) horizontal solidification (Fig. 2.2a) and (ii) vertical solidification (Fig. 2.2b).

During horizontal solidification, solutal and thermal buoyancy may either augment or oppose one other, depending on the relative densities of alloy constituents and the constituent that gets rejected into interdendritic liquid during progress of solidification. The relative strength of solutal and thermal buoyancy is given by *buoyancy parameter*, N , which is defined as follows.

$$N = \frac{\beta_S}{m\beta_T} \quad \dots 2.7$$

where, β_S and β_T are the coefficient of solutal and thermal expansion, respectively, and m is the slope of the liquidus line on the equilibrium phase diagram.

For $N > 0$, solutal buoyancy augments thermal buoyancy. Conversely, they oppose each other if $N < 0$. For $-1 < N < 0$ solutal buoyancy partially offsets thermal buoyancy, whereas for $N < -1$ solutal buoyancy opposes and totally dominates [18]. These are schematically shown in Fig. 2.3.

NH_4Cl -70 wt % H_2O , Fe- 1 wt % C and Pb-15%Sn are examples of systems with $N < 0$, whereas Sn-10 wt % Pb and Al-4.5% Cu are example of systems with $N > 0$. It is noted here that there are numerous studies on both types of system. Some of the recent studies on side cooling are reviewed below.

Shahani et al [104] studied the freezing of Sn-10 wt % Pb and Pb-15 wt % Sn solidified in a vertical square cavity. Cooling was horizontal. With respect to Fig. 2.2a, where one vertical wall is adiabatic, in this study both the walls were cooled and experiments were performed with a constant temperature difference maintained between the vertical walls, while the temperatures of both walls were brought down. Solidified ingots were analyzed for macrosegregation. Experiments were also simulated with the help of a continuum model. West's model [89] was used for permeability. Measured temperatures were used as boundary conditions in the model. Thermal and solutal buoyancy forces augmented each other during the solidification of Sn-10% Pb alloy. Predictions are in qualitative agreements with the measured macrosegregation results. In case of Pb-15 wt % Sn, convection and macrosegregation patterns are complex compared to Sn-10 wt % Pb alloy due to opposing nature of thermal and solutal buoyancy forces. The agreement with experimental data is again qualitative. In majority of the cases, predicted segregation is less than the observed segregation.

Prescott, et al [100-101] studied the freezing of Pb-19 wt % Sn alloy in a vertical cylindrical mould. Cooling was horizontal and radial. Experiments were carried out in axisymmetric, annular mould of stainless steel, cooled at the outer vertical wall. The

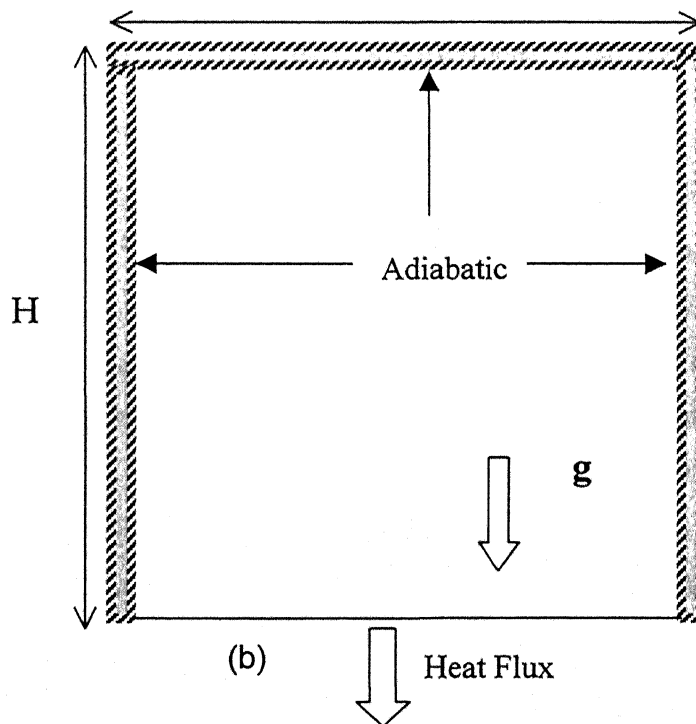
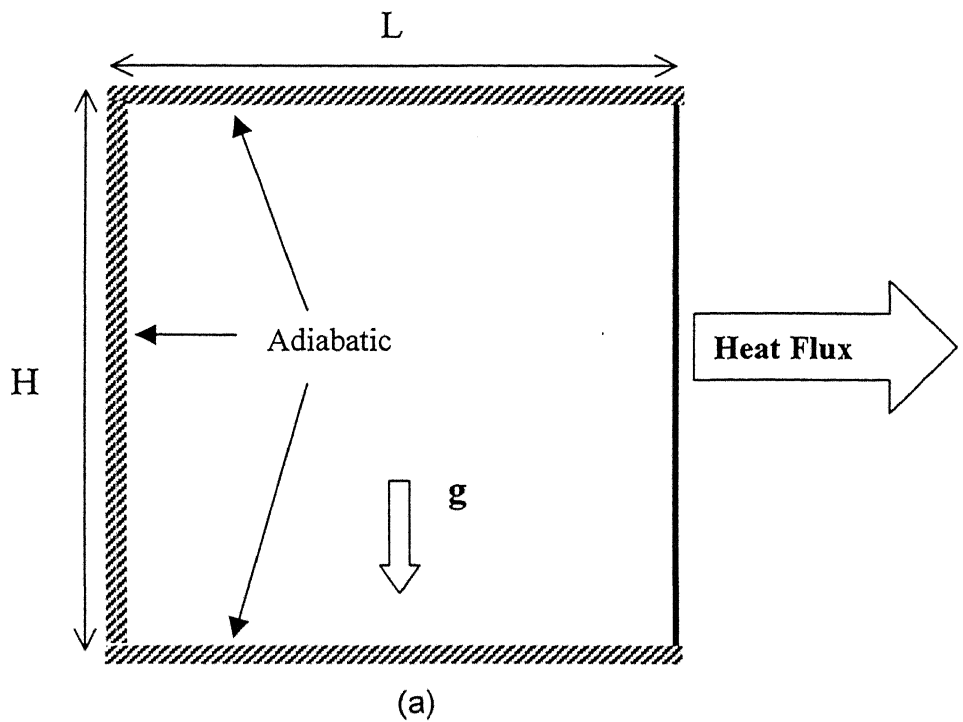
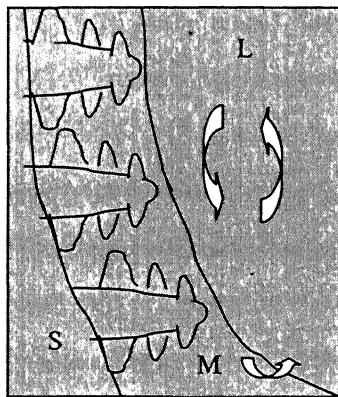


Fig. 2.2: Schematic of (a) horizontal solidification and (b) vertical solidification

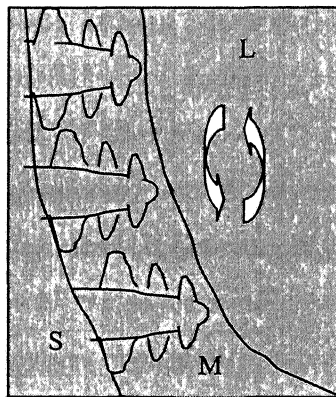
predicted thermosolutal convection patterns and the macrosegregation trends were verified through comparisons with measurements. The predicted cooling rate exceeded the measured cooling rate and the difference was attributed to uncertainties in prescribed thermodynamic properties. There was considerable variation of concentration along the circumference, demonstrating that the macrosegregation was not symmetric. The agreement between predicted and measured macrosegregation was qualitative due to large scatter in data.

Schneider and Beckermann [93] studied the combined effects of microsegregation, mushy zone permeability and flow, caused by solidification contraction and thermosolutal convection on macrosegregation and eutectic phase formation in binary Pb-Sn alloy solidification. Scheil and lever rule gave similar macrosegregation patterns though predicted eutectic fractions for the above cases differed. It was also shown that thermosolutal convection dominated over buoyancy caused by solidification contraction in this system. Krane and Incropera[105] also analyzed effect of shrinkage on macrosegregation in lead-tin alloy numerically and concluded that overall contribution of contraction-induced flow is small.

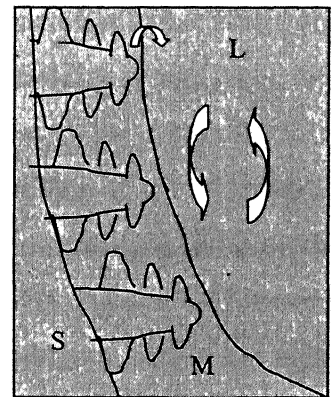
Krane and Incropera [42] carried out numerical and experimental studies on Pb-20%Sn and Pb-40%Sn. The solidification was considered in rectangular cavity (89 mm wide and 75 mm tall) and cooling was carried out through the vertical walls. Thermal history and macrosegregation were obtained from experiments. Measured thermal histories were in good agreement with the predictions. Large deviations were found between observed and predicted macrosegregation when Kozeny-Carman model [85] used for permeability. It was observed that Kozeny-Carman model (Table 2.1) over-predicted flow and consequent macrosegregation. When the coefficient of Kozeny-Carman model was reduced by an order of magnitude ($2.8 \times 10^{-11} \text{ m}^2$ in place of 2.8×10^{-10}), the model prediction provided better match with the experimental observations. Calculations were also performed using West's permeability model (Table 2.1) and results showed better match with the experimental data. It was concluded that the actual permeability near the high liquidus interface is much lower than that predicted by the Kozeny-Carman model, due possibly to the unrealistically rapid rise of the permeability near the liquidus surface.



(a) $N > 0$



(b) $-1 < N < 0$



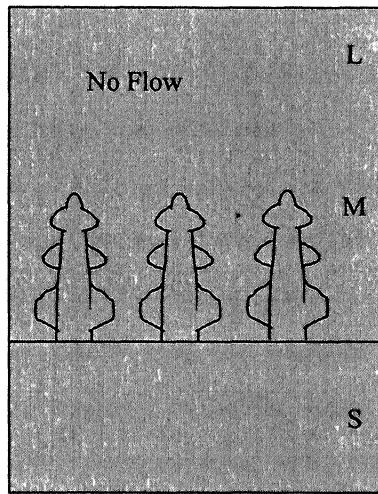
(c) $N < -1$

Fig. 2.3: Thermosolutal solutal convection pattern in the melt and mushy zone of a solidifying alloy (a) solutal buoyancy augmenting thermal buoyancy force, (b) solutal buoyancy forces opposing thermal buoyancy forces, with thermal buoyancy dominating in the mushy zone, and (c) solutal buoyancy forces opposing and dominating thermal buoyancy forces in the mushy region [18]

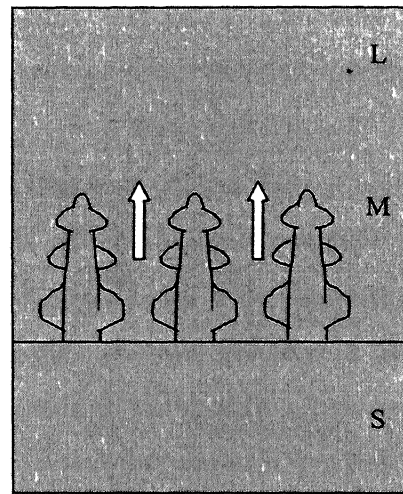
Ahmed et al [60] carried out simulations on Sn-5 wt % Pb and Pb-48 wt % Sn in rectangular cavity using both Finite Volume Method (FVM) and Finite Element Method (FEM). Cooling was horizontal. Kozeny-Carman[85] permeability model was for the mushy region. Experimental data of literature [103] were used for comparison. Heat transfer coefficient, used in the model, was estimated from the data on solid-liquid interface location, obtained through quench experiments. The macrosegregation predicted by both models were compared with the experimental data. As mentioned by Ahmed et al [60], viscosity and other thermophysical properties were calibrated to obtain best mean fit with experimental data on macrosegregation. However, the match was not good for one transverse plane near the top of the casting for Pb-48 wt % Sn alloy. Similarly, the match was not good for the transverse plane near the bottom for Sn-5 % Pb alloy. Using the model, sensitivity of macrosegregation on viscosity and dendrite arms spacing was examined. The model solutions were recommended as a numerical benchmark for FVM and FEM-based macrosegregation models.

2.3.2 Unidirectional cooling from bottom

Unidirectional cooling from the bottom is the simplest geometry. Since temperature increases in the upward direction, liquid is denser towards the bottom. Hence thermal buoyancy opposes upward motion of liquid. For alloy systems, where rejected solute in the interdendritic region is heavier than the solvent, solutal buoyancy force also acts downward making the configuration both thermally and solutally stable. For example, Sn-10 wt % Pb when cooled from bottom shows no flow due to thermosolutal convection. In contrast to this, alloys with lighter solute has solutal buoyancy acting in upward direction. This causes defects such as freckles and macrosegregation under favorable conditions. These two cases are schematically shown in Fig. 2.4. Several investigations have been carried out with static melts cooled from the bottom. Excellent review on the resultant flow in such configuration is presented by Worster[19]. During bottom cooled vertical solidification, solute-rich fluid can become unstable if the solute is the lighter component. This instability gives rise to narrow jets of fluid moving upward from the mushy region into the overlying melt[106]. This results in chimneys which are called freckles when they appear on surface of the casting. Sazarin and Hellawell[107] studied



(a)



(b)

Fig. 2.4: Schematic of flow conditions during bottom cooled solidification
 (a) heavier solute, (b) lighter solute

channel formation Pb-Sn and other alloys. In the experiments, a constant cooling rate ($0.5\text{ }^{\circ}\text{C}/\text{min}$) was applied at the bottom of the ingot and whereas the gradient in the melt was not controlled and it varied with time. It was observed that with increase in wt % Sn in Pb-Sn alloy, number of chimneys decreased. Average dendrite arms spacing and axial segregation were also reported.

Tewari and co-workers [108-111] studied solidification of Pb-Sn alloy under variety of conditions. Directional solidification was carried out in high temperature furnace by raising and lowering the furnace at various growth speeds past a stationary crucible. The crucible I.D. was 7 mm and melt height was 20 cm. Thermal gradient in the melt was determined by geometry of the furnace. As a function of composition, macrosegregation increased with increase in wt % Sn from 10 to 33.3 and there after it decreased[108]. As growth speed changed from lower to higher value, the morphology of solid liquid interface changed from planar to cellular to dendritic. It was shown that thermosolutal convection resulted from solute buildup ahead of growing solid-liquid interface in Pb-rich Pb-Sn alloys and resultant macrosegregation increased with decreasing growth speed due to morphological changes[109]. Influences of primary dendrite arm spacing and mushy zone length on macrosegregation were reported [110]. The growth speed varied in the range of 1 and $64\text{ }\mu\text{m}$ and the temperature gradient varied in the range of 17 and 110 K/cm . With increase in primary dendrite arms spacing, macrosegregation was shown to increase on expected lines. Macrosegregation increased with decrease in mush zone length. Effect of application of magnetic field on thermosolutal convection was also studied[111].

Bergman et al [112] studied solidification of Pb-Sn alloys which were bottom cooled at various cooling rates. *Modified Rayleigh Number* (Ra_m) was employed as the ratio of the driving solutal buoyancy force to retarding Darcy frictional force. Increasing Ra_m was found to increase longitudinal segregation, decrease freckle trails and increase channel formation.

Li et al [113] carried out experiments on hypoeutectic Pb-15 wt % Sn, Pb-36 wt % Sn and Sn-15 wt % Pb. For first two alloys, solutal buoyancy was acting in upward direction. For Sn-15 wt % Pb alloy, there was no driving force for convection. It was established

that more the upward flow more was the macrosegregation. It was also found that the solutal buoyancy was by and large restricted to the interdendritic liquid.

Felicelli et al [114-115] carried a simulation of thermosolutal convection, macrosegregation and freckles for the case of vertical solidification of lead-tin alloys using a volume-averaged, single-domain model. Experimental data of Sazarin and Hellawell [107] was used in the calculation. 3-dimensional calculations[115] showed complex flow pattern during evolution macrosegregation. However, the length of ingot was scaled to obtain better resolution of flow field and resulting convection.

2.4 Conclusions

In this chapter, a brief account on evolution of single-domain model was presented. Subsequently various permeability models, used in single model, were discussed. Scatter in thermophysical data in literature was highlighted. Finally, some recent studies on lead-tin system were reviewed. The following points are noted:

- (iv) Uncertainty in permeability functions is considered one of the reasons for mismatch between numerical prediction and experimental data.
- (v) There is scatter in thermophysical data used in literature. In single domain model, thermophysical properties are obtained through averaging which may be a source of error. In some cases, the thermophysical properties used for obtaining best fit with the experimental data on macrosegregation have been from properties of pure substances.
- (vi) Data on vertical solidification have, by and large, not been analyzed with the help of mathematical model.
- (vii) Experimental data are limited and these are generally not complete in all respects for usage in mathematical models.

Chapter 3

MATHEMATICAL MODEL DEVELOPMENT

3.1 Assumptions for Model Development

In present study, a continuum formulation based mixture model has been adopted for use [50]. The single domain model, used in the present study involves the following assumptions.

- The solidification process is 2-dimensional. The influence of third dimension in Rectangular Coordinate system is negligible, whereas for the Cylindrical Coordinate the conditions are axisymmetric.
- The liquid is incompressible and the flow in the cavity is laminar.
- The Boussinesq approximation is applicable for calculation of the buoyancy terms.
- Thermal and solutal fields in the mushy region are coupled through the equilibrium phase diagram.
- Darcy's Law governs the flow in the mush.
- There is no movement of solid.

3.2 The Governing Equations

Equation 3.1 through 3.5 are the governing differential equations for conservations of mass, u-momentum, v-momentum, energy and solute for model development. These are in cylindrical coordinate system, since in experiments of present study, cylindrical geometry was employed. These equations with some modification were applied to experiments reported in literature in rectangular coordinate system. The modifications will be presented later when these are applied to rectangular coordinate system.

Continuity

$$\frac{1}{r} \frac{\partial}{\partial r}(\rho u r) + \frac{\partial}{\partial z}(\rho v) = 0 \quad \text{....3.1}$$

U-momentum equation

$$\frac{\partial}{\partial t}(\rho u) + \frac{1}{r} \frac{\partial}{\partial r}(\rho r u u) + \frac{\partial}{\partial z}(\rho u v) = \frac{1}{r} \frac{\partial}{\partial r}(\mu_l r \frac{\partial u}{\partial r}) - \frac{\mu_l}{2} u + \frac{\partial}{\partial z}(\mu_l \frac{\partial u}{\partial z}) - \frac{\partial P}{\partial r} - R_r \quad \dots 3.2$$

V-momentum equation

$$\frac{\partial}{\partial t}(\rho v) + \frac{1}{r} \frac{\partial}{\partial r}(\rho r u v) + \frac{\partial}{\partial z}(\rho v v) = \frac{1}{r} \frac{\partial}{\partial r}(\mu_l r \frac{\partial v}{\partial r}) + \frac{\partial}{\partial z}(\mu_l \frac{\partial v}{\partial z}) - \frac{\partial P}{\partial z} - R_z - \rho B_z \quad \dots 3.3$$

Energy

$$\frac{\partial}{\partial t}(\rho c_l T) + \frac{1}{r} \frac{\partial}{\partial r}(\rho c_l r u T) + \frac{\partial}{\partial z}(\rho v c_l T) = \frac{1}{r} \frac{\partial}{\partial r}(k r \frac{\partial T}{\partial r}) + \frac{\partial}{\partial z}(k \frac{\partial T}{\partial z}) + L \frac{\partial}{\partial t}(\rho f_s) - \frac{\partial}{\partial t}(\rho f_s (c_s - c_l) T) \quad \dots 3.4$$

Solute

$$\frac{\partial}{\partial t}(\rho C_l) + \frac{1}{r} \frac{\partial}{\partial r}(\rho r u C_l) + \frac{\partial}{\partial z}(\rho v C_l) = \frac{1}{r} \frac{\partial}{\partial r}(\rho r D \frac{\partial C_l}{\partial r}) + \frac{\partial}{\partial z}(\rho D \frac{\partial C_l}{\partial z}) + \frac{\partial}{\partial t}(\rho f_s C_l) - \frac{\partial}{\partial t}(\rho f_s C_s) \quad \dots 3.5$$

In the above equations, r and z are the space coordinates in radial and axial directions respectively, t is time, u and v are velocity components in radial and axial directions, respectively, T is temperature, C is solute concentration, ρ is density, μ is viscosity, P is pressure, R_r and R_z are Darcian resistance terms, B_z is body force, c is specific heat, k is conductivity, f_s and f_l are fraction solid and liquid, respectively, and D is solute diffusivity. Subscript s is for solid and l is for liquid.

The details of derivation of single-phase equations are presented elsewhere [48-50]. The mass, energy and solute equations are derived by adding the individual phase equations. In the derivation of momentum equations, attention is paid to the nature of flow in the mushy region, which in case of columnar solidification is governed by the Darcy Law [83]. The momentum equation is identical to those proposed by Bennon and Incropera [48,49]. Additionally, the solid velocity is assumed zero. In the development of momentum equations several terms were deemed negligible and the terms remaining in the equations are those that are significant in at least one region of the entire domain during solidification. For example, the Darcy damping term of momentum equations render the viscous terms negligible within the mushy zone. The continuum model equations are mutually coupled, and must be used with a closure model to determine

local temperature, local composition and local fraction solid. In the development of single-phase model, a number of auxiliary equations have been invoked for mathematical closure, and these are described below.

3.2.1 Auxiliary relationships employed in the model

Treatment of the mushy region:

Darcy's Law[83] has been employed in momentum equations to account for momentum exchange between interdendritic liquid and solid dendrites. The model assumes that the rate of momentum exchange between phases is proportional to the difference in their respective velocities and inversely proportional to permeability. The permeability of a dendritic array depends on several factors, including the local volume fraction solid and its structure.

Both isotropic and anisotropic permeability correlations have been implemented in the present study to make a comparative study of role of permeability on field variables. Assuming permeability to be isotropic, the Darcian resistance terms take the following forms.

$$R_r = \frac{\mu_l}{K} u \quad \text{....3.6}$$

$$R_z = \frac{\mu_l}{K} v \quad \text{....3.7}$$

In the above equations, K is the isotropic permeability. The following Kozeny-Carman equation [85] has been most widely used in literature to represent permeability.

$$K = K_o \frac{f_l^3}{(1-f_l)^2} \quad \text{....3.8}$$

where the permeability constant K_o is an empirical constant that depends on dendrite arm spacing.

Though this correlation is intended for use with solid fraction more than 0.5, it has been widely employed for the entire mushy region. Apart from the isotropic model, the role of anisotropy has also been investigated in the present work. It is incorporated in the governing equations as given below. The details of the implementation are described by Yoo et al. [86] and Sinha et al.[87].

Let K_{PR} and K_{NR} are permeabilities in directions parallel and perpendicular to a local isotherm, represented by $G(x,y)$. Then,

$$\frac{\mu U}{K} = \frac{\mu}{(1+G'^2)} \begin{Bmatrix} P & Q \\ R & S \end{Bmatrix} \quad \dots 3.9$$

where,

$$P = \left(\frac{G'^2}{K_{NR}} + \frac{1}{K_{PR}} \right) u \quad \dots 3.10$$

$$Q = G' \left(\frac{1}{K_{NR}} - \frac{1}{K_{PR}} \right) v \quad \dots 3.11$$

$$R = G' \left(\frac{1}{K_{NR}} - \frac{1}{K_{PR}} \right) u \quad \dots 3.12$$

$$S = \left(\frac{G'^2}{K_{PR}} + \frac{1}{K_{NR}} \right) v \quad \dots 3.13$$

In the above equations, G' , the gradient, is determined at each location as a function of time.

Boussinesq approximation:

Boussinesq approximation was invoked, i.e., the density of the alloy was assumed constant and equal in both solid and liquid phases, except in the buoyancy term was applied to account for the thermo-solutal buoyancy. The correlation is described as follows:

$$\rho(T,C) = \rho_0 [1 - \beta_T(T - T_{ref}) - \beta_C(C_l - C_{ref})] \quad \dots 3.14$$

where, ρ_0 is the density at temperature T_{ref} and solute concentration C_{ref} and β_T and β_C are the thermal and solutal expansion coefficients, respectively.

Coupling of thermal and solutal field in the mush:

There are various ways to represent temperature-solute coupling. The Lever rule based correlation gives following expression for liquid fraction, which has been employed in the macroscopic model.

$$f_l(T, C) = \frac{C - K_p(T - T_{fus})/m}{(1 - K_p)(T - T_{fus})/m} \quad \dots 3.15$$

where, T_{fus} is fusion temperature, m is *slope of the liquidus* and K_p is equilibrium partition coefficient.

Transport properties:

Transport properties, such as thermal conductivity, viscosity, and mass diffusivity, must be prescribed or modeled in order to solve the governing equations for either a mixture or a two-phase model. The most common modeling technique is to take constant values of properties for solid and liquid phases and obtain the value for mushy region with the help of a mixture law. However, sufficient data are not yet available to justify detailed model that account for tortuosity. In the present study, various properties in the mushy region were accounted for through mixture law as follows:

$$\mu = \rho_l \mu_l / \rho \quad \dots 3.16$$

$$k = k_l f_l + k_s f_s \quad \dots 3.17$$

$$c = c_l f_l + c_s f_s \quad \dots 3.18$$

$$D = D_l f_l + K_p D_s f_s \quad \dots 3.19$$

3.2.2 Initial and boundary conditions

Initial condition:

Initially the cavity is filled with alloy of uniform solute concentration, C_{init} . It was assumed that the liquid is at rest initially. Initial temperature distribution, if available, was

set as boundary condition. Mathematically, the initial conditions were represented as follows.

At $t = 0$, $u = v = 0$ at all locations; $C = C_{init}$ at all locations and $T = T_{init}(r,z)$

Boundary conditions:

Different types of boundary conditions were implemented depending on problem under consideration. For energy equation, these included specified temperature (varying/constant), specified heat flux (varying/constant), as well as specified heat transfer coefficient/heat flux. For momentum equation, no-slip condition, free surface as well as symmetric boundary conditions were implemented depending on problem under consideration. For solute equation, it has been assumed that there is no loss of solute across the boundaries. For axisymmetric horizontal solidification of an alloy in a cylinder with free top surface, the boundary conditions can be specified mathematically as follows:

$$u = 0, \partial v / \partial r = 0; \partial T / \partial r = 0; \partial C / \partial r = 0 \text{ at } r = 0 \quad \dots 3.20$$

$$u = 0, v = 0; \partial T / \partial r = 0; \partial C / \partial r = 0 \text{ at } r = R \quad \dots 3.21$$

$$u = 0, v = 0; -k \partial T / \partial z = q(t); \partial C / \partial z = 0 \text{ at } z = 0 \quad \dots 3.22$$

$$\partial u / \partial r = 0, v = 0; \partial T / \partial z = 0; \partial C / \partial z = 0 \text{ at } z = H \quad \dots 3.23$$

3.3 Solution Procedure

A control volume based finite difference formulation methodology [116] was used. The salient features were: (i) The governing equations were discretized using a control volume approach, with upwind differencing (first order) for convective terms; (ii) A staggered grid arrangements was employed so that the velocities were computed at the faces of the control volumes; (iii) The pressure-velocity coupling was handled by SIMPLE [116] algorithm; (iv) the upwind scheme was used to discretize convection-diffusion terms; and (v) At each marching time step, iterations were performed to account for the coupling among various equations.

3.3.1 Finite difference formulation

Following Patankar[116], the governing equations are integrated over control volume (rdrdz for Cylindrical Co-ordinate system). The final forms of finite difference equations for various transport equations are noted below.

Energy equation:

$$a_P T_P = \{a_e + [-C_e, 0]\} T_E + \{a_w + [C_w, 0]\} T_W + \{a_n + [-C_n, 0]\} T_N + \{a_s + [C_s, 0]\} T_S + a_P^0 T_P^0 \quad \text{....3.24}$$

where,

$$a_e = \frac{k_e r_e}{r_P (r_e - r_w) (r_e - r_P)}; a_w = \frac{k_w r_w}{r_P (r_e - r_w) (r_P - r_w)} \quad \text{....3.25}$$

$$a_n = \frac{k_n}{(z_n - z_s) (z_n - z_P)}; a_s = \frac{k_s}{(z_n - z_s) (z_P - z_s)} \quad \text{....3.26}$$

$$k_e = \frac{2 k_E k_P}{k_E + k_P}; k_w = \frac{2 k_W k_P}{k_W + k_P}; k_n = \frac{2 k_N k_P}{k_N + k_P}; k_s = \frac{2 k_S k_P}{k_S + k_P} \quad \text{....3.27}$$

$$C_e = \frac{(\rho c u)_e r_e}{r_P (r_e - r_w)}; C_w = \frac{(\rho c u)_w r_w}{r_P (r_e - r_w)}; C_n = \frac{(\rho c v)_n}{(z_n - z_s)}; C_s = \frac{(\rho c v)_s}{(z_n - z_s)} \quad \text{....3.28}$$

$$a_P^0 = \frac{(\rho c)_P}{\Delta t}; S = \frac{\rho \Delta H_P (f_l - f_l^0)}{\Delta t} \quad \text{....3.29}$$

$$a_P = a_e + a_w + a_n + a_s + a_P^0 + [C_e, 0] + [-C_w, 0] + [C_n, 0] + [-C_s, 0] \quad \text{....3.30}$$

In a similar way, transport equations for r-momentum, z-momentum and solute were discretized. Since SIMPLE algorithm is used to solve momentum equations, continuity equation was used to derive pressure correction equation.

3.3.2 Numerical details

The set of algebraic equations resulting from the discretization of governing equations are solved in an iterative fashion (at each time level) as follows:

- (i) solve Eq. 3.4 to calculate T
- (ii) solve Eq. 3.5 to calculate C
- (iii) solve Eq. 3.2 to calculate u
- (iv) solve Eq. 3.3 to calculate v
- (v) solve pressure-correction equation
- (vi) update fraction liquid field

Steps (i) to (vi) were repeated until convergence was achieved, i.e., when nodal values of all variables from two successive iterations were below 1.0×10^{-8} . In order to achieve smooth convergence of the solution procedure, few relaxation factors were chosen. Values of relaxation factors for update of f_l , buoyancy term and pressure term were 0.2, 0.25 and 0.8, respectively. Generally a variable time step was used and it varied between 0.1 to 0.5 seconds. Using the converged field as initial conditions, the procedure was repeated for the next time level.

3.4 Grid Sensitivity Tests

Grid sensitivity tests were performed for both horizontal and vertical solidification. For horizontal solidification, simulations were performed on a rectangular cavity of 100 mm X 100 mm for solidification of Pb-15%Sn. A constant heat flux of 10000 KW/m^2 was extracted from the left wall of the cavity. Grids of 50x50 and 30x30 nodal points were used in simulation. Fig. 3.1 compares the simulated results in terms of streamlines, mush profiles, isotherms and iso-composition lines for the two grid configurations at $t = 1000$ seconds from start of cooling. It is readily seen that contours of various fields compare well for the two grids. Therefore, in the present work, a minimum grid of 30x30 nodal points has been employed for majority of simulations of horizontal solidification. However, in few cases, finer grids have been employed to obtain better resolution.

For vertical solidification, experiment of Sazarin and Hellawell [107] was simulated with the help of model. This case is discussed in detail in Ch. 6. Here only the result of grid sensitivity is presented. Grids of 42x62, 32x42 and 22x32 were employed to study

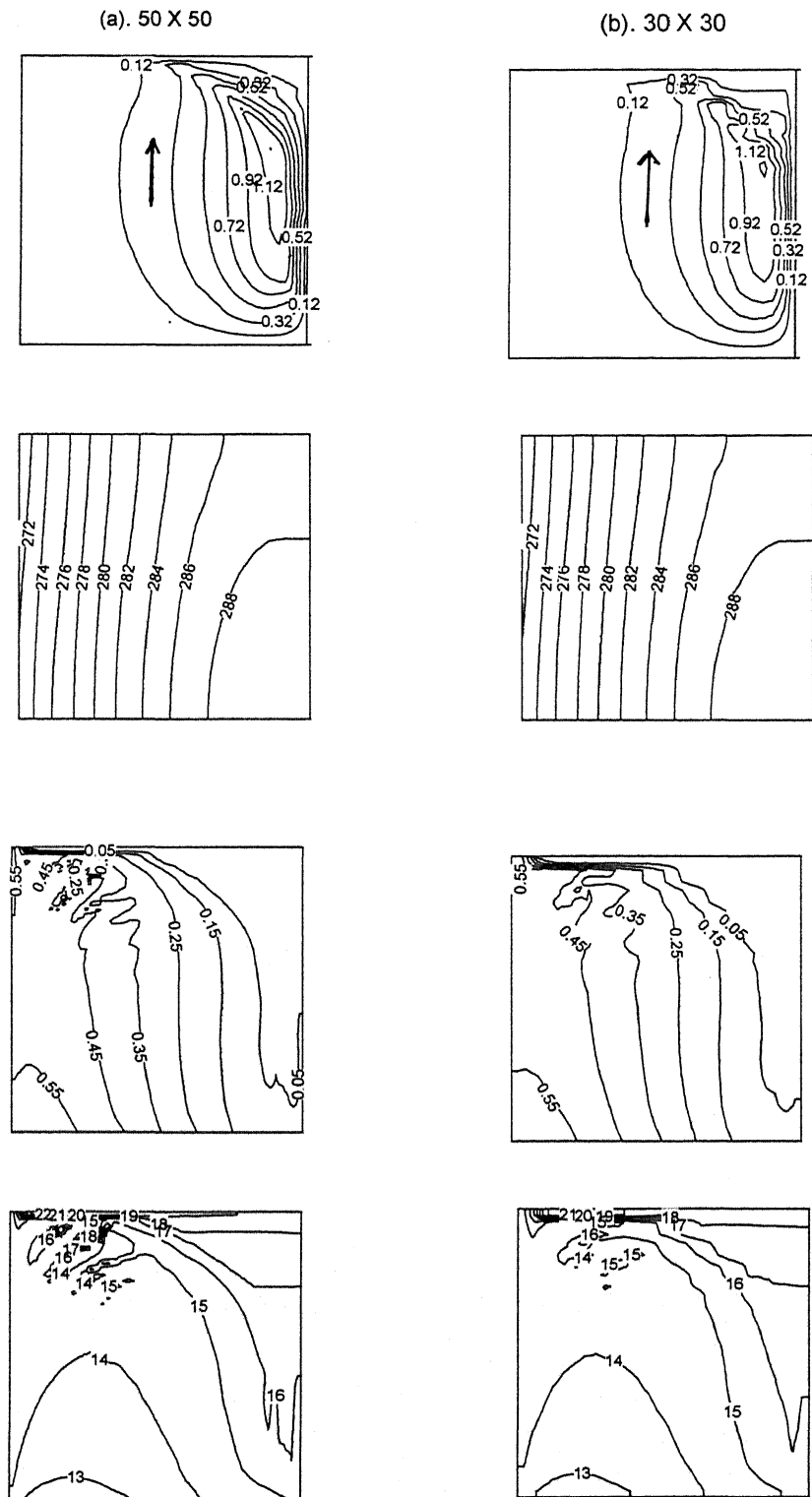


Fig. 3.1: Comparison of streamlines, isotherms, liquid fraction profile and iso-composition for (a) 50x50 and (b) 30x30 grids.

vertical solidification of Pb-20 wt % Sn alloy in a cylindrical mould (diameter = 37 mm, height = 120 mm). Predicted axial segregation for various grids are compared with each other and with experimental data in Fig. 3.2. It is readily seen that all three grids qualitatively capture the trend of axial segregation. However, finer grids show better match with experimental data.

In the present work a relatively coarser grid have been employed for cases where only axial macrosegregation have been compared with experimental data. However, finer grids have been employed where results have been discussed in terms of flow and its effect on macrosegregation.

3.4 Model Validation

In order to check the correctness of computer program, few standard problems were chosen from literature. In the first case, the model was tested with the numerical and experimental studies on solidification of $\text{NH}_4\text{Cl-H}_2\text{O}$ [86] in a rectangular cavity. Subsequently, the model was tested with numerical benchmark of Ahmed, et al on solidification of Pb-48 wt % Sn alloy in a rectangular cavity [60]. The present model was then checked with numerical results on horizontal solidification of Pb-19 wt % Sn in a cylindrical mould [117]. For the case of rectangular coordinate system, the equations 3.1 though 3.5 were modified as follows: the value of r was made 1 in all equations and the second term on the right hand side of equation 3.2 was made zero.

3.4.1 Test problem I

Experimental and numerical studies on solidification of $\text{NH}_4\text{Cl-70 wt \% H}_2\text{O}$ was carried out by Yoo and Viskanta[86]. The dimension of solidification cell was 47.6 mm x 47.6 mm. The cell was initially filled with $\text{NH}_4\text{Cl-70 wt \% H}_2\text{O}$ salt solution at 307 °K. The Cooling was initiated by lowering of temperature of the left vertical wall. The right vertical wall was maintained at the initial temperature. The top and bottom cavity walls were insulated. The details of the problem are presented in the above literature. The flow patterns at various time intervals as well as simulation results of the experiments are presented by Yoo et al. Using 50x50 grids, the present model was employed to simulate

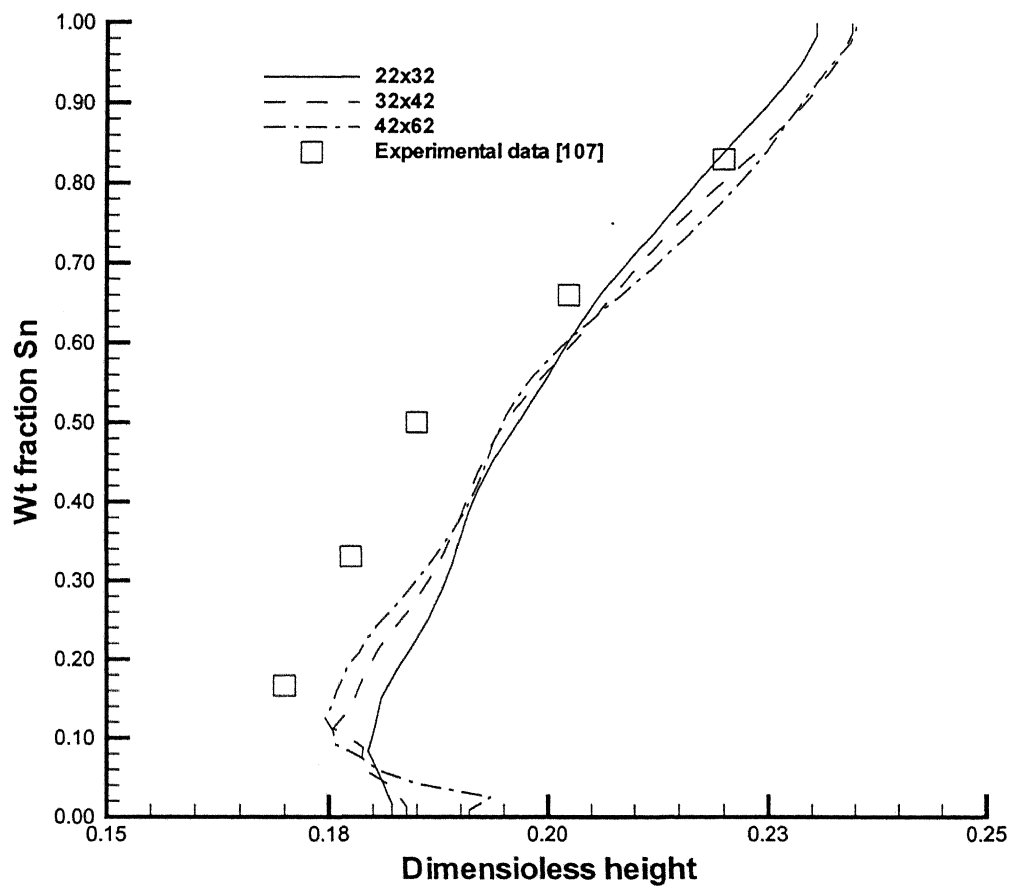


Fig. 3.2: Predicted axial macrosegregation with different grids obtained from simulation of Sazarin et al's experiment[107].

the experiment. Fig. 3.3 shows the comparison of flow field with numerical and experimental data of Yoo et al. at $t = 1200$ seconds. It is readily seen that model compares well with both numerical and experimental data.

3.4.2 Test problem II

Solidification of Pb-48 wt % Sn was simulated using finite volume method and finite element method by Ahmed et al [60]. The solidification cell was 100 mm long and 60 mm high. The cell was initially filled with Pb-48 wt % Sn at 216°C . The cooling was initiated by lowering of temperature of the left vertical wall. Other three walls were insulated. The details of the problem are presented in the above literature. Using 50×40 grids, the present model was employed to simulate the above problem. Fig. 3.4 shows the comparison of flow field and volume fraction solid with numerical results of Ahmed et al at $t = 50$ seconds. It is readily seen that prediction of present model compares well with the reported numerical results.

3.4.3 Test problem III

In the second study, the model was used to simulate the solidification of Pb-19%Sn in a cylindrical mould [117]. This validation exercise is for ensuring numerical correctness of program for cylindrical polar co-ordinate system. The details of the problem was presented by Prescott et al. Using a grid of 52×52 , the present model was used to simulate the problem. Fig. 3.5 shows the comparison of numerical prediction's of present model with those by Prescott et al. at $t = 135$ seconds. It is readily seen that the match reasonable despite the fact that energy equation is solved through enthalpy route by Prescott et al.

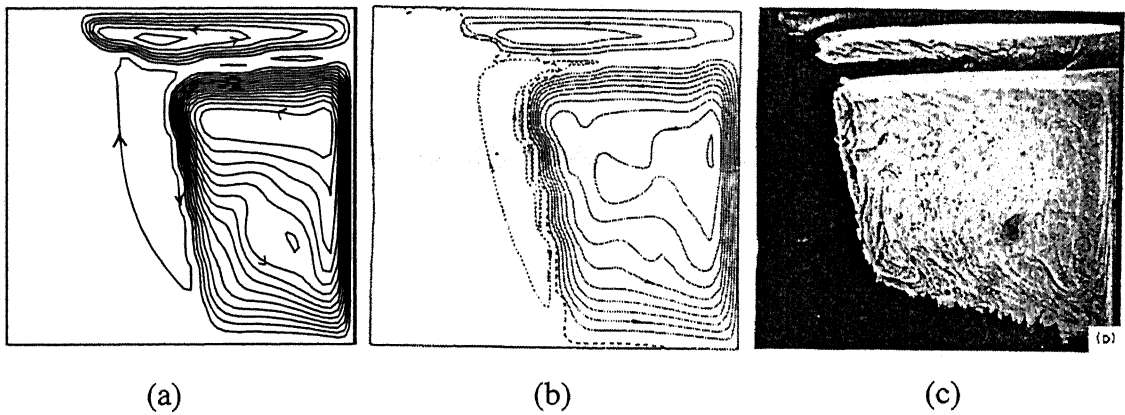


Fig. 3.3: Comparison with Yoo et al's [86] experimental results and numerical predictions; (a) predictions of present model, (b) Yoo et al's predictions, and (c) Yoo et al's experimental results (streamlines).

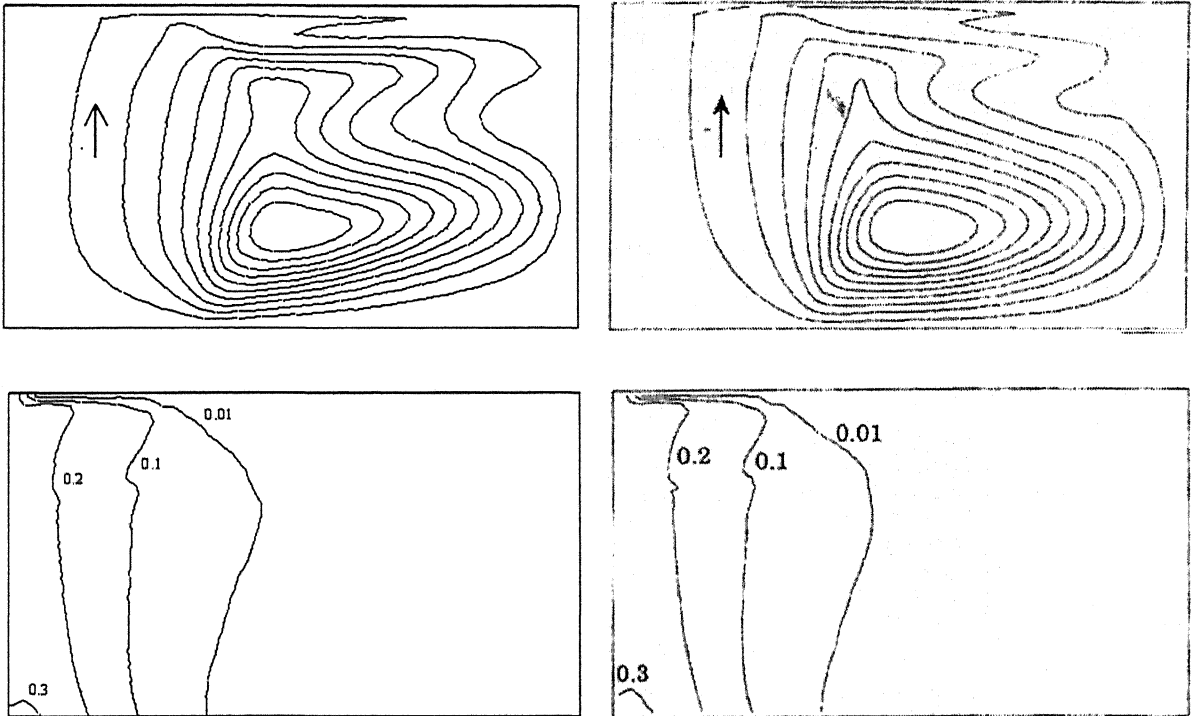


Fig. 3.4: Comparison of numerical predictions: (a) streamlines (present model), (b) streamlines [60], (c) fraction solid (present model) and (d) fraction solid [60].

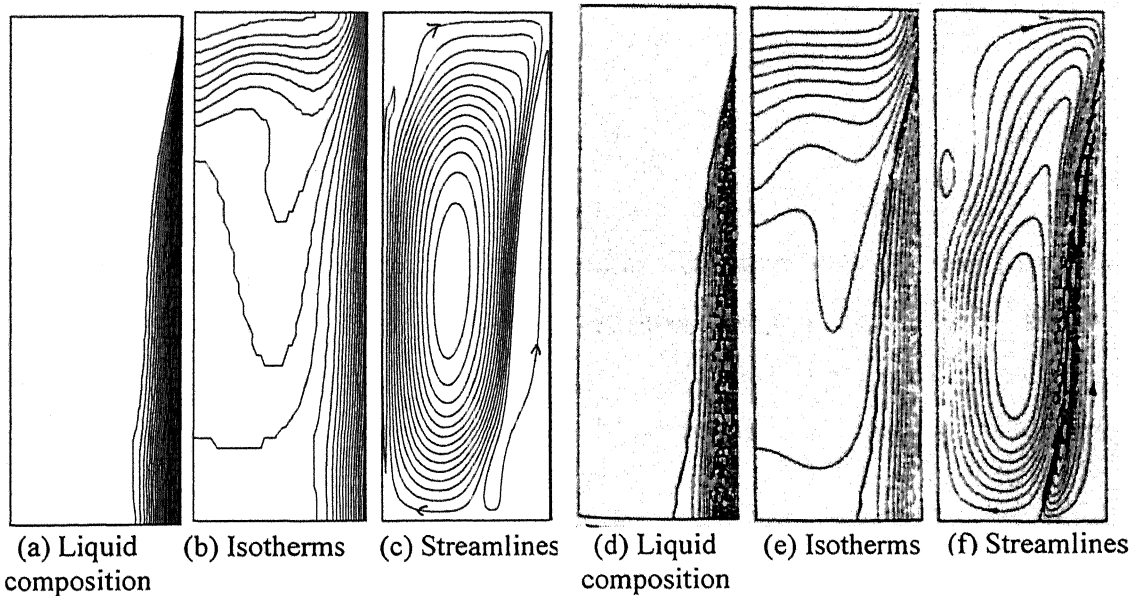


Fig. 3.5: Comparison of numerical results for solidification of Pb-19 wt % Sn alloy in a cylindrical mould: Present model - (a), (b) and (c) vs. Prescott, et al [117] (d) liquid composition, (e) isotherms and (c) streamlines mould.

Chapter 4*

MACROSEGREGATION: CASE STUDIES

4.1 Introduction

In this chapter, the evolution of macrosegregation during horizontal solidification is analyzed with the help of the mathematical model described in Ch. 3. The model was applied to some experimental and numerical investigations reported in literature. Evolution of macrosegregation during vertical solidification is analyzed in Chapter 6, which is concerned with experimental results obtained as a part of the present investigation.

First part of this chapter presents a critical study of the role of material properties on the thermosolutal convection by simulating solidification of ammonium chloride - water, iron-carbon and lead-tin binary systems. Although extensive studies have been reported on each of these systems, a comparative study is yet to be reported on the effect of material properties on solutal transport and thermosolutal convection. The alloy systems have been selected in such a way that the solute constitutes the lighter component in all three. It is worthwhile to recall here that the ammonium chloride - water system has been used as a model system to understand the evolution of macrosegregation in steel for a long time.

The second study, reported here, pertains to the role of permeability on macrosegregation. It has been emphasized in Ch. 2 that appropriate permeability model is essential for correct prediction of macrosegregation. First the adequacy of widely used Kozeny-Carman model [85] was tested. Permeability data of Poirier[90] was revisited and a permeability model, for thin mushy region was generalized. Using the new permeability model, Krane's experiment [42] was simulated to show the adequacy of the model for horizontal solidification.

* A part of this chapter formed the basis for the following publications:
1) A. K. Singh, R. Pardeshi and B. Basu, *Sadhana*, 26 (2001), 139.
2) A. K. Singh and B. Basu, *ISI International*, 41 (2001), 1481.

The last study of this section is on the effect of cooling rate on evolution of macrosegregation in iron-carbon system. It is well known that steel is cast with a wide range of cooling rate, and a systematic study of role of variation of cooling rate on evolution of macrosegregation in steel has not yet been carried out. The heat flux was varied in the range of 5 (static casting/lost foam casting) to 6000 kW/m² (in the mould of continuous casting of steel).

4.2 Role of Material Properties on Thermosolutal Convection and Macrosegregation

4.2.1 Problem definition

For the purpose of present study, solidification is considered in a rectangular cavity of length L and height H (schematically shown in Fig. 4.1). The right wall of the cavity represents the line of symmetry of the vertical section of a casting, and hence a zero heat flux condition is maintained throughout the solidification process along this wall. Initially the other three walls of the cavity are insulated and the cavity is filled with liquid alloy with initial temperature, T_{int} and composition, C_{int} . Solidification is initiated by imposing a constant heat flux, q , from vertical right side wall at $t = 0$, whereas the top and the bottom wall of the cavity are kept insulated during the solidification process. As discussed in Chapter 3, permeability of the mushy region plays an important role in determining the nature of thermosolutal convection and macrosegregation. Some of the permeability functions, used in the literature, are shown in Fig. 4.2. It may be noted that there is a large difference in various permeability functions. However, since the present study focuses on role of materials, Kozeny-Carman equation [85] has been employed for all simulations.

4.2.2 Initial and boundary conditions

Initially the cavity is filled with alloy in liquid state with homogeneous temperature, T_{int} , and composition, C_{int} . It is assumed that initially the liquid is at rest and the solidification is initiated by imposing a heat flux from left boundary of the cavity. The dimensionless forms of initial and boundary conditions are shown in Fig. 4.1. The initial temperature and composition for NH_4Cl-H_2O solution are 276.14 °C and 18% NH_4Cl respectively, whereas the same for Fe-C alloy are 1463 °C and 1 wt % carbon

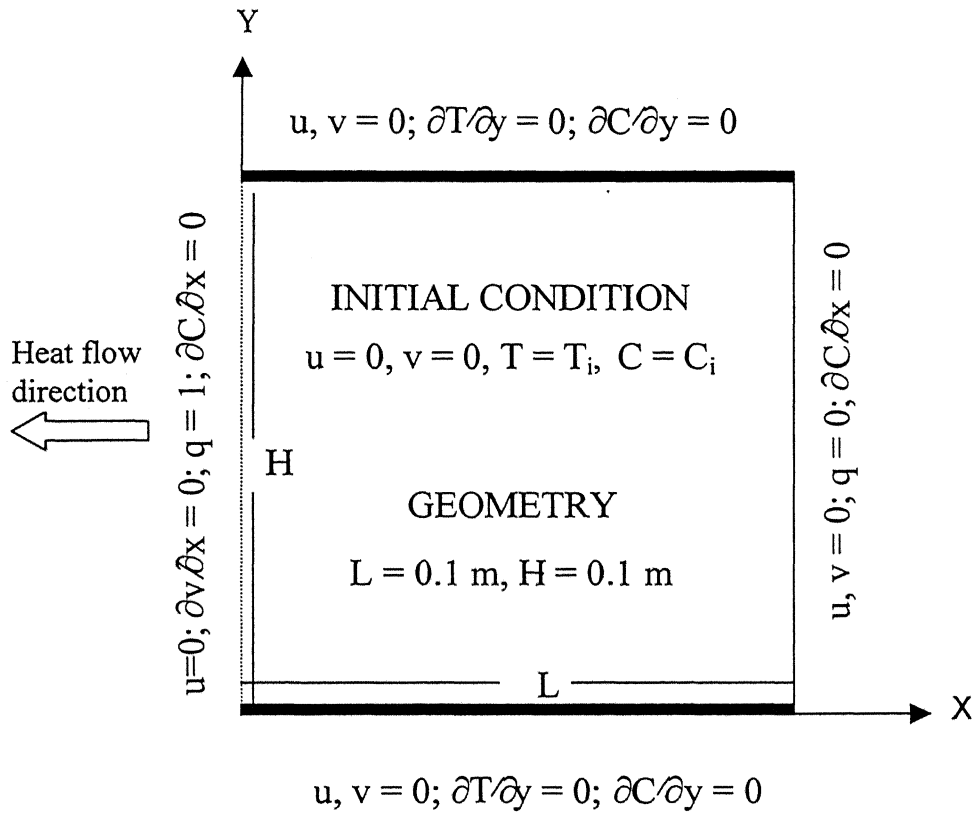


Fig. 4.1: Geometry of the cavity, initial and boundary conditions.

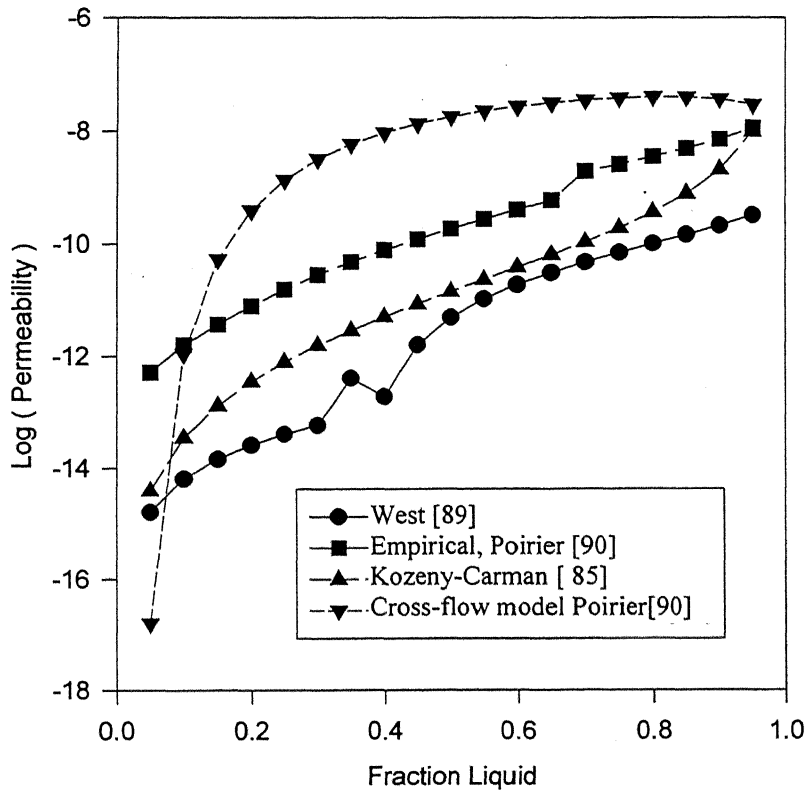


Fig. 4.2: Permeability functions used in literature

respectively, and for Pb-Sn alloy, 295.0 °C and 15 wt % Sn, respectively. The selection for these initial temperatures ensures 5 °C superheat in all three cases. The justification for selection of composition and heat flux is provided below.

4.2.3 Selection of Material and Process Parameters

Materials selected for the present study are Fe-C alloy, Pb-Sn alloy, and NH₄Cl-H₂O solution. In all the three systems, the solute is lighter than the solvent. The physical properties pertaining to these systems are listed in Table 4.1. In order to carry out a comparative study, it is important to select suitable composition and imposed heat flux at cold boundary for all three materials. The initial compositions for these systems were selected in such a way as to keep the ratio of initial composition to eutectic composition same for all the three systems. On the other hand, the heat fluxes at the cold boundary were selected in such a way as to keep the overall rate of solidification, dX/dt , same in the following expression:

$$q = \rho_s \frac{dX}{dt} (\Delta H_f + C_s \Delta T) \quad \dots 4.1$$

For Fe-C alloy, the imposed heat flux was assumed to be 60 kW/m². Using the above equation, the heat fluxes for other materials were estimated such that dX/dt was same for all three systems.

Various dimensionless parameters for these three systems are listed Table 4.2. In this table, N signifies relative importance of solutal buoyancy with respect to thermal buoyancy in the mushy phase and is defined as follows.

$$N = \frac{\beta_s}{m\beta_T} \quad \dots 4.2$$

Table 4.1: Thermo-physical properties of $\text{NH}_4\text{Cl-H}_2\text{O}$, Fe-C and Pb-Sn alloy system

Properties	$\text{NH}_4\text{Cl-H}_2\text{O}$	Fe-C	Pb-Sn
Initial temperature, $^{\circ}\text{C}$	295.0	1463.0	276.0
Initial ΔT , $^{\circ}\text{C}$	5.0	5.0	5.0
Initial C, wt. %	18.0	1.0	15.0
Cavity size, m	0.1x0.1	0.1x0.1	0.1x0.1
ρ , kg/m^3	1000.0	6940.0	10600
C_p (S), $\text{J/kg/}^{\circ}\text{C}$	3000.0	753.0	148.0
C_p (L), $\text{J/kg/}^{\circ}\text{C}$	3000.0	753.0	172.0
κ (S), $\text{W/m/}^{\circ}\text{C}$	0.4	60.0	38.2
κ (L), $\text{W/m/}^{\circ}\text{C}$	0.4	30.0	21.25
β_T , $1/^{\circ}\text{C}$	-3.83×10^{-4}	-2.7×10^{-4}	-1.09×10^{-4}
β_C	-0.26	-0.686	-0.364
μ , kg/ms	1.0×10^{-3}	6.94×10^{-3}	2.31×10^{-3}
ΔH , J/kg	3.0×10^5	2.72×10^5	2.84×10^4
Eutectic T, $^{\circ}\text{C}$	-15.4	1130.0	183.0
Eutectic C, wt %	80.3	4.3	61.9
K_o , m^2	5.0×10^{-10}	2.8×10^{-11}	2.8×10^{-11}
Melting P, $^{\circ}\text{C}$	357.0	1536.0	327.0
D (S), m^2/s	4.8×10^{-12}	4.8×10^{-12}	4.8×10^{-12}
D (L), m^2/s	4.8×10^{-9}	1.0×10^{-9}	1.5×10^{-9}

Table 4.2: Dimensionless parameters*

Dimensionless numbers	NH ₄ Cl-H ₂ O	Fe-C	Pb-Sn
Pr	7.49	0.17	1.87x10 ⁻²
Da	5.0x10 ⁻⁸	2.8x10 ⁻⁹	2.8x10 ⁻⁹
Ra _T	7.4x10 ¹⁰	9.26x10 ⁷	1.8x10 ⁷
Ra _S	1.5x10 ¹⁰	8.45x10 ⁷	8.7x10 ⁷
Le	27.7	5740	7770.0
Ste	25.0	0.554	0.262
K.	0.3	0.42	0.3
q/q _{FeC}	0.15	1.0	0.17
N	-1.4	-0.645	-14.3
P _d	6.526	0.6	0.3

* Reference: list of symbols

4.2.4 Results and discussions

Computer simulation for solidification studies were carried out for all the systems upto 2000 sec. Maxima and minima of streamlines, average composition and isotherms are listed in Table 4.3. Fig. 4.3 shows the progress of solidification for the three systems. It may be noted that for metallic systems, the overall rates of solidification are very close. On the other hand, the rate of solidification for inorganic salt solution is much lower. Although the selection of heat flux was intended to provide similar rate of solidification for all three cases, the large difference in thermal conductivity of metal and inorganic salt resulted in the difference in overall rate of solidification. Nevertheless, the overall rate of solidification is significant even for $\text{NH}_4\text{Cl-H}_2\text{O}$ solution, which makes a comparison of various fields for the three cases possible.

Fig. 4.4 shows the streamlines, mush profiles, isotherms and macrosegregation at solidification time (t) = 250 sec. for Fe-C alloy. It may be noted that the flow field is essentially thermal buoyancy driven and anti-clockwise in nature. This leads to stretching of isotherms and solid fraction profiles (Figs. 4.4(b) and 4.4(c)) mush profiles towards the bottom of the cavity. As discussed before, the permeability function, based on Kozeny-Carman model, was employed to represent the drag in the mushy phase. The flow in the mushy region is very weak due to resistance to flow, therefore, streamlines are negligible and not shown in Fig. 4.4(a). Flow is anti-clockwise in nature demonstrating thermal buoyancy driven flow. As for the macrosegregation, it may be noted that there is depletion of solute along the cold wall and deposition of solute along the bottom of the cavity. Hence, macrosegregation level is less than 1 near the cold wall on the left in Fig. 4.4(d).

The flow field also gradually shifts towards the hot wall of the cavity and weakens in strength due to spread of mushy region in the cavity. This is evident from comparison of flow fields at $t = 250$ s, and $t = 2000$ seconds, shown in Figs. 4.4 and 4.5 respectively. As the strength of flow field goes down with progress of solidification, isotherms become more and more vertical. The mushy region progressively extends up to the right wall of the cavity. As for the macrosegregation, it gradually builds with progress of solidification. It can be clearly seen that downward thermal driven flow near the mushy

Table 4.3: Maximum and minimum values of stream function, temperature and average composition for various systems

Solidification Time (Sec.)	NH ₄ Cl-H ₂ O					Fe-C					Pb-Sn				
	C _{int} = 18 wt % ; T _{int} = 276.14 °C					C _{int} = 1 wt % ; T _{int} = 1463 °C					C _{int} = 15 wt % ; T _{int} = 295 °C				
	Average Concentration		Temperature		Stream function	Average Concentration		Temperature		Stream function	Average Concentration		Temperature		Stream function
	max.	min.	max.	min.		max.	min.	max.	min.		max.	min.	max.	min.	
250	18.4	14.5	274.2	183.3	1349	1.02	0.97	1460	1441	0.3	16.8	12.8	292.1	282.2	11.6
500	19.6	13.1	271.2	122.4	250	1.04	0.97	1460	1433	1.8	19.1	12.1	291.9	277.3	2.9
1000	21.1	12.41	270.9	32.6	175	1.08	0.97	1459	1422	0.2	21.6	11.7	290.6	271.4	1.2
1500	22.3	11.9	270.9	-42.1	166	1.11	0.96	1458	1413	0.0	23.3	11.6	288.0	266.6	0.6
2000	23.3	11.5	270.8	-106.8	114	1.12	0.97	1453	1405	0.0	24.2	11.6	281.2	261.5	0.6

*C_{int} is initial concentration; T_{int} is initial temperature

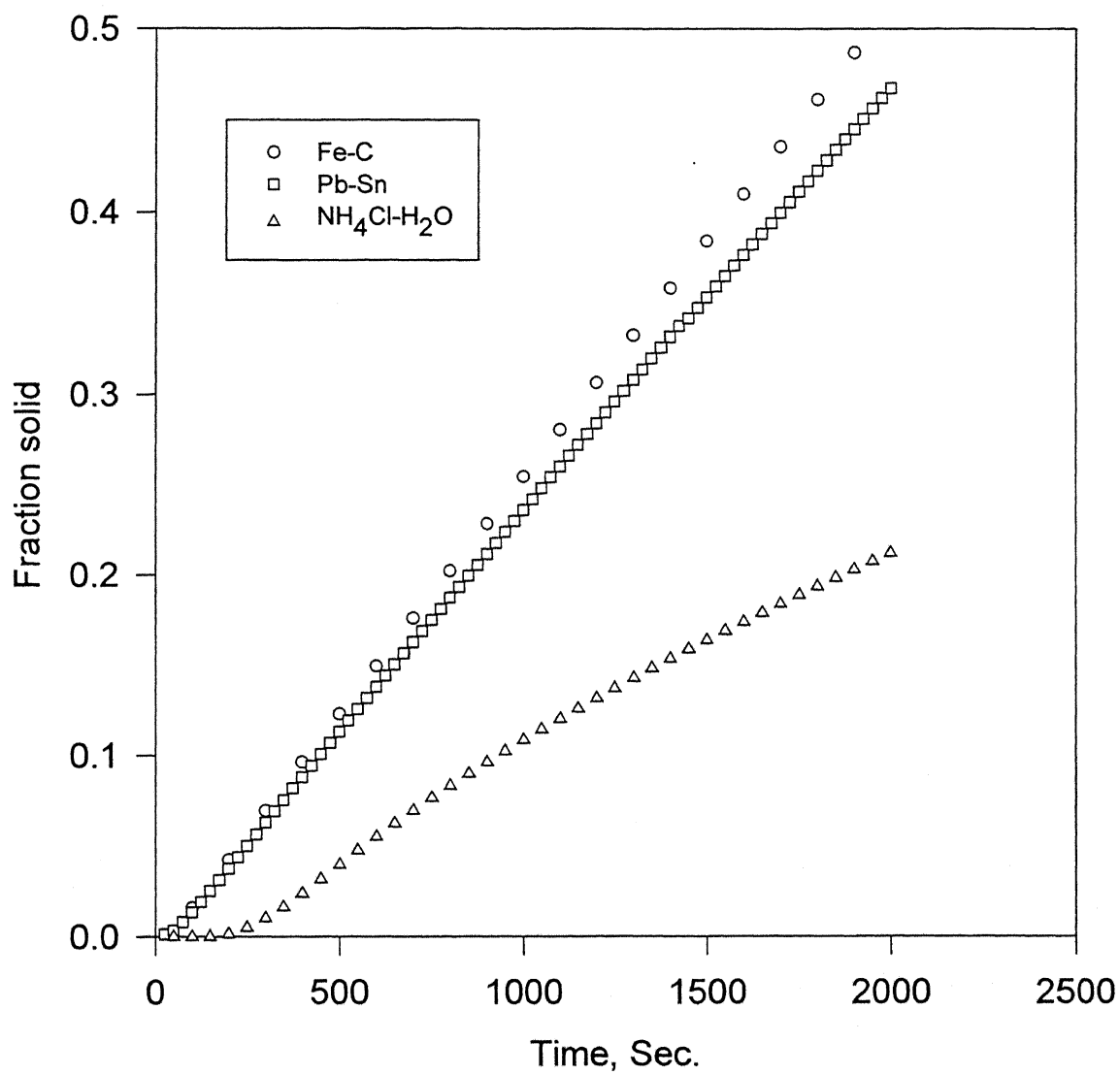


Fig. 4.3: Progress of solidification.

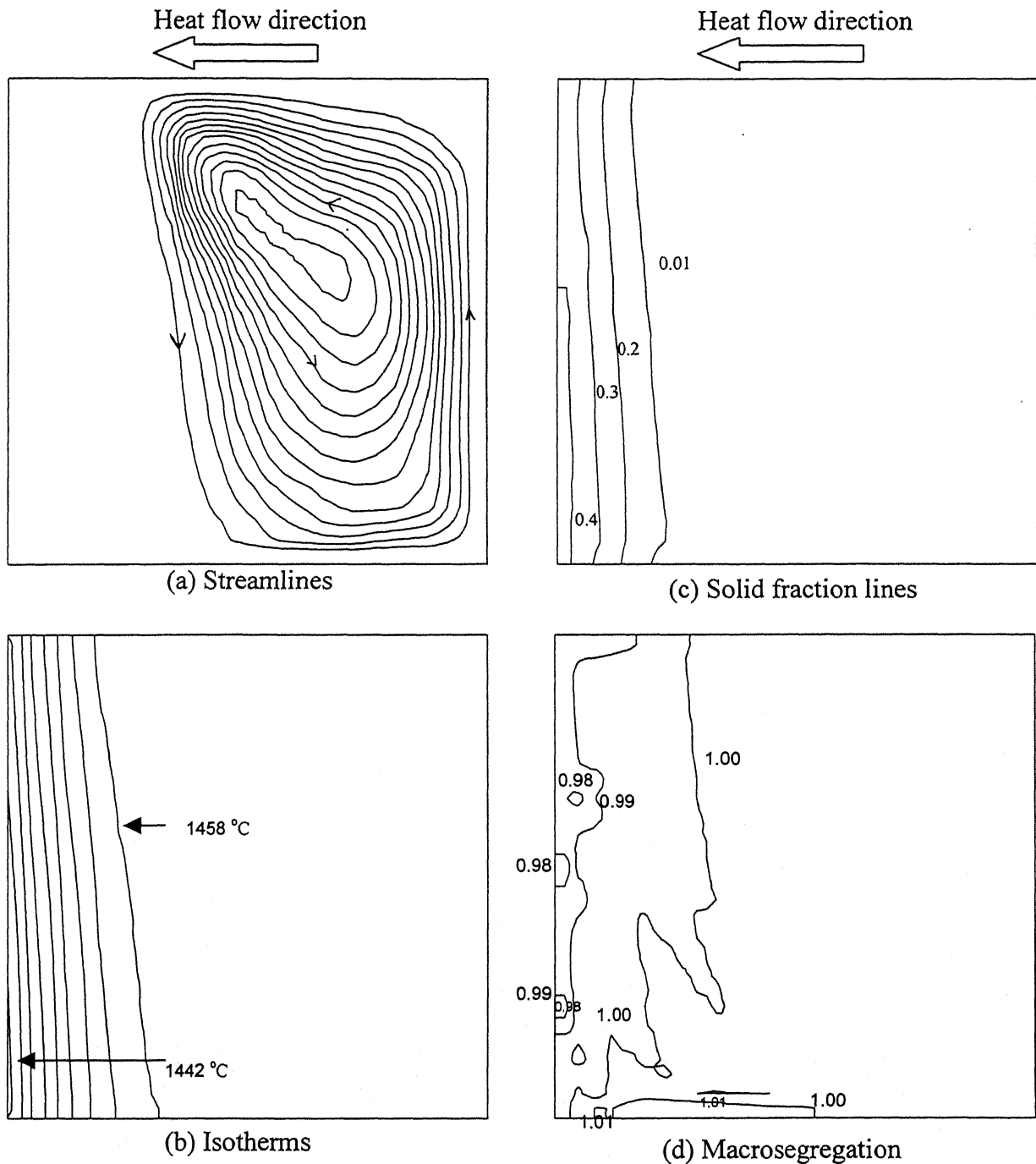


Fig. 4.4: Model predictions for solidification of Fe-1 wt % C alloy, solidification time (t) = 250 sec showing (a) streamlines, (b) isotherms, (c) solid fraction lines, and (d) isocomposition lines (wt % of carbon).

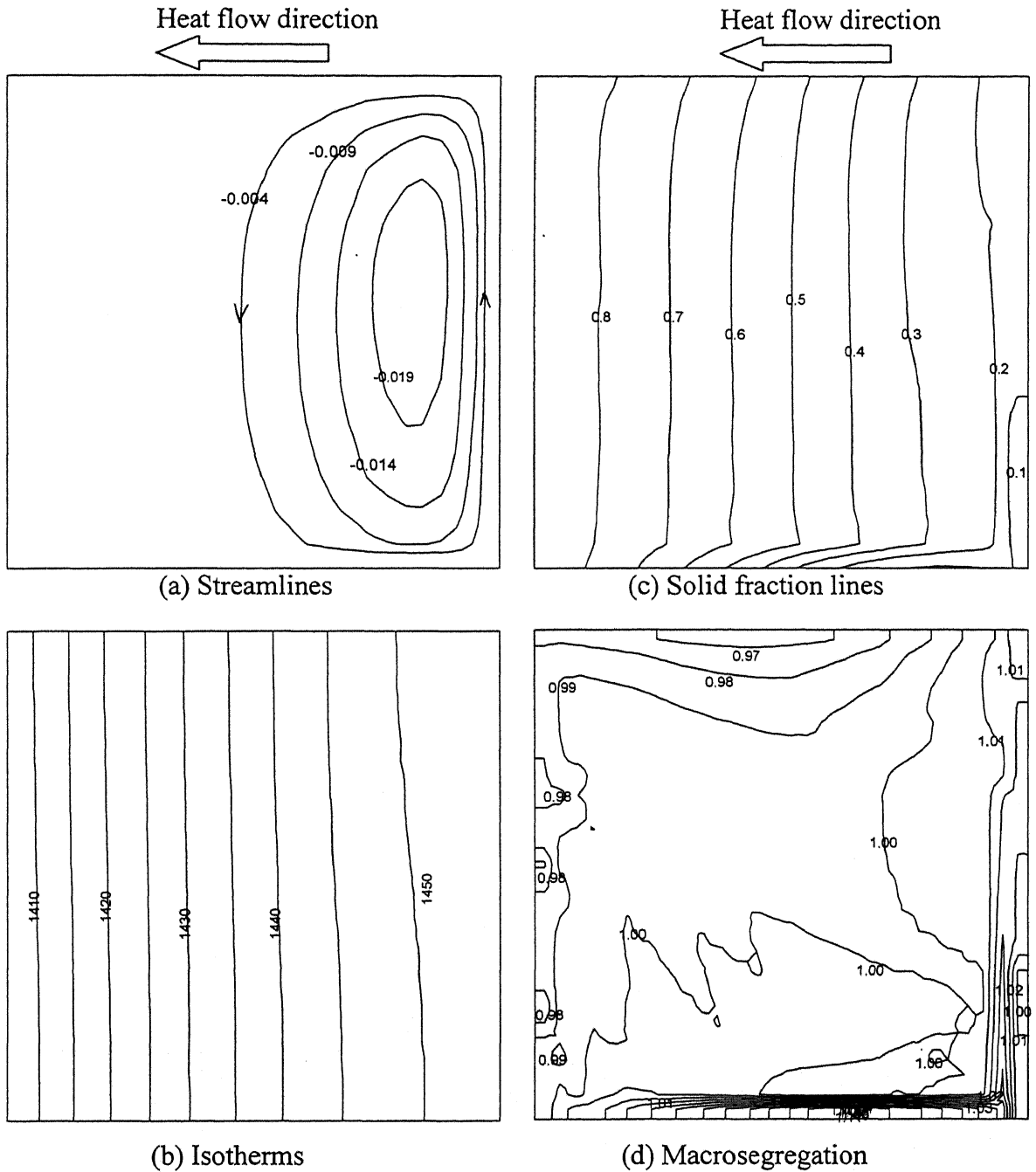


Fig. 4.5: Model predictions for solidification of Fe-1 wt % C alloy, solidification time (t) = 2000 sec showing (a) streamlines, (b) isotherms, (c) solid fraction lines, and (d) iso-composition lines (wt % of carbon).

region takes the solute with it and deposits near the bottom and right vertical wall of the cavity. Similarly, the flow leads to depletion of solute near the left vertical wall and top horizontal wall of the cavity.

As stated earlier that in case of iron-carbon system, the flow essentially thermal buoyancy driven owing to low magnitude of solutal buoyancy. Since the flow field in the mush is strongly dependent on the drag offered by the mushy phase, different permeability functions may lead to different types of flow field. For solidification of Fe-C alloy, flow field predicted by Schneider and Beckermann[81] using Poirier's correlation[90] is distinctly different from that predicted by Amberg [76] using West's correlation[89]. However, the dominance of thermal buoyancy over solutal buoyancy for Fe-C alloy has been reported by researchers [76-78]. This is essentially due to $Ra_T/Ra_s < 1$ and $|N| < 1$. Figs. 4.6-4.8 present streamlines, isotherms, mush profiles (i.e., constant solid fraction lines) and macrosegregation profiles at different times for Pb-Sn alloy. Unlike Fe-C alloy, Pb-Sn alloy has higher Ra_s , $Ra_s/Ra_T > 1$ and $|N| > 1$ (Table 4.2) and hence, it can be expected that the solutal buoyancy would play a significant role in thermosolutal convection. It may be noted from Fig. 4.6 that clock-wise solutal driven buoyancy vortex occupies most of the cavity, while a small thermal buoyancy driven vortex is located at the right bottom corner of the cavity at $t = 250$ sec. It should be noted that the flow field is entirely thermal buoyancy driven initially till initiation of solidification when solutal buoyancy starts to play dominant role, due to higher Ra_s and higher $|N|$ in a short time frame. Due to higher strength of flow field the stretching of isotherms are more at the top and similar stretching may be noticed in the mush profile also. The effect of strong upward flow in the mush is visible from the macrosegregation profile.

At other times, the results show similar trend. At 2000 sec (Fig. 4.8), the entire cavity is filled with mushy region except a thin zone near the top and right wall of the cavity. It may be noted that a similar zone of smaller extent was observed in case of Fe-C alloy but at the bottom only, since thermal buoyancy was dominant there and not the solutal buoyancy (Fig. 4.5). Segregation level in case of Pb-Sn alloy is more compared to that in Fe-C alloy owing to high level of solute rejection and dominant solutal buoyancy

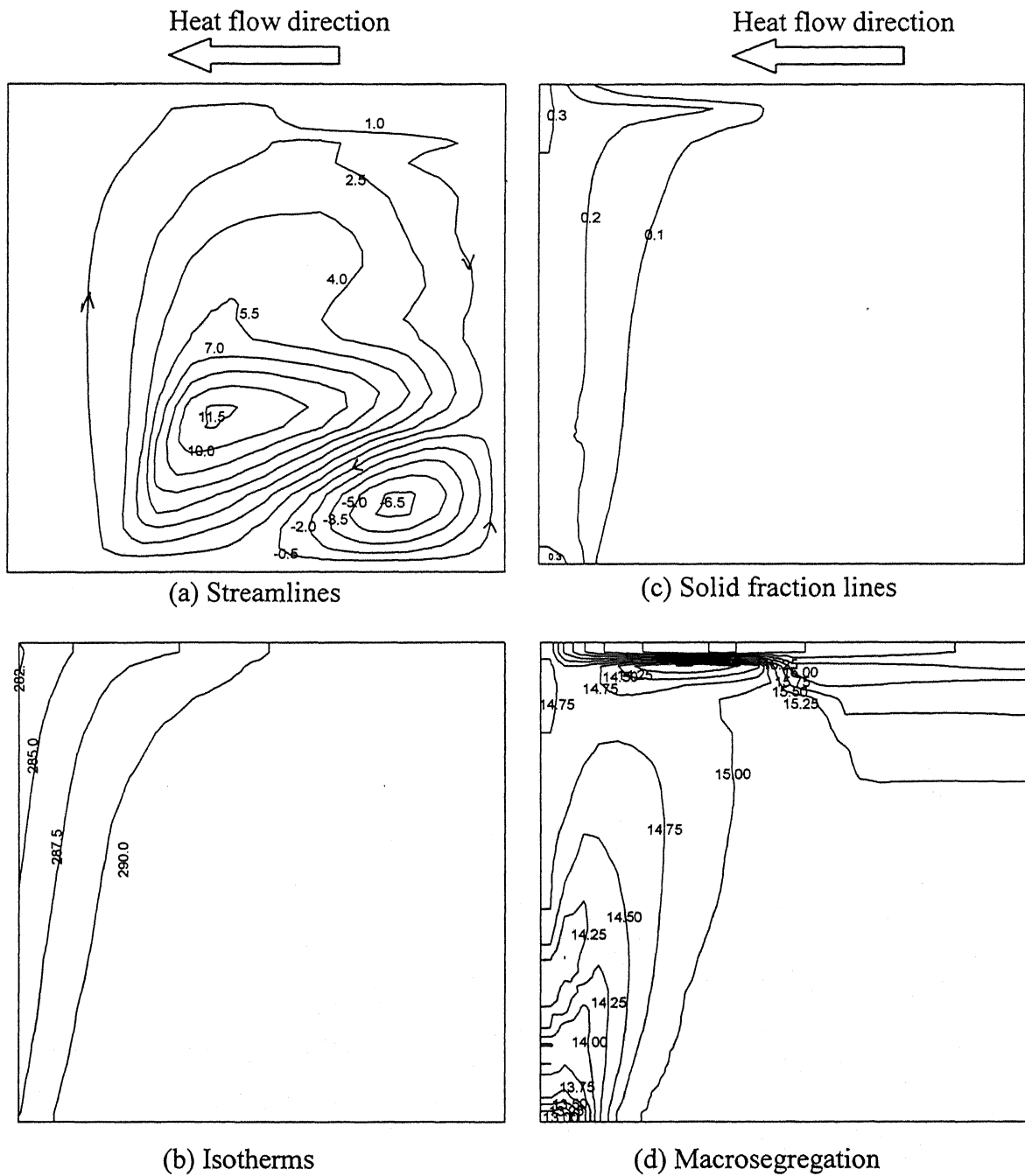


Fig. 4.6: Model predictions for solidification of Pb-15 wt % Sn alloy, solidification time (t) = 250 sec showing (a) streamlines, (b) isotherms, (c) solid fraction lines, and (d) iso-composition lines (wt % of tin).

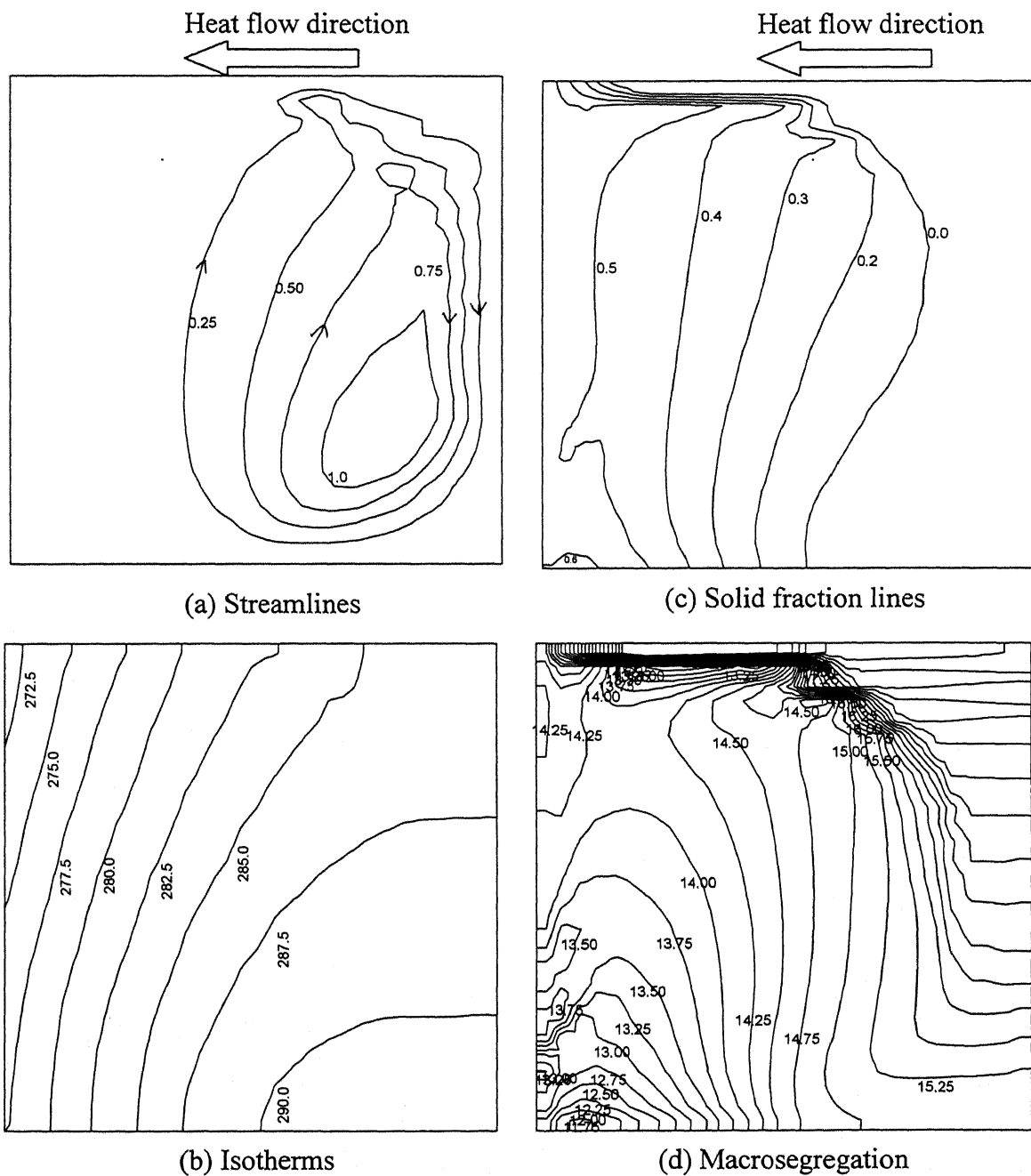


Fig. 4.7: Model predictions for solidification of Pb-15 wt % Sn alloy, solidification time (t) = 1000 sec showing (a) streamlines, (b) isotherms, (c) solid fraction lines, and (d) iso-composition lines (wt % of tin).

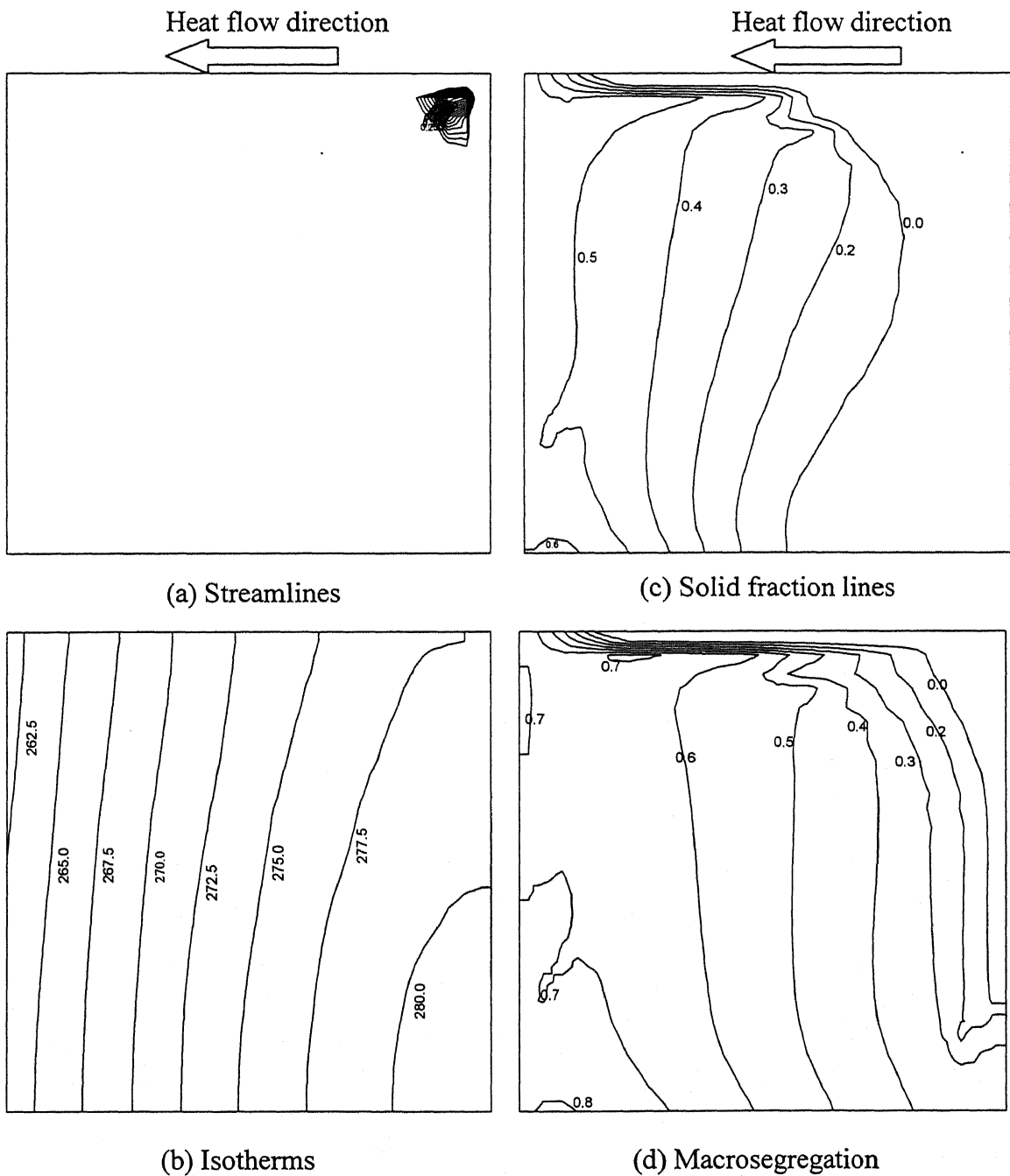


Fig. 4.8: Model predictions for solidification of Pb-15 wt % Sn alloy, solidification time (t) = 2000 sec showing (a) streamlines, (b) isotherms, (c) solid fraction lines, and (d) iso-composition lines (wt % of tin).

driven flow. Also, the pattern of segregation is more distinct in this case and positive segregation near hot wall and negative segregation band near the central portion is evident (Fig. 4.8).

In case of $\text{NH}_4\text{Cl-H}_2\text{O}$ solution, a very strong thermal buoyant flow is present at solidification time (t) = 250 sec (Fig. 4.9) due to large Ra_T as well as very high Pr (Table 4.2). Owing to this strong flow as well as very high Pr , the isotherms are near horizontal and stretched towards bottom. Although very little solidification occurred at this time, the effect of strong flow on segregation is evident due to long-range transport of the solute.

At 500 sec (Fig. 4.10), the solutal buoyancy started to play major role ($|N| = 1.4$) after initiation of solidification, and rejected solute gets transported out of the mush leading to enhanced solutal gradient in the bulk liquid. Due to strong flow, the fluid is well mixed in the cavity except in the mush. Also due to high solid fraction, flow is very weak in the mush leading to isotherms of vertical nature. The effect of thermal buoyancy can be noticed on the segregation profile from its large stretching at the bottom at this time.

Fig. 4.11 shows the situation at $t = 2000$ sec. It may be noted from Table 4.3 that solutal buoyancy goes through a minimum at 1500 sec. The possible mechanism for this is as follows. During the initial period of solidification, solutal gradient is built along the bottom wall of the cavity. During the transition phase, solutal buoyancy driven flow first reduces the solute build-up caused by thermal buoyancy driven flow and then starts to build solutal gradient along the top wall of the cavity, which adds to the solutal driven flow. The solute deposition along the top of the cavity continues, leading to greater positive segregation and simultaneously increasing depletion from the cold wall region. Unlike the metallic system where the mush covers the entire cavity, mush is relatively thin in case of $\text{NH}_4\text{Cl-H}_2\text{O}$ system and, more importantly, there is a completely solidified zone near the cold wall. This is due to low thermal conductivity and high Stefan number of $\text{NH}_4\text{Cl-H}_2\text{O}$ solution as compared to that for Pb-Sn alloy.

4.2.5 Conclusion

The effect of material properties on thermosolutal convection, and consequently, on macrosegregation is evident from comparative study of three systems. In case of Fe-C alloy, the solutal buoyancy is weak compared to thermal buoyancy, and flow field is

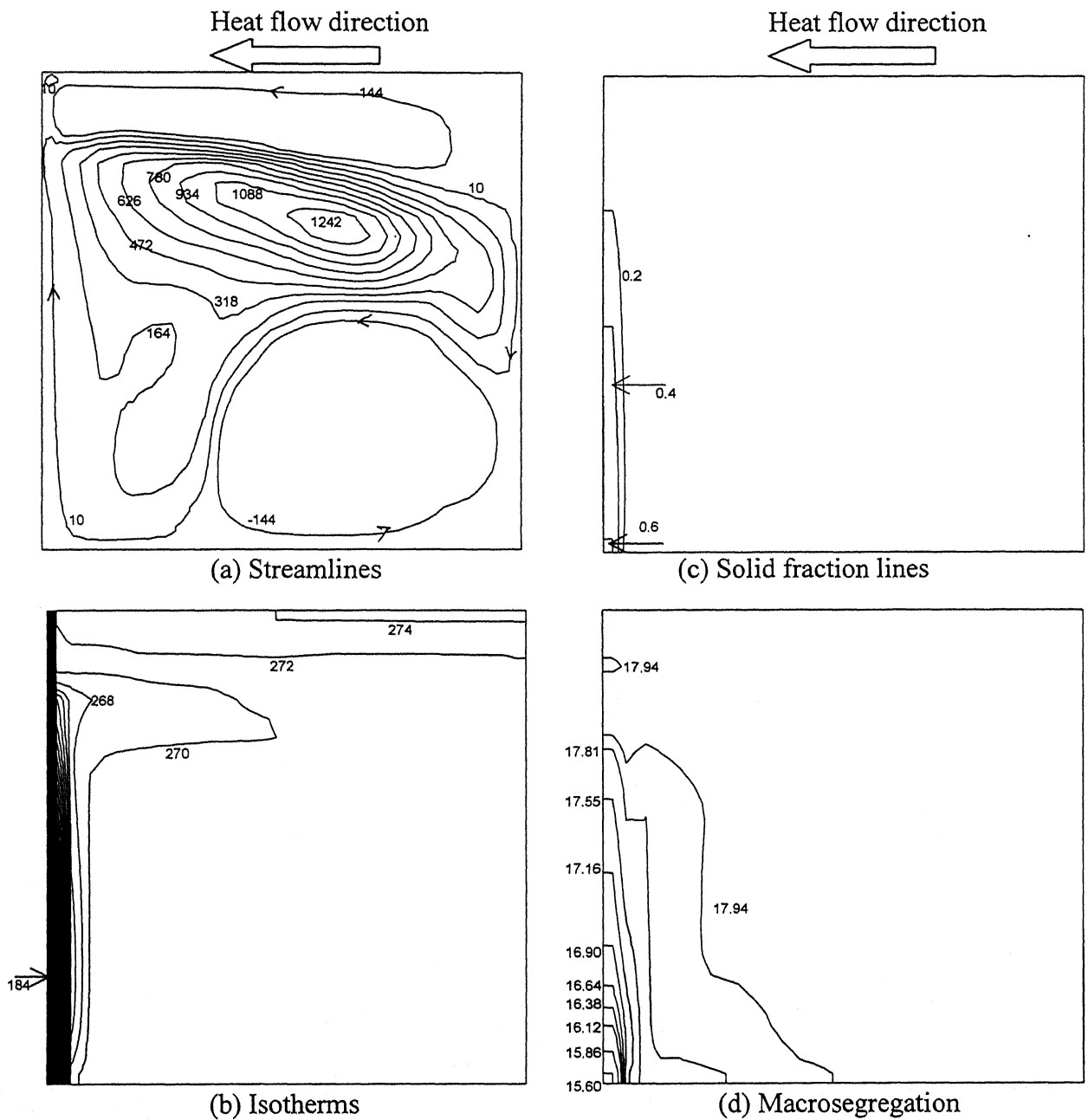


Fig. 4.9: Model predictions for solidification of NH_4Cl -18 wt % H_2O solution, solidification time (t) = 250 sec showing (a) streamlines, (b) isotherms, (c) solid fraction lines, and (d) iso-composition lines (wt % of H_2O).

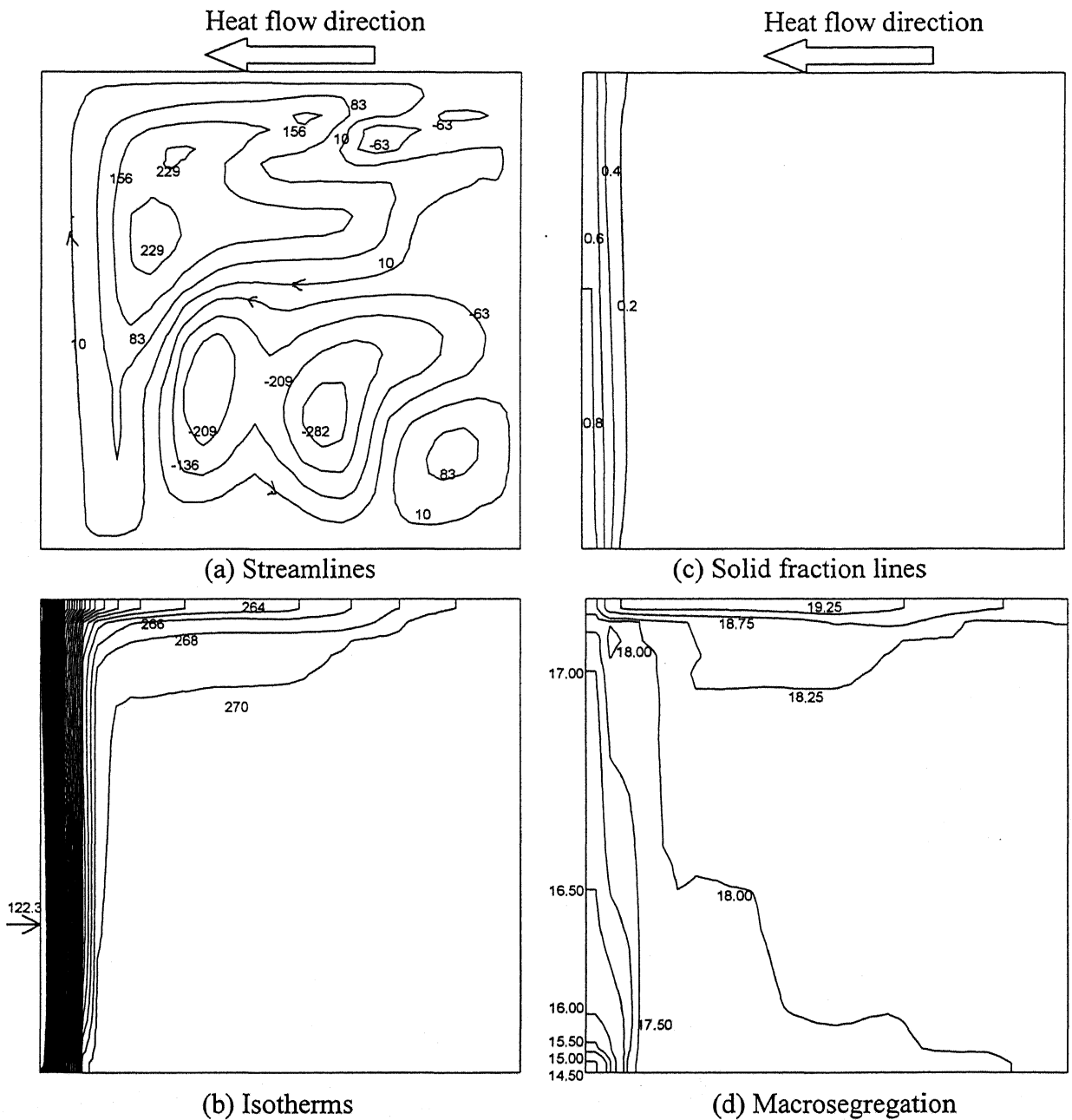


Fig. 4.10: Model predictions for solidification of NH_4Cl -18 wt % H_2O solution, solidification time (t) = 500 sec showing (a) streamlines, (b) isotherms, (c) solid fraction lines, and (d) iso-composition lines (wt % of H_2O).

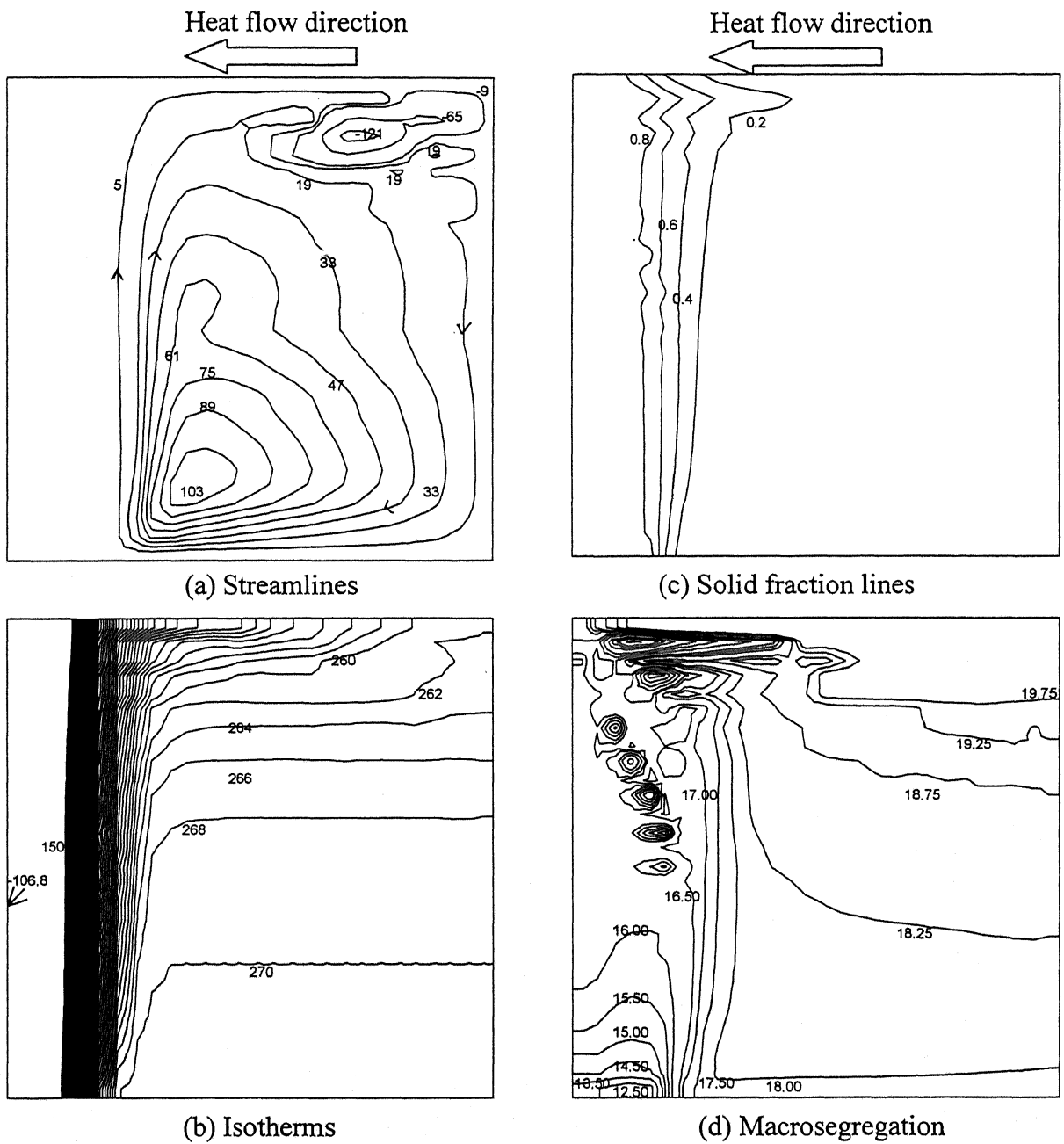


Fig. 4.11: Model predictions for solidification of NH_4Cl -18 wt % H_2O solution, solidification time (t) = 2000 sec showing (a) streamlines, (b) isotherms, (c) solid fraction lines, and (d) iso-composition lines (wt % of H_2O).

governed by thermal buoyancy. On the other hand, in Pb-Sn alloy and $\text{NH}_4\text{Cl-H}_2\text{O}$ systems, the flow is thermal buoyancy driven in initial period of solidification, but gradually transforms to solutal buoyancy driven flow. The effect of flow pattern and strength on isotherms and mush profiles are significant in these three systems.

The nature of macrosegregation profile entirely follows the flow pattern. Thus in case of Fe-C alloy the zone of positive segregation occurred along the bottom and right vertical walls of the cavity. In contrast, the positive segregation zone for Pb-Sn alloy and $\text{NH}_4\text{Cl-H}_2\text{O}$ solution are along top wall and right wall of the cavity. The segregation band is small for Fe-C alloy owing to relatively small Raleigh numbers and high resistance to flow in the mush. On the other hand, for Pb-Sn alloy and $\text{NH}_4\text{Cl-H}_2\text{O}$ solution, the extents of segregation are higher. In case Pb-Sn alloy, Ra_s is higher compared to Fe-C alloy and this is the driving mechanism for high segregation level. In comparison to these two, $\text{NH}_4\text{Cl-H}_2\text{O}$ system has very high Ra_s and Ra_T , but formation of a narrow mushy region restricts macrosegregation to a level similar to Pb-Sn alloy. Thus, it may be noted that material properties affect thermosolutal convection, and consequently macrosegregation in a very significant way.

4.3 Role of Permeability on Macrosegregation

4.3.1 Introduction

In single-phase formulation, as already stated in Ch. 3, the representation of mushy region is extremely important for meaningful prediction of field variables. The treatment of the mushy region as continuum leads to certain simplifications in formulation. As a result, the microstructural and morphological details of the mushy region get their representation in the governing equations indirectly, i.e., through use of auxiliary relationship for permeability. This point is of particular importance in case of macrosegregation as the same is caused due to long-range transport of the solute from the mushy region to the other parts of the casting. Therefore it is necessary to critically examine the role of permeability functions on macrosegregation.

4.3.2 Permeability models

In a combined experimental and modeling work, Krane et al[42] showed that the permeability coefficient of Kozeny-Carman equation needs to be altered by an order of magnitude to get a closer correspondence with the experimental data on macrosegregation and that West's correlation[89] provides a better match. However, as pointed out by Krane et al the lack of generality of West model prohibits its uses. In the first part of the present study, experiments of Krane, et al were simulated with Kozeny-Carman permeability model with various permeability coefficients and Poirier anisotropic model [90].

- (i) The first model considered for simulation was the Kozeny-Carman isotropic model, which has been extensively used in the literature. The following form is used in the present study:

$$K = K_o [(f_l)^3 / (1 - f_l)^2] \quad \dots 4.3$$

where, K_o is the permeability coefficient in m^2 , d is the dendrite arm spacing in μm , and f_l is liquid fraction in the mush.

- (ii) Poirier [90] suggested many equations for both directions. Of these, the following equations were chosen in present study. For flow parallel to primary dendrite arm, Hagen- Poisseulle equation was used for f_l between 0.17 and 0.61.

$$K = 3.75 \times 10^{-4} (d_1)^2 (f_l)^2 \quad \dots 4.4$$

For flow perpendicular to primary dendrite arms, a multi-linear regression model based on primary dendrite arm spacing was employed for f_l between 0.19 and 0.66, as follows.

$$K = 7.08 \times 10^{-4} (d_1)^{2.08} (f_l)^{3.32} \quad \dots 4.5$$

For liquid fractions outside the range of applicability of the above equations, the Kozeny-Carman model was employed for extrapolation.

4.3.3 Problem definition

Experiment carried out by Krane and Incropera [42] was simulated using the mathematical model described in Ch. 3. The melt was a binary Pb-40 Wt% Sn alloy with an initial temperature of 239°C. The rectangular cavity, which was 89 mm wide and 75 mm tall, was filled with molten alloy. Krane and Incropera estimated the average heat transfer coefficient (h) between 85 and 100 W/m²K. A value of 100 W/m²/K was used for h in these simulations. The thermophysical properties employed in this study are from references [95-99] (also listed in Table 2.2, Ch. 2). Krane and Incropera used the following expression, given by Asai and Muchi [118], for evaluation of permeability constant, K_o (m²):

$$K_o = d^2/180 \quad \dots 4.6$$

Where, d is the dendrite arm spacing in μm .

As noted by Krane et al, this value gives very high macrosegregation. Lowering the coefficient by an order of magnitude ($K_o = 2.8 \times 10^{-11} \text{ m}^2$) still result in a very high magnitude of macrosegregation. Thus, three simulations were performed in the present study as noted below.

Case I: Isotropic Kozeny-Carman model for all f_l with $K_o = 1.68 \times 10^{-10} \text{ m}^2$ corresponding to $d_1 = 174 \mu\text{m}$

Case II: Isotropic Kozeny-Carman model for all f_l with $K_o = 2.8 \times 10^{-11} \text{ m}^2$ corresponding to $d_2 = 71 \mu\text{m}$

Case III: Poirier anisotropic model [90] with $d = 174 \mu\text{m}$, and the following additional data

For flow parallel to dendrite arm:

For $f_l > 0.61$ Kozeny-Carman with $K_o = 4.6 \times 10^{-11} \text{ m}^2$

For $f_l > 0.17$ and < 0.61 Hagen-Poiseuille with $K = 3.75 \times 10^{-4} f_l^2 \text{ m}^2$

For $f_l < 0.17$ Kozeny-Carman with $K_o = 2.83 \times 10^{-12} \text{ m}^2$

For flow perpendicular to dendrite arm:

For $f_l > 0.66$ Kozeny-Carman with $K_o = 1.25 \times 10^{-11} \text{ m}^2$

For $f_l > 0.19$ and < 0.66 Multi-linear regression with $K = 3.8 \times 10^{-11} f_l^{3.32} \text{ m}^2$

For $f_l < 0.19$ Kozeny-Carman with $K_o = 3.27 \times 10^{-12} \text{ m}^2$

The simulations were carried out with (42x42) grids till complete solidification. Fig. 4.12 shows the geometry and grid placements as well as final macrosegregation profile at the end of solidification for permeability for case I.

4.3.4 Results and discussions

Comparison of final macrosegregation with the measurements for all three cases are shown in Figs. 4.13 and 4.14 for four different planes. Fig. 4.13(a), Fig. 4.13(b) and Fig. 4.14(a) show variation of macrosegregation along X-axis at heights of 15 mm, 39 mm and 69 mm. Fig. 4.14(b) shows variation of macrosegregation along Y-axis at $x = 19 \text{ mm}$ (ref: Fig. 4.1). From Figs. 4.13 and 4.14, it is readily seen that case I (Kozeny-Carman with $d_1 = 174 \text{ }\mu\text{m}$) over predicts macrosegregation significantly. Case II, which is for the Kozeny-Carman model with d_2 equal to $71 \text{ }\mu\text{m}$, also over predicts. However, the extent of segregation in case II is less than case I. Case III, which is for Poirier anisotropic model with d_1 equal to $174 \text{ }\mu\text{m}$, under predicts macrosegregation in majority of the planes. Among the three permeability models, Kozeny-Carman with d equal to $71 \text{ }\mu\text{m}$ provided better match with experimental data. Good agreements between predictions and measurements may be noted for both cases I and III.

Using the experimental thermal profile, theoretical model for secondary dendrite arm spacing gives a value in the range of $67\text{-}75 \text{ }\mu\text{m}$ (Ch. 6, Eq. 6.2). Secondary dendrite arm spacing was found to control the evolution of macrosegregation in this alloy.

However, the use of Kozeny-Carman equation [85] as extrapolation function in high liquid region has been criticized, since the same is valid for high solid fraction (0.5 and above). As demonstrated by Krane[42], the West model[89] shows a better match. This model has two parts as shown below:

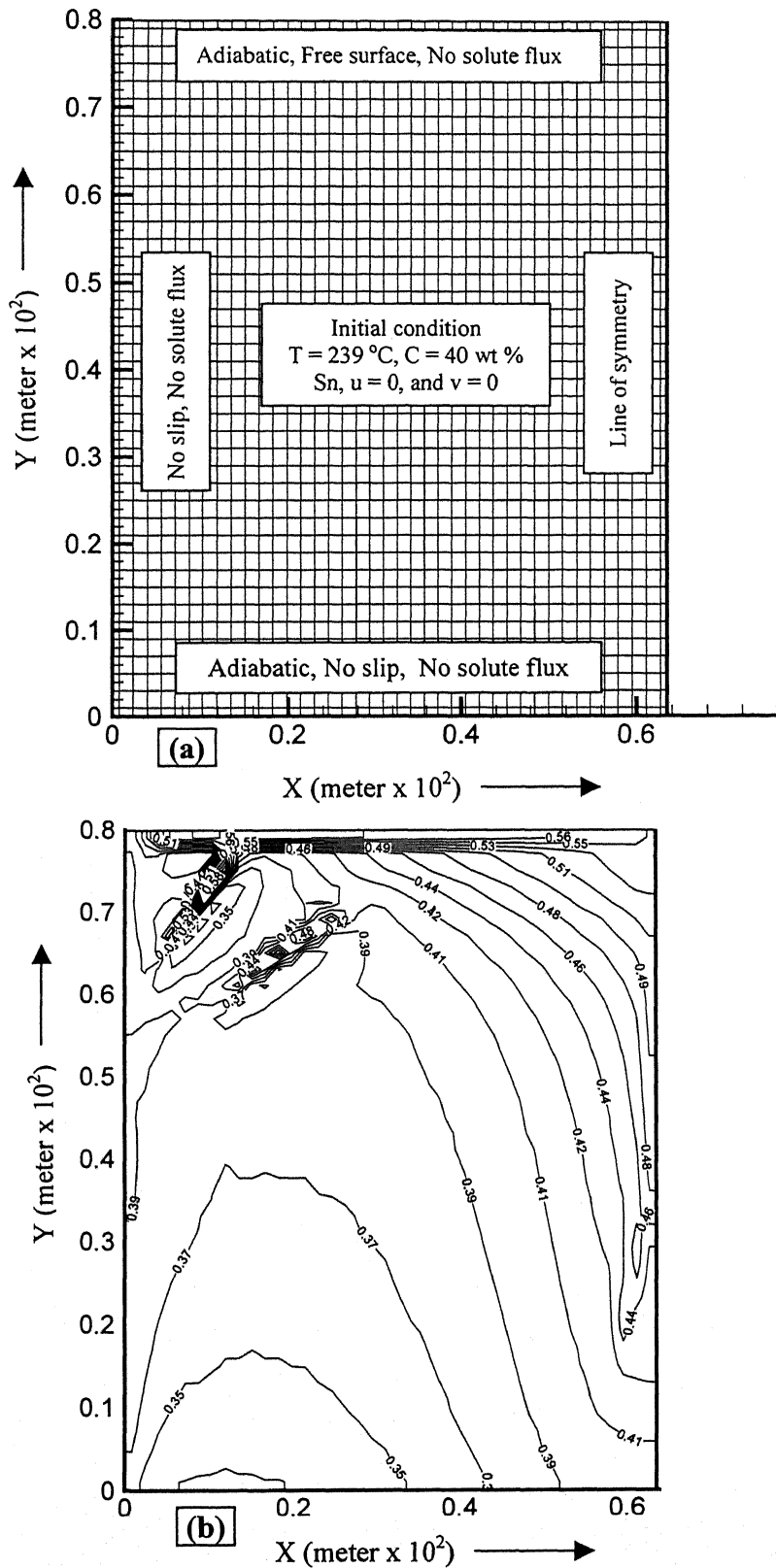
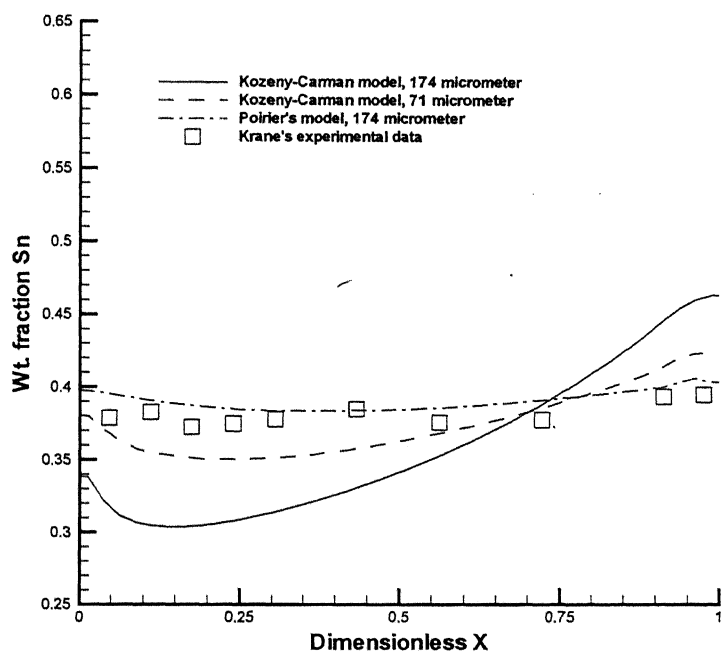
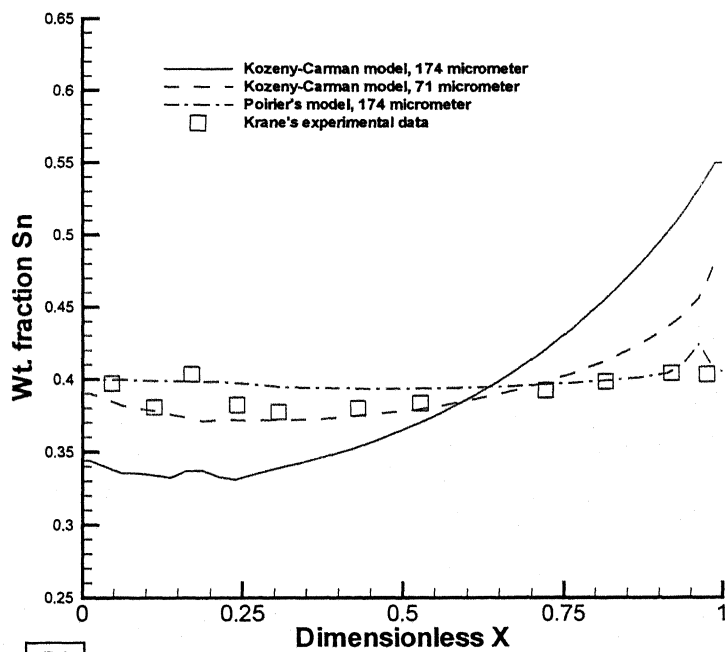


Fig. 4.12: (a) Geometry of the casting, initial and boundary conditions and (b) macrosegregation profile at the end of solidification.



(a)



(b)

Fig. 4.13: Comparison of composition profiles from various permeability models with experimental data [42] at (a) $Y = 15$ mm and (b) $Y = 39$ mm.

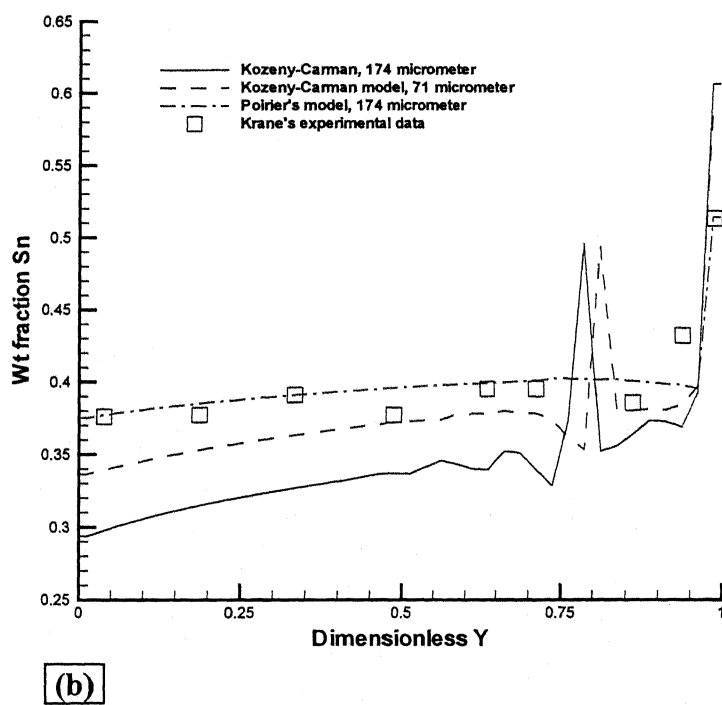
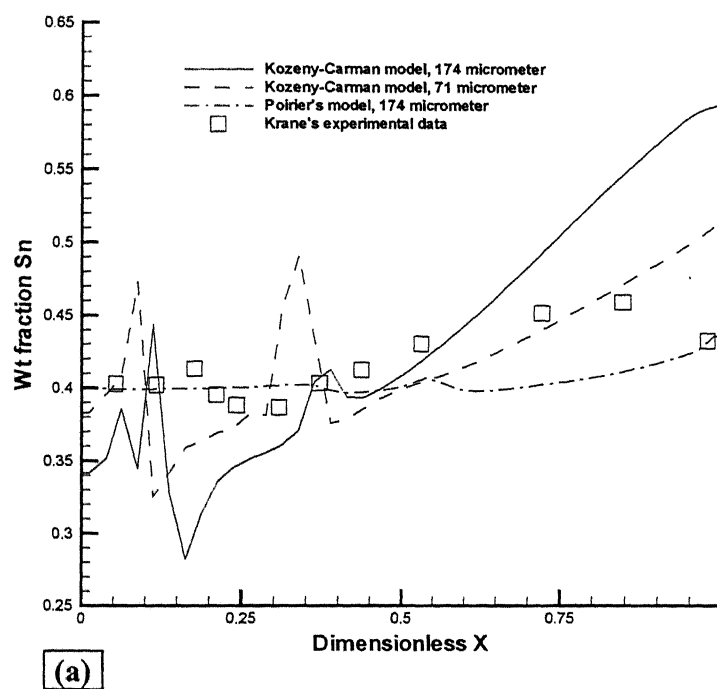


Fig. 4.14: Comparison of composition profiles from various permeability models with experimental data [42] at (a) $Y = 69$ mm and (b) $X = 19$ mm.

$$K = (6.4 \times 10^{-13}) \cdot f_l^2 \quad \text{for } f_l < 1/3 \quad \dots 4.7$$

$$K = (6.4 \times 10^{-13}) \cdot f_l^2 + (8.8 \times 10^{-11}) \cdot f_s^{2/3} \cdot [3 + 4/f_s - 3 \cdot (8/f_s - 3)^{1/2}] \quad \text{for } f_l > 1/3 \quad \dots 4.8$$

where, f_s is the solid fraction in the mush.

The form of the second term of Eq. 4.8 comes from the Brinkman model [83] for high liquid regime whereas the coefficient comes through regression with experimental data of Piowonka and Flemings[88], and does not have any microstructural parameters.

Starting with the original expression [83] for the second part of 4. 8, one gets the following:

$$K_2 = (R^2/18) [3 + 4/f_s - 3 \cdot (8/f_s - 3)^{1/2}] \quad \dots 4.9$$

In the above equation, R is the radius of spherical particle in high liquid region. Expressing R in terms of dendrite arm spacing and fraction liquid [90], the following equation is obtained.

$$R^3 = (d^3/8) (1-f_l) \quad \dots 4.10$$

$$K = (d^2/72) f_s^{2/3} \cdot [3 + 4/f_s - 3 \cdot (8/f_s - 3)^{1/2}] \quad \dots 4.11$$

where, d is the dendrite arm spacing.

The permeability function in low liquid fraction regime is relatively unimportant. Since Kozeny-Carman model is here, this was used for extrapolation of the above function into low liquid regime. The following expression provided the best fit:

$$K = K_o [(g_l)^3/(1-g_l)^2], \text{ where } K_o = d^2/(180 \times 1.75) \quad \dots 4.12$$

The combined model can thus be stated as follows:

$$K = K_o [(f_l)^3/(1-f_l)^2] , \text{ where } K_o = d^2/(180 \times 1.75), \text{ for } f_l < 0.5 \quad \dots 4.13$$

$$K = (d^2/72) f_s^{2/3} . [3 + 4/f_s - 3.(8/f_s - 3)^{1/2}], \quad \text{for } f_l > 0.5 \quad \dots 4.14$$

Eqs. 4.13 and 4.14 were plotted against the experimental data on permeability of Poirier [90], which are in terms of permeability, primary dendrite arm spacing(d_1), secondary dendrite arm spacing (d_2) and fraction liquid. Dimensionless permeability was obtained by dividing permeability value by $(d_2)^2$. The results are shown in Fig. 4.14 (a) and (b) for flow parallel and perpendicular to primary dendrite arm spacing respectively. Looking at these figures, it is readily observed that the model provides a reasonable match with the data.

Experiment of Krane et al [42] was simulated using the permeability function described by Eqs. 4.13 and 4.14. Secondary dendrite arm spacing was obtained for calculation of permeability, which was estimated from an empirical equation (Ch.6, Eq. 6.2). The local solidification time, used in the empirical equation, was obtained from time-temperature curves of Krane et al, and the dendrite arm spacing was estimated in the range of 68-75 μm . A value of 71 μm was employed in simulation. The results are shown in 4.16 and 4.17. It may be noted that while there were reasonable match for two planes, match were poor in two other planes. Hence, improvements are still needed. Following conclusions are drawn from this study:

- (i) Generalized West model based on secondary dendrites arm spacing represents permeability data in both parallel and perpendicular directions reasonably well.
- (ii) Use of permeability model for prediction of macrosegregation has yielded mixed results.

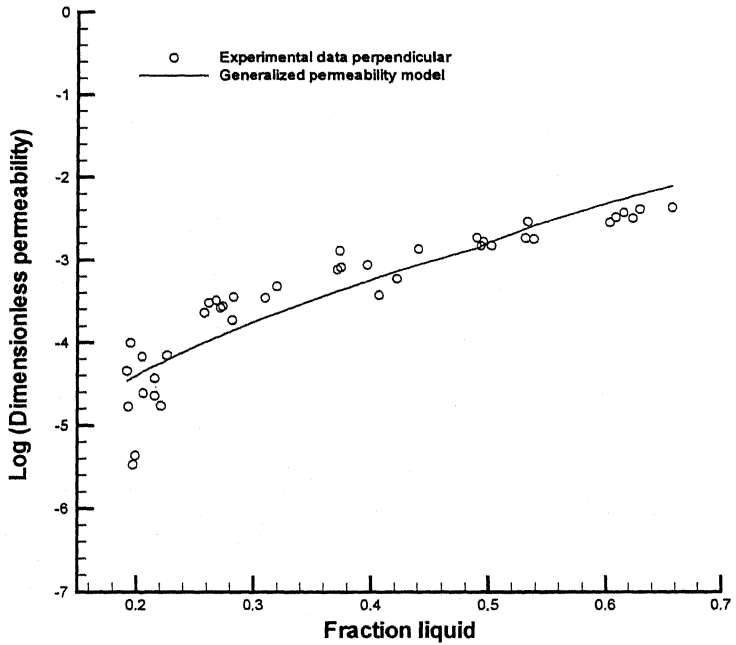
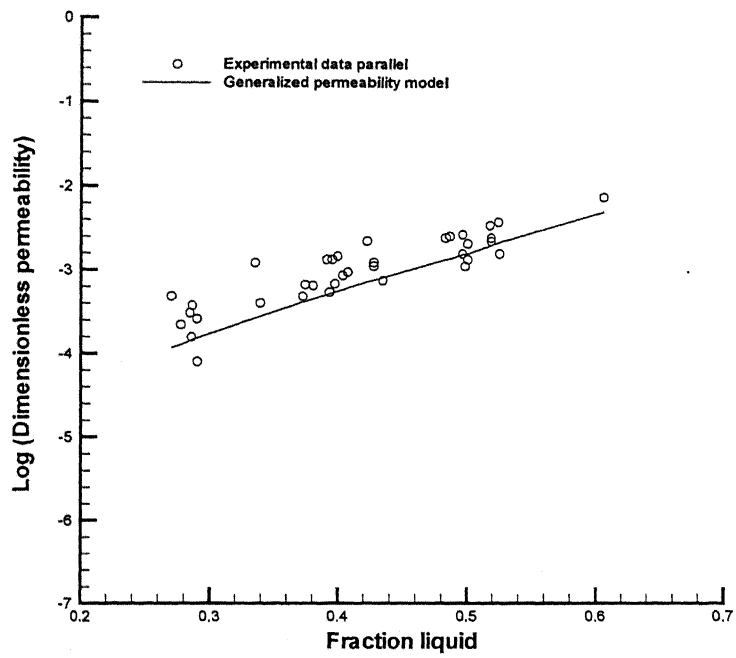


Fig. 4.15: Comparison of permeability model (this work) with experimental data [90] for flow (a) parallel and (b) perpendicular to primary dendrite arms spacing.

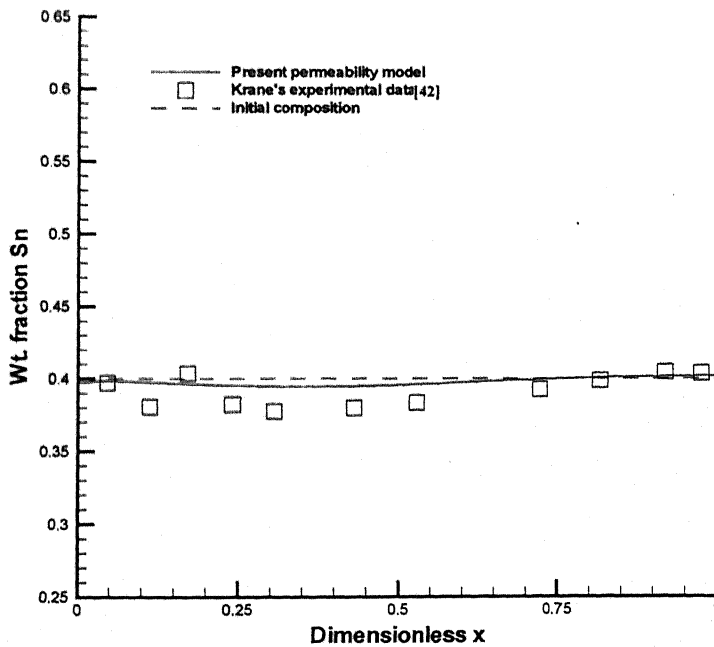
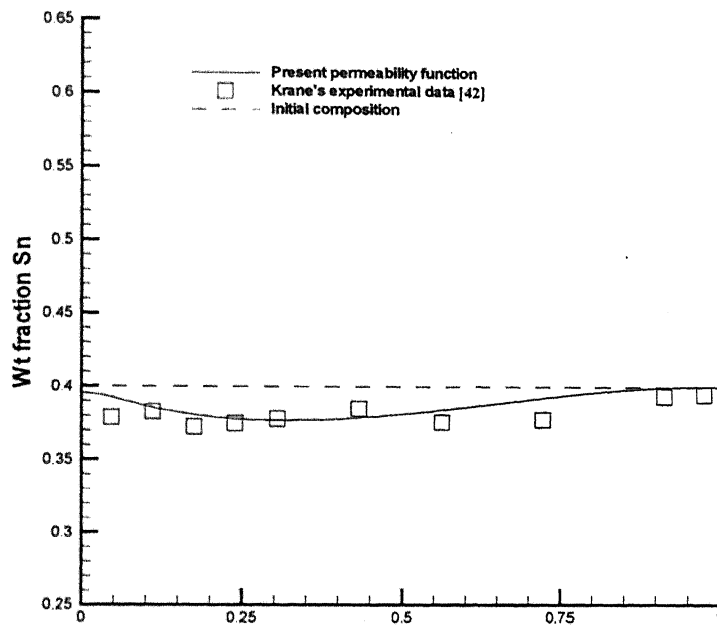


Fig. 4.16: Comparison of composition profiles (present permeability model) with experimental data [42] at (a) $Y = 15$ mm and (b) $X = 39$ mm.

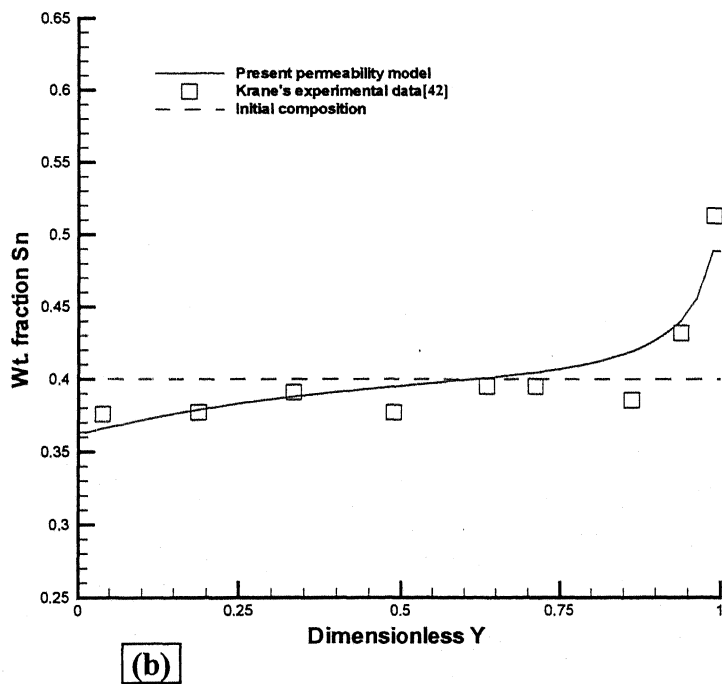
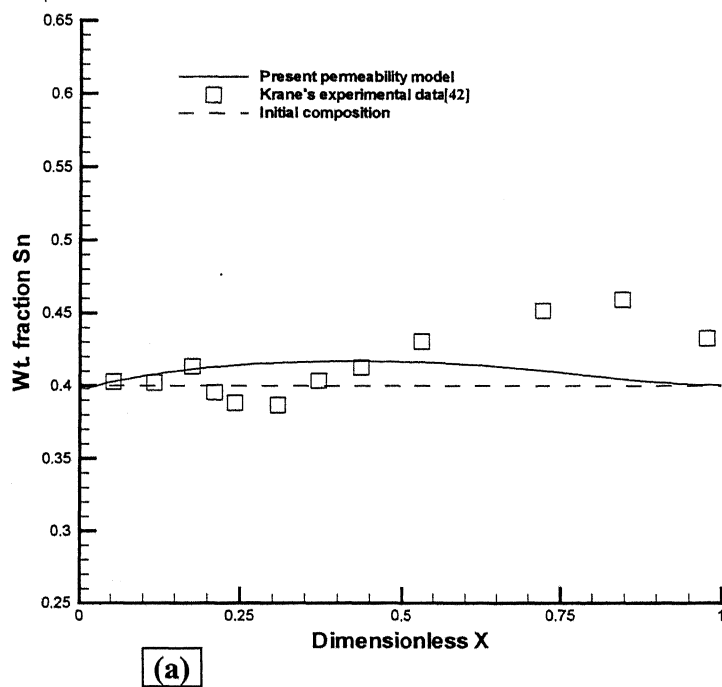


Fig. 4.17: Comparison of composition profiles (present permeability model) with experimental data [42] at (a) $Y = 69$ mm and (b) $X = 19$ mm.

4.3.5 Conclusions

Permeability in the thin mushy region is a key input to any single-domain model for macrosegregation. It was shown that the use of Kozeny-Carman equation with permeability coefficient based on primary dendrite arms spacing results in very high macrosegregation. Use of Kozeny-Carman model with permeability coefficient based on secondary dendrite arms spacing still over predicted macrosegregation but was better than the other two cases (case I and case III). Use of empirical model of permeability by Poirier, which is valid for middle range of permeability and is a function of primary dendrite arm spacing, under predicted macrosegregation. In order to obtain closer correspondence with the experimental data, West model [89] for thin mushy region, which is based on the work of Brinkman[83], was generalized in terms of secondary dendrite arm spacing in the present study, and the same was tested with limited data in literature on Pb-Sn alloy[90]. Using this model, experiment of Krane et al[42] on Pb-Sn alloy was simulated and predicted macrosegregation profiles were compared with the measured data. There were reasonable match for two planes, but match were poor in two other planes. Although the limited data from Pb-Sn alloy show better correspondence with the model based on secondary dendrite arm spacing, depending on alloy, a more generic functional dependence on primary as well as secondary dendrite arm spacing would have to be found. Further studies are required, both experimental as well as numerical, to establish a sound basis of representing convection in the mush, and in turn, improve accuracy of the macrosegregation predictions.

4.4 Effect of Cooling Rate on Thermosolutal Convection and Macrosegregation in Iron-Carbon System

It is well known that heat flux has a significant effect on macrosegregation [4], and steel is cast with a wide range of heat fluxes. Typical heat flux in the primary cooling zone of continuous caster is of the order of 2.5 MW/m^2 , whereas during some static casting, heat flux is as low as 10 kW/m^2 . Considering its importance many studies have been carried out on this system. These have been reviewed in Chapter 2.

To the authors' knowledge, however, there has been very little systematic effort to study the effect of cooling rate on macrosegregation during solidification of iron-carbon binary alloy or multi-component steel. The following study was aimed to understand the effect of cooling rate on macrosegregation during casting of steel with the help of a mathematical model.

4.4.1 Problem Definition

For the purpose of the present study, the solidification is considered in a rectangular cavity of length L (0.1 m) and height H (0.1 m). The geometry of the cavity is shown in Fig. 4.1. The boundary conditions used in the present study are as follows. (i) No-slip conditions are applied on horizontal and left vertical walls of the cavity. (ii) The left vertical wall is the line of symmetry and the gradient of u -velocity along X -axis is zero. (iii) There is no solute flux through all four bounds of the cavity. (iv) As for the thermal boundary conditions, the horizontal walls of the cavity are adiabatic and there is no heat flux at the left wall. Solidification is initiated by imposing a heat flux along the right vertical wall of the cavity. The material chosen for the present study was Fe-1 wt pct C. T_{init} for the present study was taken to be 1463 °C.

Various thermophysical data pertaining to this system are provided in Table 4.1. In numerical implementation, the heat flux was varied by changing the value of q along the right wall (chill face) of the cavity.

All the simulation studies were done with a non-uniform grid of 30x30 nodal points, whose choice was based on a grid independency test. A variable time step of 0.5-25 seconds was employed to simulate the transient time marching solution till the end of solidification. On an average, a CPU time of 1 minute was required for 5 seconds of real time simulation on a SUN ULTRA-60 workstation.

4.4.2 Results and discussion

Simulations were carried out with heat fluxes varying in the range of 5 to 6000 kW/m². Since the time taken for complete solidification was different for various cases, overall solid fraction was chosen as the basis for comparing the results for various heat fluxes. The results presented below are at three instances of overall solidification, namely, 20, 50

and 80 %. Beyond 80% solidification, the flow field was restricted near the hot wall and was very weak in magnitude except for the higher heat fluxes. In addition to these, the macrosegregation profiles for various heat fluxes are also compared at the end of solidification.

Figs. 4.18, 4.19 and 4.20 present the streamlines, isotherms, mush profiles and macrosegregation profiles at 20, 50 and 80 % solidification for heat fluxes of $q = 10, 60$ and 360 kW/m^2 respectively. In these figures, the right vertical wall of the cavity represents the chill face, whereas, the left vertical wall, which is at the line of symmetry, represents the hot face. The maxima and minima of various quantities are listed in Table 4.4.

Fig. 4.18 shows the results for heat flux of 10 kW/m^2 . At 20 % overall solidification, the flow pattern is very complex and the presence of multiple vortices is readily seen. The isotherms are affected by the flow to a large extent. They are parallel to the horizontal axis showing the dominance of convection over conduction. Although the overall solidification is only 20 %, the mush is spread over the large part of the cavity, and both mush profiles and macrosegregation patterns, shown in Fig. 4.18(c) and 4.18(d), respectively, are very complex. Since the mush covers the large part of the cavity, the resistance to the flow is high leading to the reduction in strength of thermal buoyant flow. Isotherms are almost parallel to horizontal wall near the hot wall of the cavity; the fluid near the bottom corner is thermally stable and a solutal buoyancy driven cell is readily observable.

With the progress of solidification, the strength of flow diminishes, and the isotherms show its vertical nature near the cold wall. The macrosegregation profile is highly evolved by this time. Important feature of mush profile at this juncture is that even though the overall solidification is around 50 %, pure solid regime is yet to start. As the solidification progresses further, the flow strength becomes negligible. At 80 % the flow is almost absent and isotherms are mostly vertical in nature. There is very little difference between macrosegregation profiles of this time and those at 50 % solidification.

Fig. 4.19 shows the results for heat flux of 60 kW/m^2 . At 20 % solidification, the strength of flow is higher than that of the case of 10 kW/m^2 . However, the isotherms show conduction dominance near the cold wall due to large value of f_s . The macrosegregation

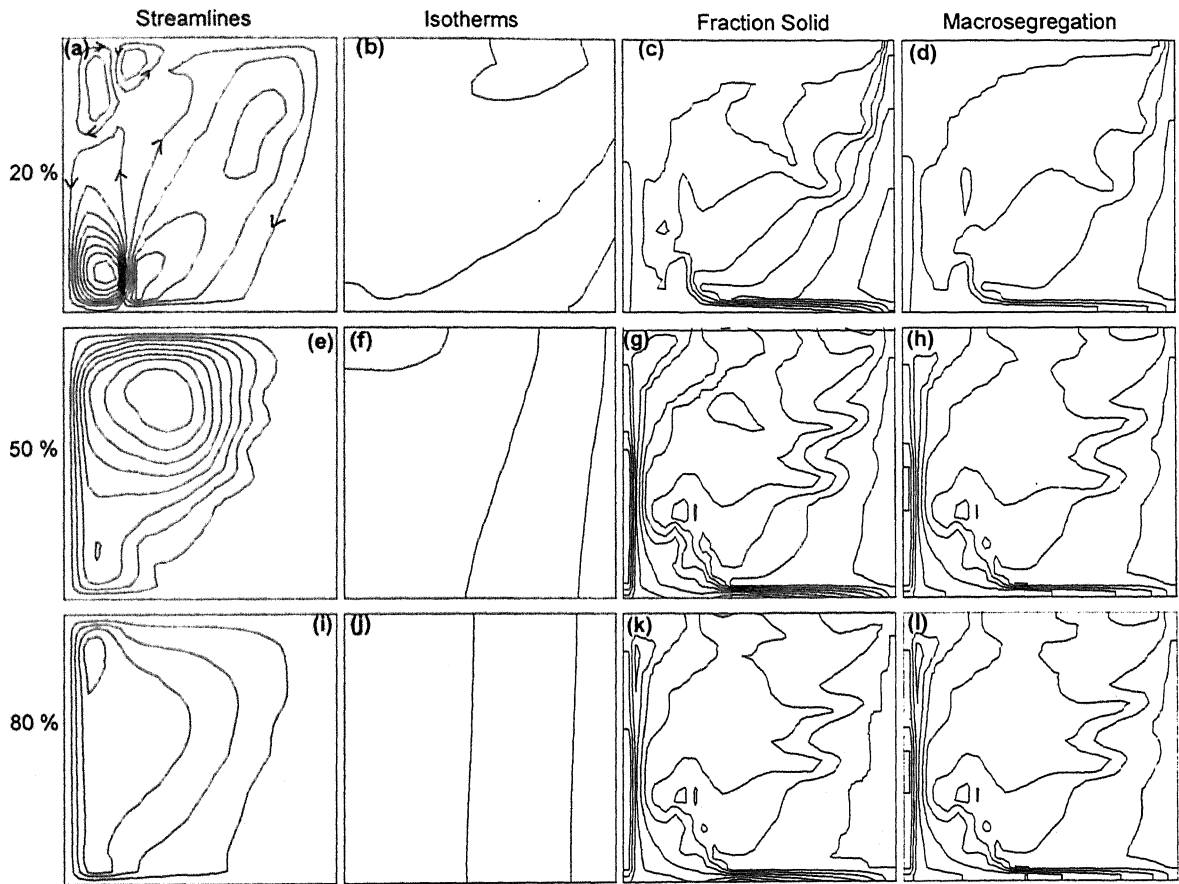


Fig. 4.18: Streamlines, isotherms, mush profile and macrosegregation pattern for 20, 50 and 80 % solidification for heat flux of 10 kW/m^2 : ψ_{\max} & ψ_{\min} : Table II, $\Delta\psi = 0.25$ for (a), 0.05 for (e), and 1.5×10^{-3} for (i); (b), (f) & (j) T_{\max} & T_{\min} : Table II, $\Delta T = 5^\circ \text{C}$; (c), (g) & (k) f_{\max} & f_{\min} : Table II, $\Delta f = 0.1$; (d), (h) & (l) C_{\max} & C_{\min} : Table II, $\Delta C = 0.1$.

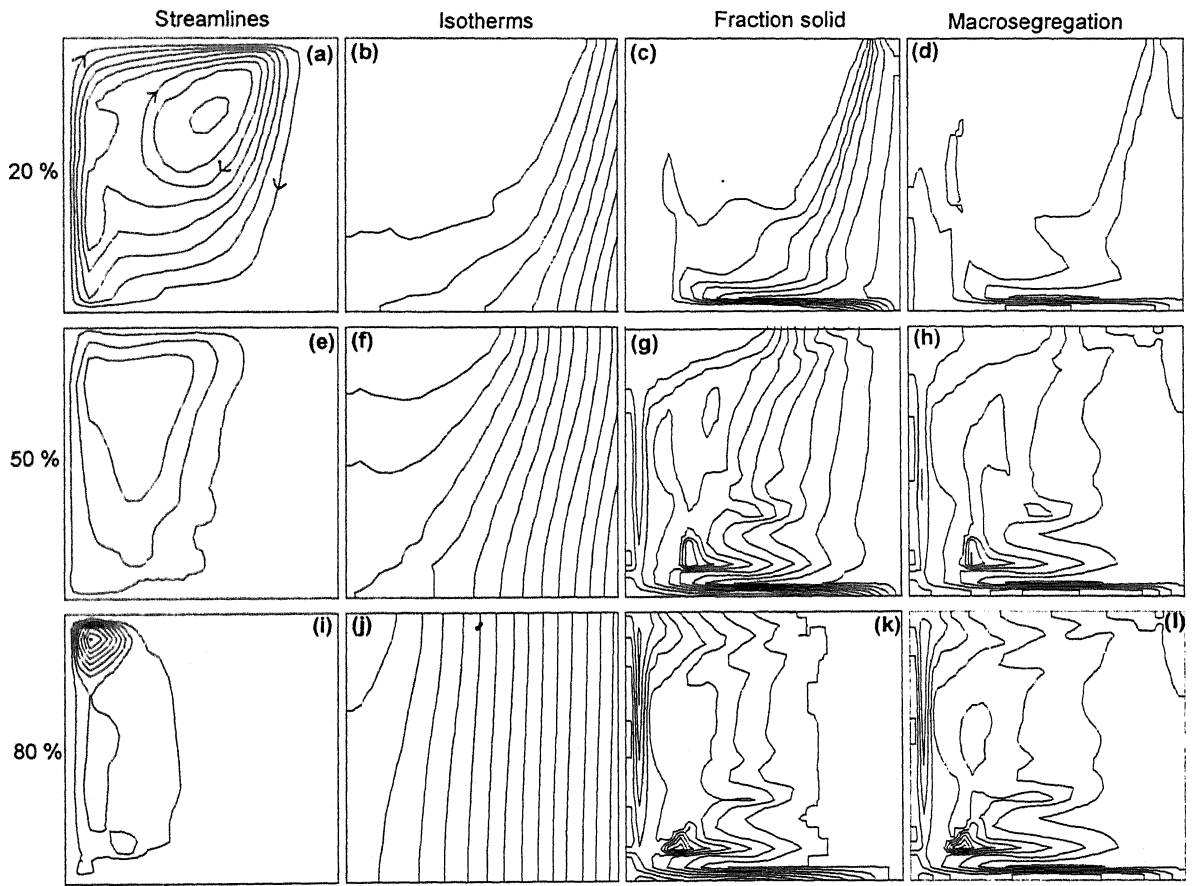


Fig. 4.19: Streamlines, isotherms, mush profile and macrosegregation pattern for 20, 50 and 80 % solidification for heat flux of 60 kW/m^2 : ψ_{\max} & ψ_{\min} : Table II, $\Delta\psi = 1$ for (a), 0.55 for (e) and 0.02 for (i); (b), (f) & (j) T_{\max} & T_{\min} : Table II, $\Delta T = 5 \text{ }^\circ\text{C}$; (c), (g) & (k) f_{\max} & f_{\min} : Table II, $\Delta f = 0.1$; (d), (h) & (l) C_{\max} & C_{\min} : Table II, $\Delta C = 0.1$.

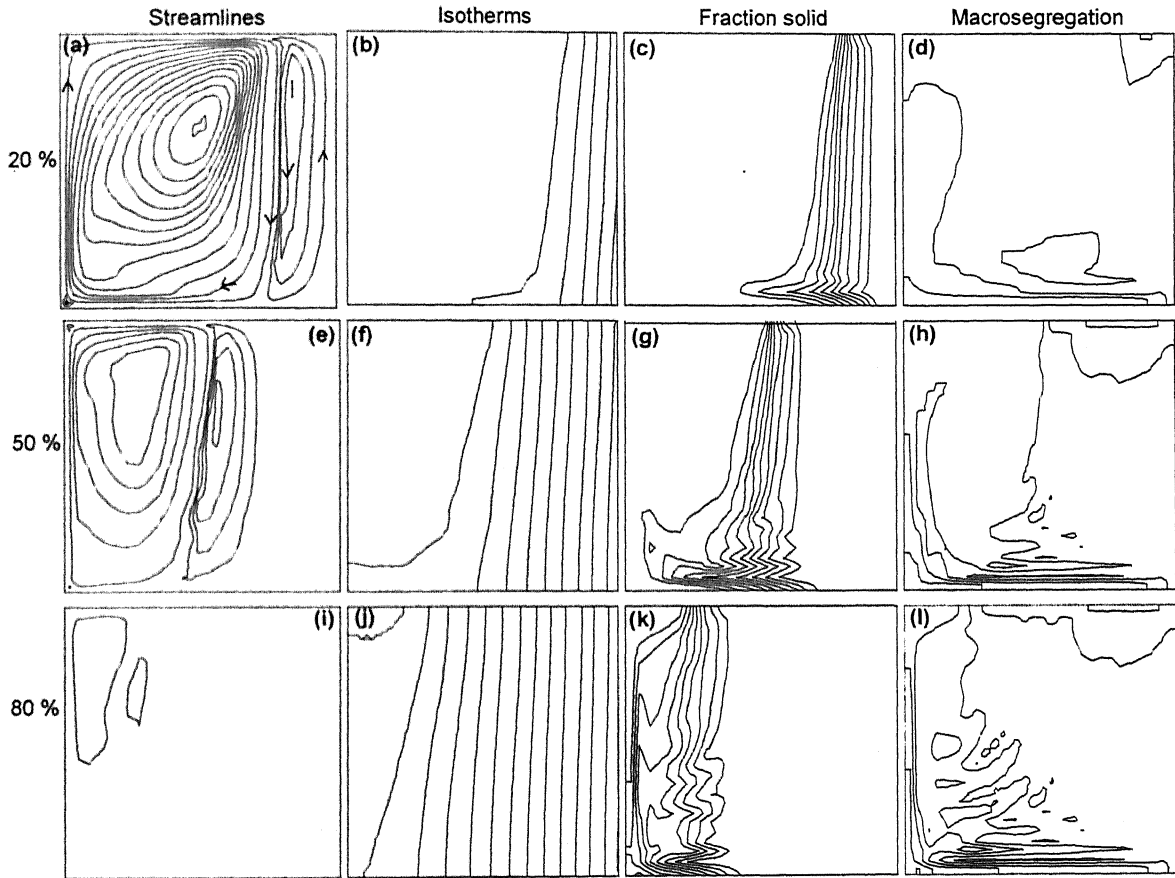


Fig. 4.20: Streamlines, isotherms, mush profile and macrosegregation pattern for 20, 50 and 80 % solidification for heat flux of 360 kW/m^2 (a), (e) & (i) ψ_{\max} & ψ_{\min} : Table II, $\Delta\psi = 2.5$ for major vortex and 0.2 for minor vortex; (b), (f) & (j) T_{\max} & T_{\min} : Table II, $\Delta T = 5 \text{ }^\circ\text{C}$; (c), (g) & (k) f_{\max} & f_{\min} : Table II, $\Delta f = 0.1$; (d), (h) & (l) C_{\max} & C_{\min} : Table II, $\Delta C = 0.1$.

Table 4.4: Maximum and minimum values of stream function, temperature and average composition for various heat fluxes for solidification of Fe-1 wt % C alloy

Heat Flux kW/m ²	% Solidification	Composition (wt %)		Temperature (°C)		Streamlines		Fraction solid	
		Max.	Min.	Max.	Min.	Max.	Min.	Max.	Min.
10	20	1.19	0.76	1450	1438	1.10	-1.97	0.66	0.0
	50	1.37	0.76	1431	1417	0.44	-0.01	0.86	0.0
	80	1.45	0.76	1393	1382	0.01	-	1.0	0.29
	100	1.45	0.76	1267	1258	-	-	1.0	1.0
60	20	1.22	0.71	1455	1410	7.70	-0.17	0.80	0.0
	50	1.31	0.71	1448	1378	1.65	-0.10	1.0	0.0
	80	1.66	0.68	1408	1336	0.20	-0.01	1.0	0.11
	100	1.66	0.68	1232	1182	-	-	1.0	1.0
360	20	1.19	0.80	1463	1438	30.66	-0.80	1.0	0.0
	50	1.25	0.79	1462	1416	12.33	-0.88	1.0	0.0
	80	1.42	0.80	1460	1395	1.57	-0.24	1.0	0.0
	100	1.46	0.80	1276	0926	-	-	1.0	1.0

patterns are less complex in this case compared to those for $q = 10 \text{ kW/m}^2$. At 50 % solidification, the flow strength is considerably diminished, and mush profiles and macrosegregation profiles are now well evolved. As solidification progresses further, the flow is restricted in a narrow zone near the hot wall. At 80 % solidification, the isotherms are vertical in most part of the cavity. Comparing the macrosegregation patterns at 50 and 80 % solidification, it is noted that though the evolution of the macrosegregation patterns are largely complete at 50 % for $q = 60 \text{ kW/m}^2$, the differences in patterns at 50 % and 80 % are more than those for $q = 10 \text{ kW/m}^2$.

Fig. 4.20 shows the results for heat flux of 360 kW/m^2 . At 20 % solidification, the strength of flow is higher than the other two cases. In addition to the major vortex (in pure liquid region), a minor vortex is clearly visible in this case (in the mushy region). The mushy region is very narrow. There is virtually no temperature gradient in the pure liquid region due to high strength of flow in the pure liquid zone (Fig. 4.20(a)). Macrosegregation pattern is much simpler in this case, and the extent of segregation is less than the other two cases.

As solidification progresses, the strengths of major and minor vortices go down. Mushy region continues to be narrow and all three regions, namely, liquid, solid and mushy are clearly visible. As solidification progresses further, the flow is restricted in a narrow zone near the hot wall. At 80 % solidification, the isotherms are vertical in most part of the cavity. Comparing the macrosegregation patterns at 50 and 80 % solidification, it is noted that though the evolution of the macrosegregation patterns are largely complete at 50 % solidification for $q = 360 \text{ kW/m}^2$, the differences in patterns at 50 % and 80 % are more than the other two cases.

Macrosegregation patterns at the end of complete solidification are shown in Figs 4.21(a)-(c). It may be noted that overall nature of macrosegregation patterns undergoes drastic changes with heat flux. The severity of segregation ($C_{\max} - C_{\min}$) at $q = 60 \text{ kW/m}^2$ is higher than those at 10 kW/m^2 and 360 kW/m^2 .

For the quantitative comparison of macrosegregation, a parameter called **global extent of segregation (GES)**, which is defined as root mean square of deviation from nominal composition of all the nodal points, is employed some times.

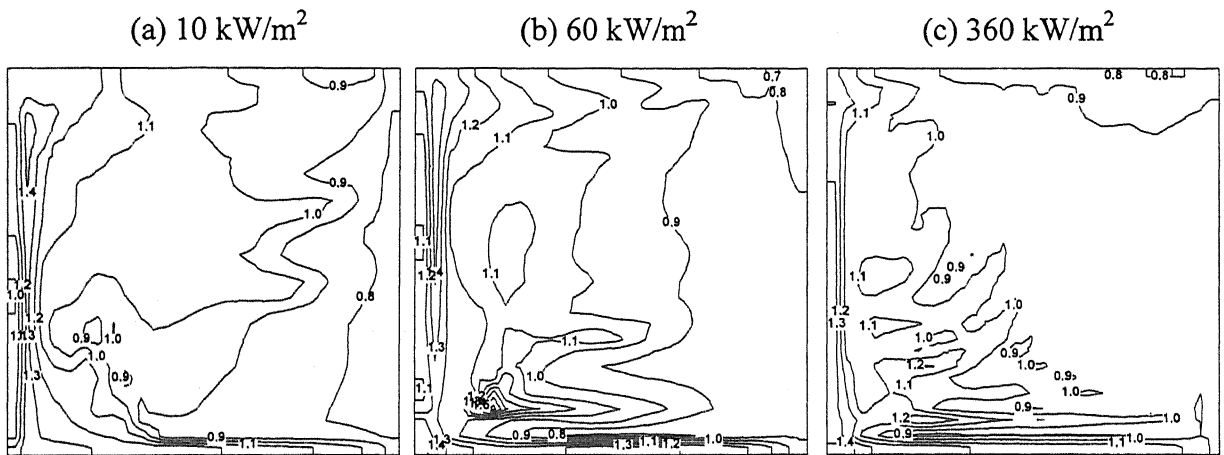


Fig. 4.21: Macrosegregation pattern upon complete solidification.

$$\% \text{ GES} = \frac{100}{C_{\text{avg}}} \left[\frac{\sum \sum (\Delta C)^2 dx dy}{\sum \sum dx dy} \right]^{1/2} \quad \dots 4.15$$

GES, as a function of heat flux is shown in Fig. 4.22. It may be noted from the graph that there is a drop in GES with an increase in heat flux in the beginning. However, GES starts to rise at around $q = 10 \text{ kW/m}^2$ and goes through a peak at $q = 60 \text{ kW/m}^2$. Beyond this point, there is a steady fall in GES with an increase in heat flux. Thus it may be noted that there are three regimes in GES curve. The first regime corresponds to $q < 10 \text{ kW/m}^2$ where GES falls monotonically with an increase in heat flux. This observation is in line with the observations of Tewari et al[110], who studied vertical solidification of Pb-Sn alloys. The main observation was that the decrease in the rate of solidification led to the increase in macrosegregation. Although the present study is on horizontal solidification, at the lower heat fluxes solutal buoyancy plays a significant role in the mushy region. The drop in GES with increase in heat flux can be attributed less time net drop in strength of buoyancy force.

Between $q = 10 \text{ kW/m}^2$ and 100 kW/m^2 , GES first rises and then starts to decrease. This peculiar behavior may be attributed the opposing nature of thermal and solutal convection, which becomes important at the lower heat fluxes. In this zone, thermal buoyancy completely overcomes solutal buoyancy and causes rise in macrosegregation. However, this rise is arrested beyond $q = 60 \text{ kW/m}^2$ as the higher heat fluxes also causes higher rate of solidification, which reduce the time for the evolution of macrosegregation. Prescott and Incropera[117] in their numerical study on Pb-Sn alloy, have observed similar phenomena. The main reasons for the fall in macrosegregation level at very high heat fluxes are due to lowering of solidification time and narrow mushy region, which allow very little solute transport to the pure liquid region. Thus, due to opposing nature of thermal and solutal convection, GES curve shows a hump between two monotonically decreasing portions. The above results reveal a complex variation of GES with heat flux.

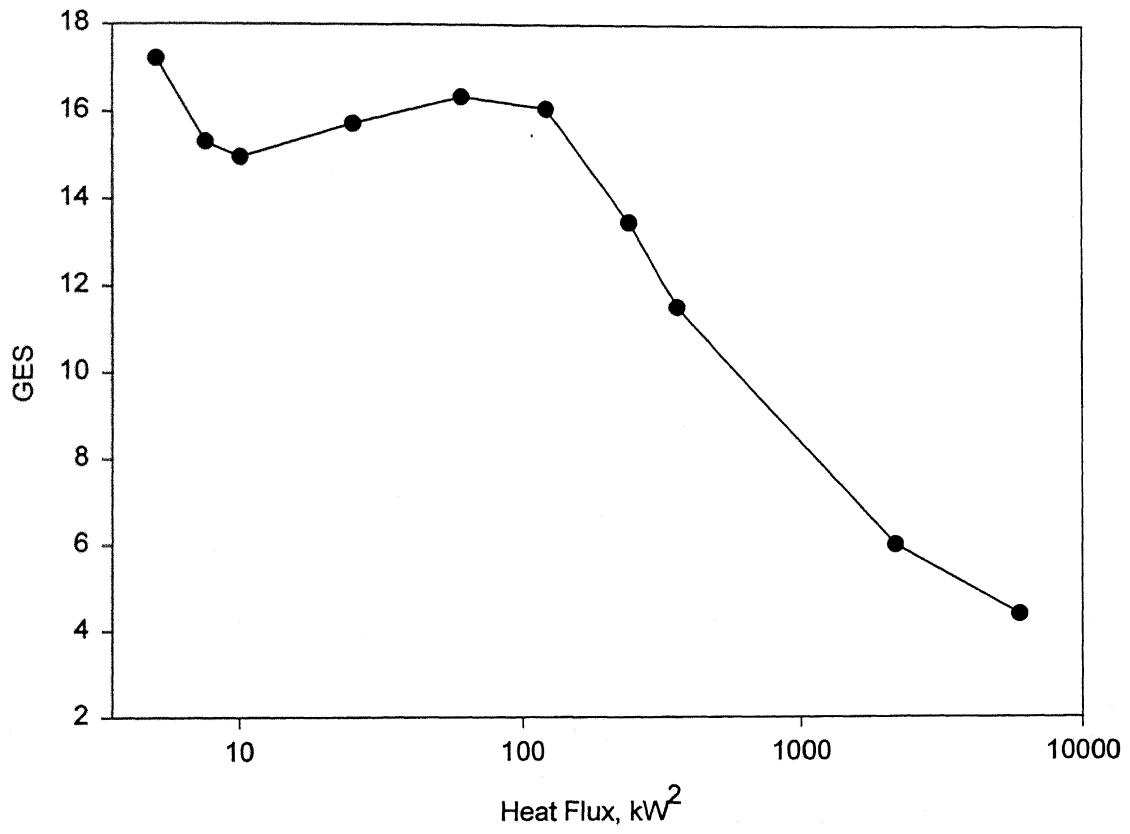


Fig. 4.22: Variation of global extent of segregation with heat flux.

4.4.3 Conclusions

The aim of this part of the work was to study the effect of cooling rate on the thermosolutal convection, and its role in evolution of macrosegregation during solidification of Fe-1 wt % C alloy. A mathematical model was employed to simulate the effect of heat flux on thermosolutal convection and, in turn, on the macrosegregation. The heat flux was varied in the range of 5 and 6000 kW/m². Some of the important findings are highlighted below.

- (i) GES goes down monotonically up to $q = 10 \text{ kW/m}^2$. Solutal buoyancy plays a crucial role in this regime. The lower the rate of solidification is, the higher the GES is.
- (ii) Between heat flux of 10 and 100 kW/m², the GES goes through a maximum. This is due to opposing nature of thermosolutal convection. In this regime, thermal buoyancy plays an important role in evolution of macrosegregation.
- (iii) For higher heat flux ($> 100 \text{ kW/m}^2$), the GES curve again goes down monotonically with an increase in heat flux. The main reasons for a decrease in GES are lowering of solidification time and narrow mushy zone, which do not allow solute transport from the mushy region.

Chapter 5

VERTICAL SOLIDIFICATION: EXPERIMENTAL

5.1 Introduction

Experimental data were collected on solidification of low-melting lead-tin alloys for two purposes: (i) direct usage of experimental data in mathematical model and (ii) validation of the model using experimental data. Temperature data and other measurements, which provided transient heat flux for the model, were in first category. Also, measurement of dendrite arm spacing, which provides a key input to the permeability model, was in the first category. Transient temperature measurements in the alloy melt and macrosegregation data, which were employed for model validation, were in this second category. The objective of the experiments was to obtain these data under controlled laboratory conditions.

The design, fabrication and operation of the instrumented mould, cooling jacket, vertical tube furnace and solidification unit are described in Section 5.2. Measurements of temperature during experiments involved thermocouple rake, constant temperature bath, data acquisition system and computer. Various accessories used in temperature measurement are described in Section 5.3. The solidified samples from experiments were prepared for determination of macrosegregation and dendrite arm spacing. The apparatus for preparation of samples and determination of macrosegregation and microstructure are described in Section 5.4. Experimental procedure is presented in Section 5.5. Measurement errors, calibration checks and reproducibility checks are outlined in Section 5.6. Final experimental procedure and results of a typical run is presented in Section 5.7.

5.2 Experimental Setup

The schematic of the experimental setup is shown in Figs. 5.1 and 5.2. The photograph of the experimental setup is shown in Fig. 5.3a and Fig. 5.3b. It consists of following equipments:

- (i) solidification cell and cooling jacket
- (ii) vertical tube furnace for homogenization of initial temperature
- (iii) a melting unit consisting of melting furnace and crucible

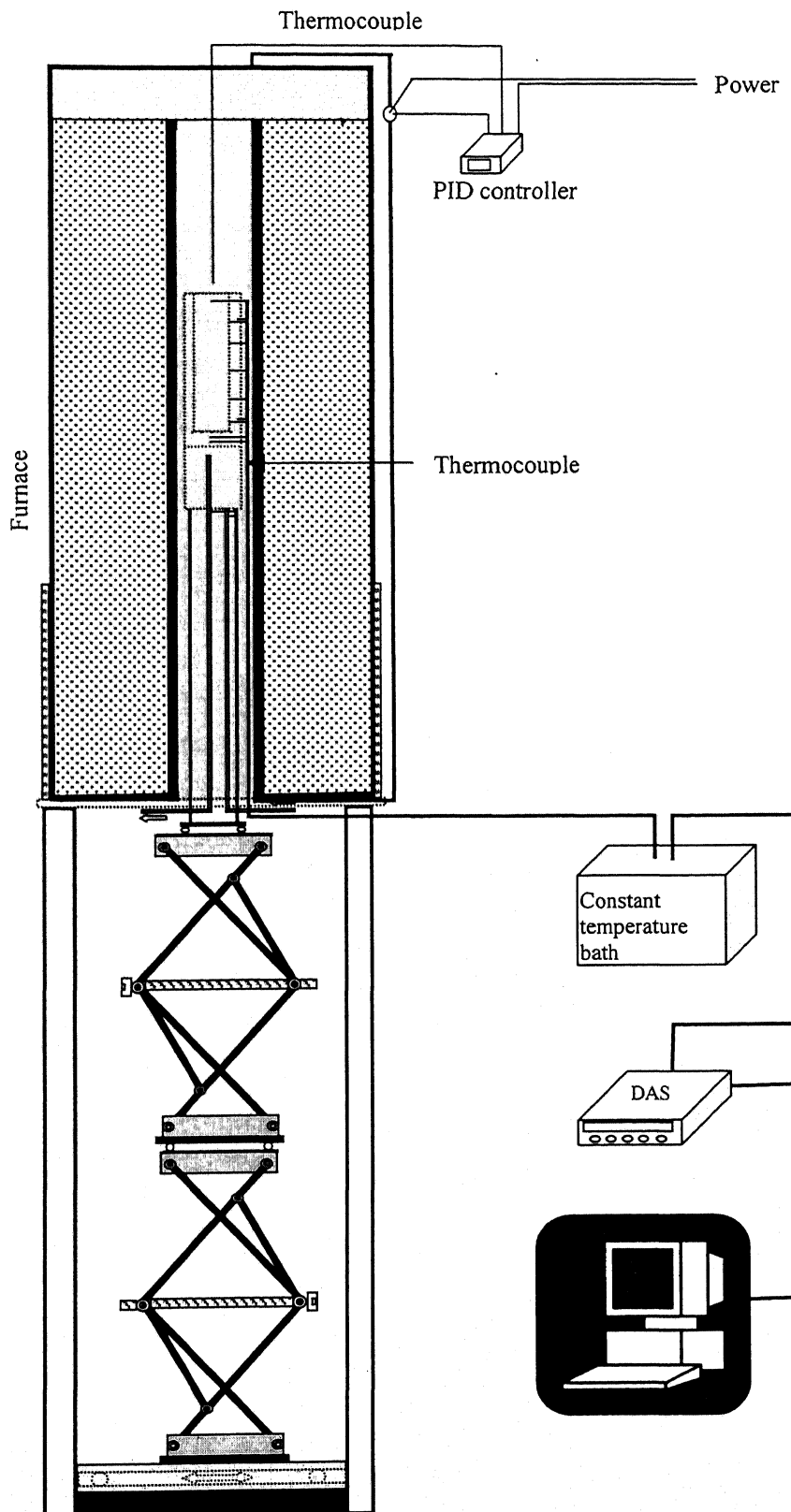


Fig. 5.1: Furnace, solidification unit and various accessories (schematic).

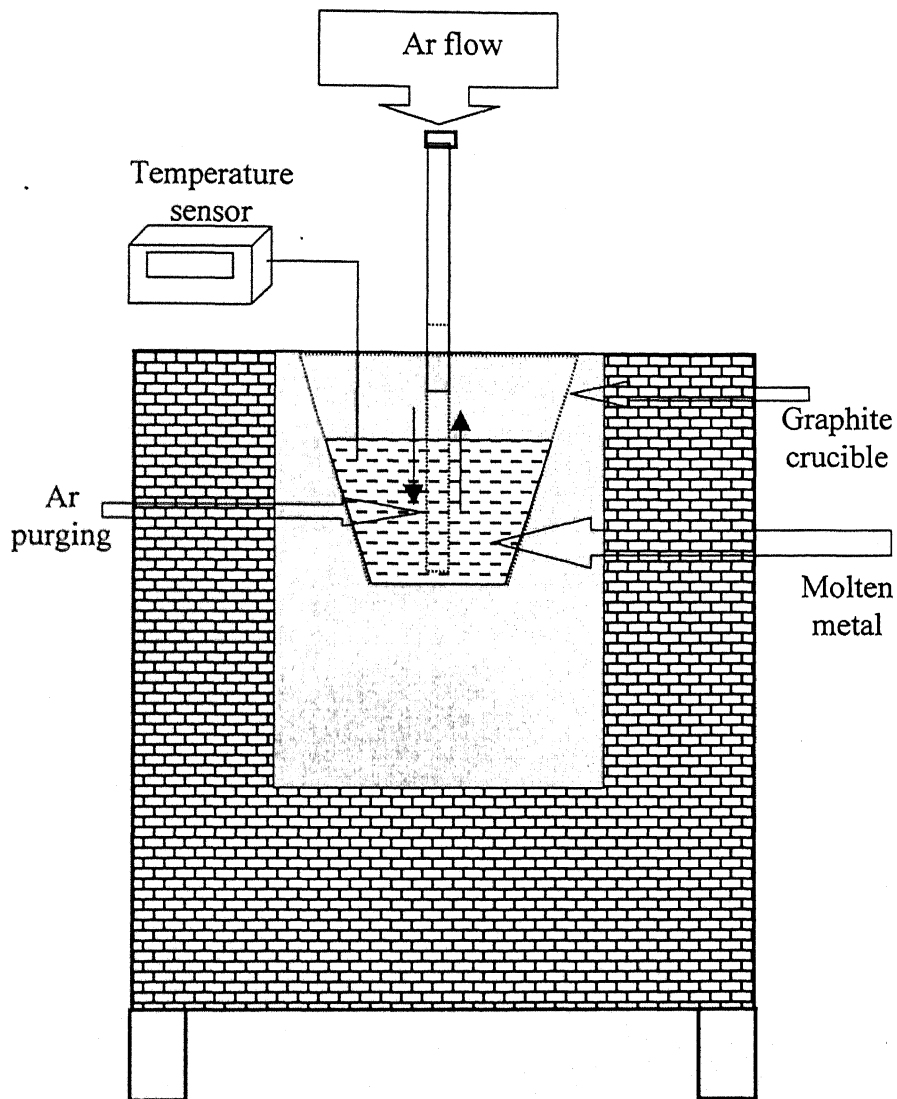


Fig. 5.2: The melting unit (schematic).

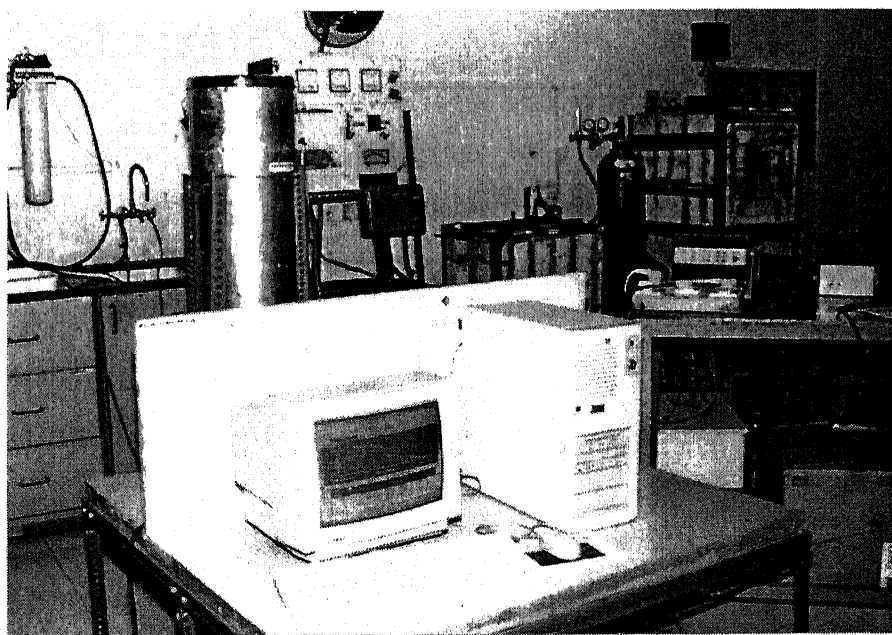


Fig. 5.3: Photograph of experimental setup: two views.

- (iv) arrangement for supply of argon gas cylinder
- (v) cooling arrangement for water flow through cooling jacket
- (vi) control panel for controlling temperature of vertical furnace
- (vii) data acquisition system for scanning temperature data during experiment
- (viii) computer for interfacing with data acquisition system, and
- (ix) water bath for maintaining constant temperature of cold junction during experiments.

5.2.1 The vertical tubular furnace

The schematic of the vertical furnace is shown in Fig. 5.1. The heating element in the furnace was Kanthal wire, which was wound on the outer side of a Sillimenite tube, 600 mm long with inner diameter 70 mm and outer diameter 90 mm. The furnace was constructed with a rating of 1000 watts and was insulated with the help of ceramic wool, which was placed between the Sillimenite tube and aluminum shell. The furnace temperature was controlled with the help of a PID controller (REX, JAPAN), and had a constant temperature zone of 150 mm in the middle portion, which was utilized for final equalization of temperature in the mould.

5.2.2 The solidification cell and cooling jacket

Design of the solidification unit is shown in Figs. 5.4 and 5.5. The complete assembly, i.e., the mould, the chill and the water-cooling jacket, was made of stainless steel (SS 304). The mould was made up of two concentric cylinders. The inner tube had the following dimensions: inner diameter: 32 mm, outer diameter: 36 mm, and length: 130 mm. The outer tube had the following dimensions: inner diameter 52 mm, outer diameter 58 mm and length 130 mm. The two tubes were welded together at three locations (120° apart) at the top. The top of the mould was open while it was attached to a chill at the bottom. The mould had a threading on internal side for close fitting with the chill. The chill was a disc with 15 mm thickness and 58 mm diameter. The top part of the chill was threaded for fitting with the mould, whereas the bottom part of the chill was welded in such a way as to form the top of the cooling jacket. The cooling jacket had cylindrical

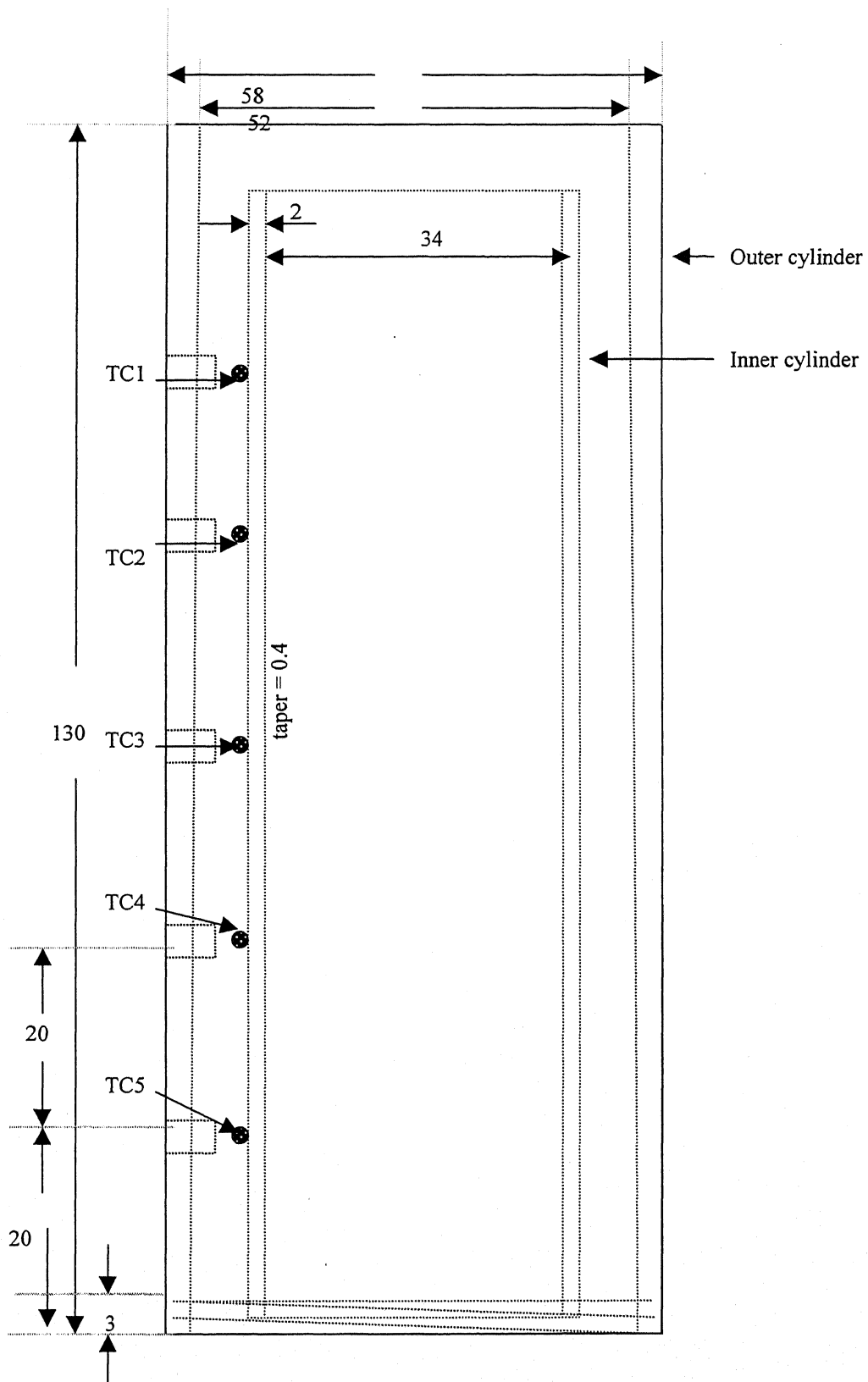


Fig. 5.4: Design of instrumented mould; dimensions in millimeter.

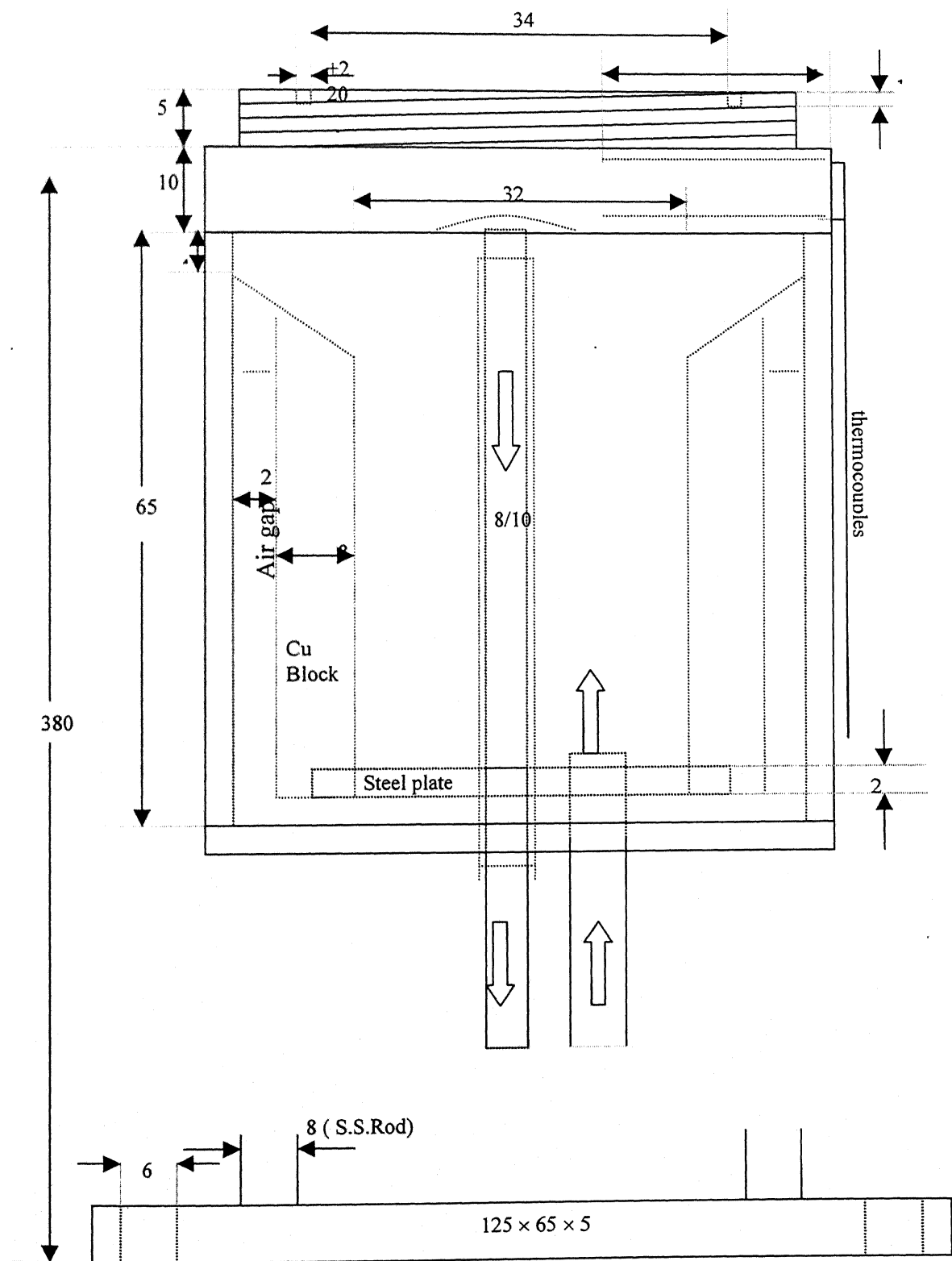


Fig. 5.5: Design of cooling jacket; dimensions in millimeter.

shape with the following dimensions: inner diameter: 52 mm, outer diameter: 58 mm, and height: 50 mm. Another stainless steel disc was brazed to the bottom end of the cooling jacket. Water inlet and outlet tubes of 5 mm diameter were provided at the bottom.

There are 12 J-type thermocouples (1.5 mm mineral insulated iron-constantan thermocouples with stainless steel casing) in all for measurement and storage of temperatures throughout the solidification period. Locations of these thermocouples are shown in Fig. 5.6. TC1 to TC5 were located vertically at 2 cm spacing, and the measuring ends of these thermocouples were touching the outer surface of the inner cylinder. Two thermocouples, TC6 to TC7 were attached to the outer cylinder at heights corresponding to TC1 and TC5, respectively. This arrangement allowed determination of horizontal temperature differences in the melt prior to and during progress of solidification. TC8 was placed above the melt to record the temperature above the melt during solidification. TC9 and TC10 were incorporated inside the chill, located at 8 mm and 14 mm, respectively, from the base of the mould. TC11 and TC12 were employed to measure temperatures of water at the inlet and outlet of the cooling jacket. The cold junctions of all the thermocouples were placed in a well-insulated water bath. The temperature of the water bath was recorded with the help of a platinum resistance thermometer to provide the cold junction compensation.

5.2.3 Melting furnace

A muffle furnace, shown schematically in Fig. 5.2, was used for melting of the charge, which was subsequently transferred to the mould inside the vertical tubular furnace for temperature equalization and subsequent cooling. It had silicon carbide rods as heating element. The melting was carried out in a graphite crucible under an atmosphere of flow of high purity argon supplied by Indian Oxygen Limited.

5.3 Accessories for Temperature Measurements

Temperature measurements were carried out with the help of J-type thermocouples (iron-constantan). The following units were used in temperature measurement:

- (i) thermocouple rake
- (ii) constant temperature bath

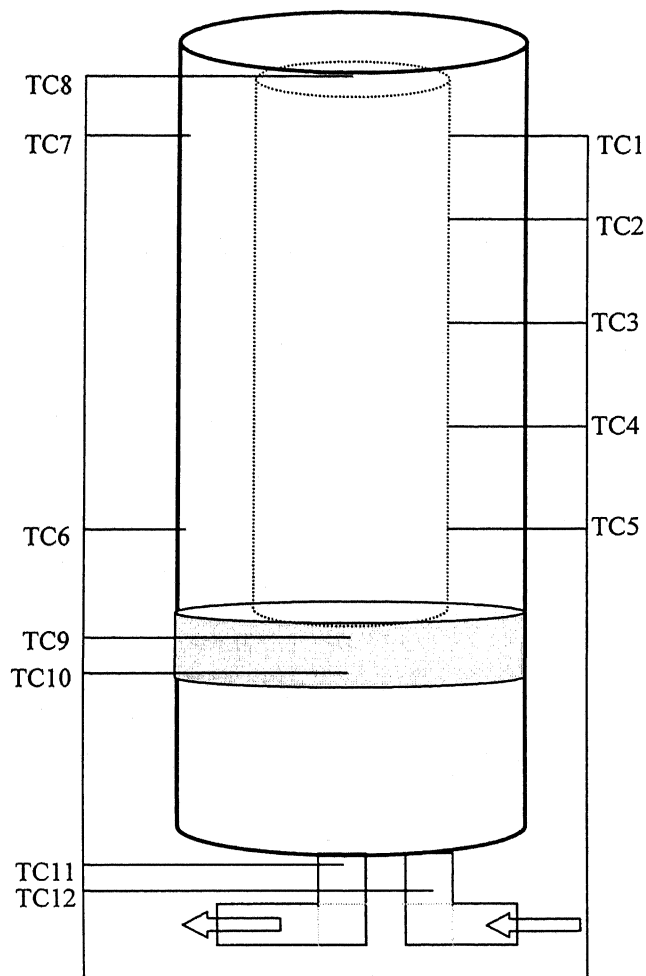


Fig. 5.6: Thermocouple placements inside the mould and the cooling jacket.

(iii) data acquisition system and

(iv) computer.

The thermocouple rake had 1 platinum resistance thermometer (Pt-100) and 12 J-type thermocouples for temperature measurements. The circuit of the thermocouple is also shown in Fig. 5.7. For each thermocouple, two copper wires, connected to data acquisition system, were joined with the thermocouple wires and the junctions were maintained in a tube containing mercury inside a constant temperature bath (well-insulated water bath). The water bath temperature was constantly monitored with the help of Pt-100 sensor and its variations were found within ± 0.1 °C during the course of the experiment.

Temperatures sensed by these thermocouples were continuously measured and acquired with the help of HP 34970 Data Acquisition System. The unit is capable of reading voltage with 6½-digit accuracy and as many as 60 channels can be connected simultaneously. The outputs of thermocouples were stored in terms of millivolts, which was converted to temperature after accounting for end corrections. The unit was also used to store the continuous measurement of the resistance of PT-100 sensor during the experiment.

Benchlink software was utilized for interfacing various channels of data acquisition system with a computer with the view of monitoring and storage of temperatures at fixed intervals of time during the experiments. The machine used for this purpose had following configurations: 200 MHz, 2 GB HDD, 32 MB RAM. The outputs of thermocouples and Pt-100 sensor were later converted into temperatures with the help of a computer program.

5.4 Equipment for Determination of Macrosegregation and Microstructure

A semi-automatic cutter was employed to cut the solidified ingots. Samples for determination of composition were taken with the help of a drilling machine from various locations of mid-plane of the casting as shown in Fig. 5.8a. About 0.5 gm of sample was

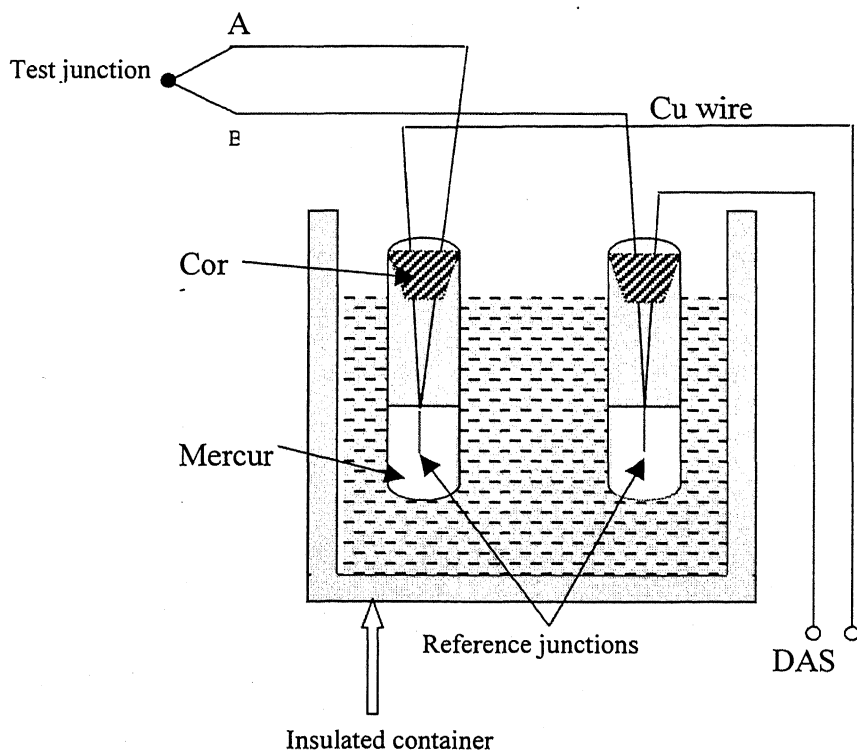


Fig. 5.7: Schematic of thermocouple circuitry.

collected from each location. Hot plate was used for digestion of Pb-Sn samples in HCl. Approximately 0.1 gm of sample was taken for digestion in one sample.

For determination of composition of alloy, atomic absorption spectrometry was carried out by a Hitachi Zeeman Spectrometer. The spectrometer works on the following principles. The concentration of the metal in the solution is proportional to the density of atoms in the flame of the spectrometer and thus the concentration of the metal in the solution can be obtained, from which the weight percent of the metal in the alloy can be found out.

For examination of microstructure and metallography, three samples were collected from each casting along the height as shown in Fig. 5.8b. Belt grinder was used for rough polishing of samples. After rough polishing, samples were polished on emery papers of different fineness. Final polishing was carried out on polishing wheel. Polished samples were observed under a Leica microscope at low magnifications for measurement of dendrite arm spacing.

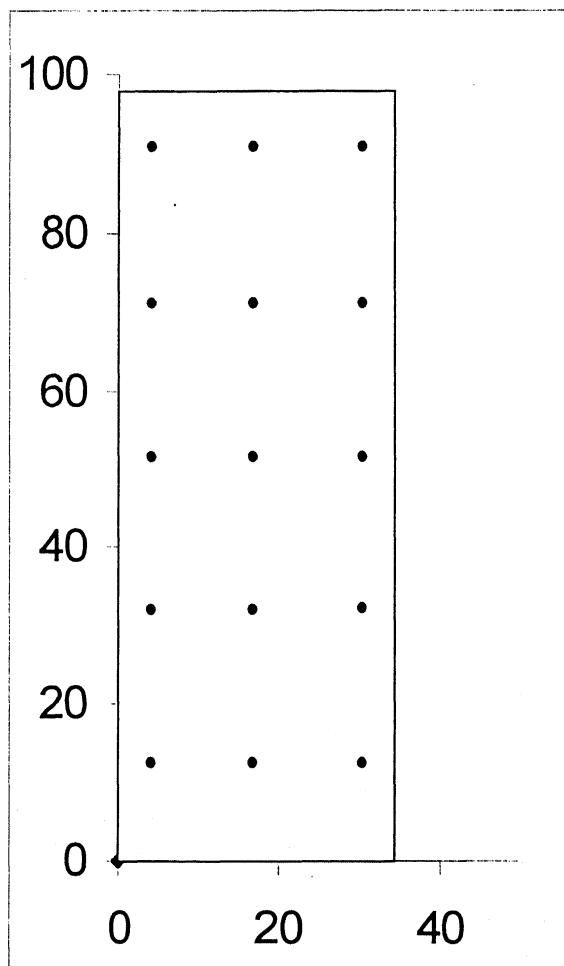
5.5 Experimental Procedures

A general outline of experimental procedure is presented in Fig. 5.9. Some details are noted below.

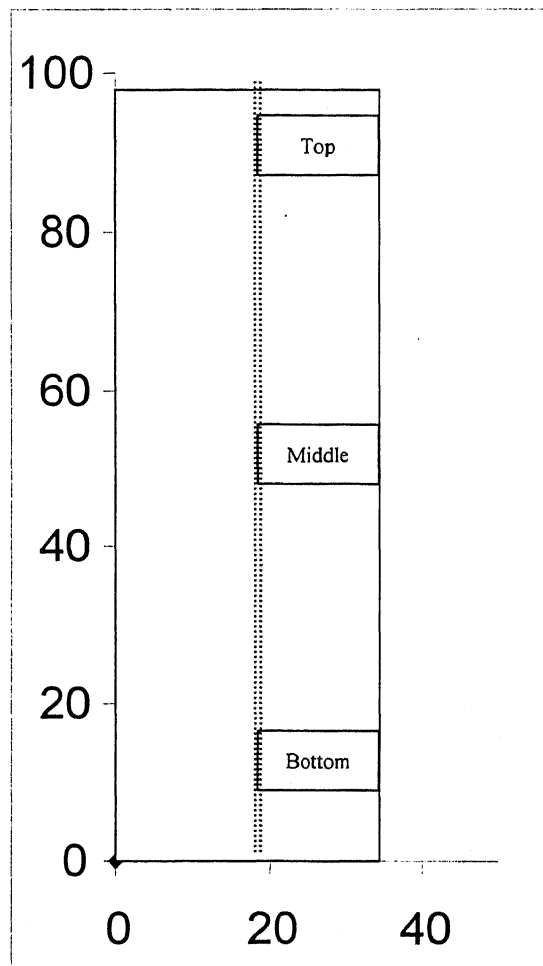
5.5.1 Alloy preparation

Alloys were made by melting in a 3-phase SiC rod heated muffle furnace, which was also used for initial melting of alloys during controlled experiments. The detailed procedure for alloy preparation is noted below.

- (i) Depending upon the composition of the alloy required, appropriate quantities of the two elements (e.g. for Pb-19 wt % Pb sample, 4 kg of Pb and 0.94 kg of Sn) were weighed.
- (ii) Pure metals were heated in the melting furnace in a clay graphite crucible.
- (iii) As the temperature reached above 100 °C argon gas flow was started. The charge was heated to 430 °C (approximately 100 °C above the melting point of pure lead). After complete melting, the resulting melt was stirred by



(a)



(b)

Fig. 5.8: (a) Locations of samples taken for AAS examination; (b) Locations of samples taken for metallographic examination; dimensions in millimeter.

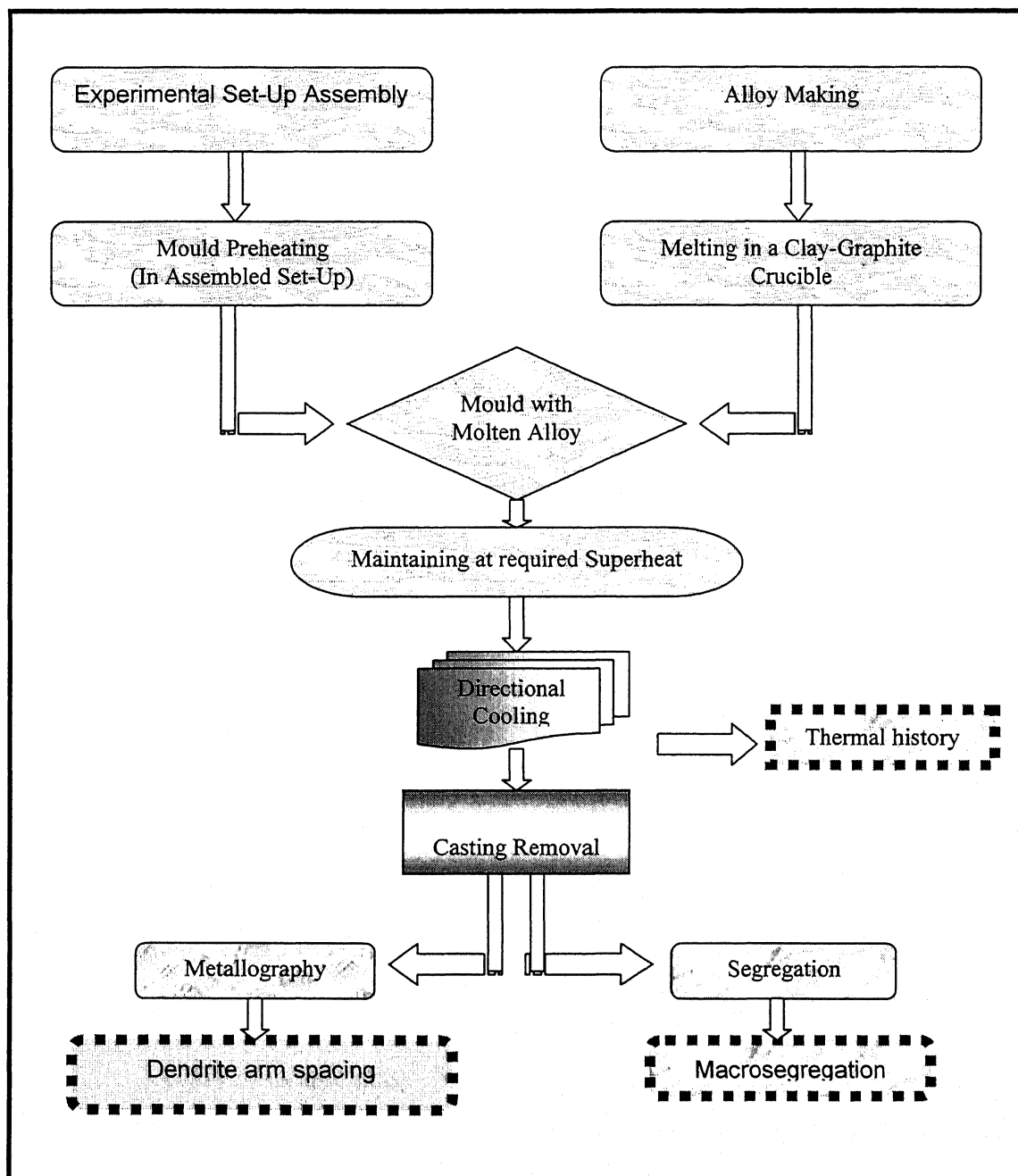


Fig. 5.9: Outline of experimental procedure

bubbling argon for 10 minutes into the molten alloy so as to homogenize. The molten alloy was also mechanically stirred.

- (iv) The dross material was removed with the help of a stainless steel spoon.
- (v) The molten alloy was poured into several small crucibles and allowed to solidify.
- (vi) The small castings thus obtained were again melted and stirred for further homogenization. The melt was again cast into small crucibles. This procedure was repeated twice. In the third cycle, the melt was cast in a tray under rapid cooling conditions.
- (vii) Chemical analysis of the alloy was carried out by atomic absorption spectroscopy (AAS) to check the homogeneity of the alloy. A total of six samples were collected from different parts of the casting.

5.5.2 Directional solidification experiments

The steps followed during directional solidification experiments were as follows:

- (i) The alloy was melted in a clay-graphite crucible under flowing argon atmosphere in the muffle furnace. The time required for melting was around 1.5 hrs for tin-based alloy and 2 hrs for lead-based alloy. The melt temperature was continuously monitored and the pouring temperature was kept 10°C above the required superheat.
- (ii) The mould and the cooling jacket assembly were cleaned thoroughly, and high temperature silicone sealant was applied at the base of the mould to prevent leakage of molten alloy. The unit was preheated in the vertical tube furnace in such a way that the mould was placed in constant temperature zone of the furnace. The thermocouples of instrumented mould were connected to the data acquisition system, and temperature evolution in the mould was monitored on computer.
- (iii) After the mould was heated to the desired superheat, the mould assembly was brought down outside the furnace and the melt was transferred from the crucible to the mould. The assembly was subsequently raised again so as to place the mould in the constant temperature zone of the furnace for attainment

of desired superheat. The temperatures of the melt and mould wall were monitored with the help of 7 thermocouples.

- (iv) Temperature measurements were carried out with the help of J-type, 1.5 mm mineral insulated thermocouples with steel casing. After attainment of steady temperature readings in all thermocouples, the temperature of metal in solidification cell had vertical gradient of about 5 °C and horizontal gradient was below 1 °C.
- (v) Upon attainment of required temperature, water flow rate was adjusted before each experiment and was measured with the help of a flask and stopwatch. It was one of the means of obtaining variation in cooling rate. Using this arrangement, the water flow rate was varied in the range of 0.2×10^{-5} to 1.9×10^{-5} m³/sec. The power to the furnace was switched off and the cooling was initiated by flowing water through the cooling jacket. The cooling process was continued till the topmost thermocouple temperature was below 150° C. The scanned data were saved on computer for further analysis.
- (vi) Mould assembly was brought down and was allowed to cool. After removing the ingot from the mould, the ingot was vertically cut at mid-plane. Samples for metallography and spectroscopy were collected from several locations (Fig. 8a and 8b) of the vertical mid-plane of two halves of the casting.

5.5.3 Temperature measurement

Measurements of temperature of melt, mould surface, mould base and inlet and outlet water were done using 1.5 mm mineral insulated J-type, i.e., iron-constantan type, thermocouple, protected in stainless steel (SS304) casings. Although, chromel-alumel is the most common in the temperature range of interest, J-type is equally good in terms of reproducibility. Besides this, it has better resolution ($46 \mu\text{V}/^\circ\text{C}$) in the temperature range of interest. Cold junctions were maintained at room temperature in a specially designed isothermal bath. The bath temperature was monitored with the help of a Pt-100 resistance thermometer and typical variation of temperature of reference bath was within ± 0.1 °C.

During a typical experimental run, temperatures of melt, mould surface, cooling jacket, and water inlet/outlet were measured every 5 seconds.

5.5.4 Microstructural examination and metallography

Small pieces were sectioned from desired locations along the length of the casting and were used as samples for microscopy. During the sectioning liberal lubrication was employed so as to restrain the temperature rise. The following procedure was adopted in the polishing and etching of lead-tin alloys.

Polishing:

The procedures followed for lead-tin and tin-lead alloys are presented below. In their pure form Pb and Sn are very soft and difficult to polish as both have their re-crystallization temperatures below the room temperature. Alloys of these metals were a little harder but still posed difficulties for polishing.

- (i) The samples were first polished on grinding belt using 120-grit emery paper.
- (ii) The samples were then polished with 240, 400 and 600-grit SiC paper with low pressure, short times and using kerosene as lubricant to minimize loading of the abrasive material. Subsequently they were polished with 1/0, 2/0, 3/0 and 4/0 papers in the order mentioned, employing the procedure as followed for the coarser papers.
- (iii) The samples were then fine polished on lapping wheel with alumina as the abrasive material in case of Sn-Pb alloys and diamond paste in case of Pb-Sn alloys. Diamond paste was employed for polishing lead rich alloys since alumina particles get embedded in the soft sample and distort the microstructure. Use of kerosene as lubricant gave good results and hence is recommended.

Etching of Pb-19 wt % Sn and Pb-35 wt % Sn alloy:

The etchant employed was mix of acetic acid (75ml) and hydrogen peroxide (25ml). The sample was etched by immersing in the etchant for 3-5 seconds at room temperature and washing under running water. The sample was then polished on the lapping wheel

without employing any abrasive. If the sample was over-etched, polishing on the lapping wheel using diamond paste followed by above mentioned etching procedure gave satisfactory results. The next etchant employed was a mix of water, conc. nitric acid and glacial acetic acid in the proportion of 16:4:3. The sample was immersed in the etchant for about 10-12 seconds at room temperature and then observed under microscope after washing under running water. The results obtained by using the acetic acid-hydrogen peroxide mix were better and hence, this was the adopted etchant.

Etching of Sn-15 wt % Pb alloy:

The samples for microscopy were polished as described earlier. The optimized etchant after trials was a mix of glycerin, acetic acid and conc. nitric acid in the proportion of 8:1:1. Nitric acid should be added just before use. The etching was done by immersing the sample in the etchant at room temperature for a period of about 4-6 seconds. The sample was then swabbed under running water. If the sample was a little over-etched it was rectified and the microstructure was observed satisfactorily after polishing on the lapping wheel using only kerosene as lubricant for a period of 2-3 minutes.

Metallography:

As a part of metallographic measurements, samples for microstructure were obtained from several locations as shown in Fig. 5.8b. Using the standard procedures outlined above, microstructures longitudinal sections were obtained and these were used for evaluation of dendritic arms spacing. The line intercept method was employed. In this method, a line is drawn approximately perpendicular to dendrite arms and the number of arms intersecting the line is counted. Secondary dendrite arms spacing was average of about 100 dendrites, whereas primary dendrite arms spacing was based on the sample size of about 40 dendrites.

5.5.5 Macrosegregation

Post-solidification measurements included determination of macrosegregation. After removing the ingot from the mould, the ingot was vertically cut at mid-plane. Small samples of materials were taken from specific locations, shown in Fig. 5.8a, by drilling 2

mm diameter holes approximately 3 mm into the section. The samples were weighed using Libor weighing scale. The weighed samples were digested in HCl and HNO₃ and diluted with 4% HNO₃ to a desired concentration. The composition of sample was determined by measuring the concentration of Pb in the sample solution with AAS.

For determination of composition of alloy, atomic absorption spectroscopy was performed with the help of Hitachi Zeeman Spectrometer. The procedure involved following steps: (a) A known quantity of metal was digested in HCl. It was diluted with 4 % HNO₃ in such a way to make concentration of lead between 10 and 40 PPM. The instrument was first calibrated with known standards of 10, 20, 30 and 40 PPM solutions. The diluted solution of unknown composition was then fed to the instrument and absorption intensity was obtained. Using the calibrated curve for standard solutions, the intensity was converted into PPM.

5.6 Measurements Errors, Calibrations and Reproducibility

Checks

5.6.1 Temperature

All thermocouples were calibrated against outputs of calibrated Pt-100 sensor at four temperatures between 20 °C and 350 °C. For the purpose of comparison, room temperature, boiling water temperature, melting point of pure tin and melting point of pure lead were used. Results for a typical J-type thermocouple is noted below in Table 5.1.

Table: 5.1: Summary of bias, precision and uncertainty for a typical thermocouple

Temperature, °C	Bias, °C	Precision, °C	Uncertainty, °C
26.4	-0.02	±0.01	0.03
96.5	0.25	±0.12	0.37
231.9	0.8	±0.15	0.95
327.0	-0.25	±0.10	0.35

In Table 5.1, term bias is the systematic error between thermocouple output and reference temperature, precision is twice the standard deviation and uncertainty is the maximum error owing to bias and precision. After correcting for bias, the maximum error in temperature measurements was less than 1 °C.

5.6.2 Concentration

The overall accuracy of concentration measurement is dependent on several factors and these are described below.

Accuracy of weight measurement: Weight of AAS samples were measured by Electronic Libor Weighing machine (EB-50). The equipment has a maximum error of ± 1 mg. Typical weight were in the range of 200 mg and the error in weight measurements were within 1 %.

Accuracy of dilution: Typical sample for composition determination is diluted 25 times after digestion. Trials showed that accuracy of results were highly sensitive to the dilution procedure. The accuracy of pipet were within ± 0.04 ml. Maximum errors in volume measurement were estimated within ± 0.1 ml and results error in composition within 0.2 %.

Other accuracy related issues in AAS measurement: For any flame atomization method, atomizing efficiency is around 10 % and sensitivity is low. The main source error is background absorption. In all the experiments, double-distilled water was used to minimize this problem. Other sources of error include error in calibration, deviation of gas flow rates and so on. In all experiments, calibration curves were drawn from freshly prepared standards to minimize error associated with old samples. Based on the analysis of experimental data, the overall uncertainty in measurement was estimated at ± 0.5 %.

5.7 Experimental Results of a Typical Run

The experimental data were obtained for different alloys, superheats and cooling rates. The details of experimental results are presented in Chapter 6. This section describes the data obtained during a typical experiment. The following experimental conditions were employed in this experiment:

Initial alloy composition:	Pb-35 wt % Sn
Initial melt temperature:	315 °C
Water flow rate:	$0.833 \times 10^{-5} \text{ m}^3/\text{s}$
Plate thickness:	1.7 mm
Initial melt height:	100 mm

5.7.1 Time-temperature curve

Fig. 5.10 shows the time-temperature response of eight thermocouples (TC1 to TC8). These include five thermocouples along the length of the mould, two thermocouples to measure horizontal gradient at the bottom and top in the annulus, and a thermocouple to measure the temperature above the melt (TC8). Initial rate of cooling was fast but it gradually slowed down as solidification progressed. Horizontal gradient within the annulus was small. Through a separate experiment, it was established that the gradient in the inner mould was below 1 °C. Concentric tube arrangement thus reduced temperature gradient in the inner mould due to higher resistance to radial heat flow. It may be noted that TC8 was always more than TC5. This ensured that there was no heat loss from the top. Fig. 5.11 shows the time-temperature response of TC9 to TC12 in the mould assembly. TC9 and TC10 show the temperature response of thermocouples located in the chill block. At the start of cooling, the temperature difference was high. However, the difference stabilized after initial few minutes. TC11 and TC12 showed temperature response at water inlet and outlet. Here again, the difference between the inlet and the outlet temperature was high only for initial few minutes.

5.7.2 Macrosegregation and microstructure

Measured macrosegregation in the ingot is presented in Fig. 5.12. It also shows the average macrosegregation at these five locations. Macroseggregation is practically absent in this experiment. Typical micrograph is presented in Fig. 5.13. It clearly shows the dendritic structure with well-developed primary and secondary dendrite arms. As discussed earlier, line intercept method was employed on the micrographs for determining dendrite arms spacing. Details of various experiments and their analysis are contained in Chapter 6.

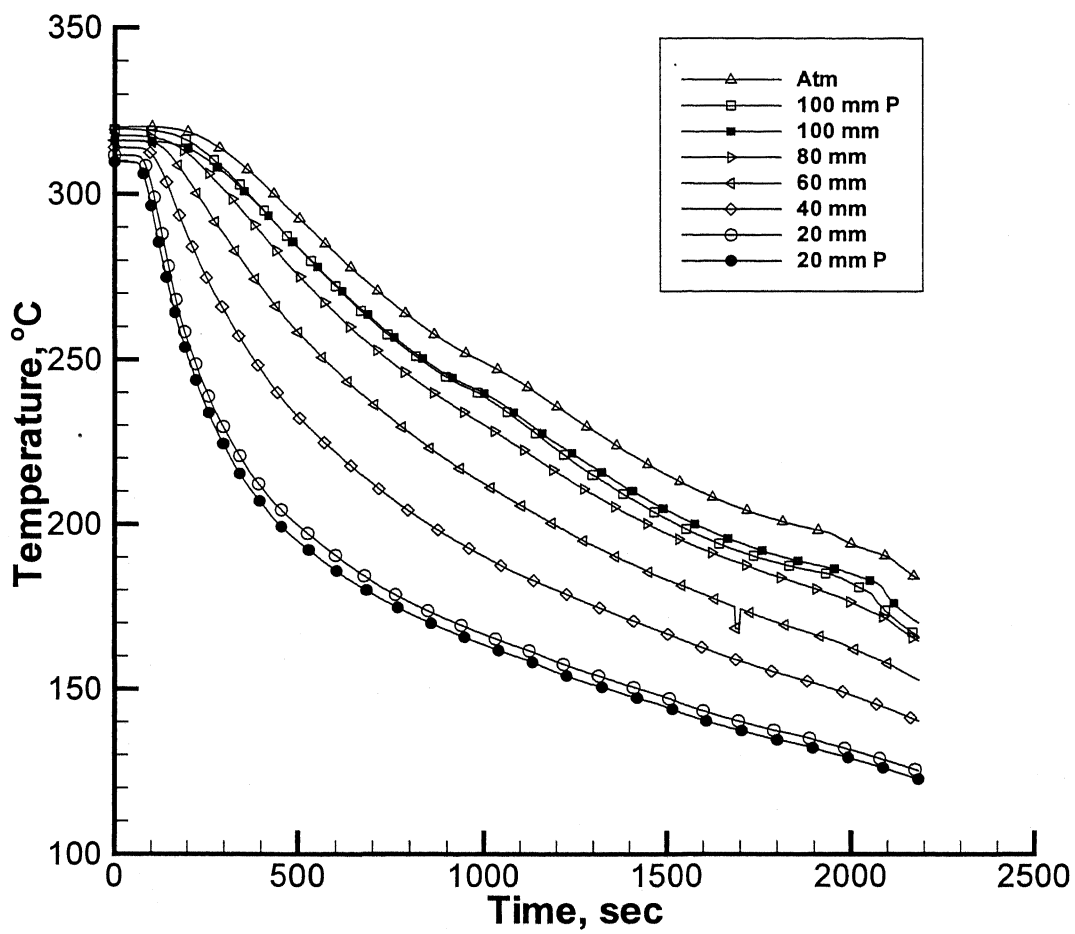


Fig. 5.10: Transient temperature response of thermocouples TC1 to TC8 in the melt and other locations.

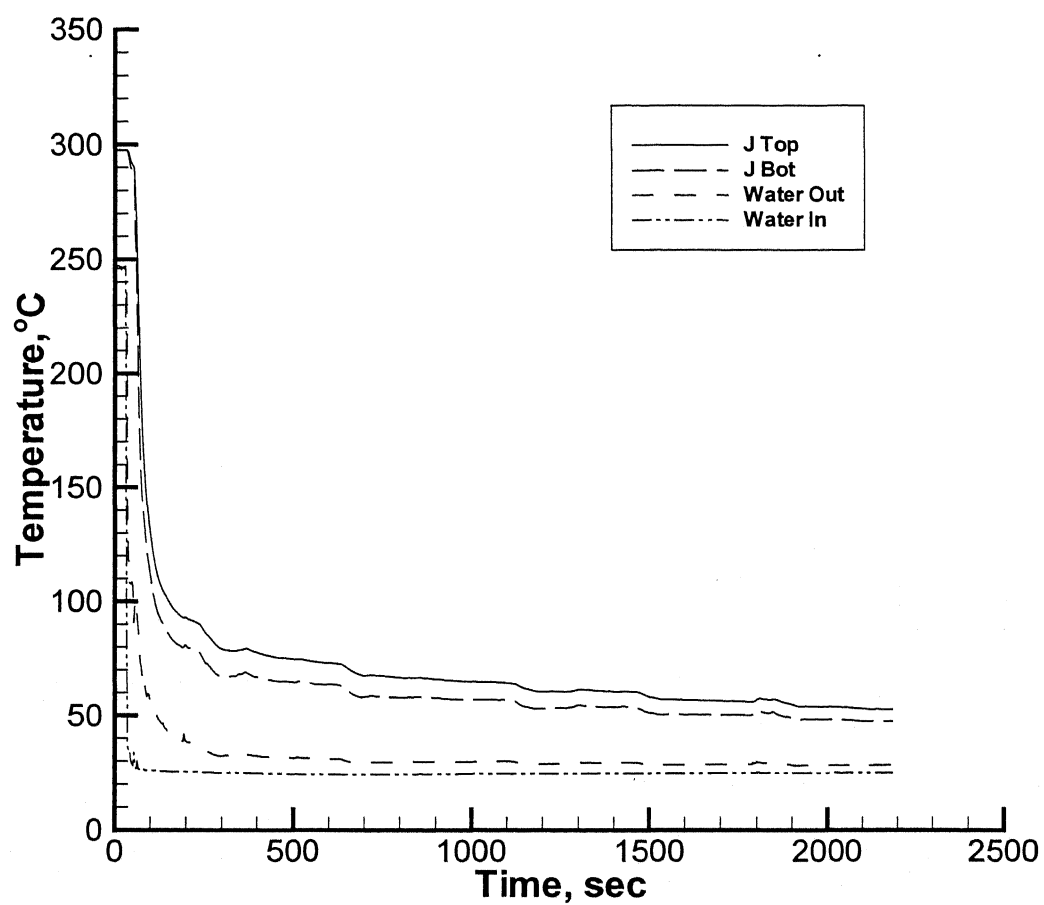


Fig. 5.11: Transient temperature response of thermocouples in chill block and water inlet/outlet.

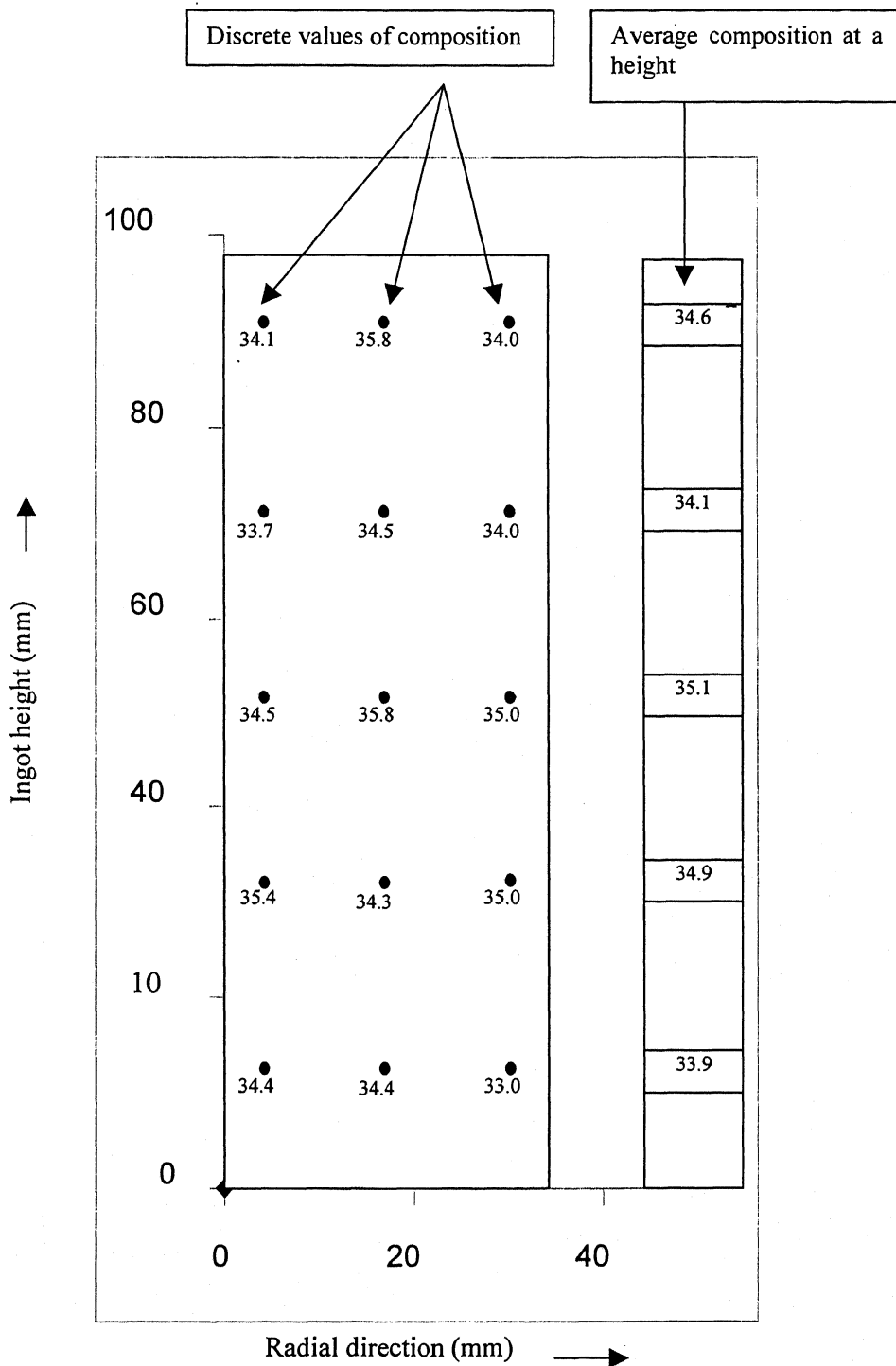


Fig. 5.12: Composition of solute at various locations and averaged value at various heights.

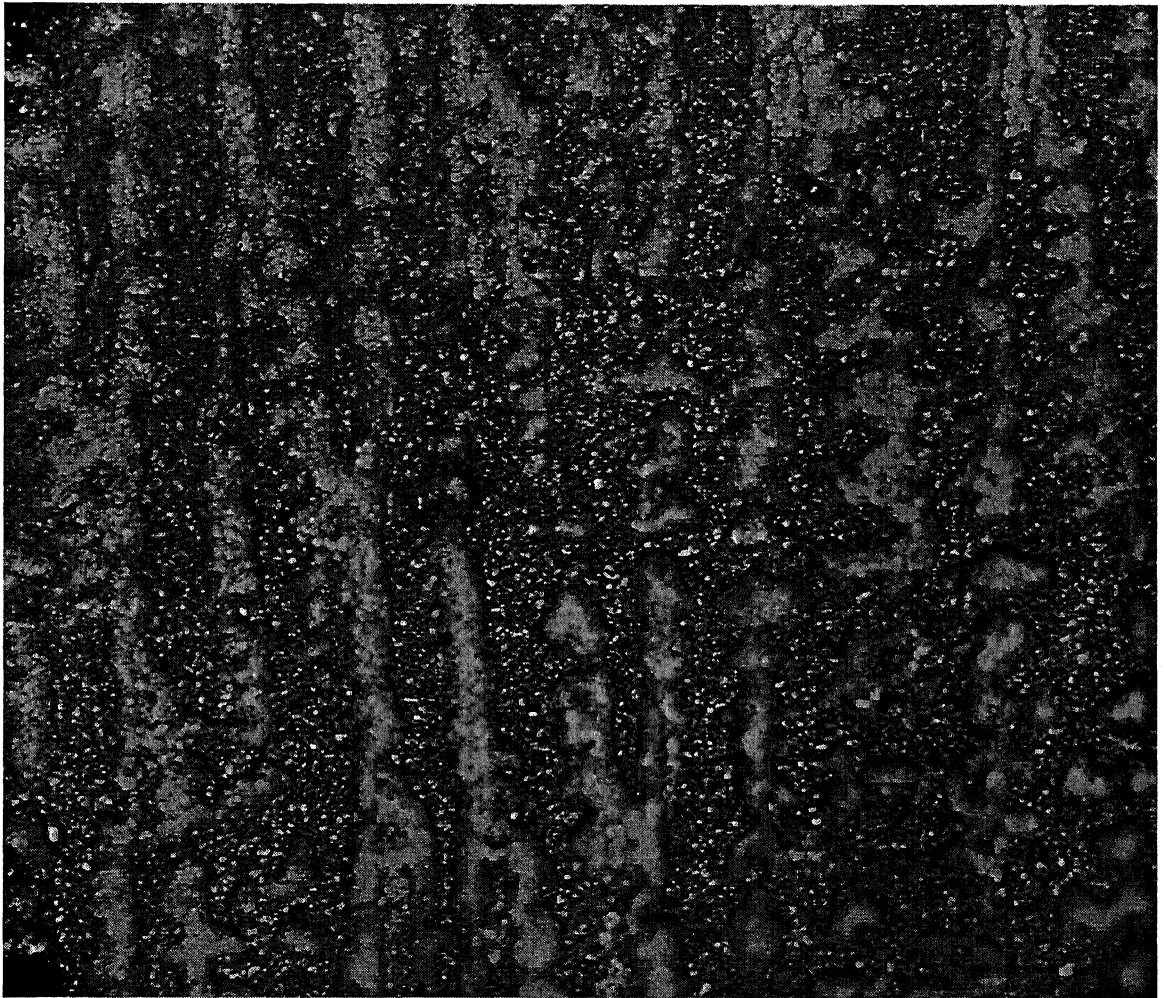


Fig. 5.13: Microstructure of Pb-35 wt % Sn alloy

Chapter 6

RESULTS AND DISCUSSIONS OF RESULTS

6.1 Experimental Conditions

A total of 20 experiments were performed. The first set of 14 experiments (E1 to E14), presented in Table 6.1, were fully characterized, and inputs of these experiments were used to fine-tune the model wherever necessary. For the second set of experiments (E15 to E20), presented in Table 6.2, only the temperature response and macrosegregation data were obtained. In this chapter the first set of experimental results are presented and discussed primarily. Data from the second set have been discussed only where necessary. Three alloy compositions were chosen for this study. These were Pb-19 wt % Sn, Pb-35 wt % Sn, and Sn-15 wt % Pb alloys. Changes in cooling rate were made by varying the water flow rate between 0.2×10^{-5} to 1.9×10^{-5} m³/s, and by introducing additional steel plates between the mould and top of the cooling jacket. Most of the experiments were carried out for two different superheats. The diameter of the cast ingot was 25 mm and the length was $97 \text{ mm} \pm 3 \text{ mm}$. The above conditions were employed to examine the effect of cooling rate and superheat on flow and consequent macrosegregation during bottom cooled vertical solidification of the alloy melts.

6.2 Experimental Results

The results from the experiments are in terms of (i) temperature vs. time curves (a) in the mould, (b) in the chill block, and (c) of inlet and outlet water, (ii) macrosegregation data obtained from the post solidification analysis of samples, and (iii) primary and secondary dendrite arm spacings obtained from the microstructures.

6.2.1 Thermal data in the melt

Chapter 5, Secs. 5.3, 5.4.3, 5.6 and 5.7, have presented details of temperature measurement techniques and assessment of errors etc. during solidification of alloys. Experiments were carried out as per experimental conditions shown in Table 6.1 and 6.2. Fig. 5.6 has shown the locations of various thermocouples in the melt. Fig. 6.1 shows the

Table 6.1: Experiments of Set 1

Alloy	Exp.	Water flow rate (m ³ /sec.) x 10 ⁵	Material Temp. (° K)	No. of Plates	Plate thickness mm
Pb-35% Sn	E1	0.833	588.0	1	1.7
	E2	0.833	546.7	1	1.7
	E3	0.833	549.5	2	3.4
	E4	0.833	600.7	2	3.4
	E5	1.66	543.7	1	1.7
	E6	1.66	584.7	1	1.7
Pb-19 % Sn	E7	0.95	608.5	2	3.4
	E8	1.8	608.9	1	3.4
	E9	1.9	660.8	1	3.4
	E10	0.77	654.3	2	3.4
Sn-15 % Pb	E11	1.8	571.3	1	1.7
	E12	1.8	526.6	1	1.7
	E13	0.9	571.4	2S	3.4
	E14	0.9	539.7	2S	3.4

Table 6.2: Experiments of Set 2

Composition	Exp.	Water flow rate (m ³ /sec.) x 10 ⁵	Material Temp. (° K)	No. of Plates	Plate thickness mm
Pb-35% Sn	E15	0.45	600.0	3	5.1
	E16	0.45	559.4	5	5.1
	E17	0.45	557.8	8	9.6
Pb-19 % Sn	E18	0.46	614.1	3	3.4
	E19	0.3	620.4	8	9.6
Sn-15 % Pb	E20	0.45	521.0	3	5.1

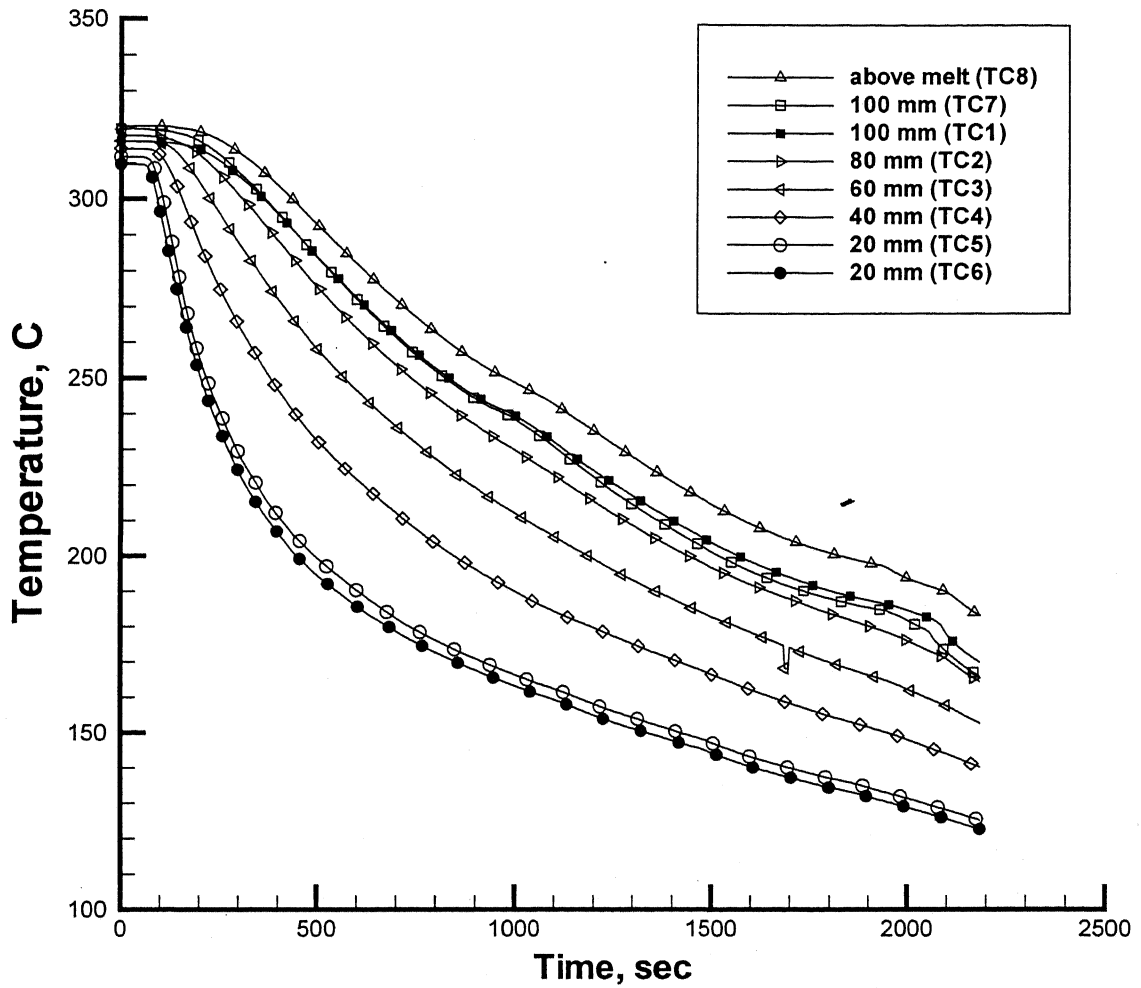


Fig. 6.1: Transient temperature response (experiment E1) in the solidification cell for TC1 to TC8 of Fig. 5.6; vertical distances of thermocouples from the base of the mould are indicated.

temperature profiles for eight thermocouples (TC1 to TC8) for experiment E1 as an example. It may be noted that the cooling rate and the temperature gradient vary with time and location. As cooling is started, significant temperature gradient is set up in the melt, which with the progress of time, gradually decreases. Similarly, cooling rate is high in the beginning but slows down with passage of time. This feature is observed in all the experiments. Temperature profiles for experiments E1 to E14 are compiled in Appendix I.

Solidification conditions are often described in terms of (i) thermal gradient ahead of the solidification front, and (ii) cooling rate. In the experiments carried out in this work, both the thermal gradient and the cooling rate vary as function of time and vertical distance from the base of the mould. Therefore, these values have been listed for TC3 at the beginning of solidification for all experiments in Table 6.3 to provide an approximate comparison of experiments. The values of thermal gradient, cooling rate, and growth velocity, for first and second sets of experiments are listed in Table 6. 3. It is readily seen from this table that as the heat flux is reduced, the thermal gradient in the melt goes down. Similarly, the cooling rate goes down with reduction in boundary heat flux. Local solidification time is an important solidification parameter, and the same is listed for various thermocouple locations in Table 6.4.

Fig. 6.2 shows the temperature response of thermocouples TC 9 to TC 12 (see Fig. 5.6). These provide the temperatures in the chill block (TC9 and TC10) as well as for water inlet (TC 11) and water outlet (TC12). The temperature responses in chill block and water inlet and outlet have been used for estimation of heat flux at the bottom boundary of the mould as detailed in Section 6.3.

6.2.2 Macrosegregation data

Chapter 5, Section 5.4, has discussed experimental procedure. Technique of macrosegregation measurements has been presented there. Fig. 5.8 shows locations for sampling for this at various heights from the base of the mould. For all experiments, compositions were measured with the help of atomic absorption spectroscopy. The results are compiled in Appendix II. For Pb-35 wt %Sn, the longitudinal segregation was practically absent for the fast cooling rates, whereas for intermediate and slow cooling

Table 6.3: Solidification condition at TC3 for various experiments

Location->		TC3		
Alloy	Exp. No	G* °C/m	R* °C/s	V* µm/sec
Pb-35 wt % Sn	E1	865	0.097	112
	E2	580	0.1105	189
	E3	390	0.068	174
	E4	645	0.08	124
	E5	650	0.1115	176
	E6	925	0.1125	121
	E15	615	0.068	111
	E16	290	0.0395	136
	E17	319	0.0575	180
Pb-19 wt % Sn	E7	615	0.0825	134
	E8	905	0.1325	146
	E9	1050	0.1245	119
	E10	770	0.088	114
	E18	660	0.085	129
	E19	325	0.0375	115
Sn-15 wt % Pb	E11	580	0.0645	111
	E12	410	0.0515	125
	E13	720	0.043	60
	E14	745	0.0565	76
	E20	295	0.033	112

* G is thermal gradient, R is cooling rate and V is rate of solidification

Table 6.4: Local solidification time (seconds) at various thermocouple locations

Alloy	Exp. No.	TC1	TC2	TC3	TC4	TC5
Pb-35 wt % Sn	E1	462	729	894	1081	1160
	E2	324	558	723	843	1002
	E3	489	759	921	1037	1203
	E4	645	915	1041	1131	1290
	E5	324	555	729	837	975
	E6	333	585	747	849	969
	E15	840	1104	1251	1365	1554
	E16	1677	1881	2016	2196	2412
	E17	1530	1870	2020	2200	2455
Pb-19 wt % Sn	E7	900	1050	1083	1065	1053
	E8	390	624	705	705	702
	E9	447	657	777	765	792
	E10	810	993	1020	948	966
	E18	852	1047	1080	1068	1050
	E19	2100	2045	2010	1965	1920
Sn-15 wt % Pb	E11	300	414	534	612	525
	E12	297	480	624	690	747
	E13	522	645	804	852	855
	E14	321	453	582	684	663
	E20	939	1182	993	1074	1128

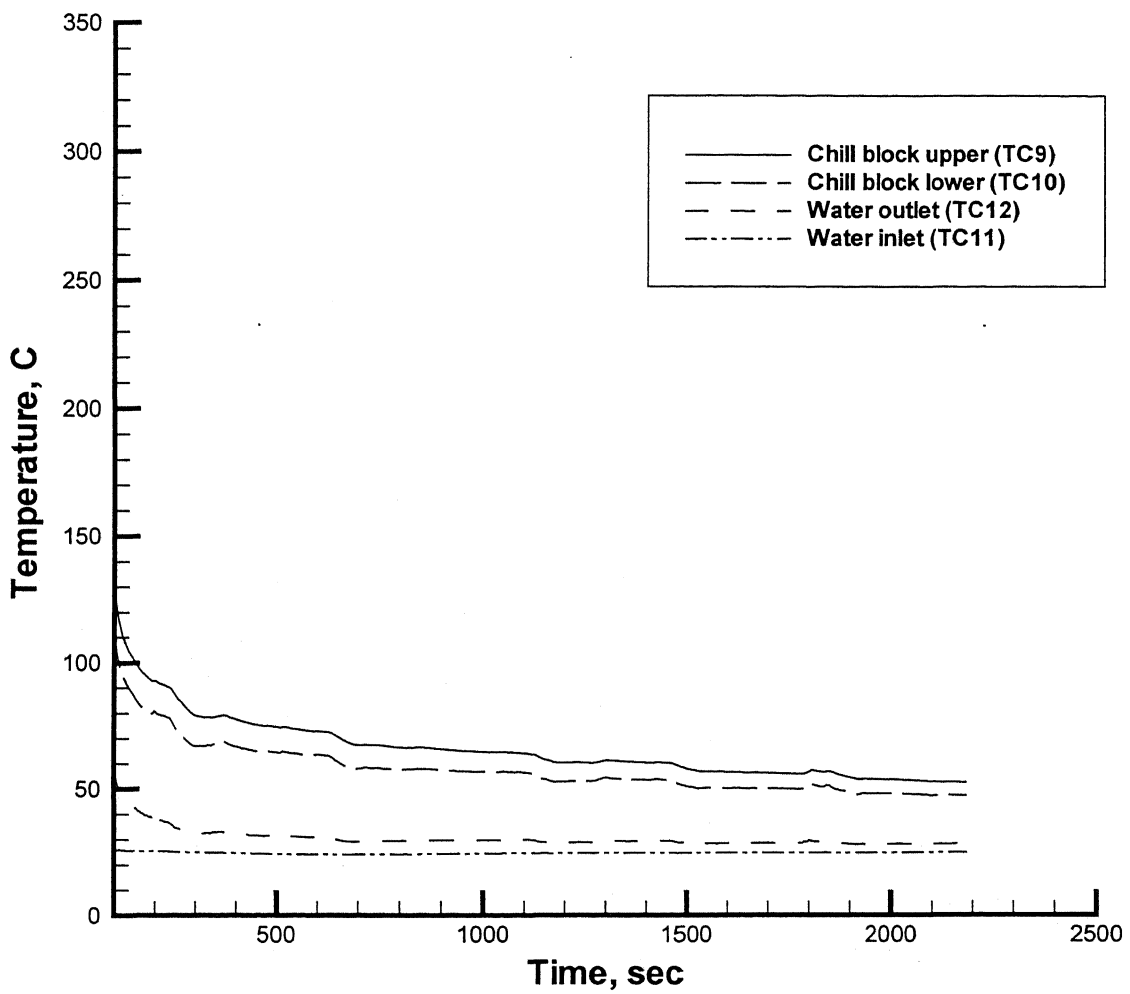


Fig. 6.2: Transient temperature response (experiment E1) in the solidification cell for TC9 to TC12 of Fig. 5.6.

rates it exhibited some segregation. For Pb-19 wt % Sn, segregation was not significant for all cooling rates although localized variation could be observed. For Sn-15 % Pb alloy no segregation was observed. Some typical macrosegregation profiles are shown in Figs. 6.3 to 6.5.

6.2.3 Microstructure

Solidification microstructures were observed in experiments of set 1. For all three alloy systems, the solidification microstructures were dendritic. Some typical micrographs are shown in Figs. 6.6 to 6.8. Primary and secondary arms could be readily observed. As expected, the bottom portion of the casting provided finer secondary dendrite arm spacing, which coarsened in the upward vertical direction. Primary and secondary dendrite arm spacings for various experiments were measured from microphotographs. Dendrite arm spacings from these experiments are compiled in Table 6.5.

6.2.4 Other observations

Apart from the above measurements, visual inspection of cast surface was also done. For Pb-35 % Sn, cast surfaces were found smooth for faster and intermediate cooling rates (E1 to E6). However for slower cooling conditions (E15 to E17) aligned porosities along vertical direction were observed. Similar trends were observed for Pb-19 wt % alloy. For experiments E7 to E10 surfaces of the castings were smooth. However for E18 and E19, cast surfaces were rough with pores. As opposed to these, surfaces of Sn-15 wt % Pb were smooth for all experiments (E11 to E14 and E20). This phenomenon may be attributed to presence of convection during solidification of lead-rich alloys. As discussed in Ch.2, Sec. 2.3, thermosolutal convection is theoretically expected in Pb-rich alloys, but not in Sn-rich alloys. Hence the above observations confirm the expectations.

6.3 Analyses of Experimental Data

6.3.1 Dendrite arm spacing

Theoretical models of dendrite arm spacing:

Primary dendrite arm spacing (d_1) can be expressed in terms of alloy composition (C_0), linear rate of solidification (R), and thermal gradient (G) by the following equation [108]:

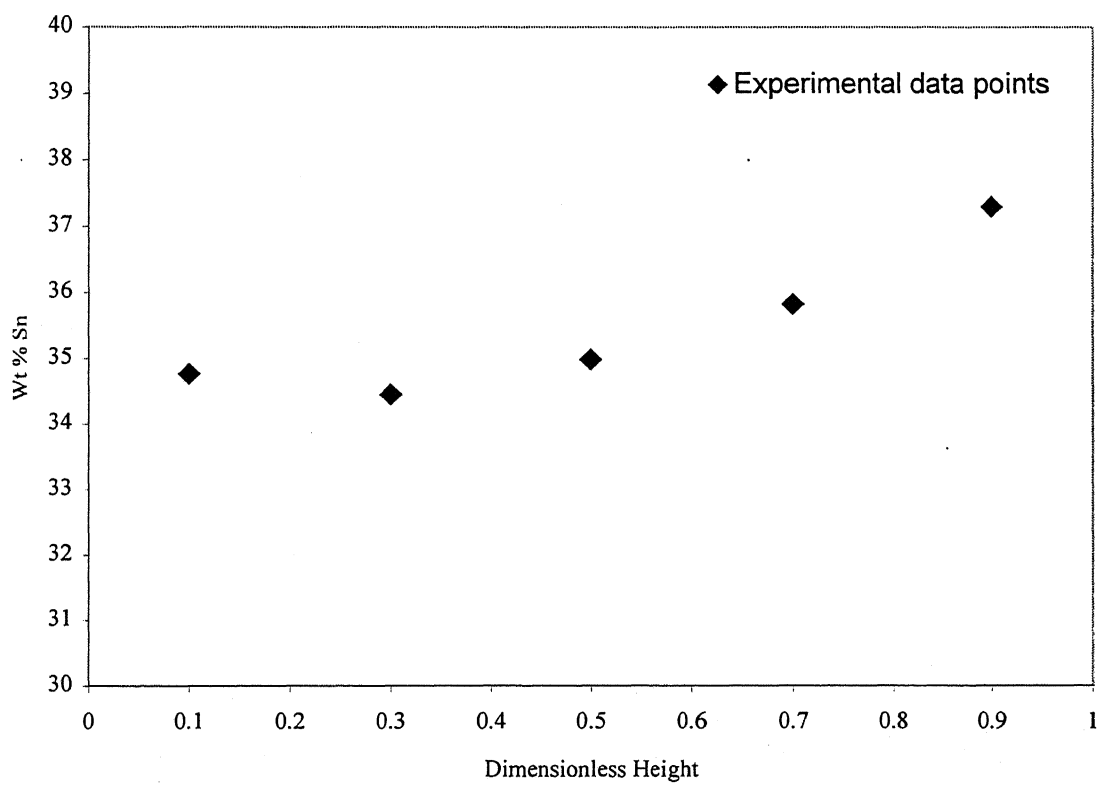


Fig. 6.3: Longitudinal macrosegregation for experiment E17 (Pb-35 wt % Sn).

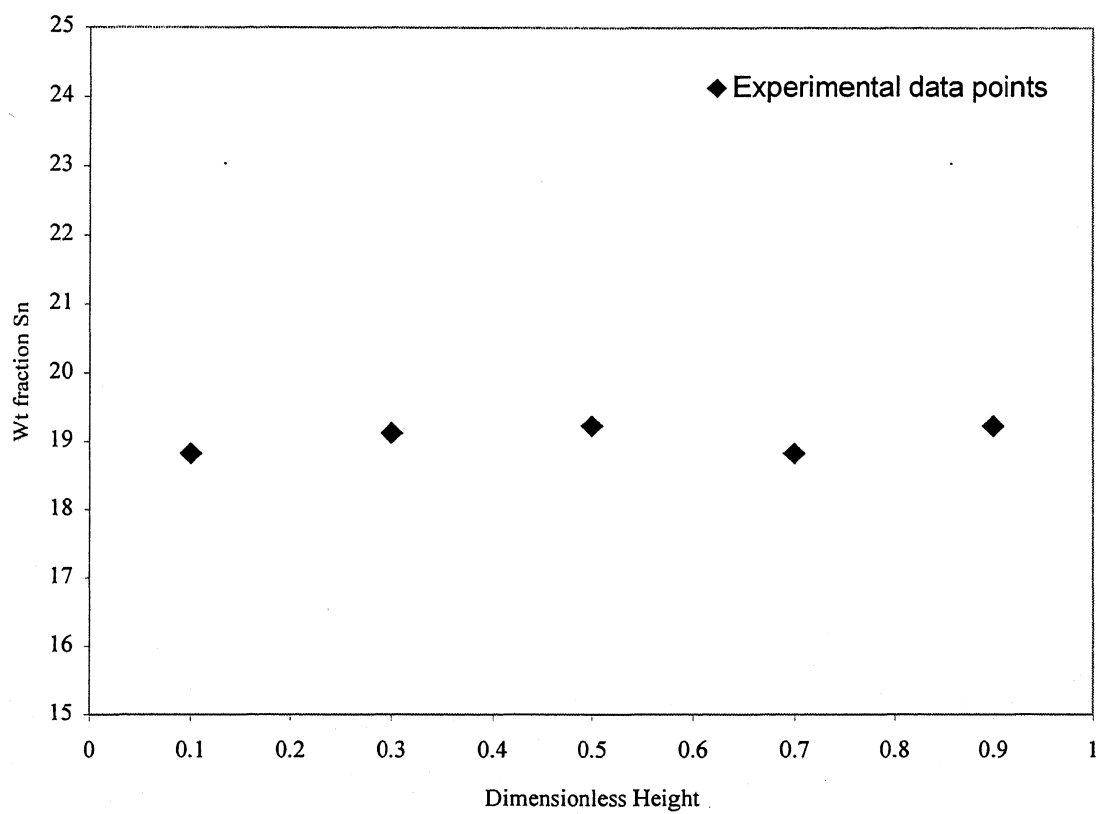


Fig. 6.4: Longitudinal macrosegregation for experiment E8 (Pb-19 wt % Sn).

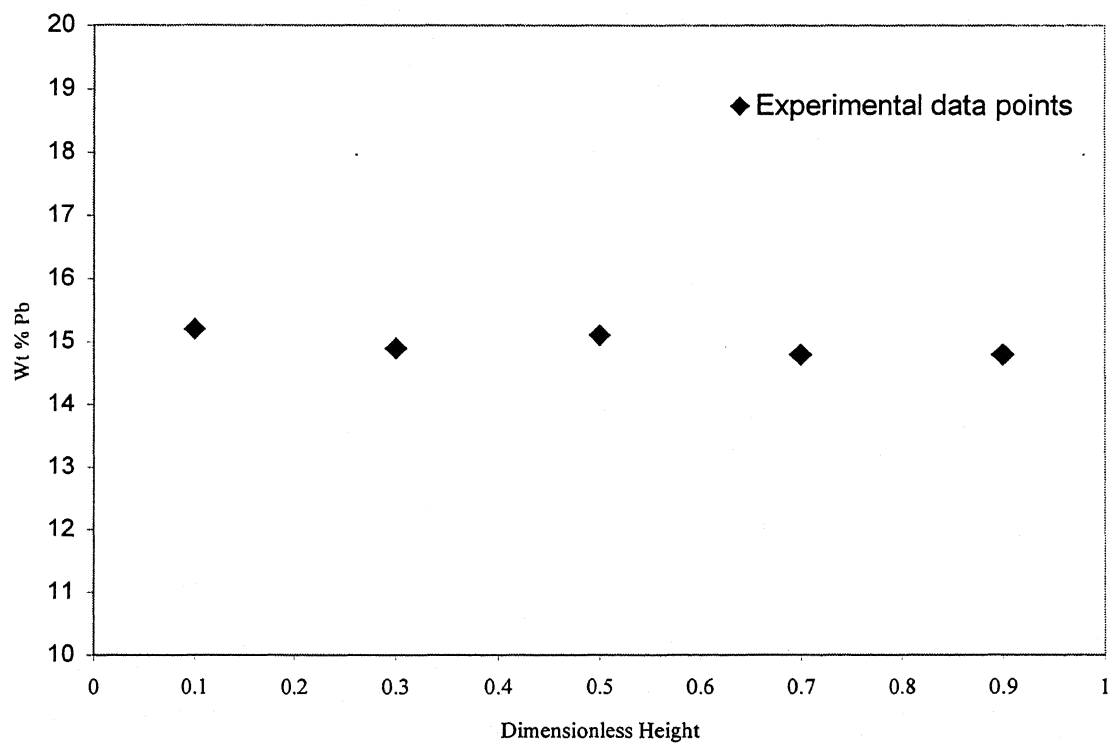


Fig. 6.5: Longitudinal macrosegregation for experiment E14 (Sn-15 wt % Pb).

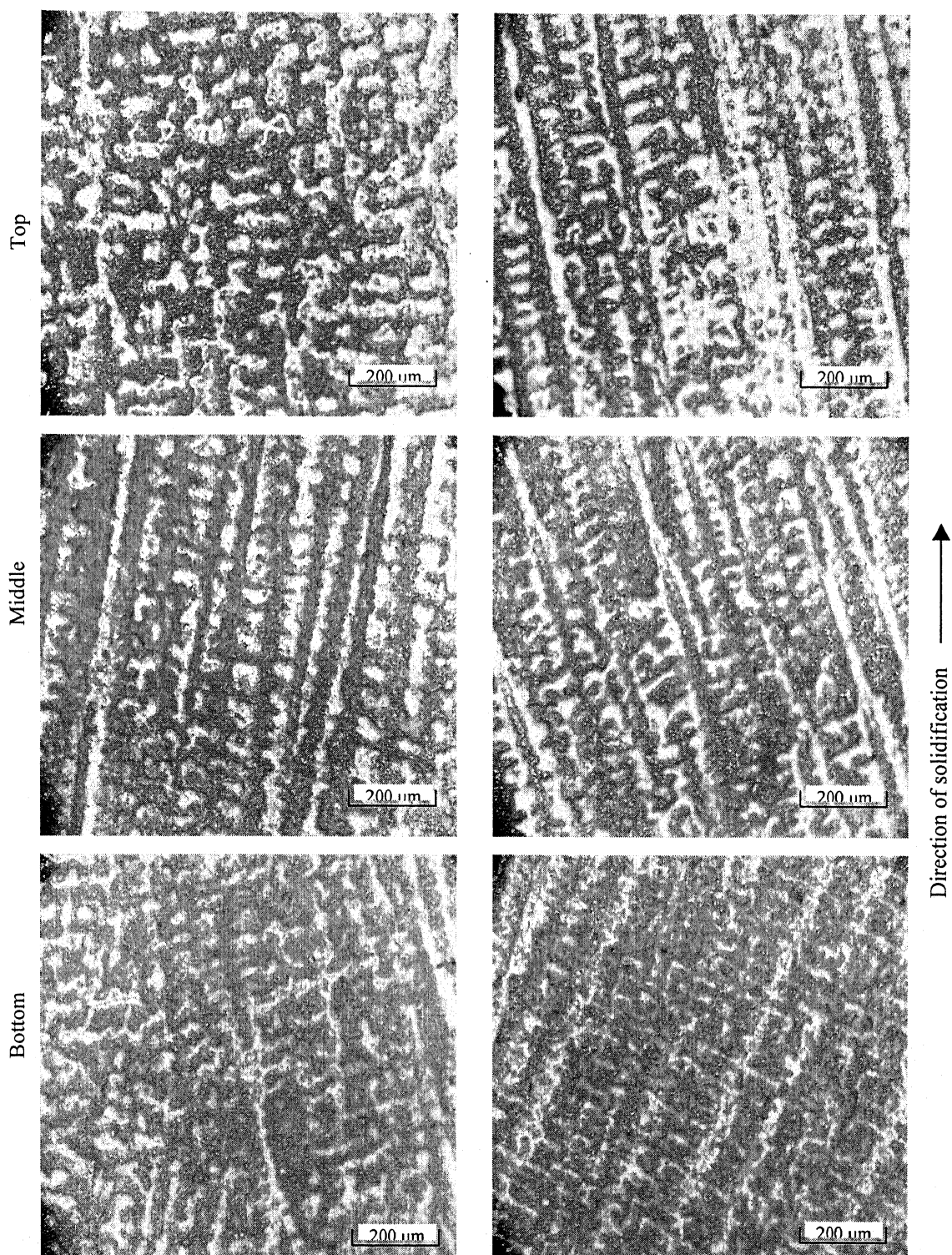


Fig. 6.6: Microphotographs of experiments E5 and E6 from different locations of casting (bottom, middle and top).

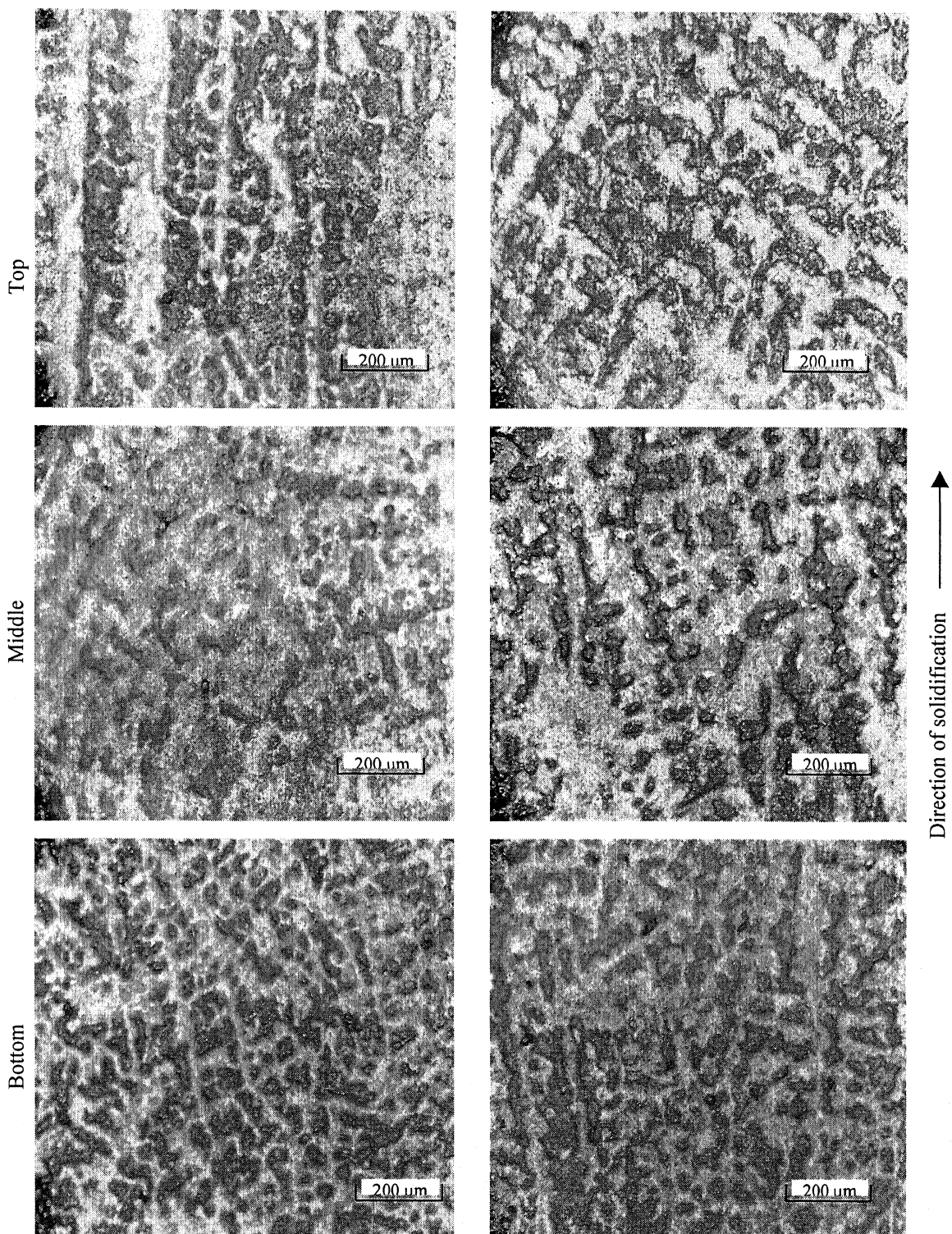


Fig. 6.7: Microphotographs of experiments E9 and E10 from different locations of casting (bottom, middle and top).

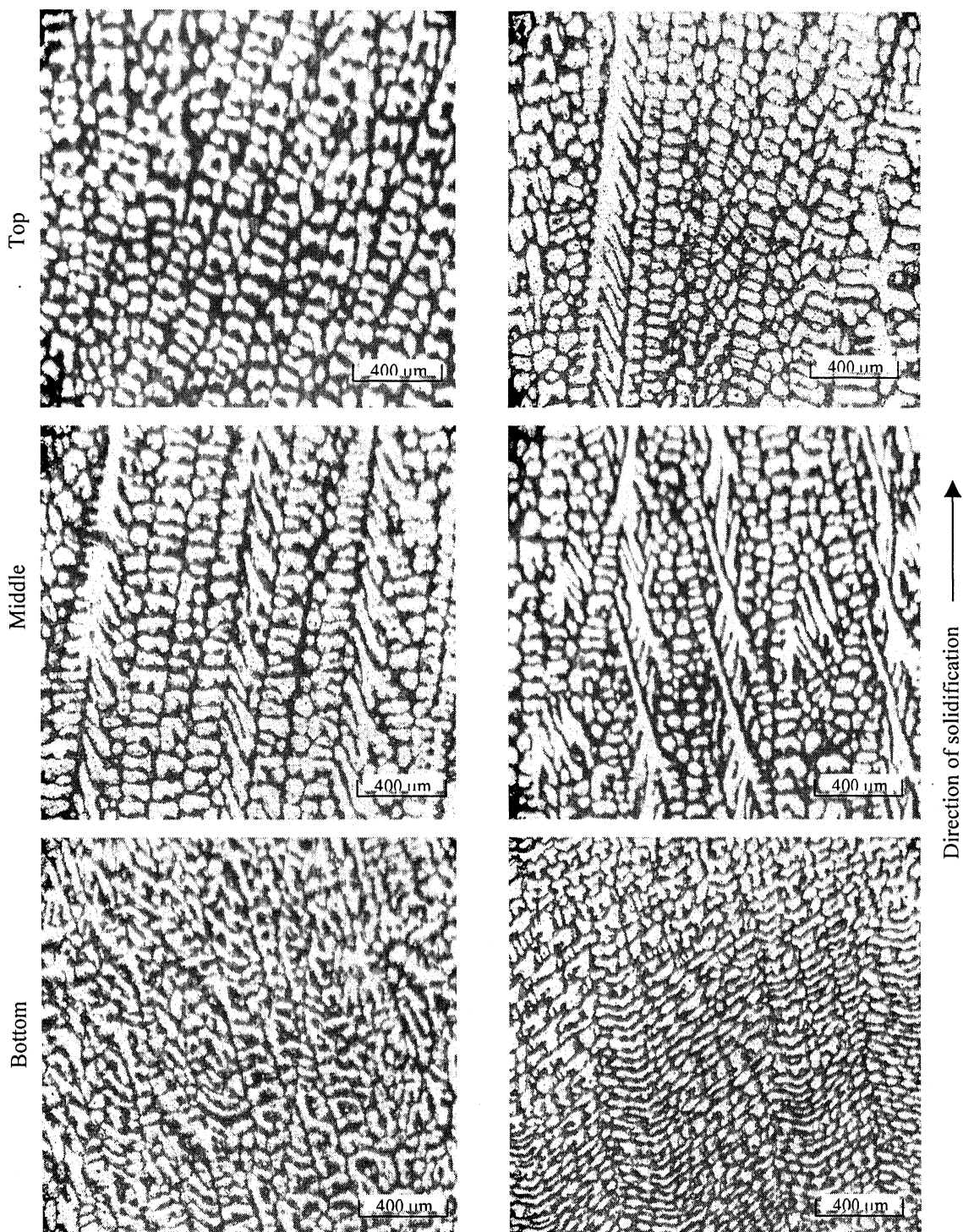


Fig. 6.8: Microphotographs of experiments E13 and E14 from different locations of casting (bottom, middle and top).

Table 6.5: Dendrite arms spacing from selected experiment

Exp. No.	d_2 (μm)			d_1 (μm)
	Bottom	Middle	Top	
E1	37	43	57	200
E2	31	39	43	210
E3	42	47	50	194
E4	43	48	57	190
E5	46	46	49	210
E6	40	46	46	204
E7	52	60	77	210
E8	41	43	82	240
E9	45	50	60	212
E10	51	59	87	180
E11	57	63	70	310
E12	52	64	76	260
E13	50	66	78	280
E14	43	65	63	212

$$d_1 = B C_o^{0.25} R^{-0.25} G^{-0.5} \quad \dots 6.1$$

where, B is a constant, d_1 is in μm , C_o is solute concentration in wt % Sn, G is in $^\circ\text{C}/\text{cm}$, and R is in cm/sec .

As noted by Tewari et al[108], values of B based on theoretical model of Hunt[119], Trivedi[120] and Laxmanan[121] are 130, 270 and 270, respectively. Tewari et al obtained the value of B through linear least-squared fit of experimental data points. It was found to be 84 (with a standard deviation ± 37). Value of $B = 88$ gives best fit with present data. Using Eq. 6.1 and solidification conditions listed in Table 6.3, the value of d_1 was calculated. These are compared with experimental data in Table 6.6 as well as shown in Fig. 6.9.

Secondary dendrite arm spacing can be expressed in terms of thermodynamic and thermophysical properties of alloy system and local solidification time as follows [3]:

$$d_2 = 5.5 (M t_f)^{0.33} = E (t_f)^{0.33} \quad \dots 6.2$$

where, t_f is the local solidification time in sec. and M is a parameter defined below

$$M = \frac{\Gamma D \ln (C_1^m / C_o)}{m(1-K)(C_o - C_1^m)} \quad \dots 6.3$$

where,

Γ (Gibbs-Thomson coefficient) = $1.0 \times 10^{-7} \text{ J}/\text{m}^2$, D (diffusivity) = $1.0 \times 10^{-9} \text{ m}^2/\text{s}$, K = 0.3 for lead-rich and 0.065 for tin-rich, m (slope of liquidus) = $-2.32 \text{ }^\circ\text{C}/\text{wt \% Sn}$ for lead-rich and $-1.53 \text{ }^\circ\text{C}/\text{wt \% Pb}$ and $C_1^m = C_e$, where C_e is eutectic composition.

Using the above parameters, theoretical values of E for Pb-35 wt % Sn, Pb-19 wt % Sn and Sn-15 wt % Pb were calculated to be 8.7, 9.47 and 10.5, respectively.

However, the values of E, which provided best-mean fit between experimental data on d_2 (Table 6.5) and local solidification time (Table 6.4), were 5.15, 6 and 8 for Pb-35 wt % Sn, Pb-19 wt % Sn and Sn-15 wt % Pb, respectively. Using these values of E and local solidification time from Table 6.4, d_2 for various experiments were compared using Eq.

Table 6.6: Comparison of calculated primary dendrite arms with experimental data

Exp. No.	d_1 (μm) Measured	d_1 (μm) Predicted
E1	200	218
E2	210	242
E3	194	255
E4	190	209
E5	210	222
E6	204	198
E7	210	231
E8	240	174
E9	212	202
E10	180	161
E11	310	209
E12	260	238
E13	280	233
E14	212	213

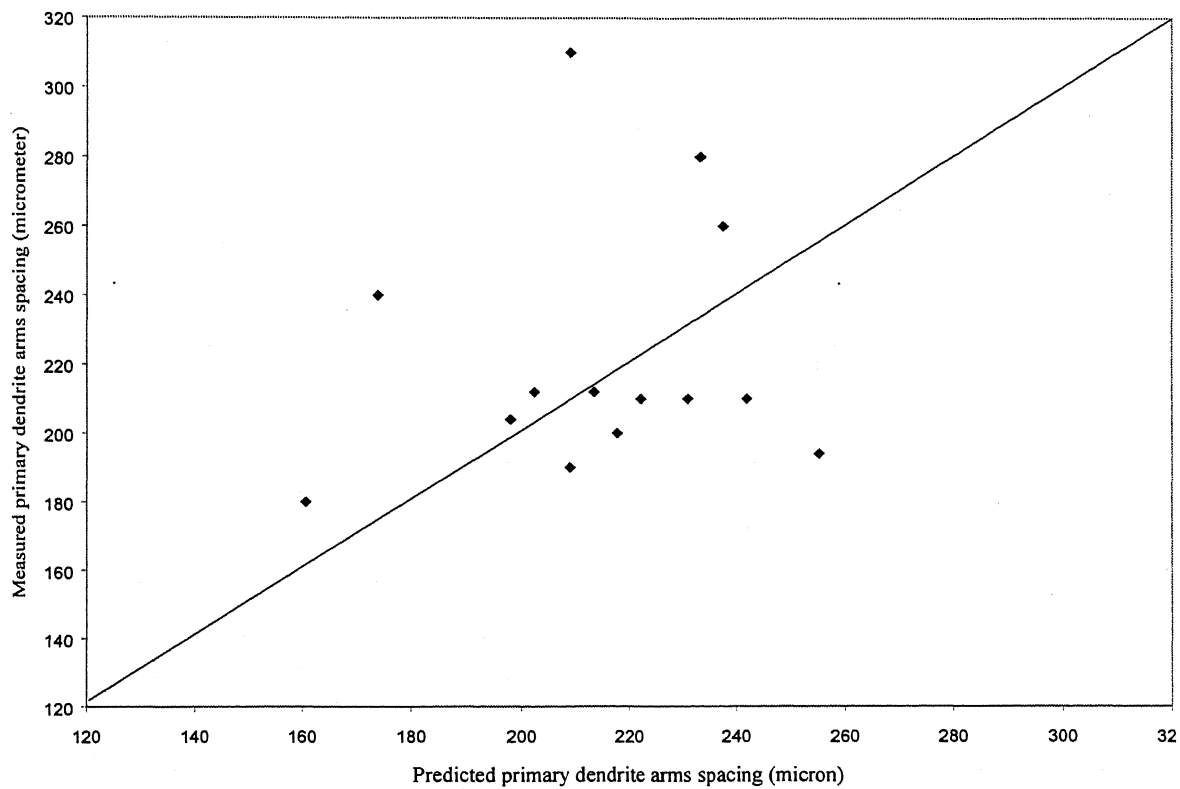


Fig. 6.9: Predicted vs. measured primary dendrite arm spacing (μm).

6.2. Few comparisons with experimental data are presented in Fig. 6.10. All the predicted data are compared against measured data in Fig. 6.11. The measured and calculated values are also listed in Table 6.7. Equations 6.1 and 6.2 were incorporated into the model for predicting microstructural details, i.e., arriving at profiles of secondary dendrite arms spacing.

6.3.2 Procedure for obtaining heat flux values for various experiments

The heat flux values, which were employed in numerical calculations using comprehensive model described in Ch. 3, were obtained through an iterative procedure. In this procedure, part of the mathematical model (only conduction mode by switching off convection) was also employed as outlined in this section.

Using the experimental temperature-time data, transient rates of heat transfer to water (Q) were calculated as follows:

$$Q = \rho_w w_t c_w (T_{12} - T_{11}) \quad \dots 6.4$$

where, ρ_w is density of water in kg/m^3 , w_t volumetric water flow rate in m^3/s , c_w is specific heat of water in $\text{J/kg}^\circ\text{C}$, and T_{11} and T_{12} are temperature responses of thermocouples at the water inlet and water outlet (thermocouples TC11 and TC12), respectively (Fig. 5.6) in $^\circ\text{C}$.

Using Eq. 6.4 as boundary condition to chill block and utilizing temperatures inside the chill block (thermocouples TC9 and TC10), the heat flux values at the metal mould interface was calculated by inverse method [122]. Using this heat flux, temperatures in the mould were numerically calculated the conduction model. Predicted temperatures were then compared with the experimental data. It was observed that calculated heat fluxes predicted faster rates of cooling as compared to the experimental values. The reason lies in the apparently higher value of heat removal by water, a part of which could be from furnace.

Owing to this discrepancy, a quasi-steady state value of heat flux (q) was employed at the metal-mould interface by the use of following expression:

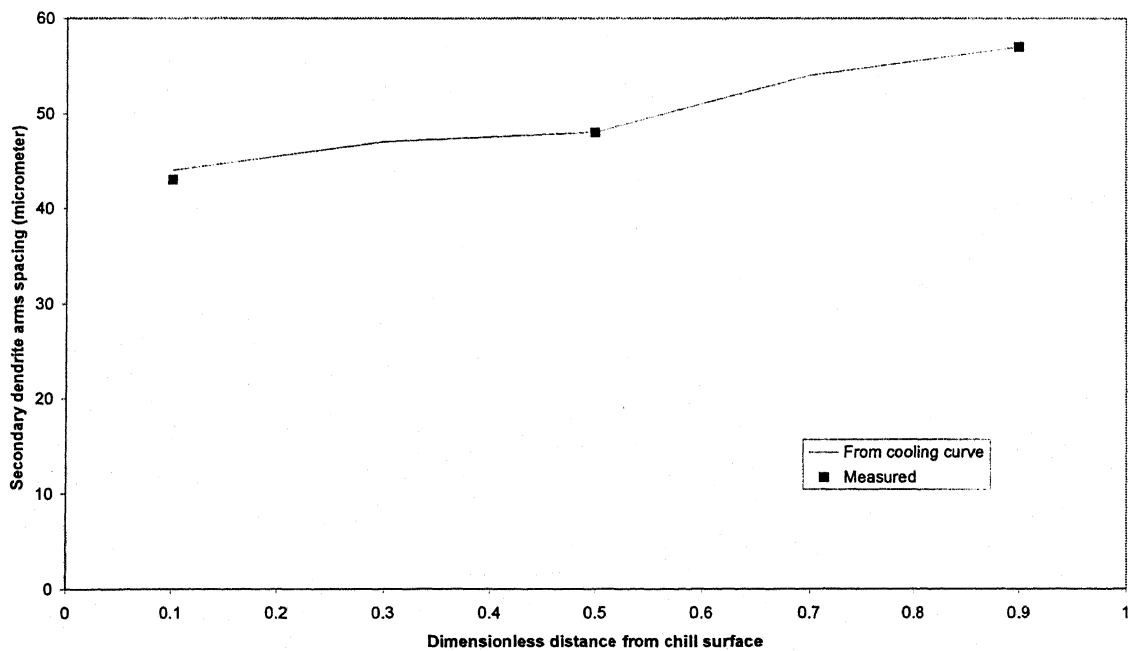
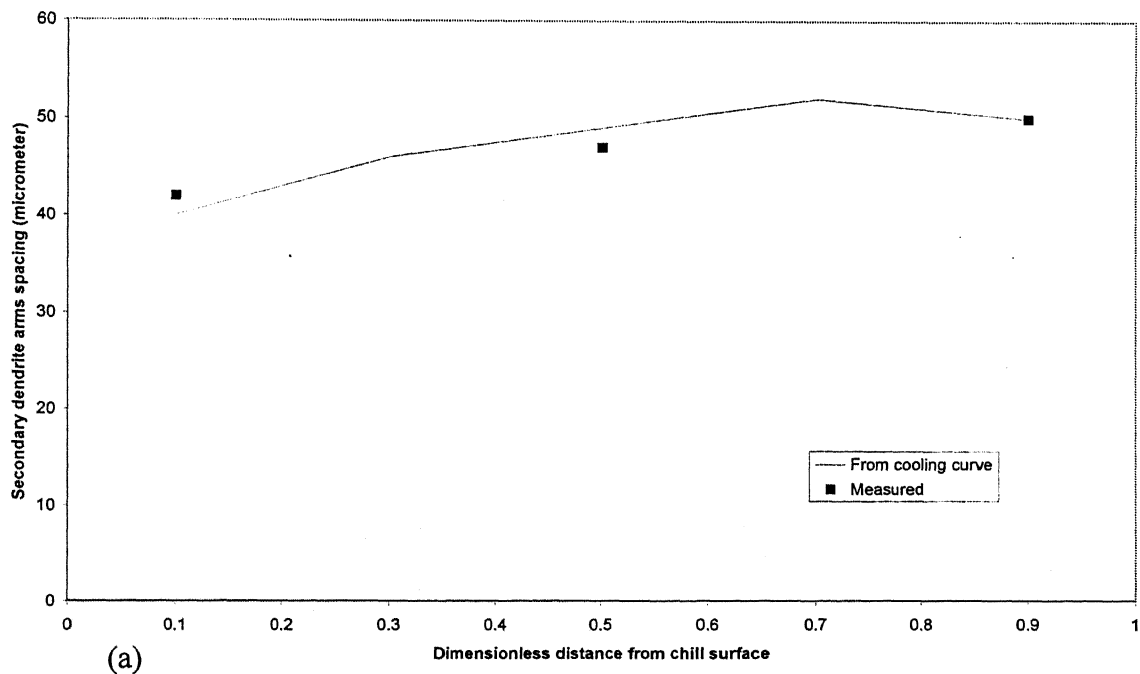


Fig. 6.10: Comparison of computed secondary dendrite arm spacing with experimental data (a) E3 and (b) E4.

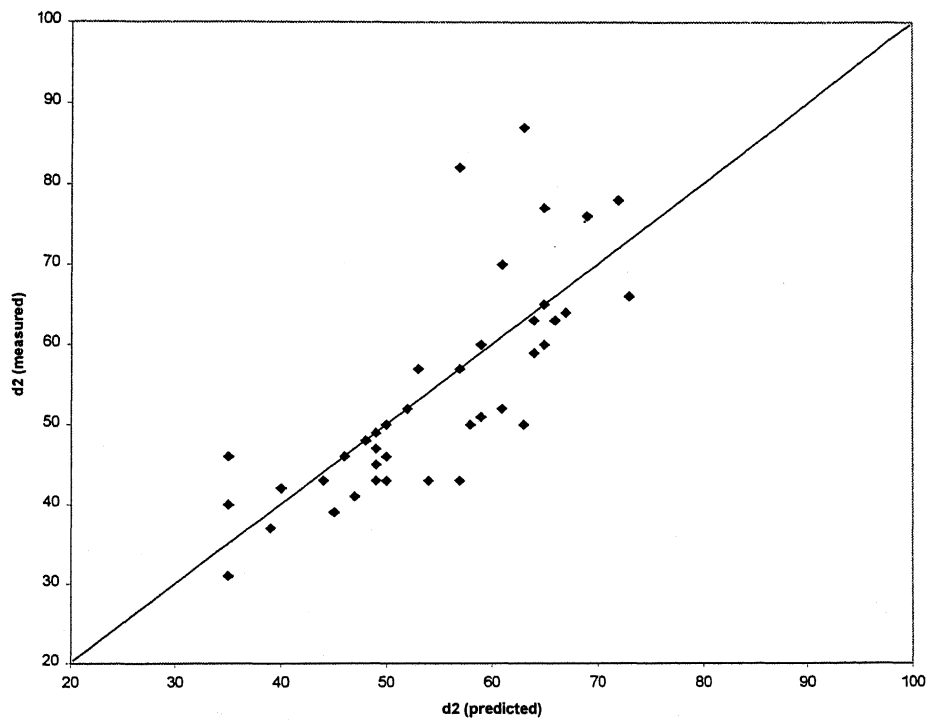


Fig. 6.11: Predicted vs. measured secondary dendrite arm spacing (μm).

Table 6.7: Comparison of calculated secondary dendrite arms spacing from selected experiments (μm)

Exp. No.	Secondary Dendrite Arms Spacing (μm)					
	Bottom		Middle		Top	
E1	37	39	43	49	57	53
E2	31	35	39	45	43	50
E3	42	40	47	49	50	50
E4	43	44	48	48	57	57
E5	46	35	46	46	49	49
E6	40	35	46	46	46	50
E7	52	61	50	65	77	65
E8	41	47	43	57	82	57
E9	45	49	50	58	60	59
E10	51	59	59	64	87	63
E11	57	53	63	64	70	61
E12	52	52	64	67	76	69
E13	50	63	66	73	78	72
E14	43	54	65	65	76	69

$$Q = qA = - A F_t k_c (T_{10} - T_9) / \Delta Z \quad \dots 6.5$$

where, Q is rate of heat removal J/s, A is area in m^2 , k_c is conductivity $W/m^\circ K$ of the chill block, T_9 and T_{10} are temperature responses of the two thermocouples (TC9 and TC10) in the chill block (Fig. 5.6), F_t is a dimensionless tuning parameter and ΔZ is the distance between the two thermocouples in meters.

Equation 6.5 can be used as flux at the metal-mould interface provided the thermal profile in the chill block is linear. This was checked independently with the help of a 1-D model. Except for the early stages of cooling the temperature profile inside the chill block was found linear.

Using the heat flux value obtained from equation 6.5, the model was used to simulate various experiments. Apart from F_t , conductivities of liquid and solid were also adjusted to obtain best mean fit with the experimentally observed temperature profiles. Through an iterative procedure, the following parameters were obtained: Depending on superheat, F_t varied between 1.35 to 1.55 for experiments with 1 plate and highest water flow rate, i.e., $1.9 \times 10^{-5} m^3/s$; For all other conditions F_t varied between 0.8 to 1.15. The adjusted conductivities of solid and liquid, which provided best mean fit were $30 W/m^\circ K$ and $15 W/m^\circ K$ for Pb-35 wt % Sn, $27 W/m^\circ K$ and $14 W/m^\circ K$ for Pb-19 wt % Sn, respectively. The heat flux values thus obtained were employed in main calculations with the comprehensive mathematical model (including convection).

6.4 Analysis of Macrosegregation with Mathematical Model

Using the comprehensive mathematical model (including convection), described in detail in Ch. 3, the experiments carried out in this study were quantitatively analyzed. Heat flux values, obtained by procedure outlined in the previous section, were employed in these calculations as boundary conditions. Initial conditions were obtained from the experimental data. Measured/estimated (from cooling curves) secondary dendrite arm spacing values for an experiment were averaged and the averaged d_2 value was used in the model. These ranged from 40 to 80 μm . When generalized West permeability model

(Chapter 4) was employed in these simulations, no segregation could be predicted. On the other hand, when the Kozeny-Carman[85] equation (Eq. 4.13, Ch.4) with modified permeability coefficient, K_o , was used for the entire mush, it provided better predictions, and therefore was selected. It is worthwhile to note that generalized West model (combination of equations 4.13 and 4.14) and Kozeny-Carman equation with modified K_o differ only near the mush/liquid interface.

Fig. 6.12 shows the schematic of calculation domain and grid layout used in the calculation. Results of grid sensitivity test for vertical solidification are shown in Ch. 3. Two types of grids were used in present simulations. Experiments E6, E1 and E17 were simulated with 42x52 grids to compare the evolution of flow fields, isotherms, iso-composition lines and fraction liquid profiles at three distinct cooling rates. Although, it was perhaps desirable to employ finer grids for all calculations, a coarser grid of 22x32 was employed for simulations of other experiments in view of large computational time involved. Only axial macrosegregation are compared for these cases. A time-step of 0.25 second was employed in all the simulations. For 22x32 grids, 1 seconds of real time simulation required 5 seconds of CPU time on Pentium IV processor. The corresponding CPU time for 42x52 grids was 60 seconds.

The reasons for selection of E1, E6, and E17 for detailed analysis are as follows. These three experiments are from Pb-35 Wt % Sn, which showed more segregation than Pb-19 wt % Sn alloy under similar conditions of solidification. The three experiments from Pb-35 wt % Sn category are for fast (E6), intermediate (E1) and slow (E17) cooling rates. Accordingly, E6 shows minimum segregation and E17 shows maximum segregation with level of segregation for E1 lying in between. The time taken for complete solidification for E1, E6 and E17 are 2145 seconds, 1845 seconds and 3665 seconds respectively. The results of these simulations are presented in terms of evolution of flow, thermal field, composition and progress of solidification for 25 % and 50 % solidification. Besides these, the final macrosegregation and secondary dendrite arm spacing at the end of solidification have also been presented.

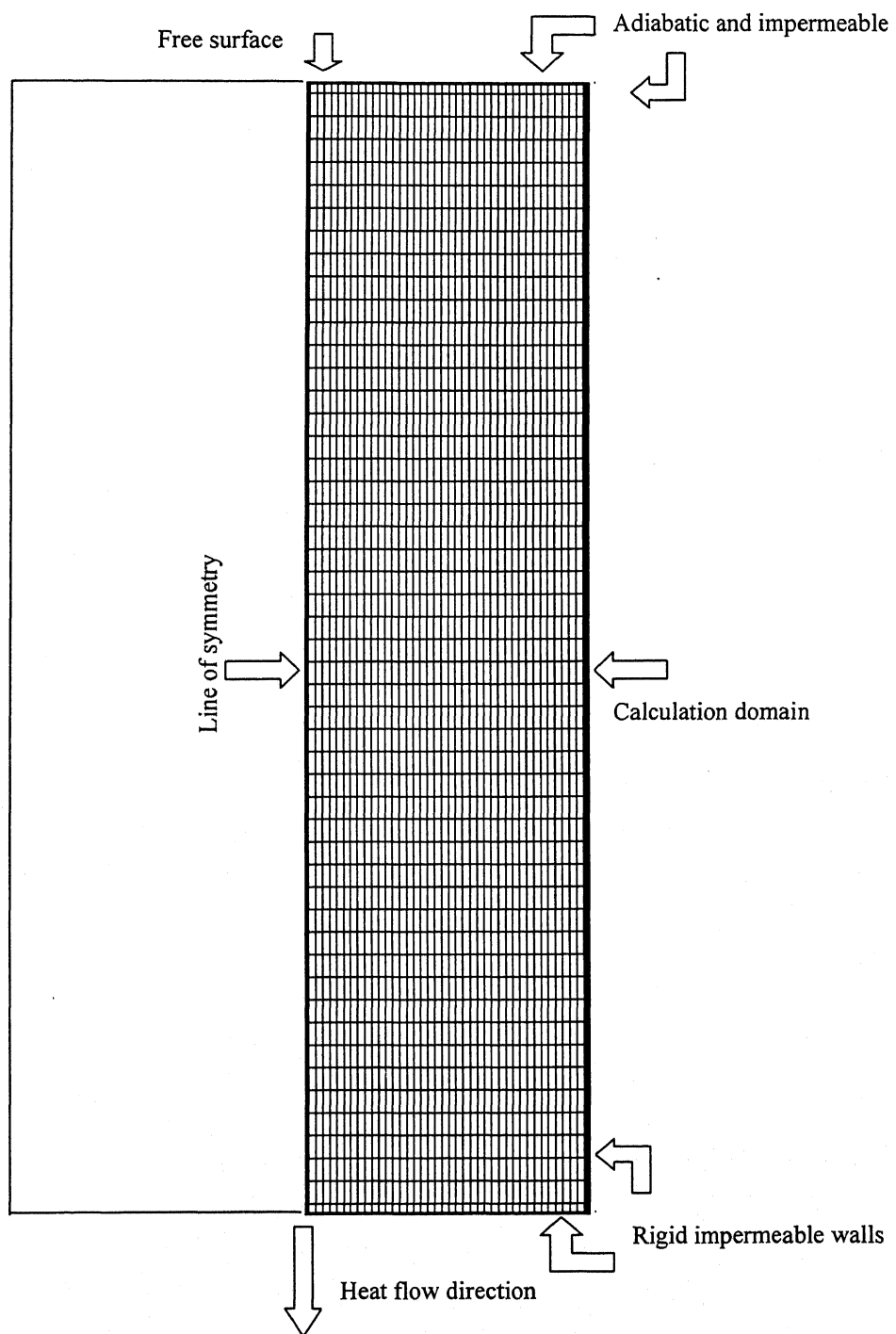


Fig. 6.12: Schematic of the calculation domain and grid locations.

6.4.1 Experiment E6 (Fast cooling rate)

Predicted temperature profiles are compared with the experimental data at various locations in Fig. 6.13, showing reasonable match. Fig. 6.14 presents the calculated profiles at 25% solidification. Streamlines of Fig. 6.14a are characterized by multiple vortices. All of them are active in the top of the mushy region to fully liquid region. Higher cooling rates lead to higher thermal gradient, and in turn, stronger flow. The effect of flow on isotherms (Fig. 6.14b) is small considering weak nature of flow. The average composition profile of Fig. 6.14d shows a highly complex macrosegregation pattern in the mushy region. Fig. 6.14c presents iso-liquid fraction in the mushy region, which is in the bottom half of the cavity. Although, streamlines penetrate the mushy zone, the strength of convection rapidly diminishes within the mushy zone where the permeability is low.

Fig. 6.15 presents the calculated results for E6 at 50% solidification. It may be noted from the streamlines of Fig. 6.15a that a weak flow is concentrated near the top, and there is a single large vortex at this time. The strength of convection is practically negligible in other parts of the mushy region. The contours of iso-fraction liquid profiles in Fig. 6.15c show channels at the centre and the side of the casting, which is vertically located near the top of the casting. It also shows that the entire casting is covered either solid or mushy region. Owing to higher rate of solidification, thermosolutal convection creates small solute enrichment of liquid at the top. Fig. 6.15d shows localized segregated regions reveals a relatively less complex segregation profile.

Macrosegregation profile, at the end of solidification, is shown in Fig. 6.16a. It is very similar to the profile at the end of 50 % solidification (Fig. 6.15c). Due to lower solidification time, long range transport of solute is less in this case and the minimum composition is 34.33 wt % Sn, whereas the maximum segregation is 36.54 wt % Sn. Fig. 6.16b shows the variation of secondary dendrite arm spacing in the casting. Finally, the computed macrosegregation were averaged in the radial direction and variation of macrosegregation in the vertical direction is compared with experimental data on macrosegregation in Fig. 6.17. In this case macrosegregation is practically non-existent.

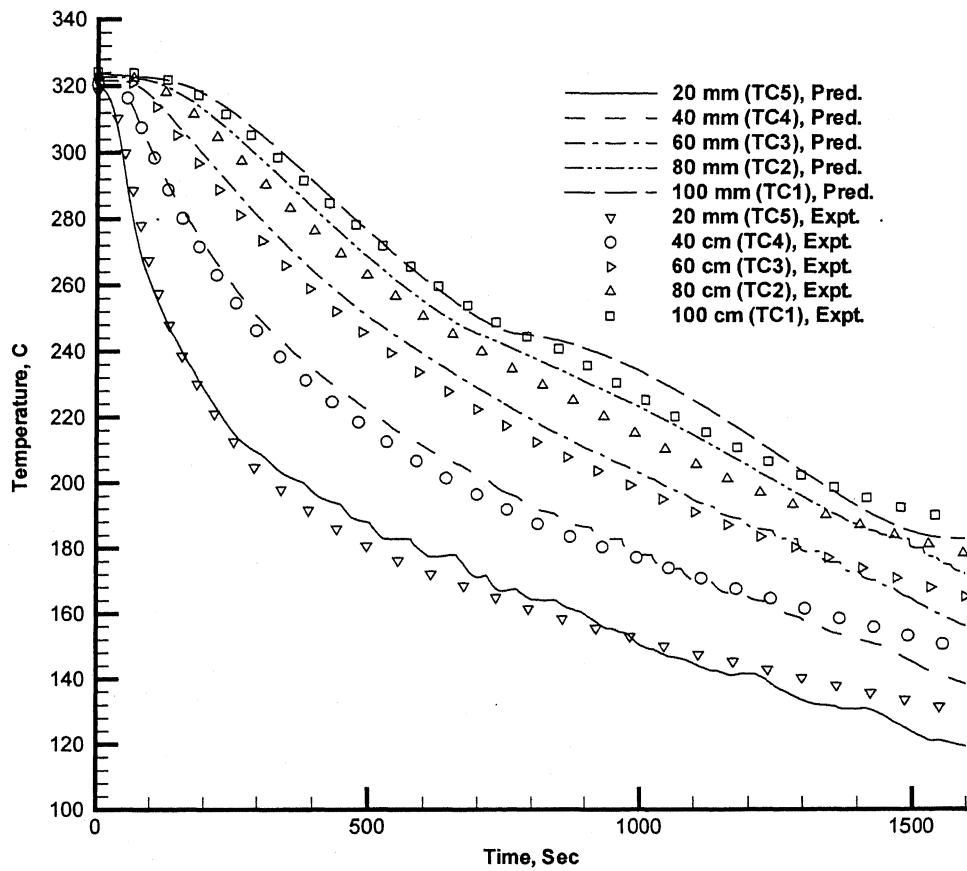


Fig. 6.13: Comparison of predicted temperatures with experimental data for experiment E6.

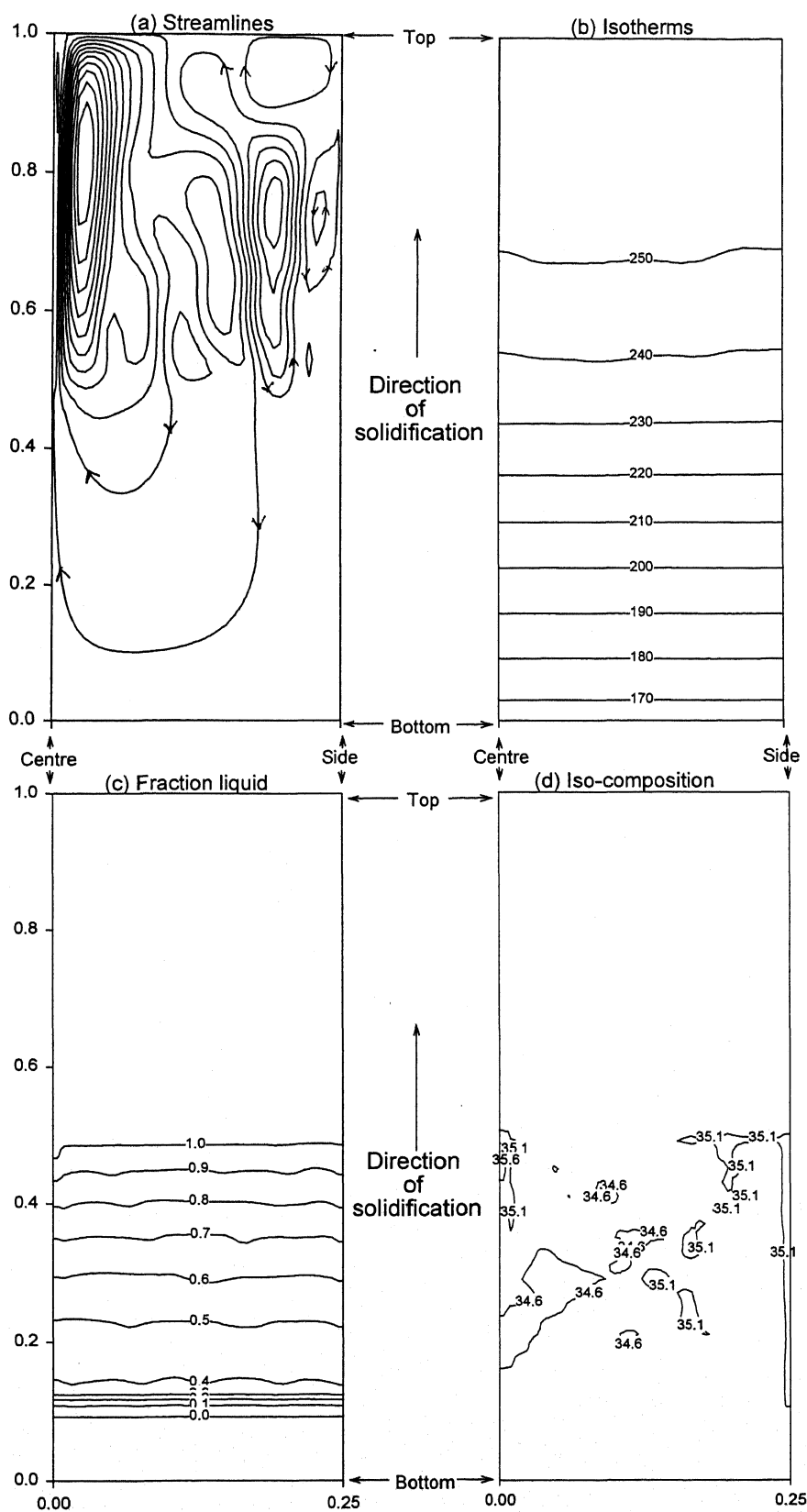


Fig. 14: Simulated results for E6 at 25 % solidification (a) Streamlines (ψ_{\min} : -0.557, ψ_{\max} : 1.1, equal increment, (b) isotherms, (c) iso-liquid fraction, and (d) iso-composition profiles.

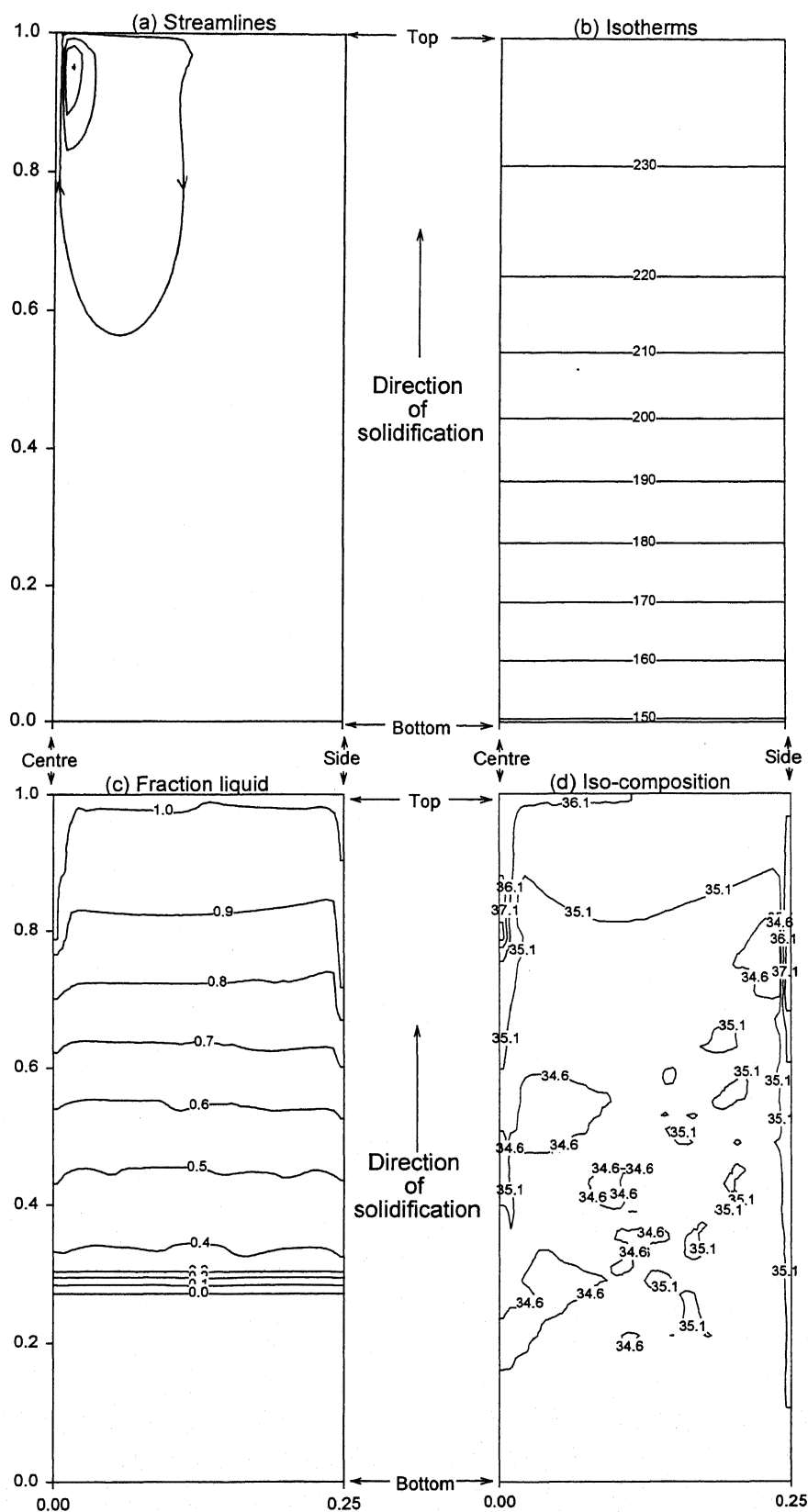


Fig. 15: Simulated results for E6 at 50 % solidification (a) Streamlines (ψ_{\min} : -0.088, ψ_{\max} : 0.33, equal increment, (b) isotherms, (c) iso-liquid fraction, and (d) iso-composition profiles.

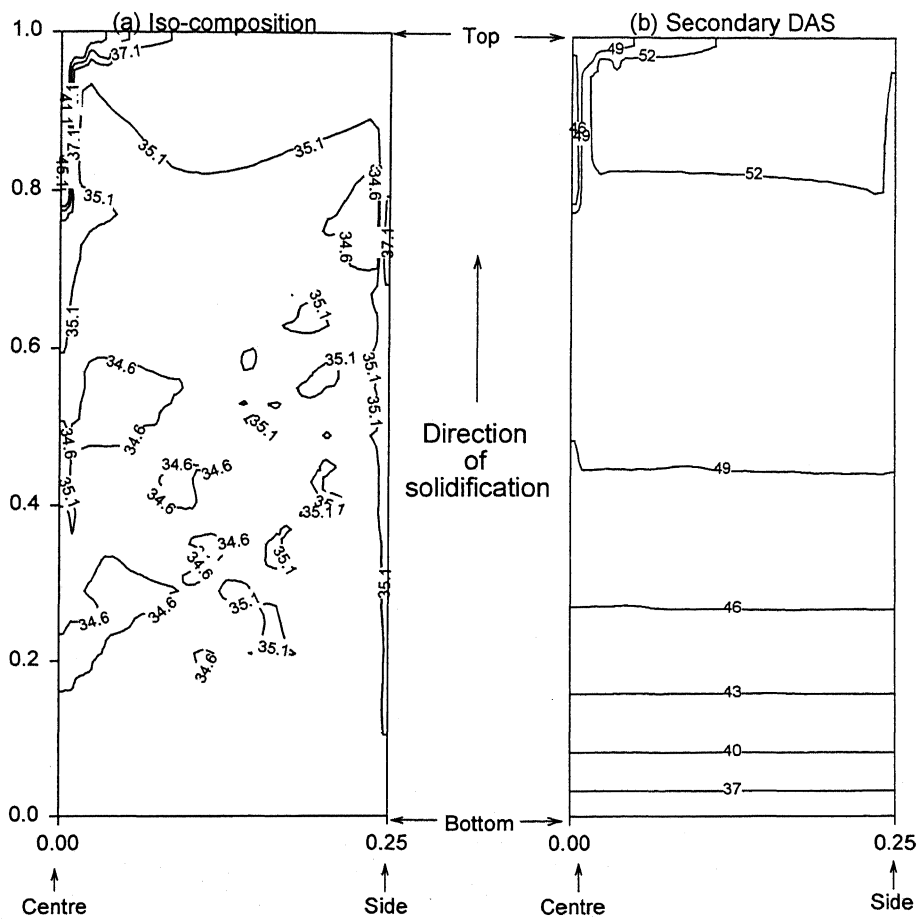


Fig. 16: Calculated results for E6 at the end of solidification (a) Final solute distribution (initial composition 35 wt % Sn) and (b) Secondary dendrite arms spacing (μm).

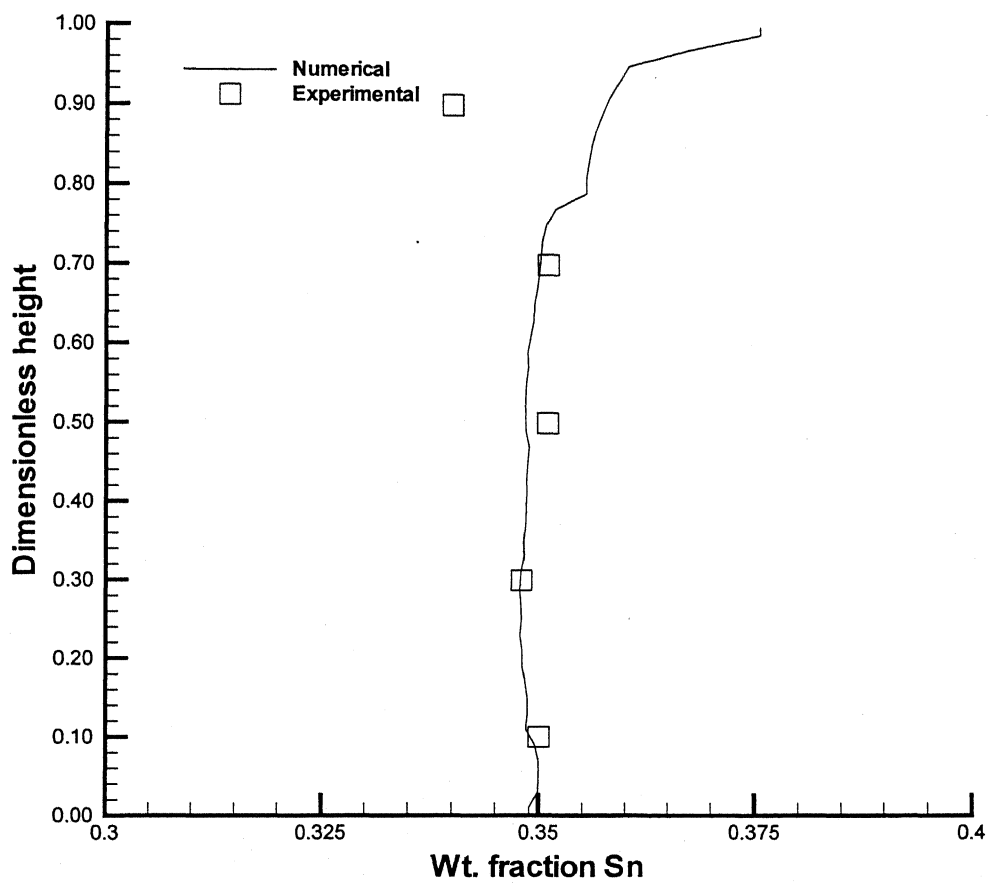


Fig. 17: Comparison of experimental and computed average macrosegregation along vertical direction for experiment E6.

6.4.2 Experiment E1 (Intermediate cooling rate)

Predicted temperature profiles are compared with the experimental data at various locations in Fig. 6.18, which shows reasonable match. Fig. 6.19 shows the calculated profiles at 25% solidification. Streamlines of Fig. 6.19a show an upward flow, encompassing top of the mushy region and the fully liquid region. The flow field consists of multiple vortices. The effect of flow on isotherms (Fig. 6.19b) is small considering weak nature of flow. The average composition profile of Fig. 6.19d shows a highly complex macrosegregation pattern in the mushy region. Fig. 6.19c presents iso-liquid fraction in the mushy region, which extends up to half of the cavity. Although the streamlines penetrate the mushy zone, the strength of convection rapidly diminishes within the mushy zone where the permeability is low.

Fig. 6.20 shows the calculated results at 50% solidification. It can be seen from the streamlines of Fig. 6.20a that the flow is concentrated near the channel and is upward within the channel. It extends into the top horizontal layer. The strength of convection is practically negligible in other parts of the mushy region. The contours of iso-liquid fraction profiles in Fig. 6.20c show the channel location at the top left corner of the cavity. Fig. 6.20c also shows that the entire casting is practically either solid or mushy region. Fig. 6.20d shows the segregation profile, and highly segregated region can be seen in the region surrounding the channel at top central portion of the ingot.

Macrosegregation profile, at the end of solidification, is shown in Fig. 6.21a. The complex nature of macrosegregation profile is readily attributed to complex thermosolutal convection in interdendritic liquid in the mushy region. The minimum composition is 33.6 wt % Sn whereas the maximum is 46.45 wt % Sn. Both maximum and minimum are concentrated over a small region of the segregated channel at the top central part of the ingot. Fig. 6.21b shows the variation of calculated secondary dendrite arm spacing in the casting. Finally, the computed macrosegregation were averaged in the radial direction and variation of macrosegregation in the vertical direction is compared with experimental data on macrosegregation in Fig. 6.22. The abrupt rise in the predicted axial macrosegregation profile at the middle of the casting is attributed to onset of channel formation.

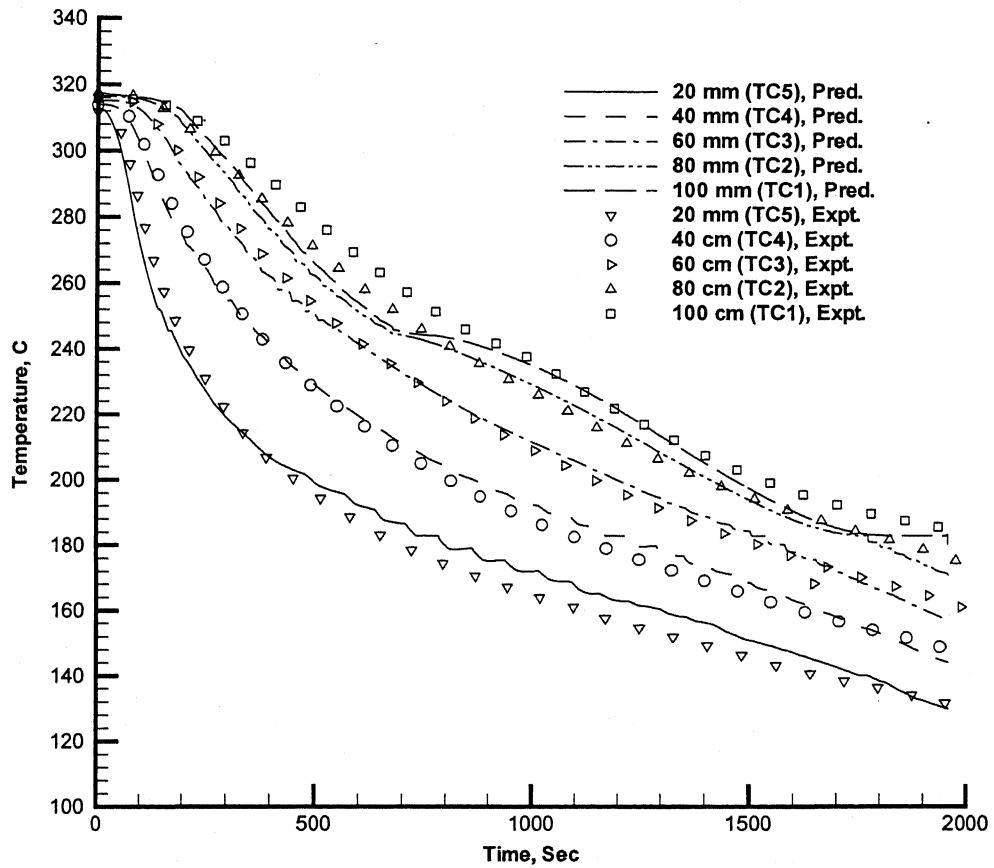


Fig. 6.18: Comparison of predicted temperatures with experimental data for experiment E1.

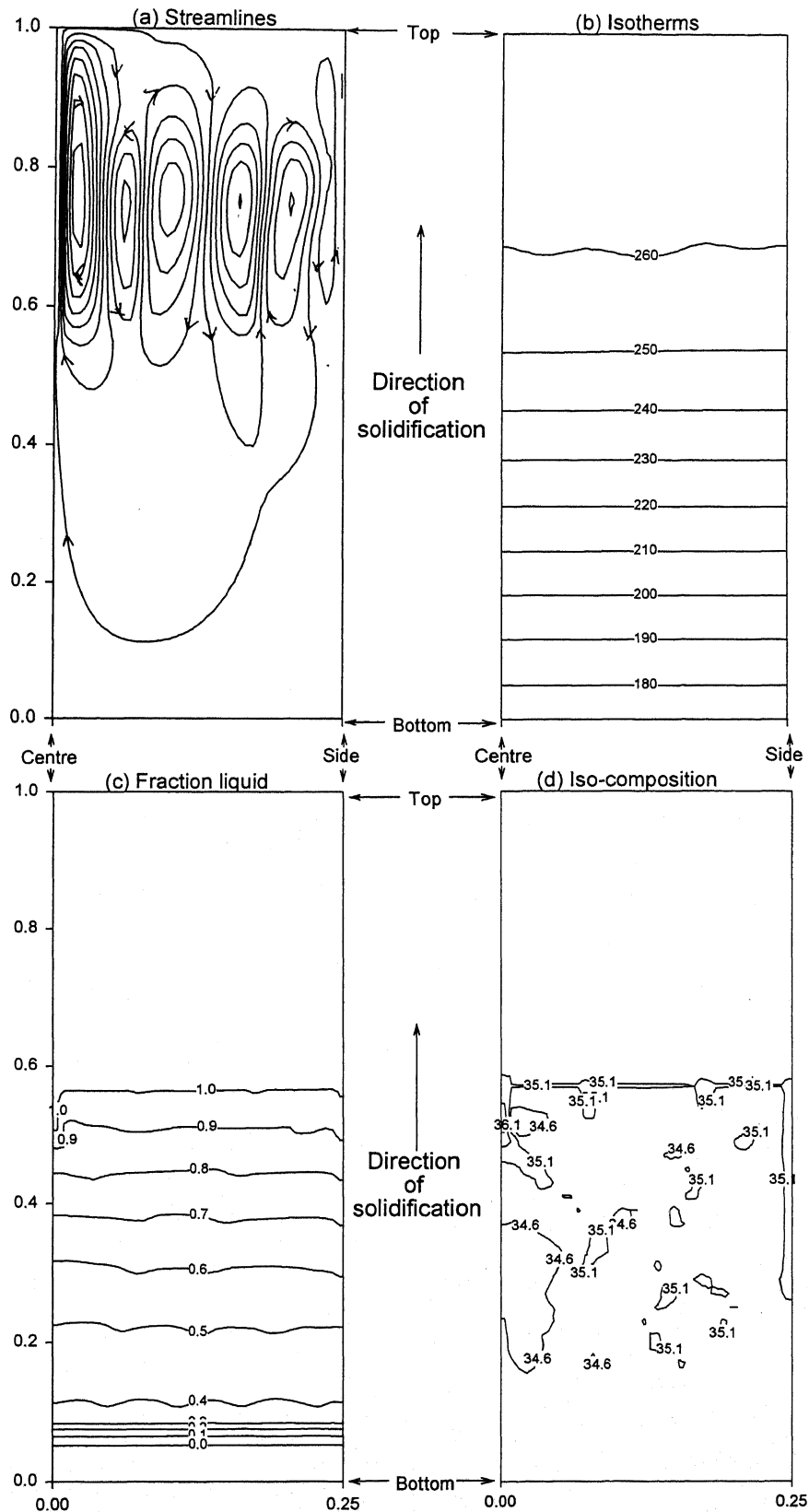


Fig. 6.19: Simulated results for E1 at 25 % solidification (a) Streamlines (ψ_{\min} : -0.495, ψ_{\max} : 0.772, equal increment, (b) isotherms, (c) iso-liquid fraction, and (d) iso-composition profiles.

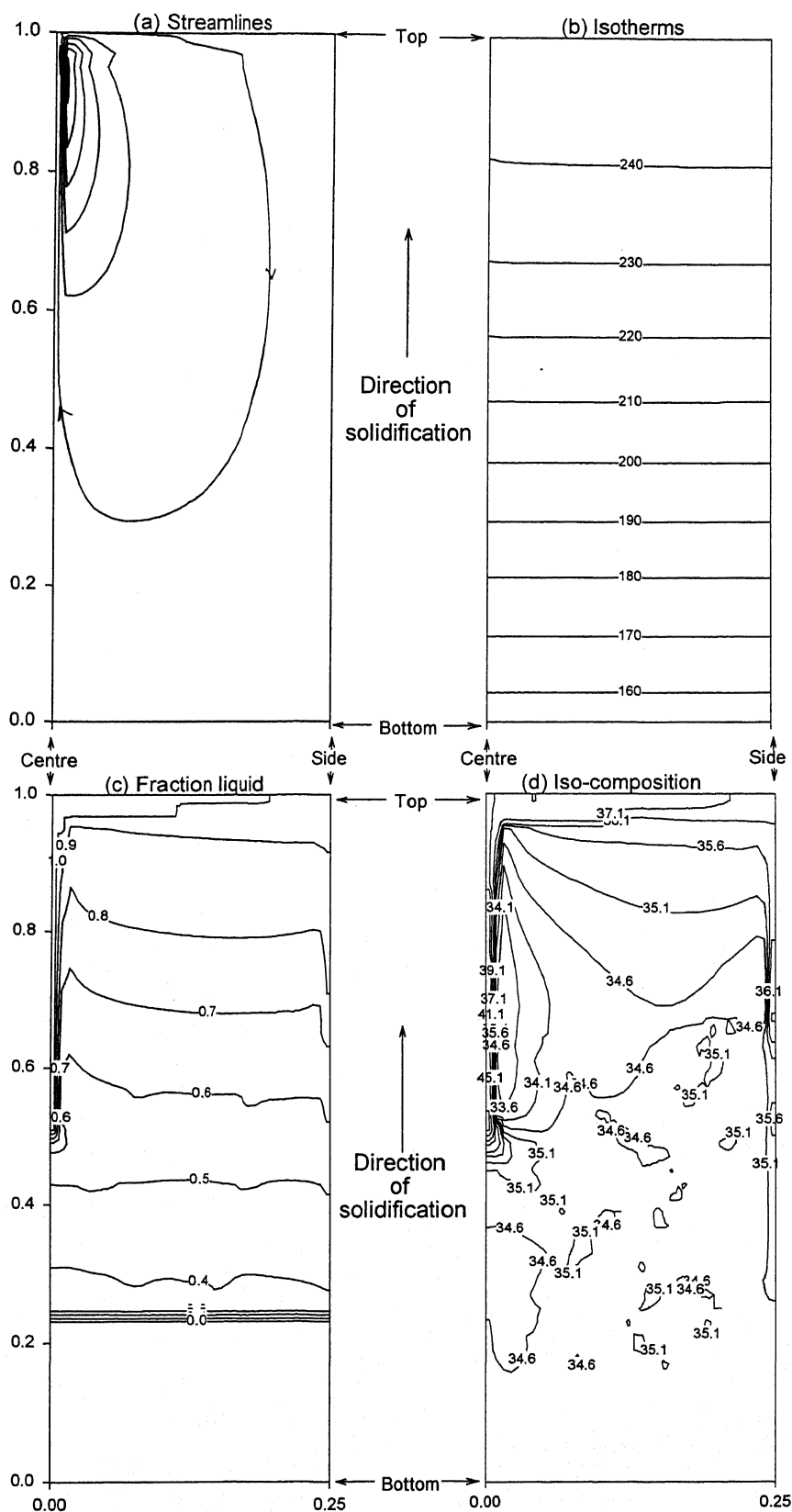


Fig. 6.20: Simulated results for E1 at 50 % solidification (a) Streamlines (ψ_{\min} : -0.121, ψ_{\max} : 0.535, equal increment), (b) isotherms, (c) iso-liquid fraction, and (d) iso-composition profiles.

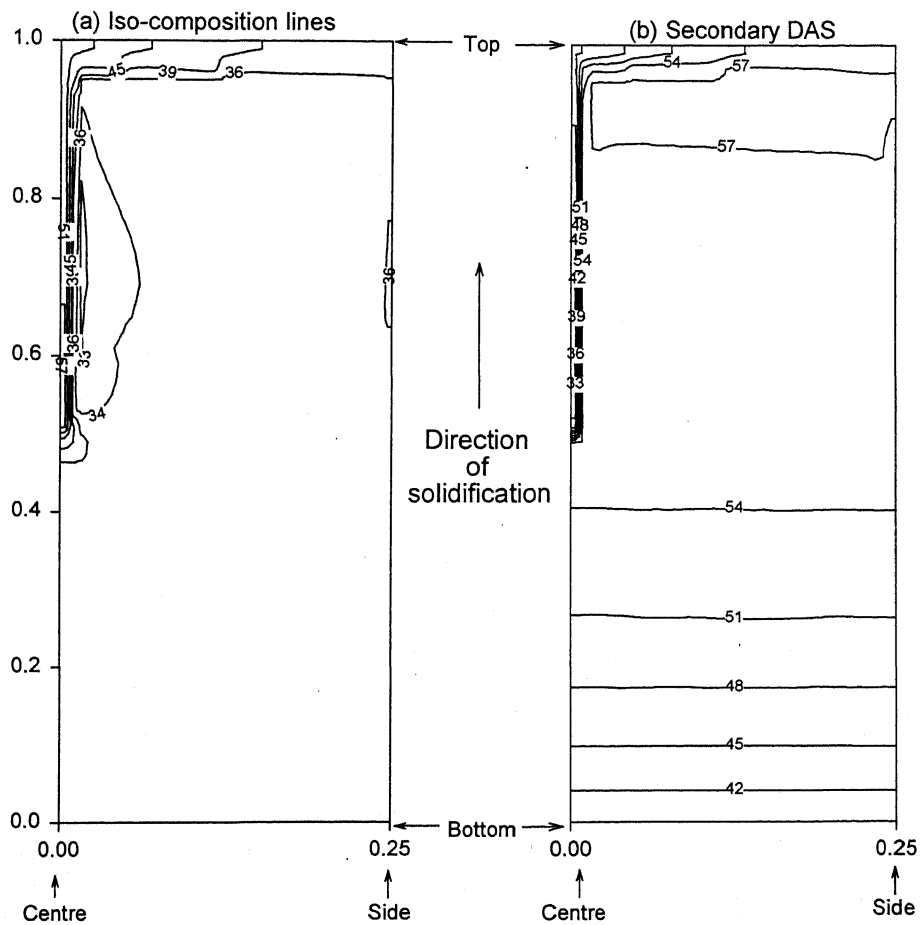


Fig. 6.21: Calculated results for E1 at the end of solidification (a) Final solute distribution (initial composition 35 wt % Sn) and (b) Secondary dendrite arms spacing (μm).

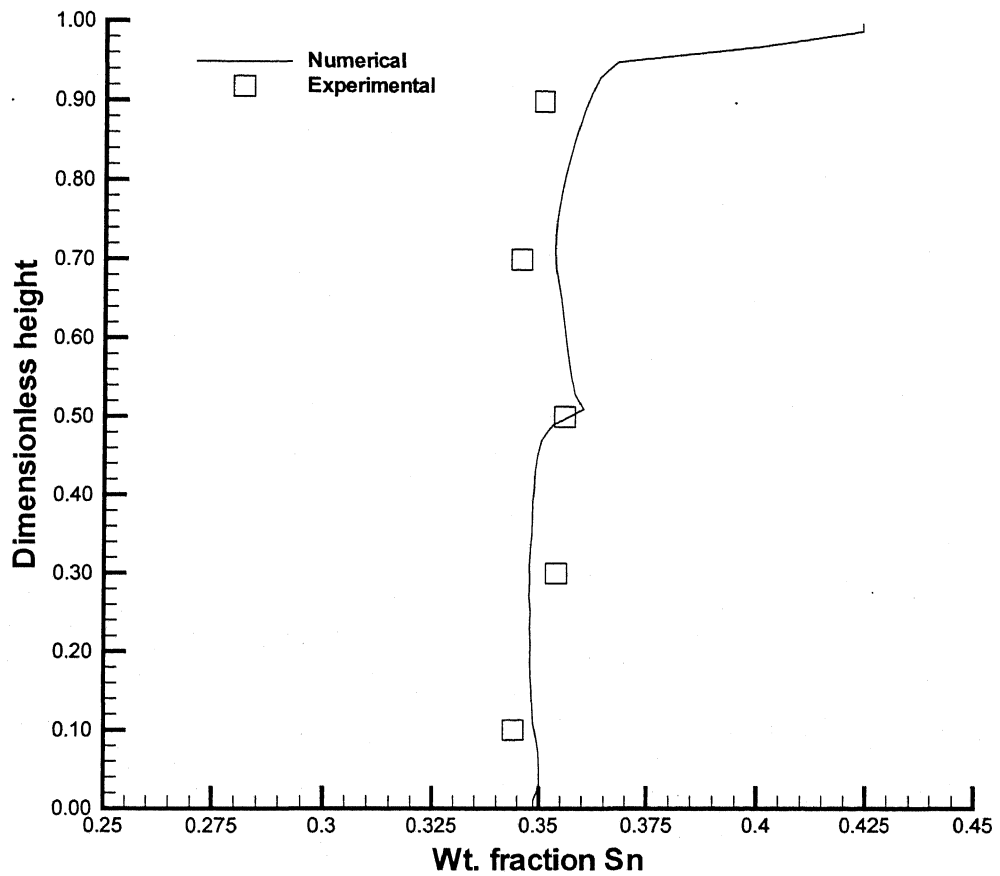


Fig. 6.22: Comparison of experimental and computed average macrosegregation along vertical direction for experiment E1.

6.4.3 Experiment E17 (Slow cooling rate)

Predicted temperature profiles are compared with the experimental data at various locations in Fig. 6.23, showing reasonable match. Fig. 6.24 presents the calculated profiles for E17 at 25% solidification. Streamlines of Fig. 6.24a are characterized by a weak upward flow only near the left boundary. Due to very weak flow, isotherms in Fig. 6.24b show conduction like pattern at all heights. This is due to the presence of mushy region in the entire casting (Fig. 6.24c), which weakens the flow considerably. As opposed to E1, where channel forms at a later instant of time, Fig. 6.24d shows that the channel formation has already taken place in this case.

Fig. 6.25 presents the calculated profiles for this case at 50% solidification. The main features of segregation remain identical to the results at previous times due mainly to absence of flow. Macrosegregation profile at the end of solidification is shown in Fig. 6.26a. The nature of macrosegregation profile is complex largely due to channel. The minimum composition is 32.5 wt % Sn, whereas the maximum segregation is 54.2 wt % Sn. Again, as in case of E1, both maximum and minimum are concentrated over a small region of the segregated channel. Fig. 6.26b shows the variation of secondary dendrite arm spacings in the casting. With higher time of solidification the dendrite arm spacings are comparatively larger than those in E1 and E6. Variation of macrosegregation in the vertical direction is compared with experimental data on macrosegregation in Fig. 6.27.

The above results clearly demonstrate role of cooling rate on evolution of macrosegregation pattern and axial segregation. For low rate of solidification, the long-range segregation is practically absent. Weak flow causes local fluctuations in segregation pattern. However, larger segregation comes through channel formation and supply of solute to the bulk liquid region. It may be noted from these results that segregation evolution is directly linked with top portion of the mush interacting with bulk liquid. Once the casting is covered by mush no further evolution of segregation takes place.

These results are obtained through use of Kozeny-Carman equation with coefficient defined by equation 6.6. In case of horizontal solidification (Ch. 4), it was noted that Kozeny-Carman model over-predicted macrosegregation. As shown by Krane et al. [42], for horizontal solidification, a better match can be obtained with reduction of

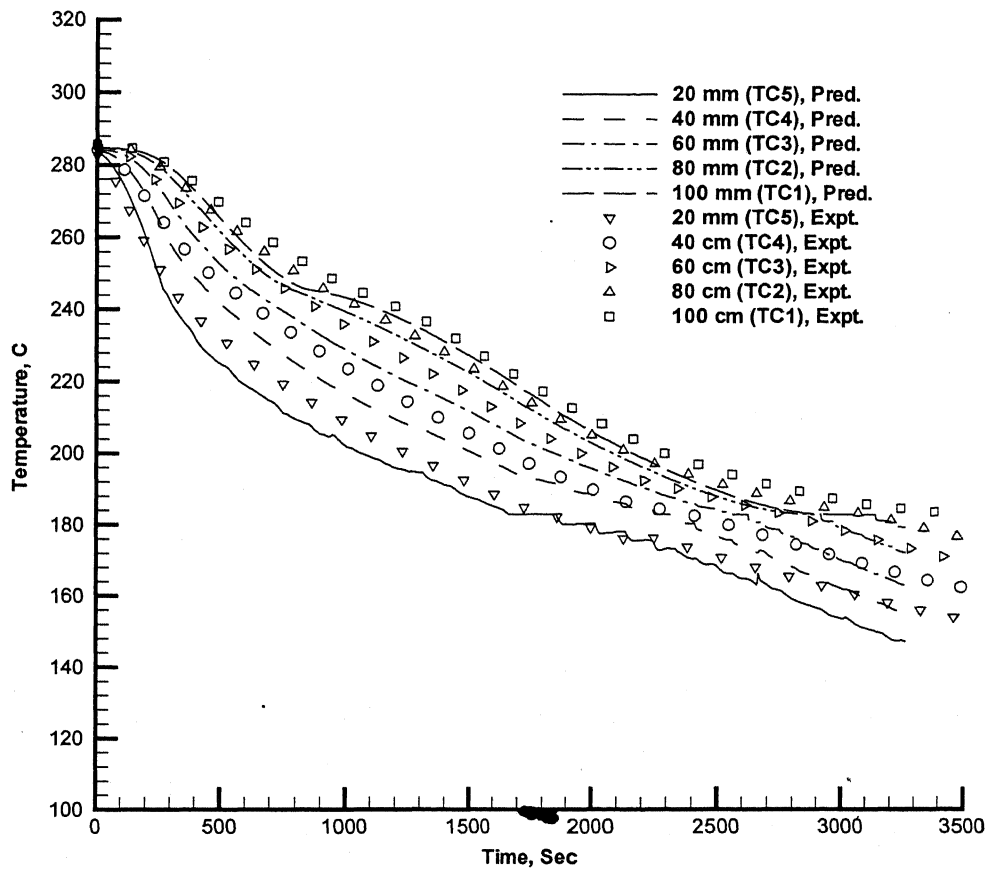


Fig. 6.23: Comparison of predicted temperatures with experimental data for experiment E17.

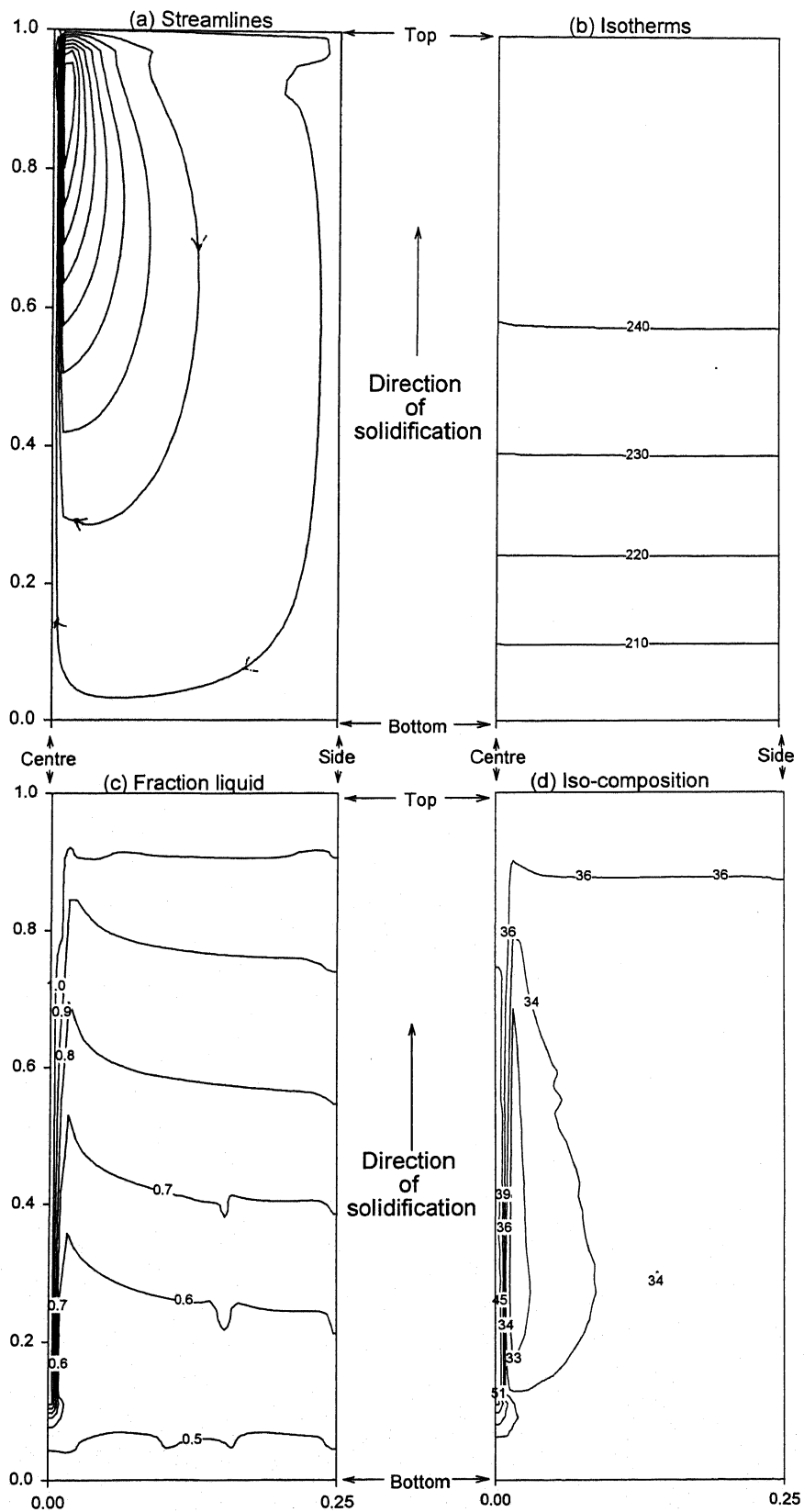


Fig. 6.24: Simulated results for E17 at 25 % solidification (a) Streamlines (ψ_{\min} : -0.195, ψ_{\max} : 0.90, equal increment, (b) isotherms, (c) iso-liquid fraction, and (d) iso-composition profiles.

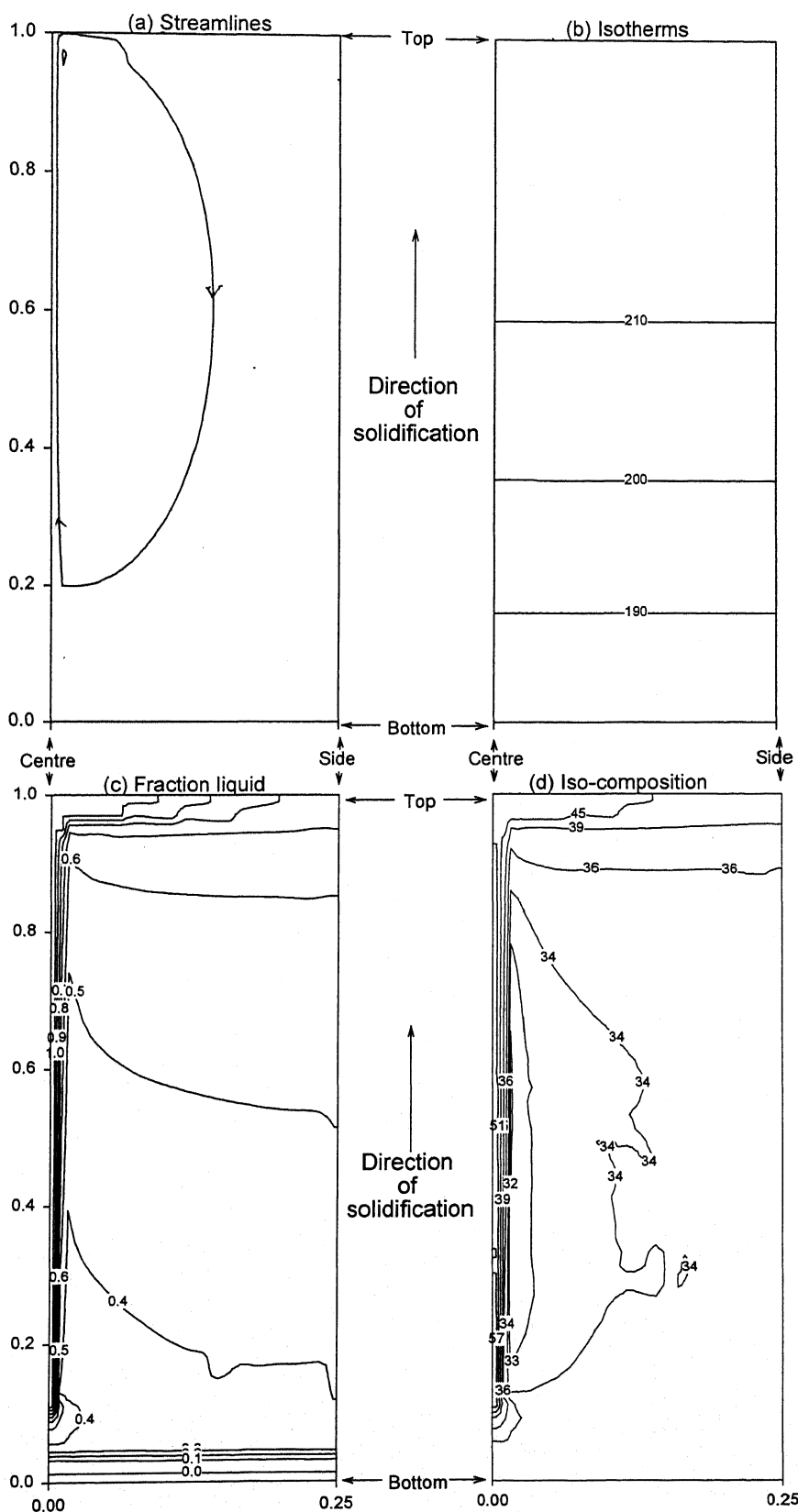


Fig. 6.25: Simulated results for E17 at 50 % solidification (a) Streamlines (ψ_{\min} : -0.027, ψ_{\max} : 0.126, equal increment, (b) isotherms, (c) iso-liquid fraction, and (d) iso-composition profiles.

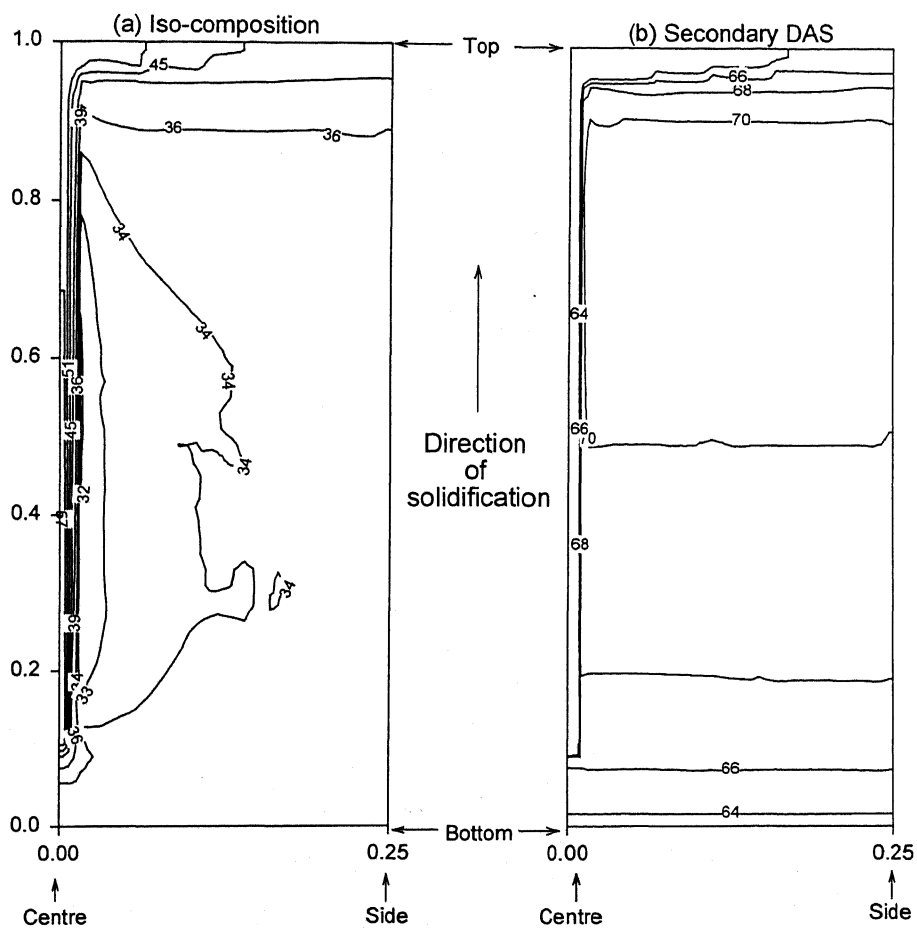


Fig. 6.26: Calculated results for E17 at the end of solidification (a) Final solute distribution (initial composition 35 wt % Sn) and (b) Secondary dendrite arms spacing (μm).

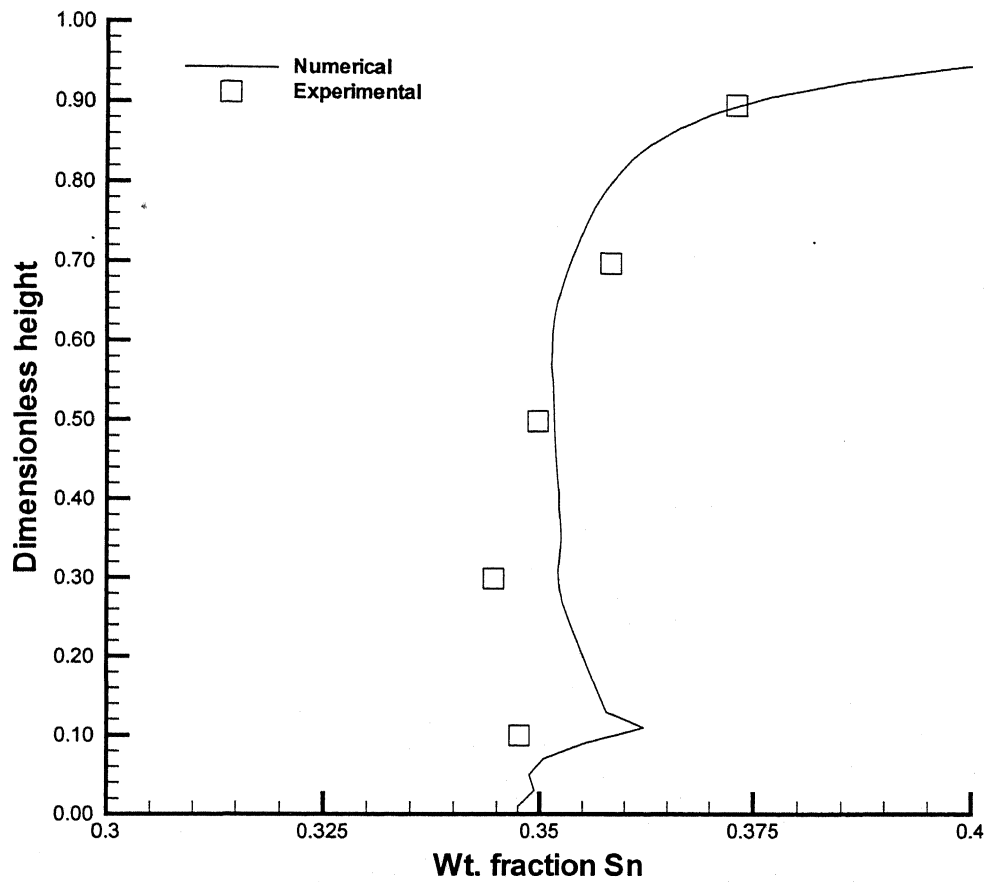


Fig. 6.27: Comparison of experimental and computed average macrosegregation along vertical direction for experiment E17.

permeability coefficient by an order of magnitude. Part of this is due to use of primary dendrite arm spacing. Generalized West model, which uses d_2 provided better match in case of horizontal solidification. However, for vertical solidification, driving force for flow is small. Therefore, use of generalized West model in this case, which predicts comparatively lower permeability above $f_l > 0.8$ than Kozeny-Carman equation[85], results in virtually no segregation. Although for horizontal solidification this difference is less crucial owing to high strength of velocity in the mush, it is of high significance for vertical solidification. A high permeability near the liquidus, as depicted by Kozeny-Carman equation appears crucial in case of vertical solidification.

Macrosegregation profiles in the casting for three cases discussed above, i.e., E1, E6 and E17 are compared in Fig. 6.28. E6, with fastest cooling rate shows minimum segregation whereas E17 with slowest cooling rate shows maximum segregation. The level of segregation for E1 (intermediate cooling rate) falls between these two. Comparisons of predicted and experimental macrosegregation for all other experiments (except tin-rich cases, since no macrosegregation is expected in these cases, and E1, E6 and E17, since these have already been presented in this section), are shown in Figs. 6.29 to 6.40.

6.4.3 Simulation of Sazarin and Hellawell experiment [107]

Sazarin et. al[107] carried out experiments with Pb-Sn alloys at a much slower rate of cooling ($0.00833\text{ }^\circ\text{C/s}$ as opposed to $\sim 0.1\text{ }^\circ\text{C/s}$ in the present experiment). Consequently, the extents of segregation in their experiments were much higher. This case was selected for simulation to test the applicability of model for wide range of cooling rates. The cylindrical experimental cell had a diameter of 37 mm and height of 120 mm. Cooling was carried out from bottom at a fixed rate. Initial gradient in the melt was $1125\text{ }^\circ\text{C/m}$. Three compositions were employed, namely, 5, 10 and 20 wt % Sn. Among these, the maximum segregation was found for case of Pb-20 wt % Sn alloy. This experiment has been simulated in the past by Felicelli et al[114]. However, the actual dimensions, on which simulations were carried out, were reduced in view of coarser grid $[30 \times 20]$ to capture the freckle dynamics comprehensively. In the present simulation, the emphasis is on prediction of axial macrosegregation. Therefore, the present study was carried out on

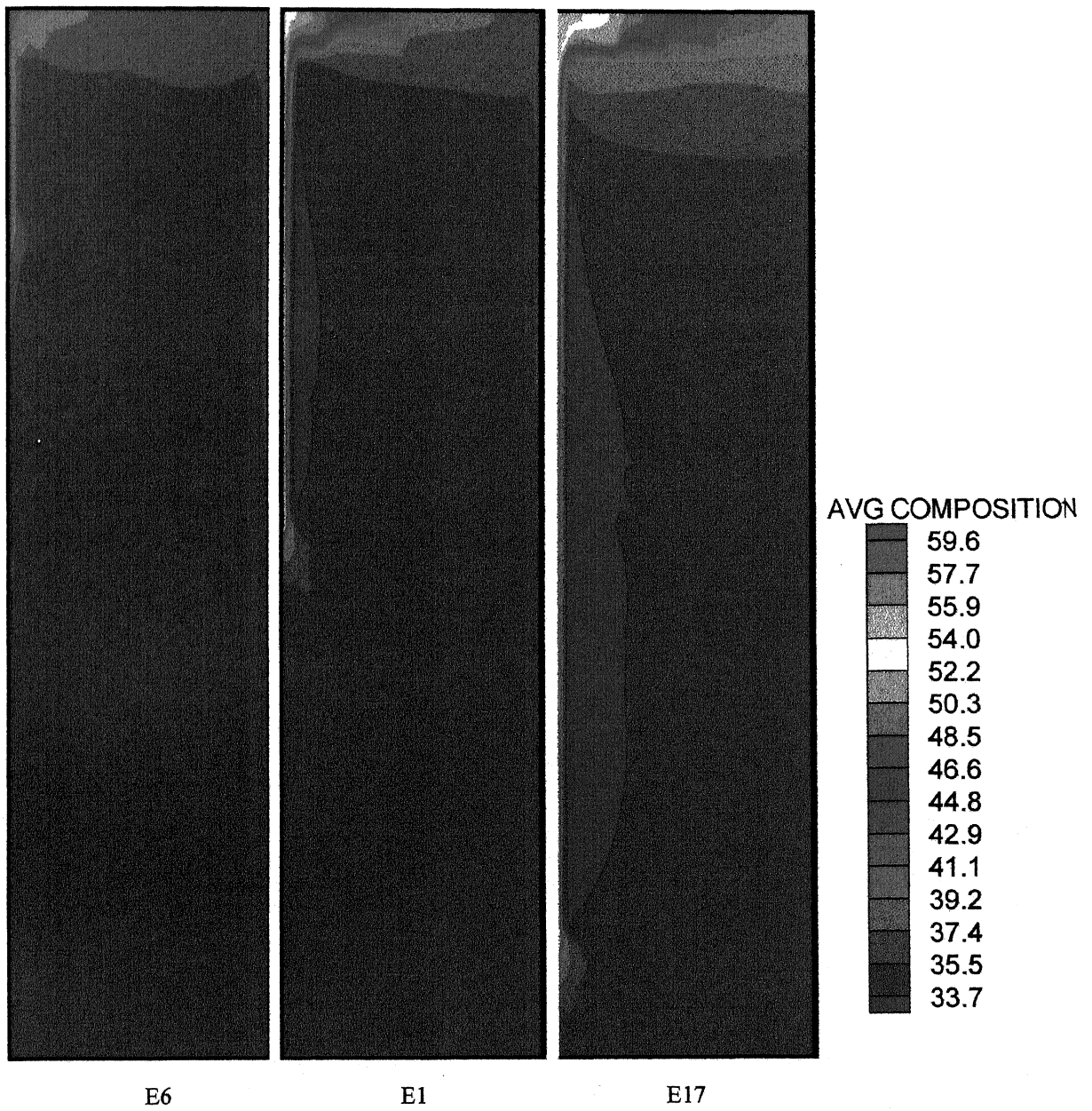


Fig. 6.28: Comparison of final solute distribution for three cases (E6, E1 and E17).

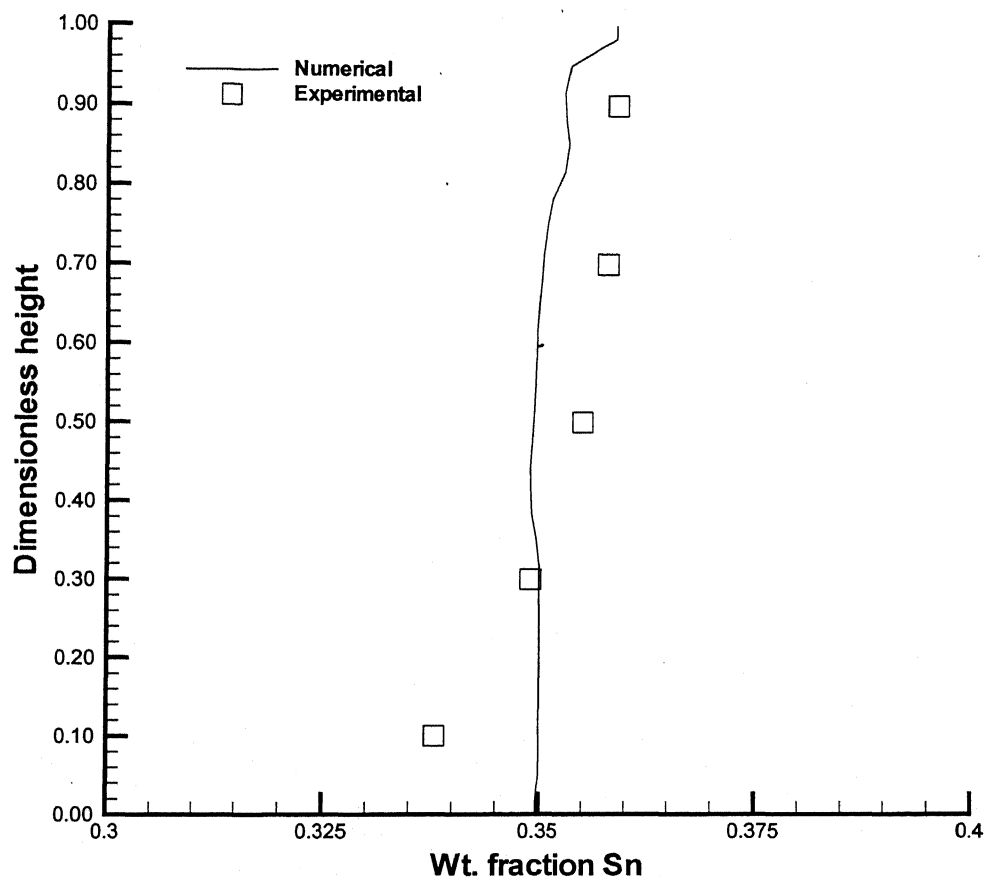


Fig. 6.29: Comparison of experimental and computed average macrosegregation along vertical direction for experiment E2.

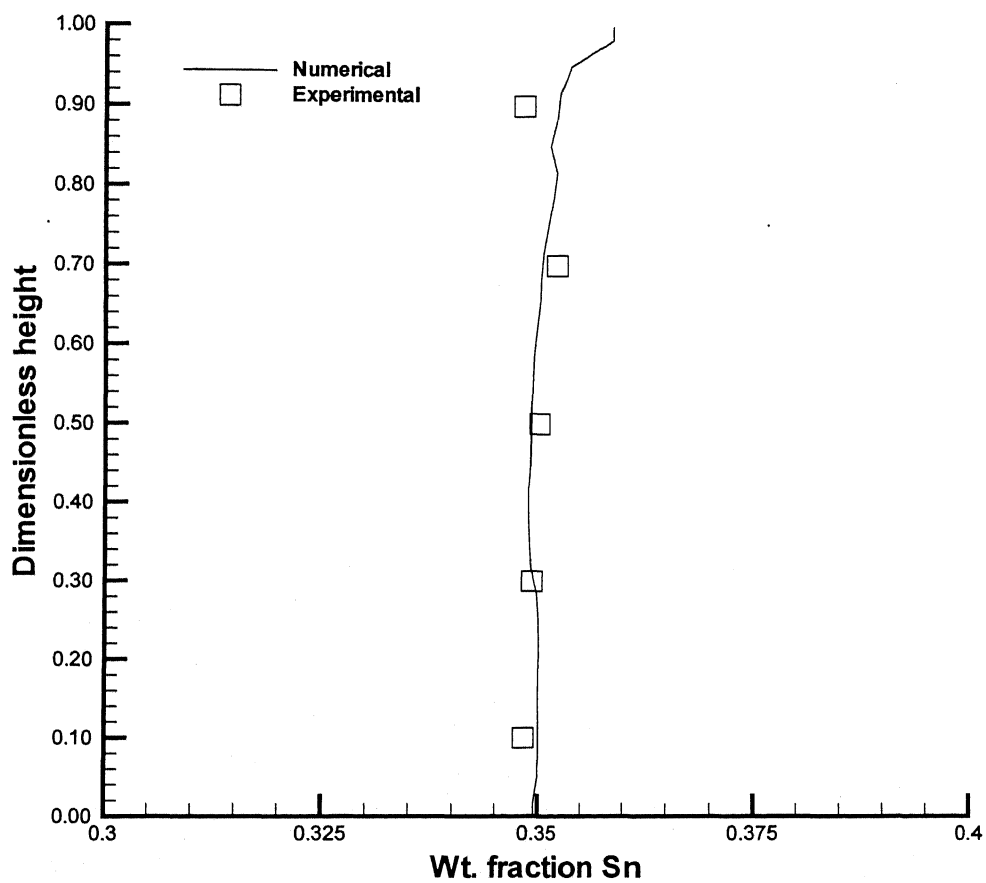


Fig. 6.30: Comparison of experimental and computed average macrosegregation along vertical direction for experiment E3.

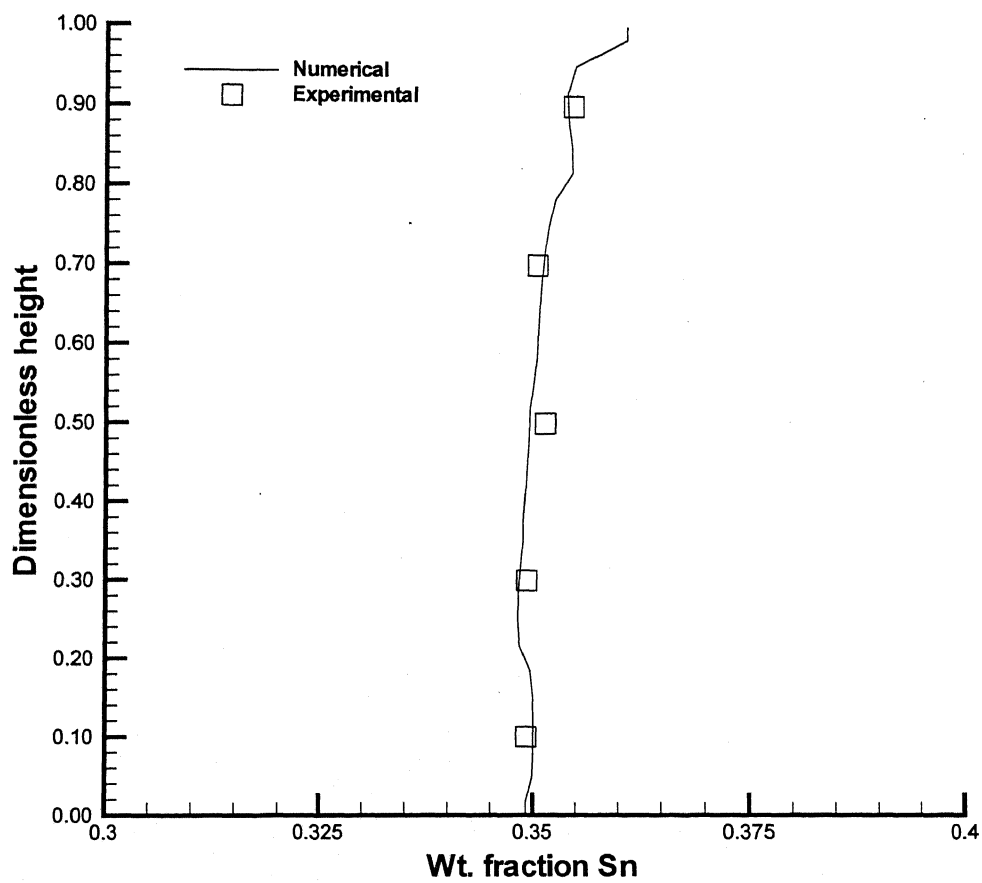


Fig. 6.31: Comparison of experimental and computed average macrosegregation along vertical direction for experiment E4.

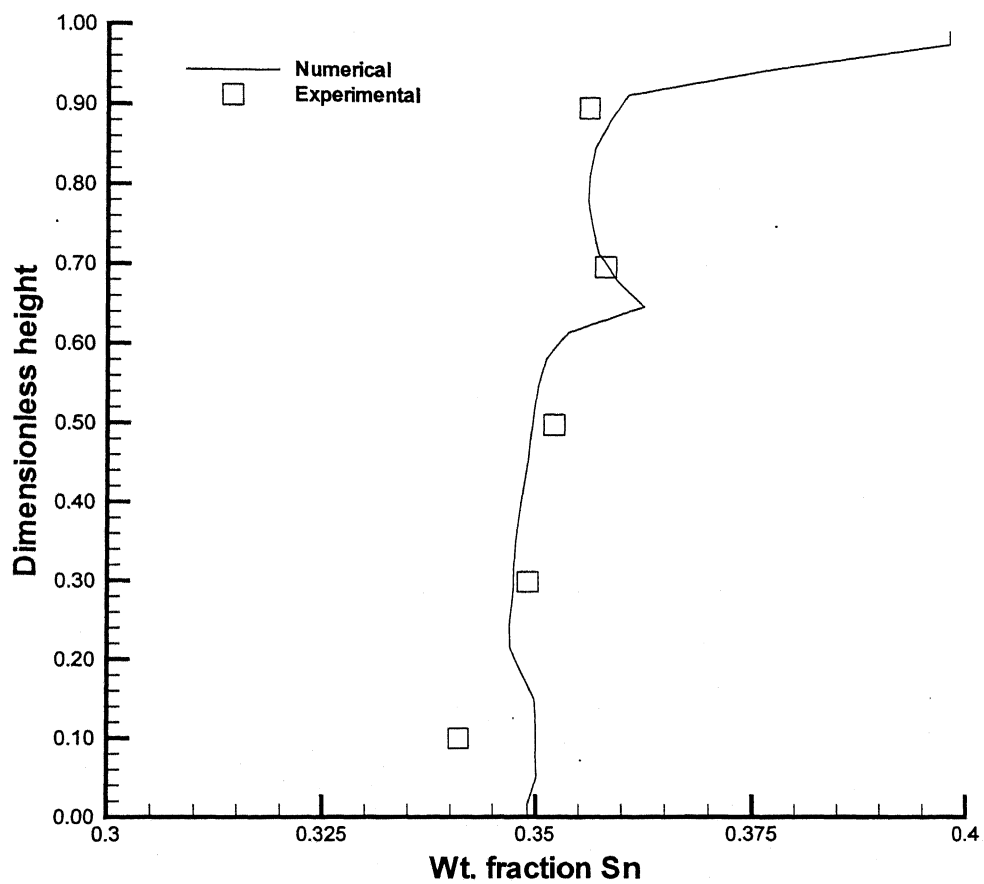


Fig. 6.32: Comparison of experimental and computed average macrosegregation along vertical direction for experiment E5.

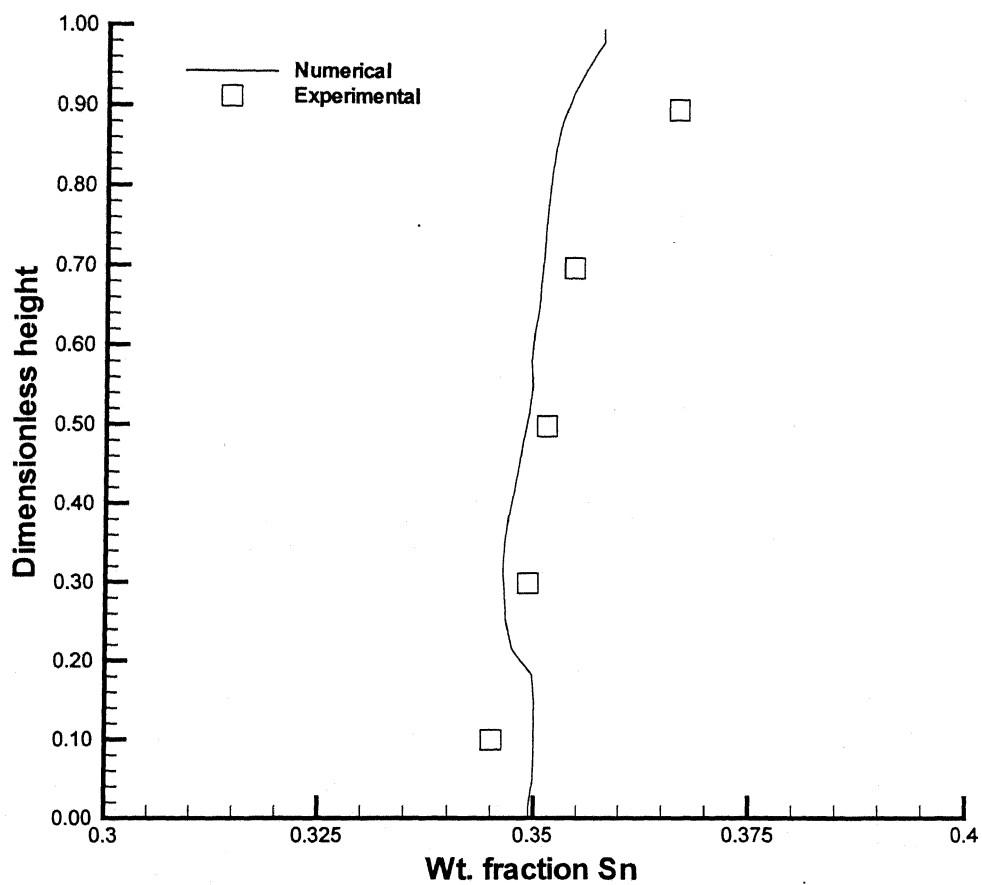


Fig. 6.33: Comparison of experimental and computed average macrosegregation along vertical direction for experiment E15.

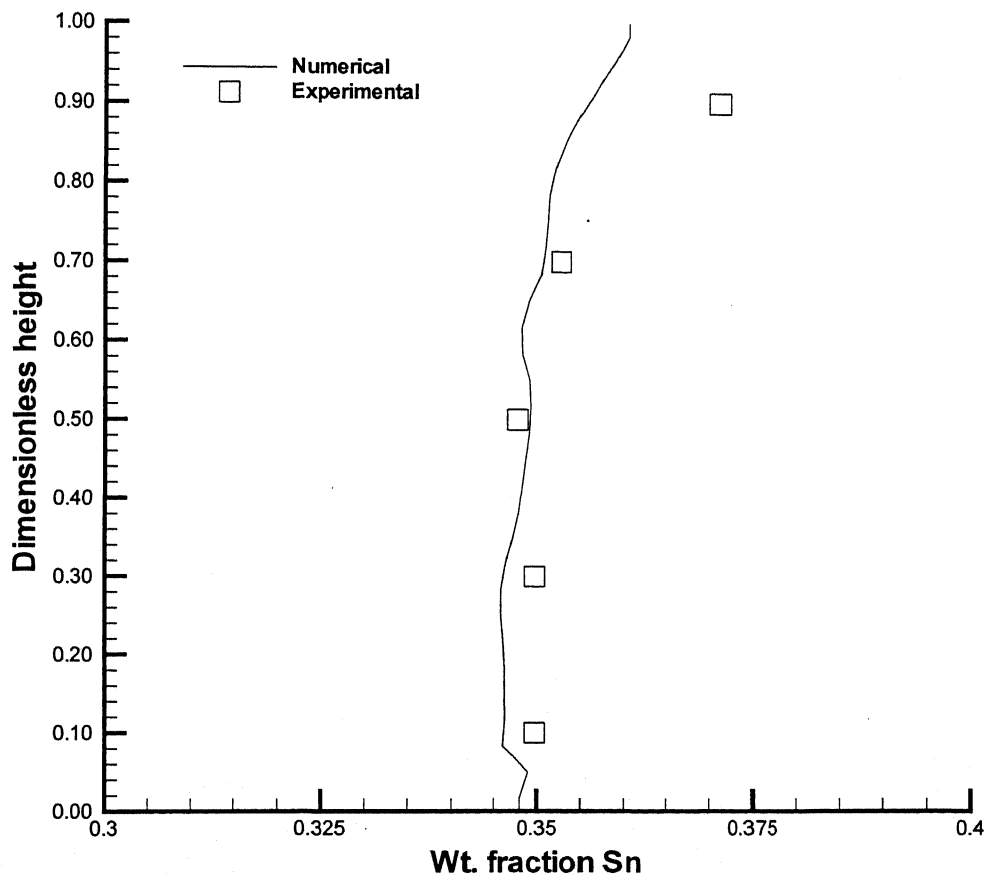


Fig. 6.34: Comparison of experimental and computed average macrosegregation along vertical direction for experiment E16.

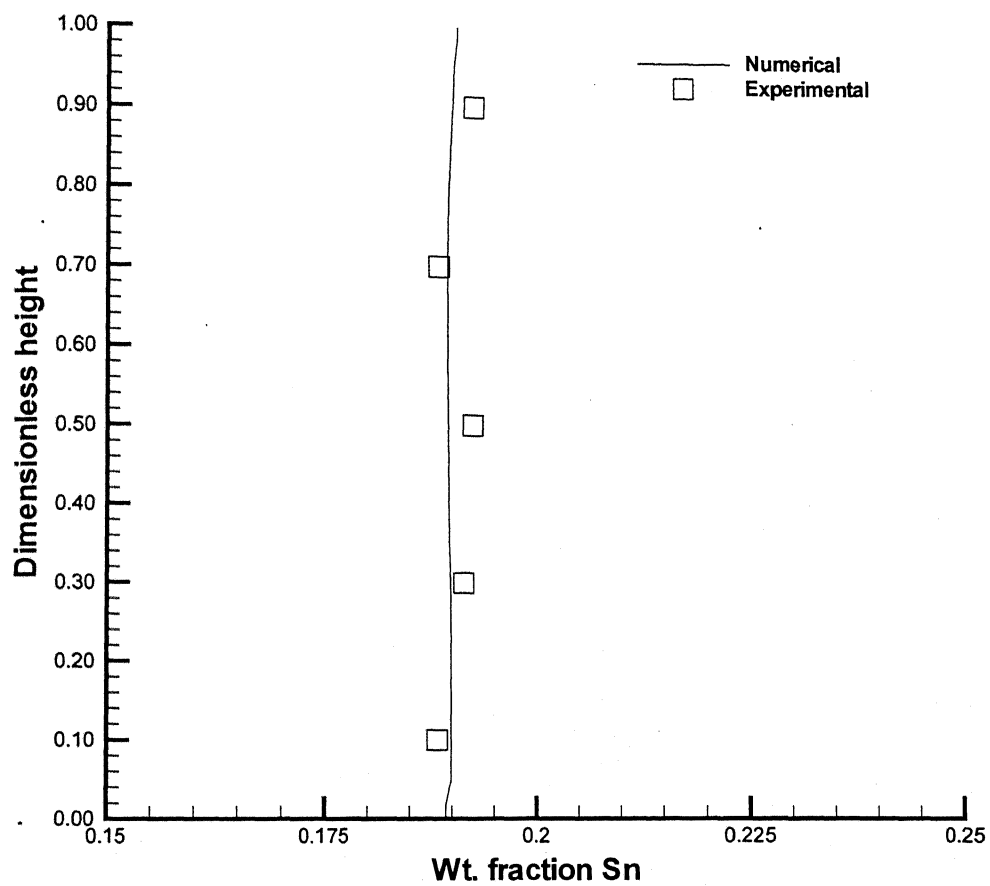


Fig. 6.35: Comparison of experimental and computed average macrosegregation along vertical direction for experiment E7.

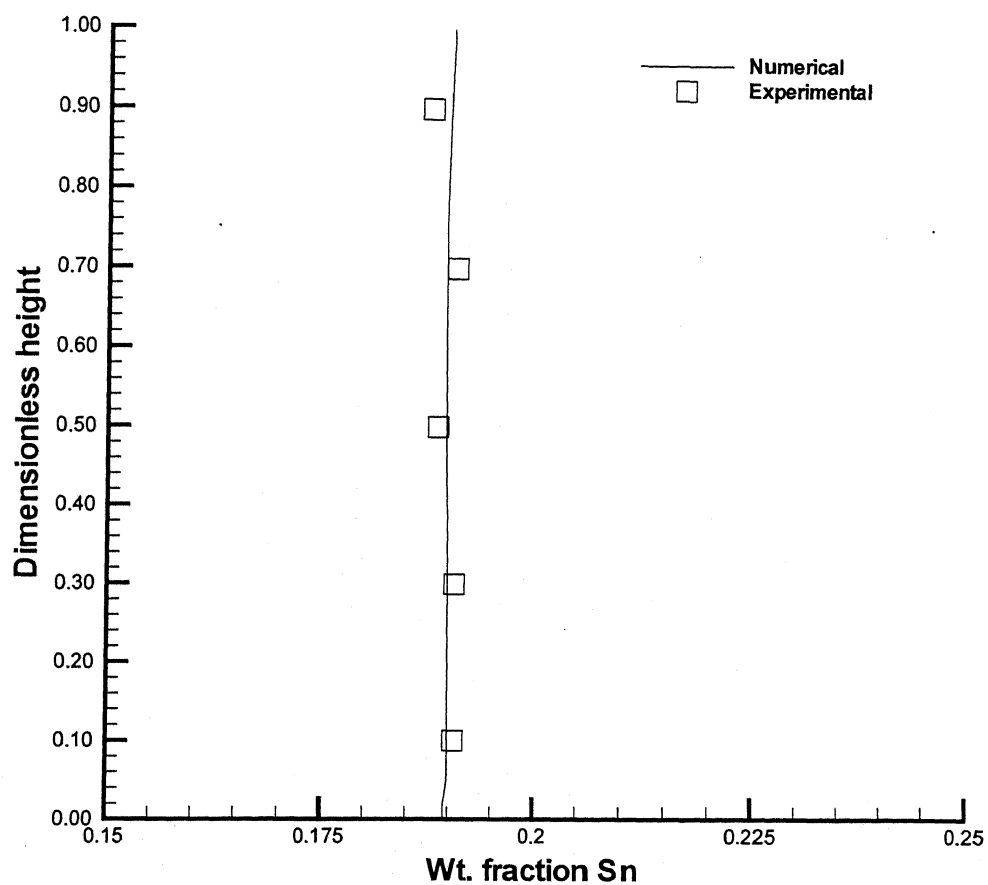


Fig. 6.36: Comparison of experimental and computed average macrosegregation along vertical direction for experiment E8.

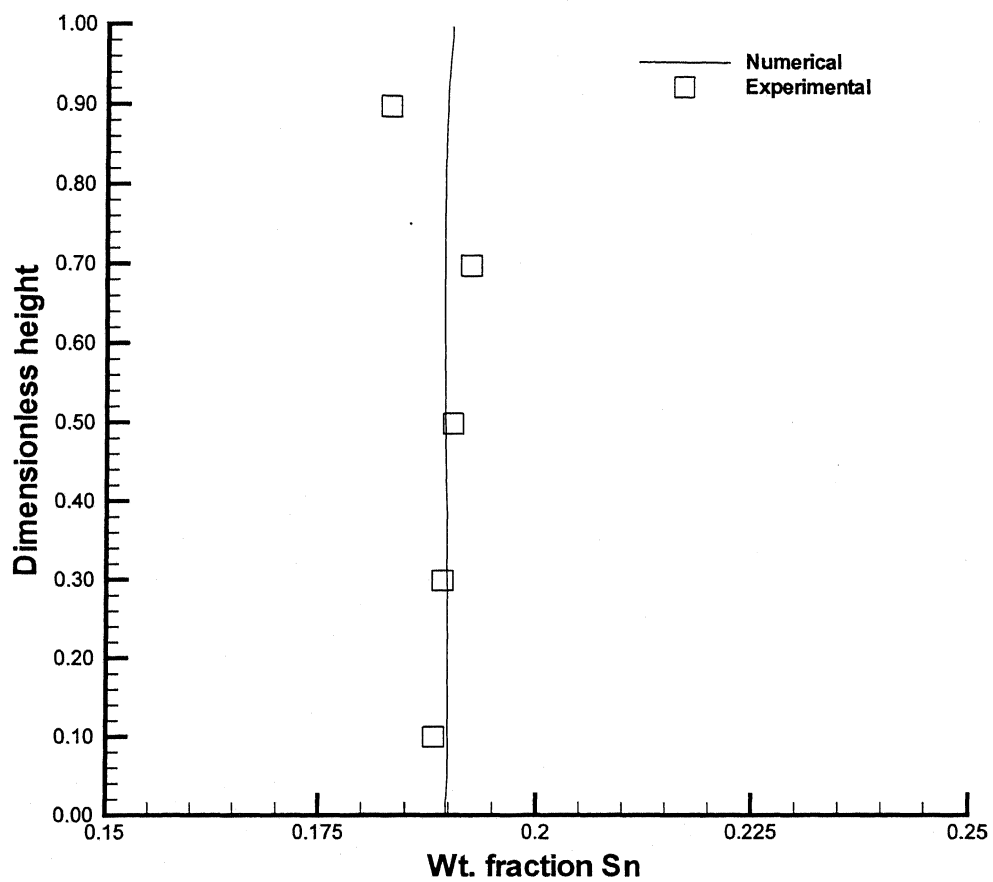


Fig. 6.37: Comparison of experimental and computed average macrosegregation along vertical direction for experiment E9.

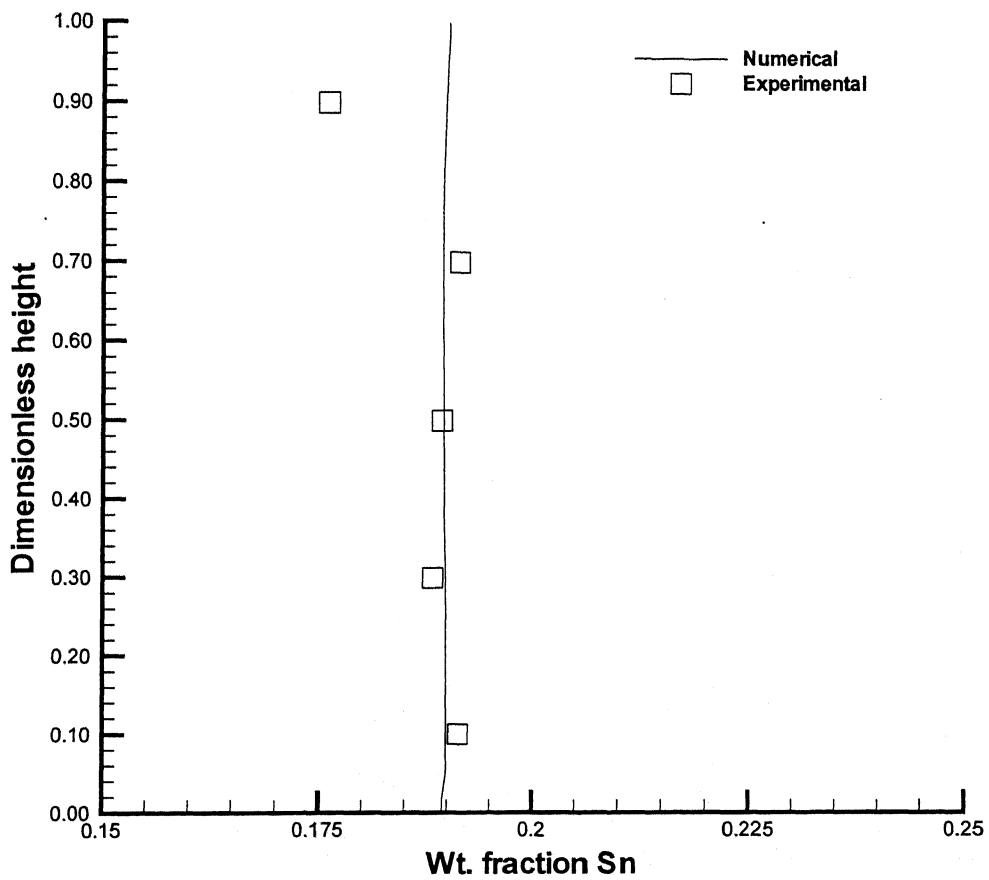


Fig. 6.38: Comparison of experimental and computed average macrosegregation along vertical direction for experiment E10.

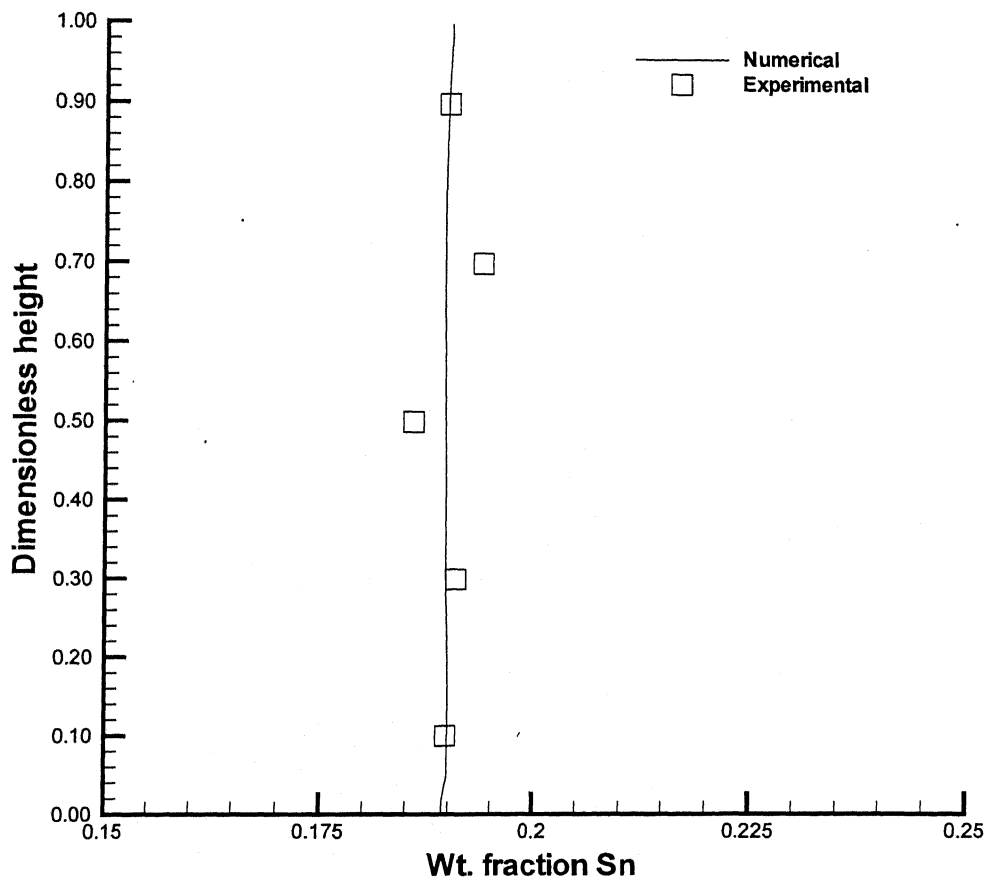


Fig. 6.39: Comparison of experimental and computed average macrosegregation along vertical direction for experiment E18.

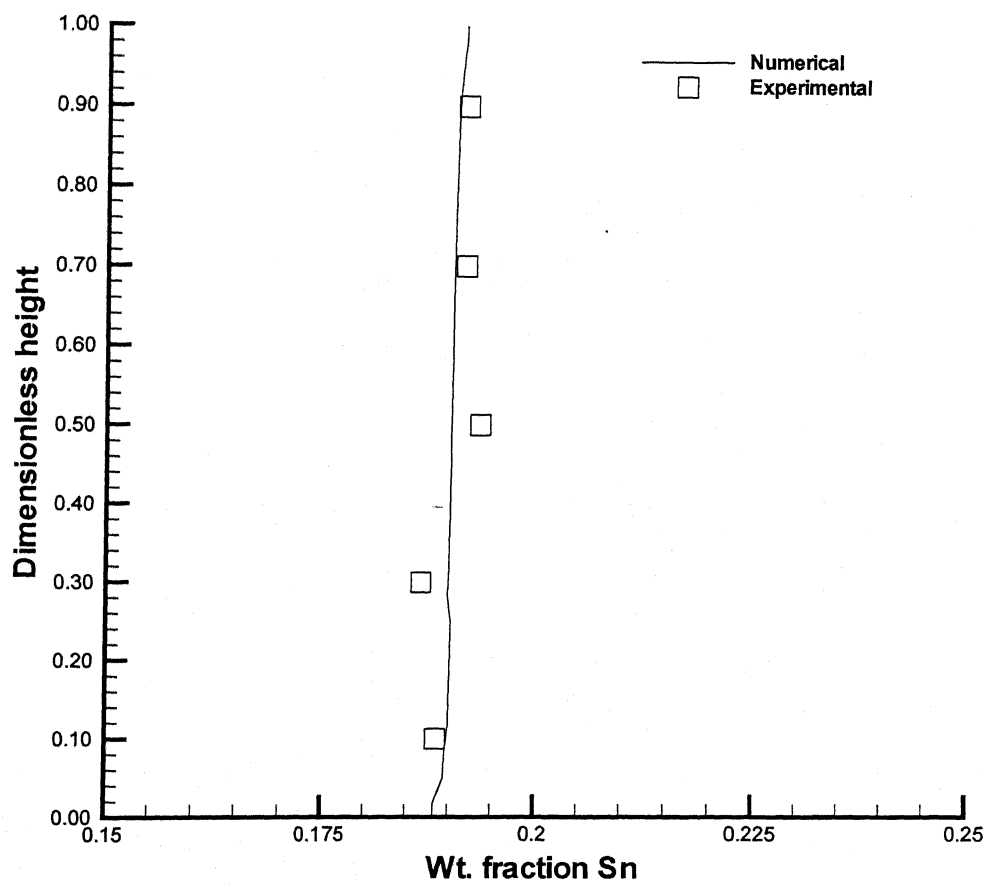


Fig. 6.40: Comparison of experimental and computed average macrosegregation along vertical direction for experiment E19.

on full dimension with actual thermal condition. In view of the large simulation time, a coarse grid [32x22] was employed. Hence, only a qualitative comparison can be carried out.

Numerical simulation was done for with Pb-20 wt % Sn alloy. It is to be noted here that in the present investigation, numerical simulations were carried out for Pb-19 wt % Sn alloy (Experiments E7-E10, E18 and E19) and very little segregation could be observed due to faster rates of solidification. Primary dendrite arm spacings were reported by Sazarin et. al and a value of 350 μm was chosen for the present simulation. The simulations are carried out till the end of solidification.

Fig. 6.41 shows the calculated profiles upon simulation of experimental conditions of Sazarin et al at 25% solidification. Streamlines of Fig. 6.41a exhibit a weak flow at the top of the cavity. Freckle is seen at the outer surface in this case (Fig. 6.41c and 6.41d). At 50 % solidification, the flow is practically absent as the mould is fully covered with mushy region (Fig. 6.42). As flow is absent at 50 % solidification, the macrosegregation profile at the end of solidification is very similar to that of Fig. 6.41d. The computed axial macrosegregation is compared with experimental data in Fig. 6.43. It is evident that qualitatively the model predicts the trend well.

Therefore, on the basis of above discussions, it is concluded that the model is applicable to a wide range of cooling rates and is capable of predicting the essential features of macrosegregation in vertical direction for bottom cooled melts of similar nature. It was tested on Pb-rich Pb-Sn alloys. It is desirable to test it further in other alloy systems.

6.5 Conclusions

- (i) Results of experiments on vertical solidification have been reported in this section. Using these experimental data, few parameters have been extracted for direct application in the mathematical model.
- (ii) The model was employed to simulate the experiments. Evolution of flow and its effect on other variables, namely, temperature, composition and mush profile has been studied for various experiments. Use of generalized West correlation as permeability model showed no segregation. Modified Kozeny-Carman equation provided satisfactory result.

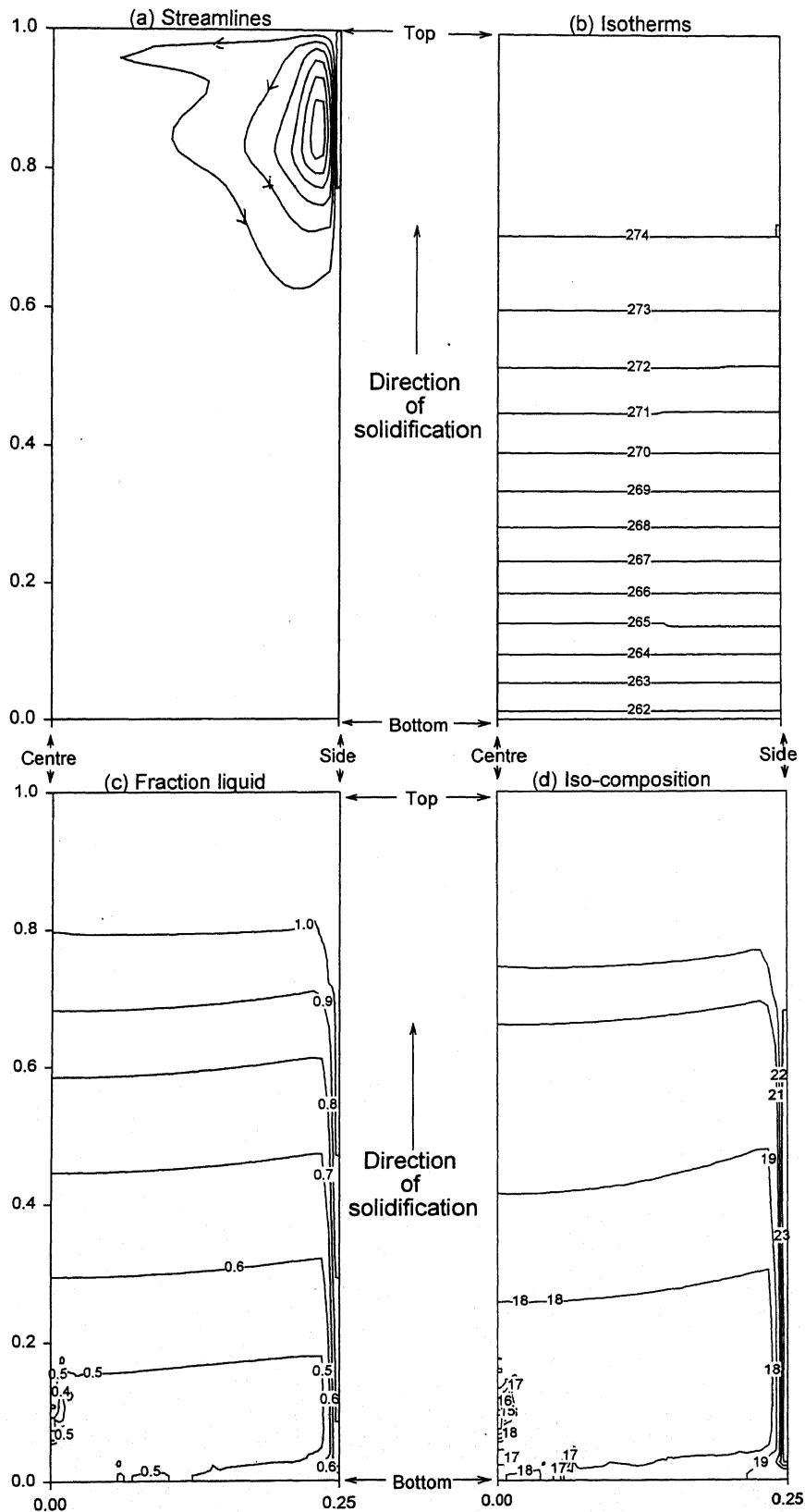


Fig. 6.41: Simulated results for experiments of Sazarin, et al [107] at 25 % solidification (a) Streamlines (ψ_{\min} : -0.132, ψ_{\max} : 1.3×10^{-3} , equal increment), (b) isotherms, (c) iso-liquid fraction, and (d) iso-composition profiles.

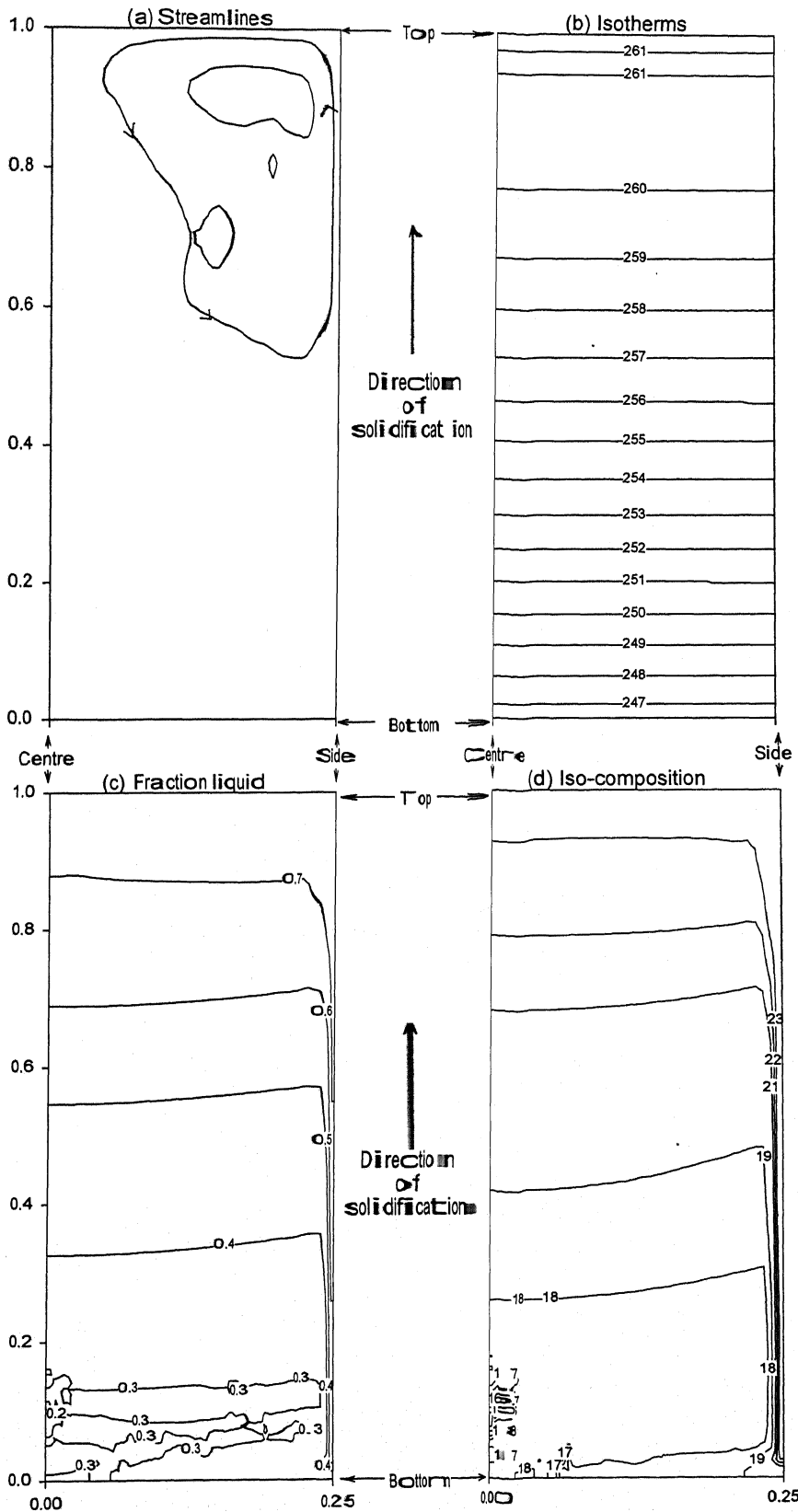


Fig. 6.42: Simulated results for experiments of Sazarin, et al [107] at 50 % solidification (a) Streamlines ($\psi_{\min} = -2.3 \times 10^{-7}$, $\psi_{\max} = 1.8 \times 10^{-6}$, equal increment), (b) isotherms, (c) iso-liquid fraction, and (d) iso-composition profiles.

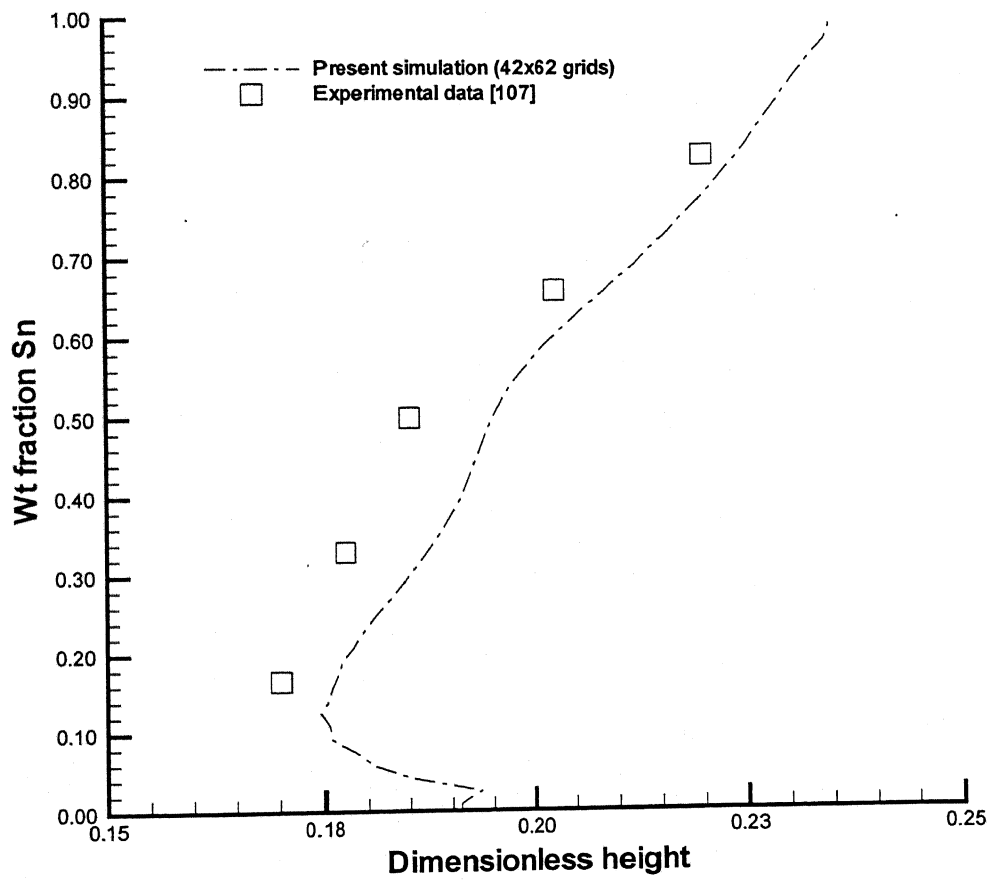


Fig. 6.43: Comparison of experimental and computed average macrosegregation along the vertical direction for experiment of Sazarin et al [107].

- (iii) The role of permeability near the mush/liquid interface was identified as the crucial parameter in determining the evolution of macrosegregation during vertical solidification. This factor was not so apparent in case of horizontal solidification due to high strength of velocity and unconditionally unstable thermal field.
- (iv) As the cooling rate was lowered, the tendency of solutal buoyancy driven convection and resulting in macrosegregation increase. At intermediate rate of cooling, the solutal buoyancy makes the flow field unstable. Though the flow strength decreases for very low rate of solidification, it also allows sufficient time for macrosegregation to evolve.

Chapter 7

SUMMARY AND CONCLUSIONS

The investigation reported here was concerned with influence of thermosolutal convection on macrosegregation during solidification of binary alloys. The review of past literature revealed that uncertainty in permeability functions of mush was one of the main reasons for quantitative mismatch between numerical predictions and experimental data on macrosegregation. Other than permeability, thermophysical properties of material and cooling rate seemed to have major influence on macrosegregation. Experimental data were limited, and these were generally not complete in all respects for usage in mathematical models. In the present investigation, a combined modeling and experimental approach was taken to focus on these issues, and to throw further light on understanding of evolution of macrosegregation during solidification.

A model based on continuum formulation was developed in two dimensional rectangular and cylindrical co-ordinate systems. The governing equations for the model were for conservation of mass, momentum, energy and species. The following auxiliary relationships were used in the model:

- (i) Darcy Law for representation of flow through the mushy region,
- (ii) Boussinesq approximation to account for thermosolutal buoyancy, and
- (iii) Lever rule to account for the relation between temperature, composition and fraction liquid, f_l , in the mushy region.

The model was rigorously validated with numerical and experimental results cited in literature.

Using the mathematical model, computer simulations were performed to study the influence of:

- (i) material properties,
- (ii) choice of permeability function for mushy region, and
- (iii) cooling rate on evolution of thermosolutal convection and consequent macrosegregation during horizontal solidification of binary alloys.

To show the role of material, three alloy systems, namely, Pb-Sn alloy, Fe-C alloy and $\text{NH}_4\text{Cl-H}_2\text{O}$ system, all with lighter solute, were chosen in present study. Initial

conditions were set through considerations of superheat and mushy zone length. Boundary conditions for simulations were arrived at through considerations of equality in rate of solidification. Difference in stability number (N), which is a function of the coefficient of solutal buoyancy to the coefficient of thermal buoyancy, appeared to govern the evolution of thermosolutal convection and subsequent macrosegregation. It was shown that the differences in material properties led to entirely different thermosolutal convection and macrosegregation pattern. Thus, it was concluded that extrapolation of results from one material to other needs to be done with utmost care.

To show the inadequacies of various permeability functions, experimental data on solidification of Pb-Sn alloy, reported in literature, was utilized. The reason for discrepancy has been attributed in the past to inadequacy of permeability function in thin mushy region. To address this, West's correlation [89] for thin mushy region ($f_l > 0.5$) was selected and generalized in terms of secondary dendrite arm spacing (Eq. 4.14, Ch.4). For low liquid fraction, Kozeny-Carman equation, with modified coefficient (Eq. 4.13, Ch.4) was used. The resultant function was tested with limited experimental data on permeability on Pb-Sn alloy [90]. Using this permeability function in the model, the experiment reported in literature [42] was simulated. Predicted macrosegregation profiles were compared with experimental data, which were reported at four different planes of the casting. There were reasonable matches for two planes, whereas the matches for two other planes were poor. It was concluded from this study that selection of better function for thin mushy region and use of secondary dendrite arm spacing in it resulted in better correspondence between predicted and experimental values of macrosegregation. It was also concluded that further research was needed in this area.

The effect of cooling rate on macrosegregation was investigated for solidification of Fe-1 wt % C alloy. Variation of global extent of segregation with variation of heat flux from 5 to 6000 kW/m² was studied. Factors controlling extent of segregation at various cooling rates were identified. It was shown how thermal and solutal buoyancy forces control the extent of segregation at various rates of cooling and the variation in global extent of segregation with cooling rate was explained.

In the experimental part of the work, the apparatus was designed and fabricated in the laboratory. The setup and experimental procedure were finalized through a series of

trials. Molten lead-tin alloy, contained in a cylindrical mould, was subjected to unidirectional solidification vertically downward by water cooling from the bottom. Experiments were conducted on Pb-19 wt % Sn, Pb-35 wt % Sn, and Sn-15 wt % Pb alloys. For each alloy, experiments were carried out for two superheats and at least two different cooling rates. The data from the experiments were obtained in terms of temperature-time curves, macrosegregation and microstructural details in terms of primary and secondary dendrite arm spacing. The data from the experiments were analyzed to obtain heat transfer coefficients. Experimental data on primary and secondary dendrite arm spacings were used to fine-tune microstructural modules of the model.

The mathematical model was then used to analyze evolution of thermosolutal convection, isotherms, liquid fraction profiles and macrosegregation profiles during vertical solidification of lead-rich binary lead-tin alloys for conditions of experiments of present investigation. It was shown that the evolution of segregation in vertical solidification was very sensitive to the nature of permeability function near mush/liquid interface. Generalized West permeability function (Eq. 4.14, Ch. 4), which differs with Kozeny-Carman equation (with modified coefficient, Eq. 4.13, Ch. 4) near mush/liquid interface only, appeared to suppress the flow and consequent macrosegregation. Permeability function was further modified near mush/liquid interface to account for the observed level of segregation. It was observed that the flow field did not show significant effect on thermal field but it affected macrosegregation substantially.

The model was also used to simulate an experiment cited in literature for extremely slow solidification condition (solidification time for this case was 8 hours as opposed to 0.5-1 hours in experiments of present investigation). A reasonable prediction of macrosegregation profile for this case as well demonstrated the capability of the mathematical model to simulate solidification processes with variety of cooling rates.

In this work, a new procedure was established where by large number of experimental inputs were incorporated into the model.

- Temperature profiles of the melt prior to initiation of cooling was used as initial condition for the model.
- Boundary heat fluxes were derived from experimental temperature-time curves in chill block.

- Microstructural module of the model was fine-tuned based on the data of dendrite arm spacing from post solidification analysis.
- Using the model in conduction mode average dendrite arms spacing for usage in permeability model was obtained.
- Finally, experimental data on macrosegregation were used for validation of the mathematical model.

The following are the major finding of this work:

- The critical role of stability number (N) on evolution of double-diffusive convection and consequent macrosegregation was demonstrated through a comparative study of solidification of Fe-C, Pb-Sn and $\text{NH}_4\text{Cl-H}_2\text{O}$ system.
- Factors controlling the extent of segregation at various cooling rates were identified. Using the proposed mechanism the variation in extent of segregation for wide range of cooling rates was explained.
- A modified permeability model was proposed. Its suitability to explain segregation in horizontal solidification was demonstrated.
- It was shown that the permeability model required further modification to explain experimental observation on macrosegregation during vertical solidification. The role of permeability near the mush/liquid interface was considered crucial in determining the evolution of macrosegregation during vertical solidification. This factor was not so apparent in case of horizontal solidification due to higher convection and unstably stratified liquid.

Chapter 8

SUGGESTIONS FOR FURTHER WORK

Modeling of macrosegregation has received considerable attention recently and focus has now shifted to quantitative prediction of macrosegregation in variety of manufacturing processes involving solidification of alloys. The following areas of research will prove helpful in this direction.

- (1) Controlled experiments for generation of data under variety of solidification conditions for rigorous validation of mathematical model.
- (2) Comprehensive treatment of multi-component solidification as the industrial solidification is mostly with multi-component alloys.
- (3) Comprehensive treatment of turbulence in mathematical model to enable better quantitative prediction of macrosegregation in castings with larger dimensions.
- (4) Experiments to improve permeability model near mush/liquid interface and high liquid fraction regime of mushy region.
- (5) Rigorous treatment of columnar-to-equiaxed transition for better prediction of macrosegregation in cases where transition is encountered.

Bibliography

- 1) B. Chalmers, *Principles of Solidification*, John Wiley & Sons Inc., 1964.
- 2) M. C. Flemings, *Solidification Processing*, McGraw-Hill, 1974.
- 3) W. Kurz and D. J. Fisher, *Fundamentals of Solidification*, Trans. Tech. Publications, 1992.
- 4) A. Ghosh, *Principles of Secondary Processing and Casting of Liquid Steel*, Oxford and IBH Publishing Co. Pvt. Ltd., 1989.
- 5) B. Basu (ed.), *Advances in Solidification Processing*, Academy Proc. in Engg. Sc., SADHANA, **26**, 2001.
- 6) B. K. Dhindaw, B. S. Murthy and S. Sen (eds.), *International Conference on Solidification Science and Processing: Outlook for 21st Century*, Oxford and IBH Publishing Co., New Delhi, 2001.
- 7) P. R. Sahm, P. N. Hansen and J. G. Gonley (eds.), *Modeling of Casting, Welding and Advanced Solidification Processes-IX*, Shaker Verlag GmbH, Aachen, 2001.
- 8) H. M. Pielet, Thesis, MIT, 1971.
- 9) E. Scheil, *Z. Metallkunde*, **34** (1942), 70.
- 10) H. D. Brody and M. C. Flemings: *Trans. TMS-AIME*, **236** (1966), 615.
- 11) J. A. Burton, R. C. Prim, W. P. Splichter: *J. Chem. Phys*, **21** (1953), 1987.
- 12) S. C. Flood and J. C. Hunt: *Metals Handbook*, ASM International, 1988, 130.
- 13) M. Rappaz, *Int. Mater. Rev.*, **34** (1989), 93.
- 14) R. Trivedi and W. Kurz, *Int. Mater. Rev.*, **39** (1994), 49.
- 15) G. Phanikumar and K. Chattopadhyaya, *Sadhana*, **26** (2001), 25.
- 16) W. J. Boettinger, S. R. Coriell, A. L. Greer, A. Karma, W. Kurz, M. Rappaz and R. Trivedi, *Acta Mater.*, **48** (2000), 43.
- 17) J. A. Sekhar, *Acta Mater.*, 2002 (In press).
- 18) A. Ghosh, *Sadhana*, **26** (2001), 5.
- 19) M. G. Worster, *Ann. Rev. Fluid Mech.*, **29** (1997), 91.
- 20) B. Basu and A. W. Date, *Sadhana*, **13** (1988), 169.
- 21) C. Beckermann and R. Viskanta, *Appl. Mech. Rev.*, 1993, **46**, 1.
- 22) B. Basu and A. W. Date, *Int. J. Heat Mass Transfer*, **33** (1990), 1149.
- 23) B. Basu and A. W. Date, *Int. J. Heat Mass Transfer*, **33** (1990), 1165.

- 24) B. Basu and A. W. Date, *Int. J. Heat Mass Transfer*, **35** (1992), 1049.
- 25) B. Basu and A. W. Date, *Int. J. Heat Mass Transfer*, **35** (1992), 1059.
- 26) B. Basu, J. A. Sekhar, R. J. Schaefer and R. Mehrabian, *Acta Metall. Mater.*, **39** (1991), 725.
- 27) J. P. Gu and C. Beckermann, *Metall. Mater. Trans. A*, **30A** (1999), 1357.
- 28) H. Lin, *International Conference on Solidification Science and Processing: Outlook for 21st Century*, ed. B. K. Dhindaw, B. S. Murthy and S. Sen, Oxford and IBH Publishing Co., New Delhi, 2001, 171.
- 29) B. Li and Y. Ruan, *J. Thermal Stresses*, **18** (1995), 359.
- 30) M. R. R. I. Shamsi and S. P. Mehrotra, *Metall. Trans B*, **24B** (1993), 521.
- 31) W.-S. Kim, D.-S. Kim, and A.V. Kuznetsov, *Int. J. Heat Mass Transfer*, **43** (2000), 3811.
- 32) A.V. Kuznetsov, *Int. J. Heat Mass Transfer*, **40** (1997), 2949.
- 33) B. Basu, S. Enger, M. Breuer and F. Drust, *J. Crystal Growth*, **219** (2000), 123.
- 34) B. Basu, S. Enger, M. Breuer and F. Drust, *J. Crystal Growth*, **230** (2001), 148.
- 35) H. Zhang, V. Prasad and M. K. Moallemi, *Numer. Heat Transfer*, **29** (1996), 399.
- 36) B. Minaie, K. A. Stelson, V. R. Voller, *ASME J. Engg. Mater. Tech.*, **113** (1991), 296.
- 37) C. Beckermann and C. Y. Wang, *Ann. Rev. Heat Transfer*, **6** (1995) 115.
- 38) P. J. Prescott and F. P. Incropera: *Adv. Heat Transfer*, **28** (1996), 231.
- 39) H. Combeau, B. Appolaire and G. Lesoult, *Modeling of Casting Welding and Advanced Solidification Processes-VII*, Ed. B. G. Thomas and C. Beckermann, 1998, 245.
- 40) M. C. Flemings, *Iron Steel Inst. Jpn. Int.*, **40** (2000), 833.
- 41) C. Beckermann and R. Viskanta, *PCH Physicochem. Hydrodynamics*, **10** (1988), 195.
- 42) M. J. M. Krane and F. P. Incropera, *ASME J. of Heat Transfer*, **119** (1997), 783.
- 43) M. C. Flemings and G. E. Nereo, *Trans. TMS-AIME*, **239** (1967), 1449.
- 44) M. C. Flemings, R. Mehrabian and G. E. Nereo, *Trans. TMS-AIME*, **242** (1968), 41.
- 45) M. C. Flemings and G. E. Nereo, *Trans. TMS-AIME*, **242** (1968), 50.

- 46) R. Mehrabian, M. Keane and M. C. Flemings, *Metall. Trans.*, **1** (1970), 1209.
- 47) J. Szekely and A. S. Jassal, *Metall. Trans. B*, **9B** (1978), 389.
- 48) W. D. Bennon and F. P. Incropera, *Int. J. Heat Mass Transfer*, **30** (1987), 2161.
- 49) W. D. Bennon and F. P. Incropera, *Int. J. Heat Mass Transfer*, **30** (1987), 2171.
- 50) V. R. Voller, A. D. Brent, and C. Prakash, *Int. J. Heat Mass Transfer*, **32** (1989), 1719.
- 51) Q. Z. Diao and H. L. Tsai, *Metall. Trans. A*, **24A** (1993), 963.
- 52) M. Rappaz and V. Voller, *Metall. Trans. A*, **21A** (1990), 740.
- 53) S. Ganesan and D. R. Poirier, *Metall. Trans. B*, **21B** (1990), 173.
- 54) D. R. Poirier, P. J. Nandapurkar and S. Ganesan, *Metall. Trans. B*, **22B** (1991), 889.
- 55) S. Chang and D. M. Stefanescu, *Metall. Trans. A*, **27A** (1996), 2708.
- 56) B. Goyeau, T. Benihaddadene, D. Gobin and M. Quintard, *Transport in Porous Media*, **28** (1997), 19.
- 57) B. Goyeau, T. Benihaddadene, D. Gobin and M. Quintard, *Metall. Mater. Trans. B*, **30B** (1999), 613.
- 58) J. Ni and F. P. Incropera, *Int. J. Heat Mass Transfer*, **38** (1995), 1271.
- 59) J. Ni and F. P. Incropera, *Int. J. Heat Mass Transfer*, **38** (1995), 1285.
- 60) N. Ahmed, H. Combeau, J. -L. Desbiolles, T. Jalanti, G. Lesoult, J. Rappaz, M. Rappaz, and C. Stomp: *Metall. Mater. Trans. A*, **29A** (1998), 617.
- 61) M. J. M. Krane, F. P. Incropera and D. R. Gaskell, *Int. J. Heat Mass Transfer*, **40** (1997), 3828.
- 62) M. J. M. Krane and F. P. Incropera, *Int. J. Heat Mass Transfer*, **40** (1997), 3837.
- 63) M. J. M. Krane, F. P. Incropera and D. R. Gaskell, *Metall. Mater. Trans. A*, **29A** (1998), 843.
- 64) B. J. Yang, D. M. Stefanescu and J. Leon-Torres, *Metall. Mater. Trans. A*, **32A** (2001), 3065.
- 65) S. Chakraborty and P. Dutta, *Int. J. Num. Methods Fluids*, **38** (2002), 895.
- 66) S. Chakraborty and P. Dutta, *Materials Science and Technology*, **17** (2001), 1531.
- 67) D. Xu, *Metall. Mater. Trans. B*, **32B** (2001), 1129.
- 68) D. Xu, *Metall. Mater. Trans. B*, **33B** (2002), 451.

- 69) J. E. Simpson and S. V. Garimella, *Int. J. Heat Mass Transfer*, **11** (1998), 2485.
- 70) J. E. Simpson, S. V. Garimella, H. C. deGroh III and R. Abbaschian, *ASME J. Heat Transfer*, **123** (2001), 990.
- 71) S. Kuppurao, S. Brandon and J. J. Derby, *J. Crystal Growth*, 155 (1995), 93.
- 72) S. Kuppurao, S. Brandon and J. J. Derby, *J. Crystal Growth*, 155 (1995), 103.
- 73) Y. F. Zou, G. -X. Wang, H. Zhang, and V. Prasad, *ASME J. of Heat Transfer*, **121** (1999), 148.
- 74) G. Phanikumar, K.. Chattopadhyaya and P. Dutta, *International Journal of Numerical Methods for Heat and Fluid Flow*, **11** (2001), 156.
- 75) S. K. Choudhary and A. Ghosh, *Iron Steel Inst. Jpn. Int.*, **34** (1994), 338.
- 76) S. K. Choudhary and D. Mazumdar, *Steel Res.*, **66** (1995), 199.
- 77) G. Amberg, *Int. J. Heat Mass Transfer*, **34** (1991), 217.
- 78) A. K. Singh and B. Basu, *Metall. Mater. Trans. B*, **26B** (1995), 1069.
- 79) A. K. Singh and B. Basu, *Metall. Mater. Trans. A*, **31A** (2000), 1687.
- 80) H. Vannier, H. Combeau, and G. Lesoult, *Numerical Methods in Industrial Forming Processes*, A. A. Balkema, Rotterdam, 1992, 79.
- 81) F. Roch, H. Combeau, J. Chevrier and G. Lesoult: *Modelling of Casting, Welding and Advanced Solidification Process - V*, ed. by M. Rappaz, M. R. Ozgu and K. W. Mahin, TMS, Pennsylvania, 1991, 789.
- 82) M. C. Schneider and C. Beckermann, *Metall. Mater. Trans. A*, **26A** (1995), 2373.
- 83) H. C. Brinkman: *Appl. Sci..Res.*, **A1** (1947), 27.
- 84) B. Basu: *Numerical Methods in Thermal Problems*, Lewis, R.W., Chin, J.H. and Homsy, G.M., (Eds.), VII, 1991, 346.
- 85) P. C. Carman, *Trans. Inst. Chem. Eng.*, **15** (1937), 150.
- 86) H. Yoo and R. Viskanta, *Int. J. Heat Mass Transfer*, **35** (1992), 2335.
- 87) S. K. Sinha, T. Sundararajan and V. K. Garg, *Int. J. Heat Mass Transfer*, **35** (1992), 2865.
- 88) T. S. Piowonka and M. C. Flemings, *Trans. TMS-AIME*, **236** (1966), 1157.
- 89) R. West, *Metall. Trans. A*, **16A** (1985), 693.
- 90) D. R. Poirier: *Metall. Trans. B*, **18B** (1987), 245.
- 91) S. Ganesan, C. L. Chan and D. R. Poirier, *Mater. Sc. Engg.*, **A151** (1992), 97.

- 92) M. S. Bhat, D. R. Poirier, J. C. Heinrich and D. Nagelhout, *Scr. Metall. Mater.*, **31** (1994), 339.
- 93) M. C. Schneider and C. Beckermann, *Int. J. Heat Mass Transfer*, **38** (1995), 3455.
- 94) A. K. Singh, B. Goyeau, B. Basu and D. Gobin, *3rd Int. Workshop on Modeling in Crystal Growth*, Stony Brook, New York, 2000, 18.
- 95) *ASM Handbook*, Tenth Edition, 1990, 519.
- 96) *Metals Reference Book*, ed. by C. Smithel, Butterworths, London, 1978.
- 97) D. R. Poirier: *Metall. Trans. B*, **19A** (1988), 2349.
- 98) Y. S. Touloukian, R. W. Powell, C. Y. Ho, P. G. Klemens, *Thermophysical Properties of Matters*, IFI/Plenum, New York, 1970.
- 99) H. R. Thresh and A. F. Crawley, *Metall. Trans.*, **1** (1970), 1531.
- 100) P. J. Prescott and F. P. Incropera: *ASME J. Heat Transfer*, **116** (1994), 735.
- 101) P. J. Prescott, F. P. Incropera and D. R. Gaskell: *ASME J. Heat Transfer*, **116** (1994), 742.
- 102) T. C. Toye and E. R. Jones, *Proc. Phys. Soc.*, **71** (1958), 88.
- 103) D. J. Hebditch and J. D. Hunt, *Metall. Trans.*, **5** (1974), 1557.
- 104) H. Shahani, G. Amberg and H. Fredriksson: *Metall. Trans. A*, **23A** (1992), 2301.
- 105) M. J. M. Krane and F. P. Incropera, *Metall. Mater. Trans. A*, **26A** (1995), 2329.
- 106) S.M. Copley, A.F. Giamei, S.M. Johnson and M.F. Hornbecker, *Metall. Trans.*, (1970), **1**, 2193.
- 107) J. R. Sazarin and A. Hellawell, *Metall. Trans. A*, **19A** (1988), 1861.
- 108) S. N. Tewari and R. Shah, *Metall. Trans. A*, **23A** (1992), 3383.
- 109) S. N. Tewari, R. Shah and M. A. Chopra, *Metall. Trans. A*, **24A** (1993), 1661.
- 110) S. N. Tewari and R. Shah, *Metall. Mater. Trans. A*, **27A** (1996), 1353.
- 111) H. Song, S. N. Tewari and H. C. deGroh III, *Metall. Mater. Trans. A*, **27A** (1996), 1095.
- 112) M. I. Bergman, D. R. Fearn, J. Bloxham and M. C. Shannon: *Metall. Mater. Trans. A*, **28A** (1997), 859.
- 113) M. Li, T. Mori and H. Iwasaki: *Iron Steel Inst. Jpn. Int.*, **39** (1999), 33.
- 114) S. D. Felicelli, J. C. Heinrich and D. R. Poirier, *Metall. Trans. B*, **22B** (1991), 847.

- 115) S. D. Felicelli, J. C. Heinrich and D. R. Poirier, *Journal of Crystal Growth*, **191** (1998), 879.
- 116) S. V. Patankar, *Numerical Heat Transfer and Fluid Flow*, Hemisphere, Washington D.C., 1980.
- 117) P. J. Prescott, P. J. and F. P. Incropera, *Metall. Trans. B*, **22B** (1991), 529.
- 118) S. Asai and I. Muchi, *Trans. ISIJ*, **18** (1978), 90.
- 119) J. D. Hunt, *Solidification and Casting of Metals*, The Metals Society, London, 1979, 3.
- 120) R. Trivedi, *Metall. Trans. A*, **15A** (1984), 529.
- 121) V. Laxmanan, *J. Crystal Growth*, **75** (1986), 573.
- 122) S. Gupta and B. Basu, *Internal Report*, TRDDC, Pune, 2001.

APPENDIX I: Temperature-time curves for solidification cell thermocouples

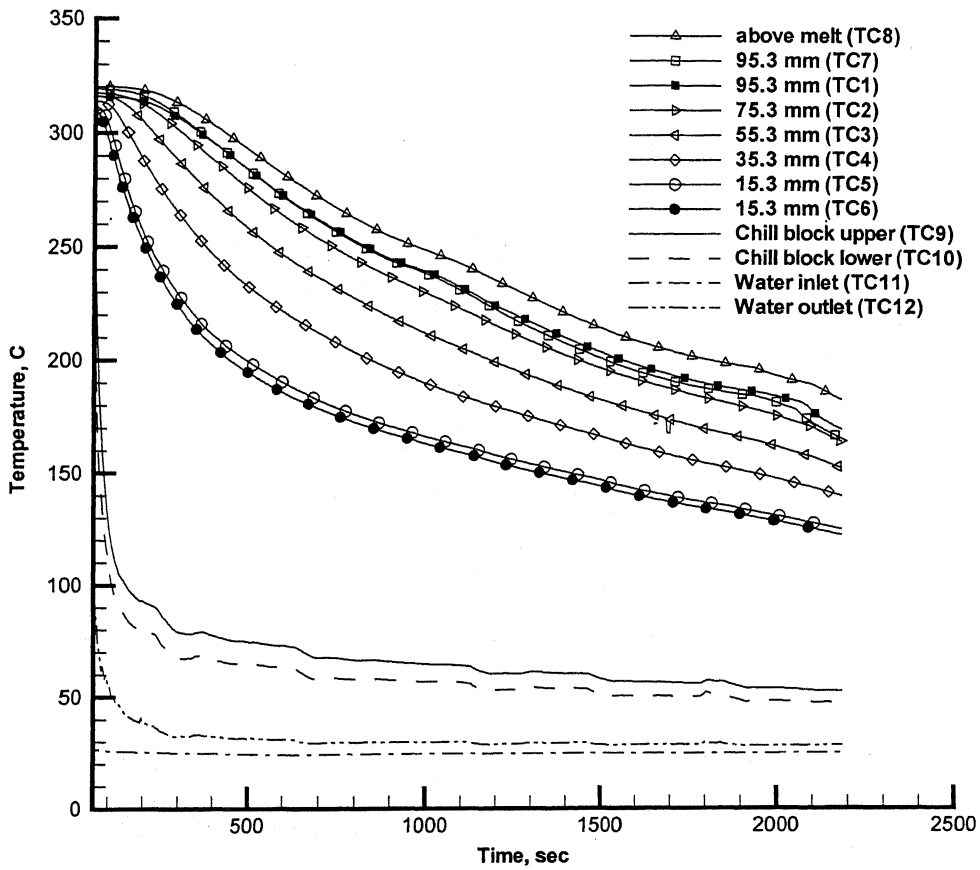


Fig. AI.1: Transient temperature response for E1 in the solidification cell for TC1 to TC12 of Fig. 5.6; vertical distances of thermocouples from the base of the mould are indicated.

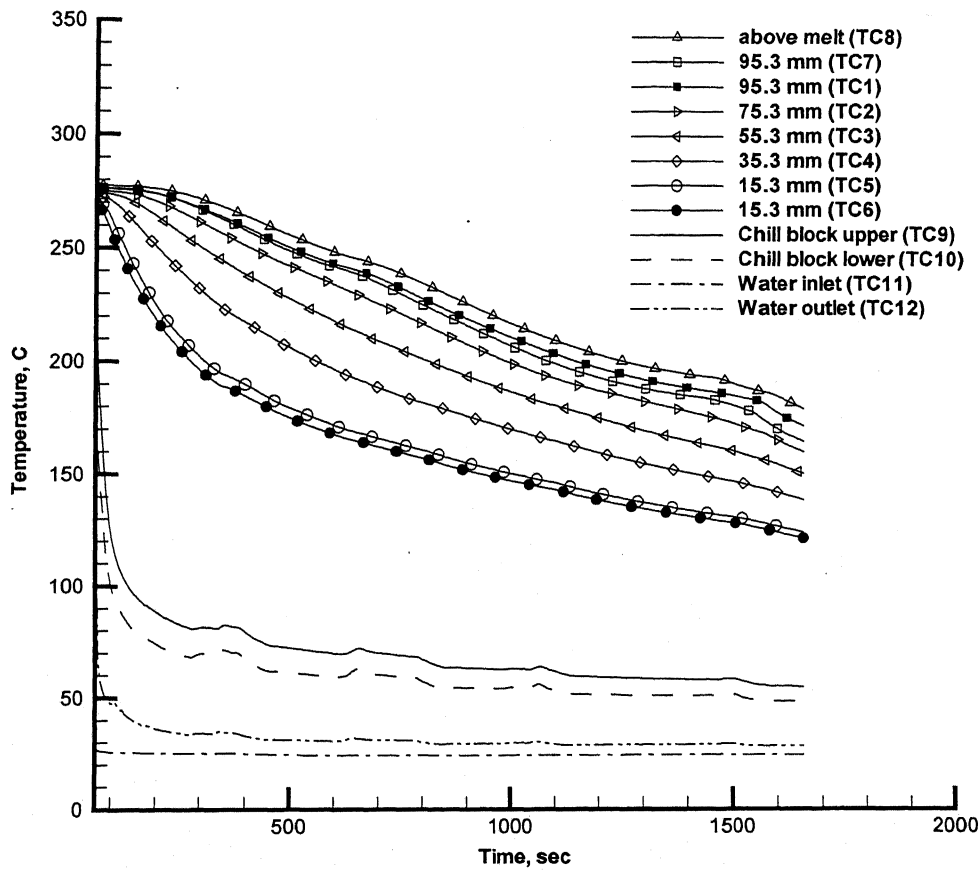


Fig. A1.2: Transient temperature response for E2 in the solidification cell for TC1 to TC12 of Fig. 5.6; vertical distances of thermocouples from the base of the mould are indicated.

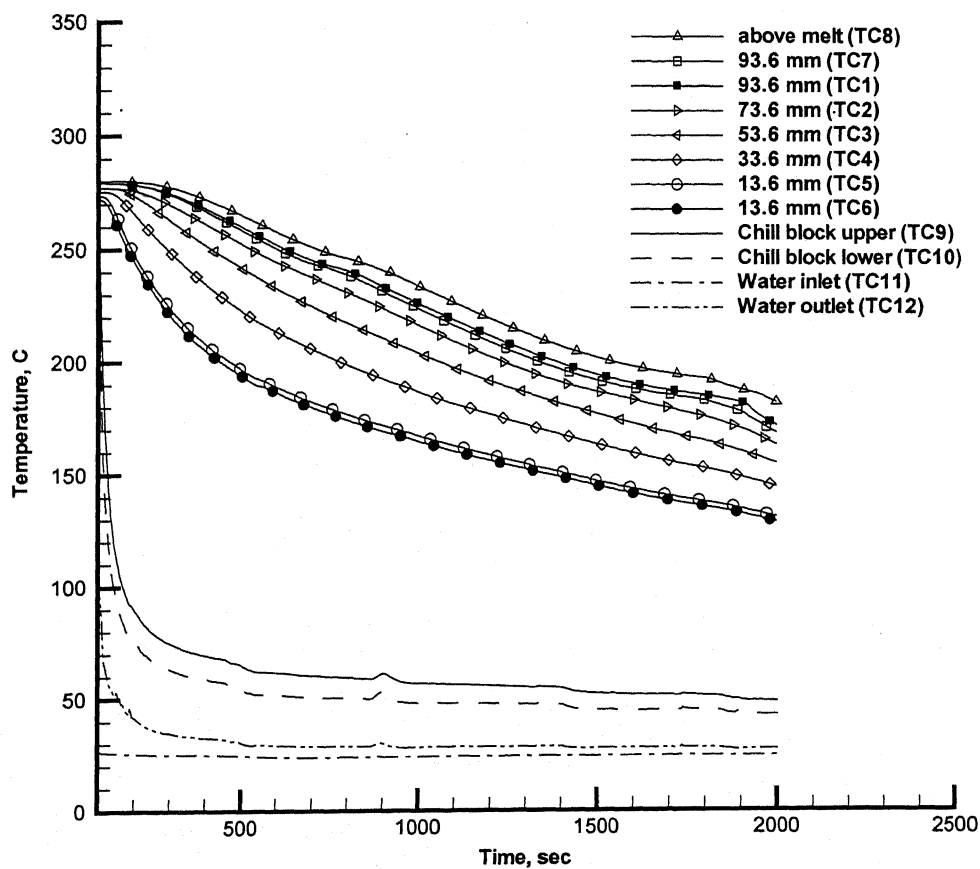


Fig. AI.3: Transient temperature response for E3 in the solidification cell for TC1 to TC12 of Fig. 5.6; vertical distances of thermocouples from the base of the mould are indicated.

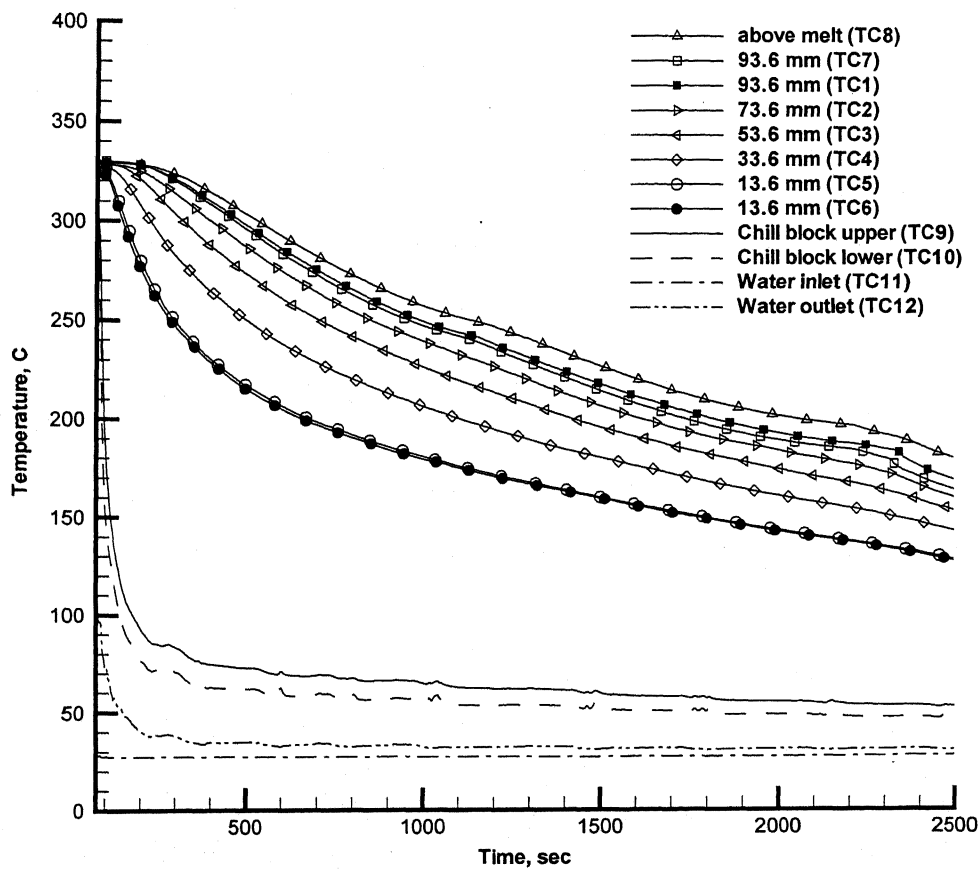


Fig. AI.4: Transient temperature response for E4 in the solidification cell for TC1 to TC12 of Fig. 5.6; vertical distances of thermocouples from the base of the mould are indicated.

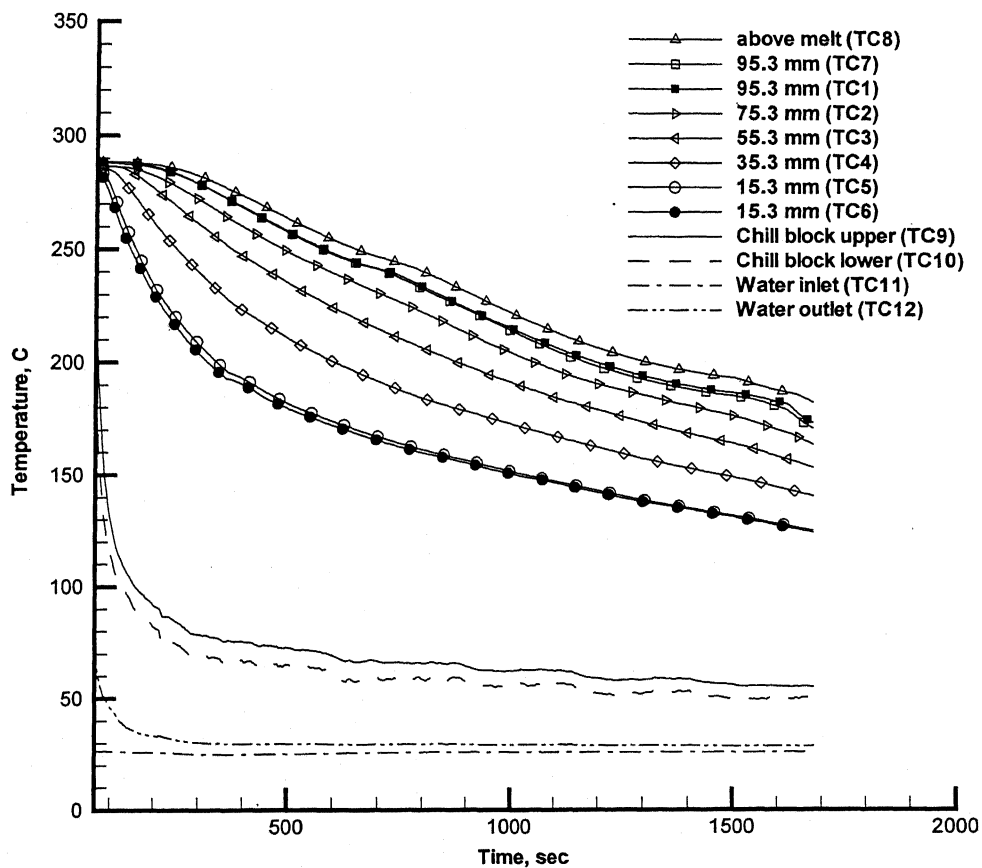


Fig. A1.5: Transient temperature response for E5 in the solidification cell for TC1 to TC12 of Fig. 5.6; vertical distances of thermocouples from the base of the mould are indicated.

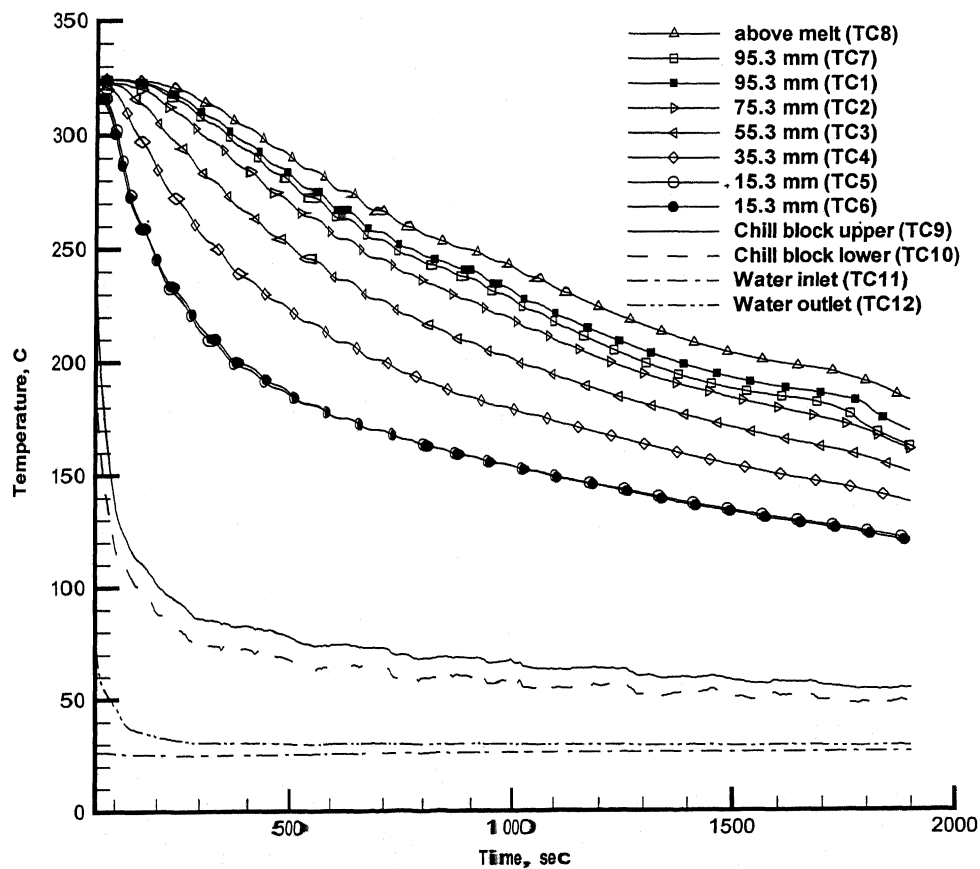


Fig. A1.6: Transient temperature response for E6 in the solidification cell for TC1 to TC12 of Fig. 5.6; vertical distances of thermocouples from the base of the mould are indicated.

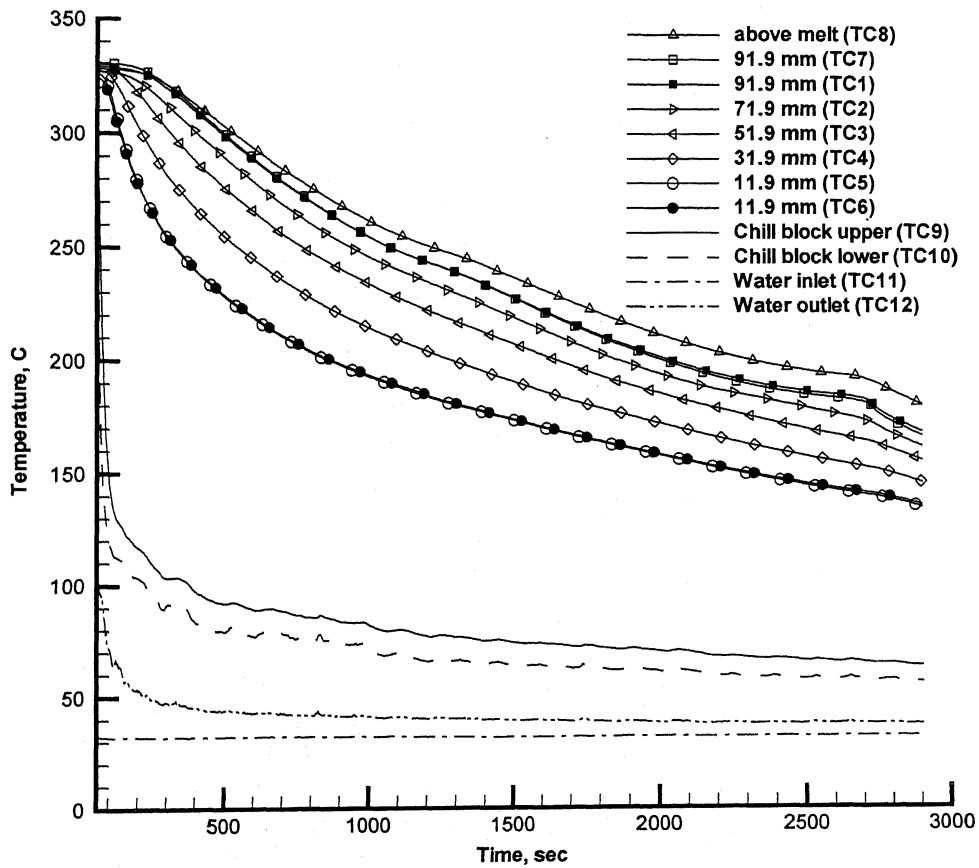


Fig. A1.7: Transient temperature response for E15 in the solidification cell for TC1 to TC12 of Fig. 5.6; vertical distances of thermocouples from the base of the mould are indicated.

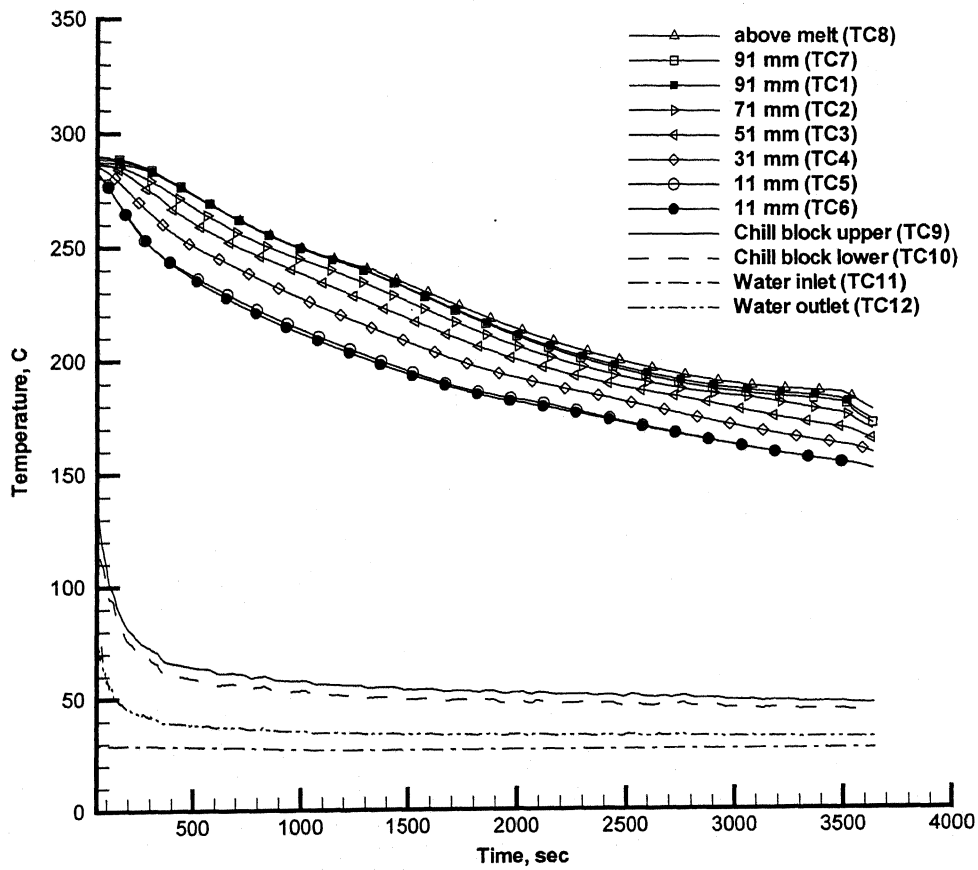


Fig. AI.8: Transient temperature responses for E16 in the solidification cell for TC1 to TC12 of Fig. 5.6; vertical distances of thermocouples from the base of the mould are indicated.

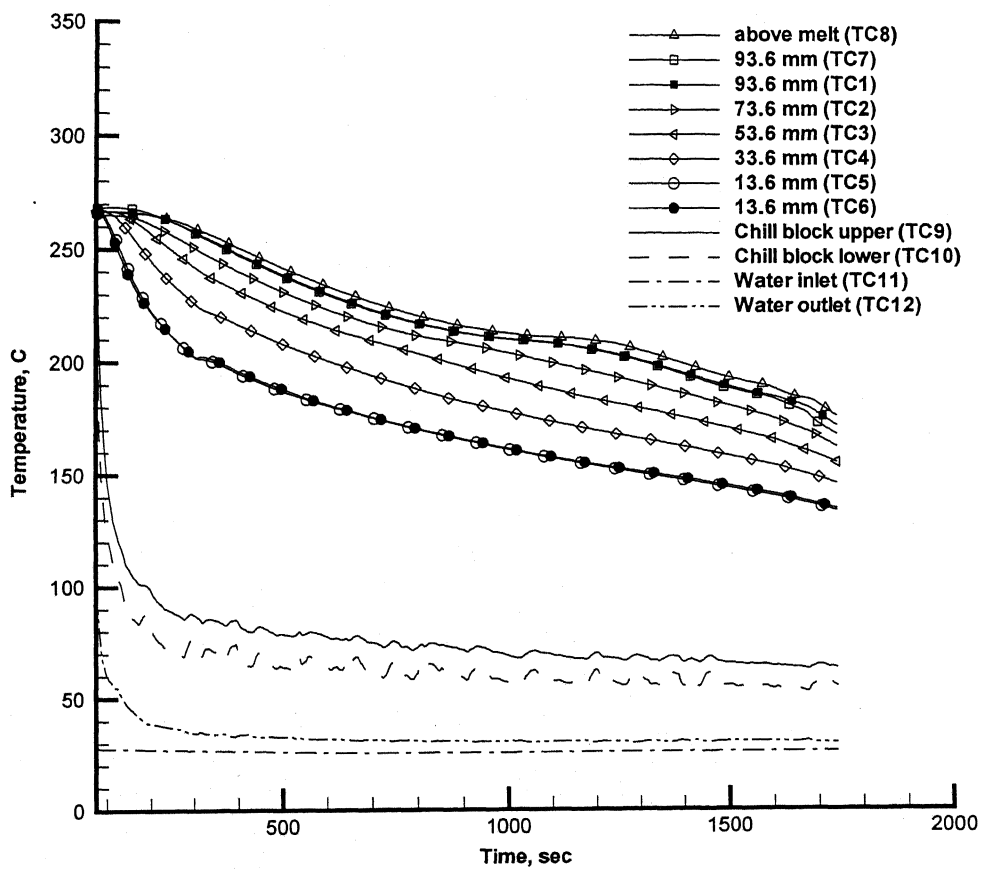


Fig. AI.9: Transient temperature response for E17 in the solidification cell for TC1 to TC12 of Fig. 5.6; vertical distances of thermocouples from the base of the mould are indicated.

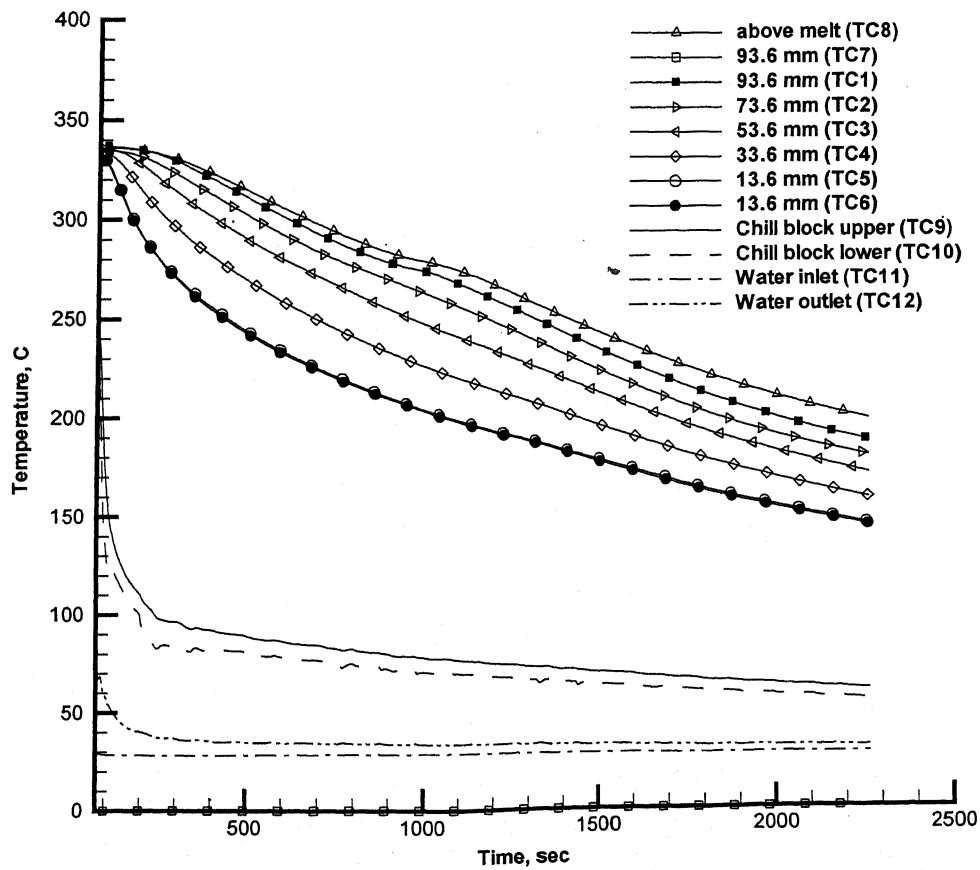


Fig. A1.10: Transient temperature response for E7 in the solidification cell for TC1 to TC12 of Fig. 5.6; vertical distances of thermocouples from the base of the mould are indicated.

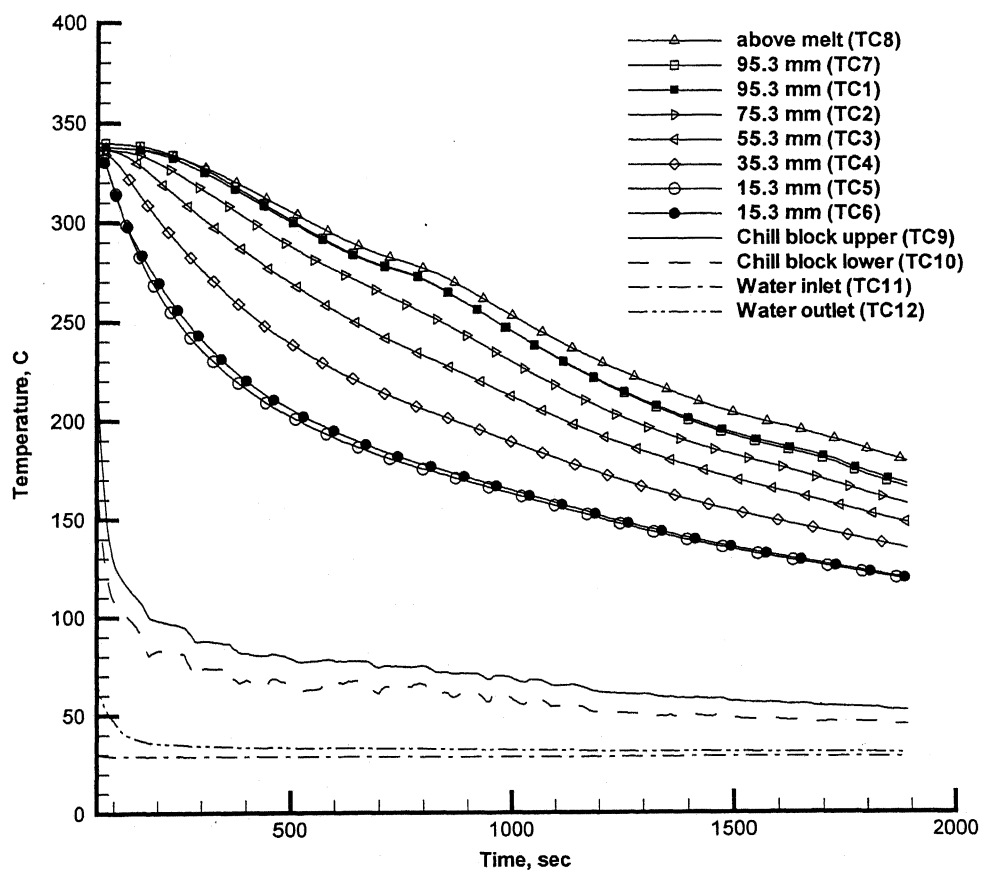


Fig. AI.11: Transient temperature response for E8 in the solidification cell for TC1 to TC12 of Fig. 5.6; vertical distances of thermocouples from the base of the mould are indicated.

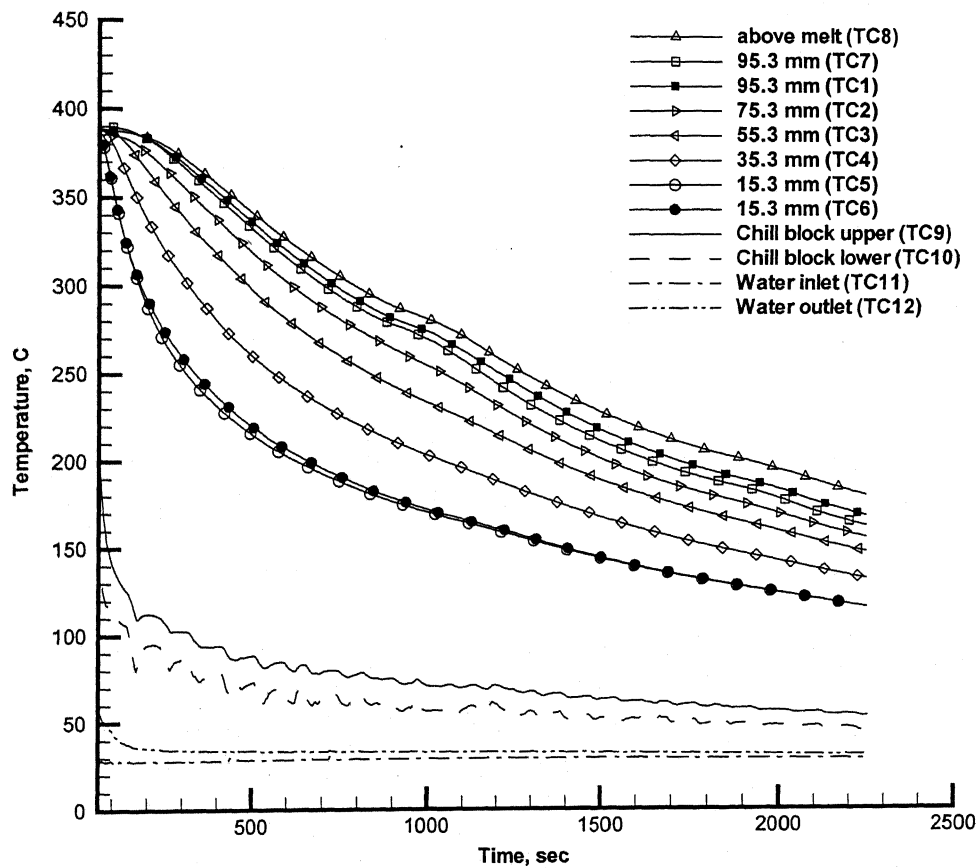


Fig. AI.12: Transient temperature response for E9 in the solidification cell for TC1 to TC12 of Fig. 5.6; vertical distances of thermocouples from the base of the mould are indicated.

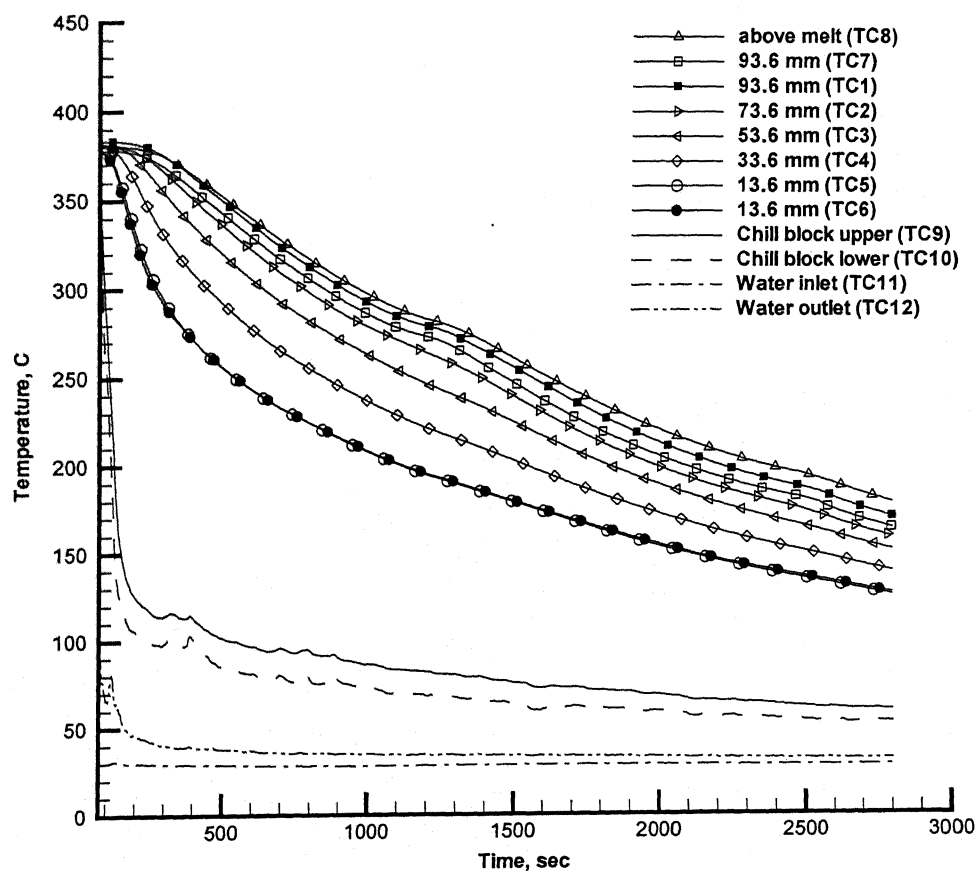


Fig. AI.13: Transient temperature response for E10 in the solidification cell for TC1 to TC12 of Fig. 5.6; vertical distances of thermocouples from the base of the mould are indicated.

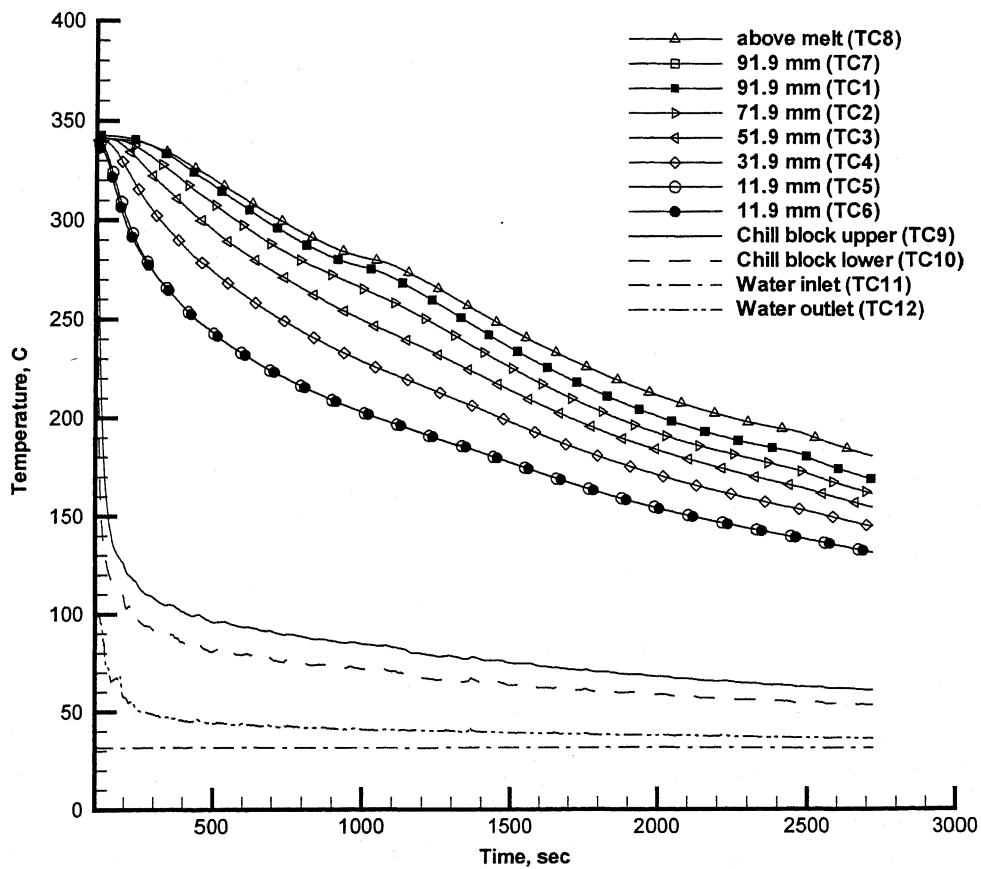


Fig. A1.14: Transient temperature response for E18 in the solidification cell for TC1 to TC12 of Fig. 5.6; vertical distances of thermocouples from the base of the mould are indicated.

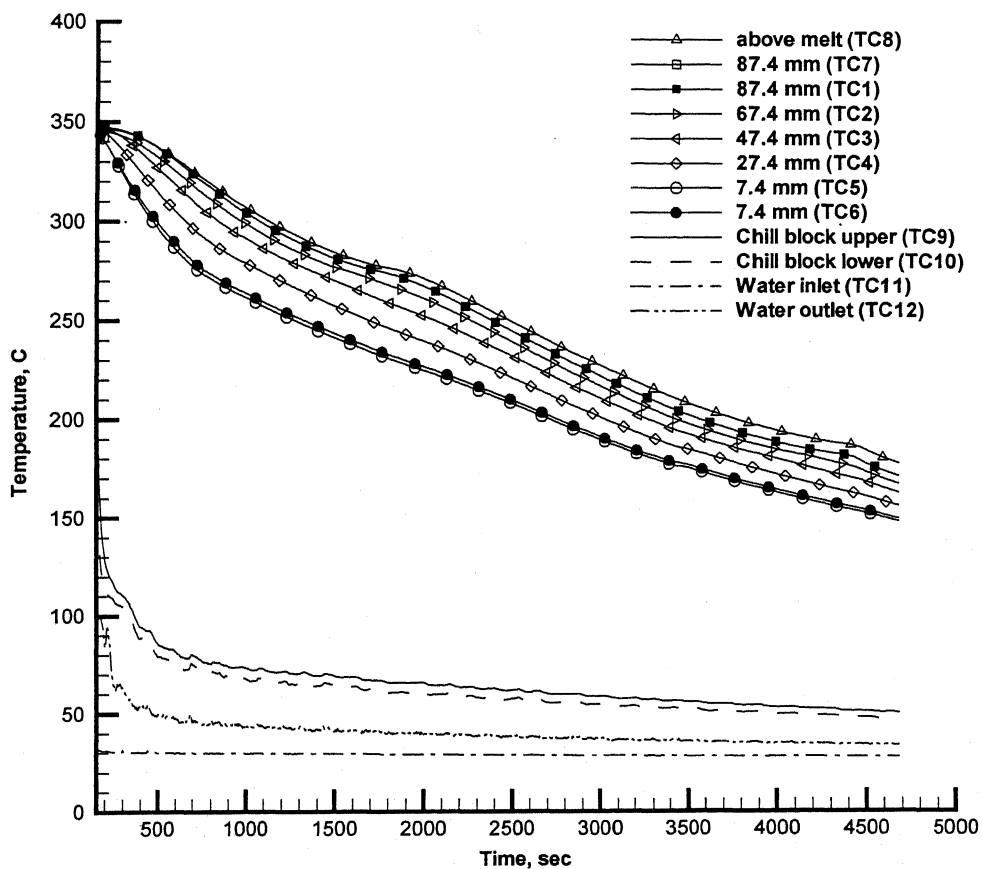


Fig. AI.15: Transient temperature response for E19 in the solidification cell for TC1 to TC12 of Fig. 5.6; vertical distances of thermocouples from the base of the mould are indicated.

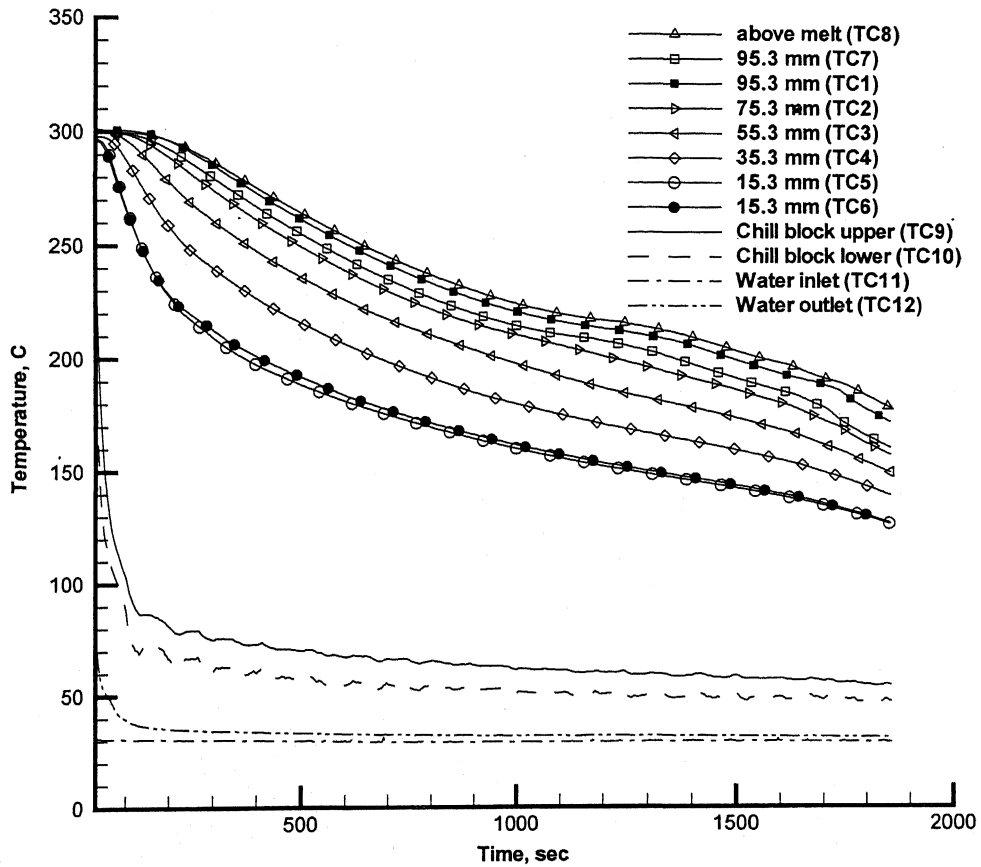


Fig. AI.16: Transient temperature response for E11 in the solidification cell for TC1 to TC12 of Fig. 5.6; vertical distances of thermocouples from the base of the mould are indicated.

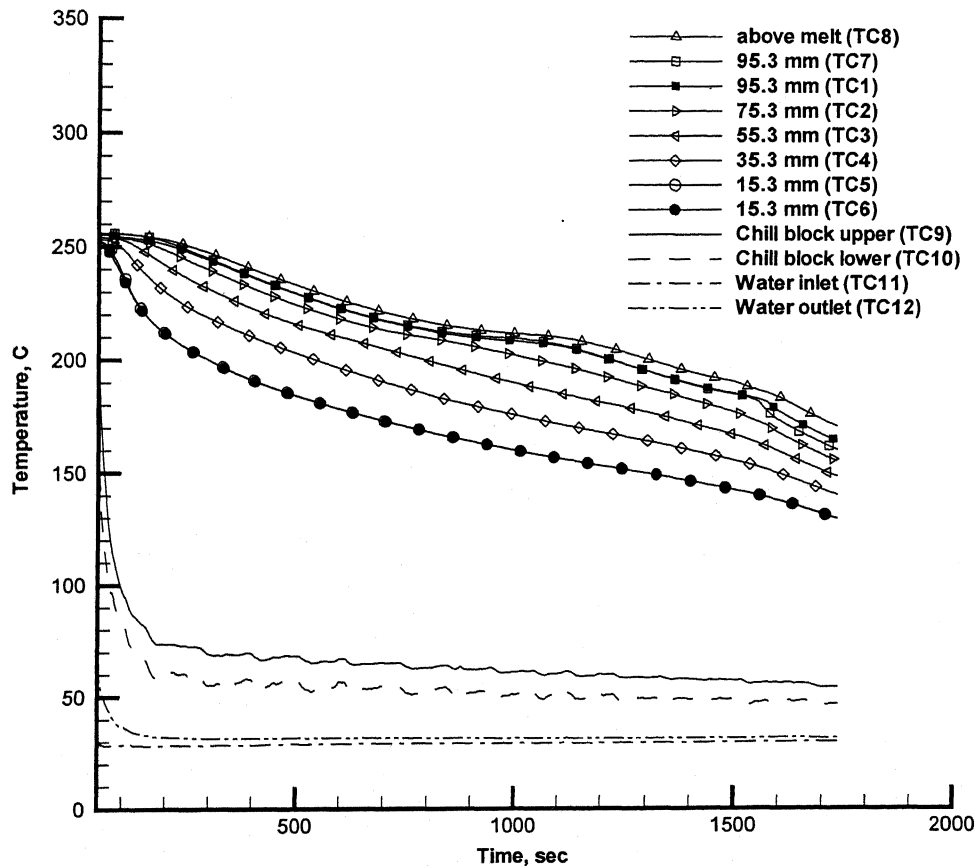


Fig. AI.17: Transient temperature response for E12 in the solidification cell for TC1 to TC12 of Fig. 5.6; vertical distances of thermocouples from the base of the mould are indicated.

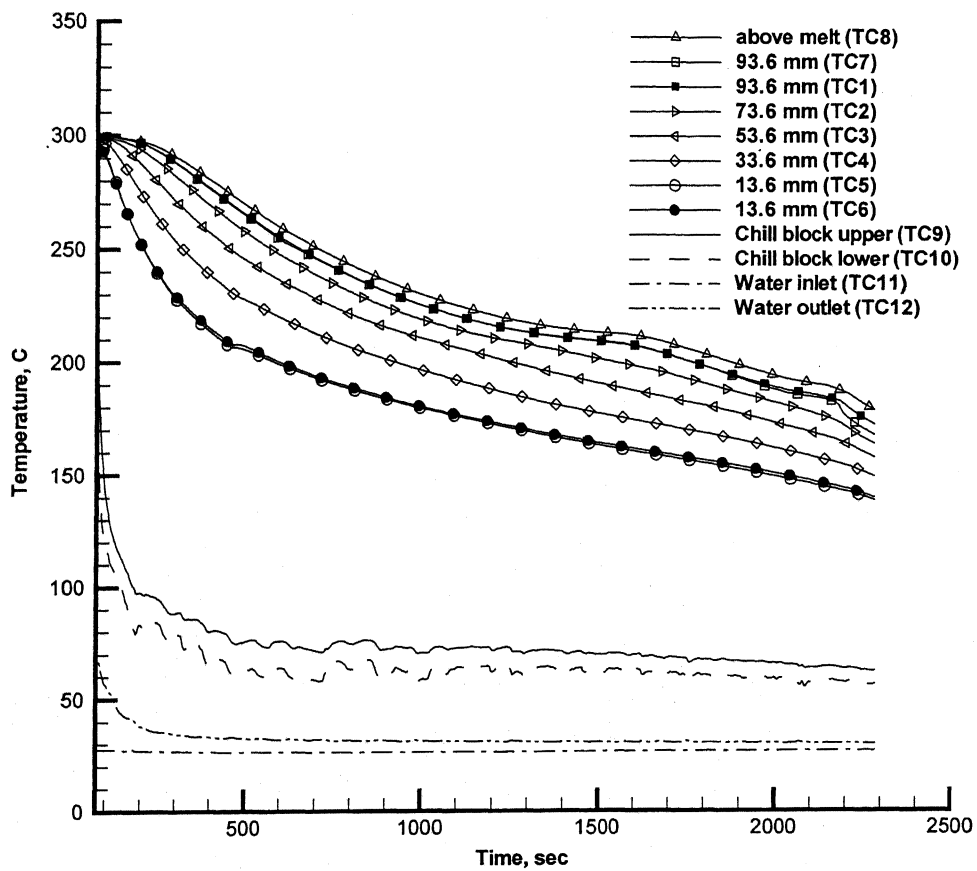


Fig. AI.18: Transient temperature response for E13 in the solidification cell for TC1 to TC12 of Fig. 5.6; vertical distances of thermocouples from the base of the mould are indicated.

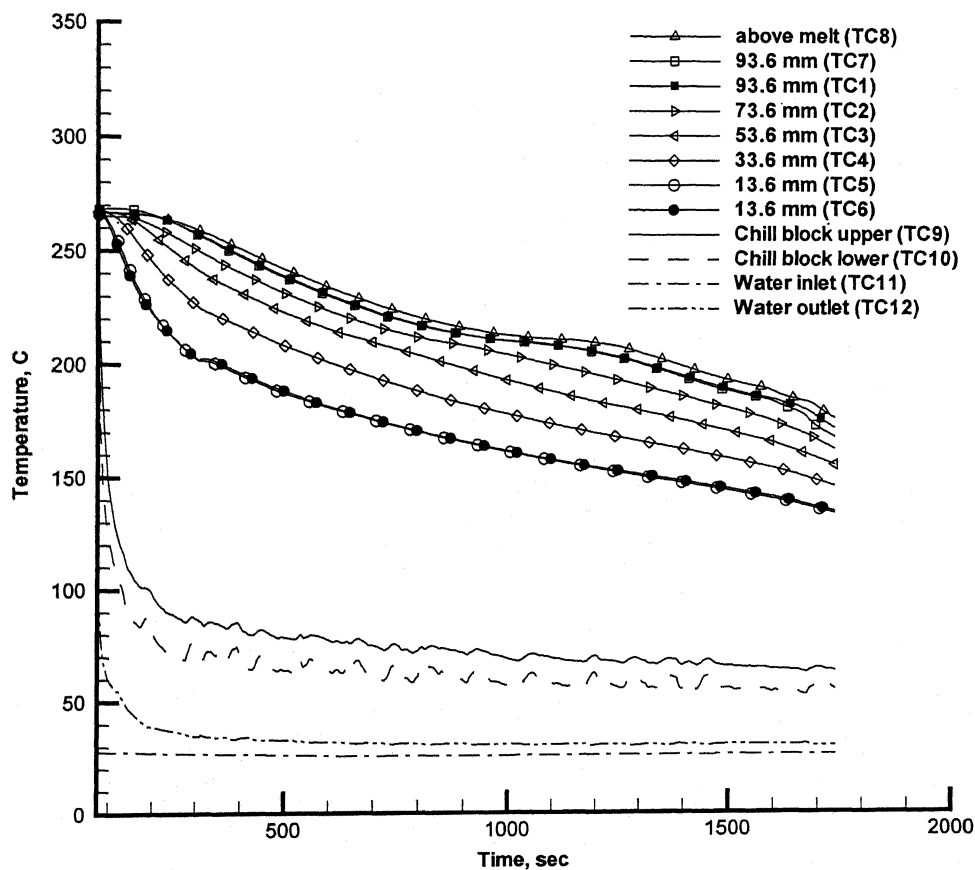


Fig. AI.19: Transient temperature response for E14 in the solidification cell for TC1 to TC12 of Fig. 5.6; vertical distances of thermocouples from the base of the mould are indicated.

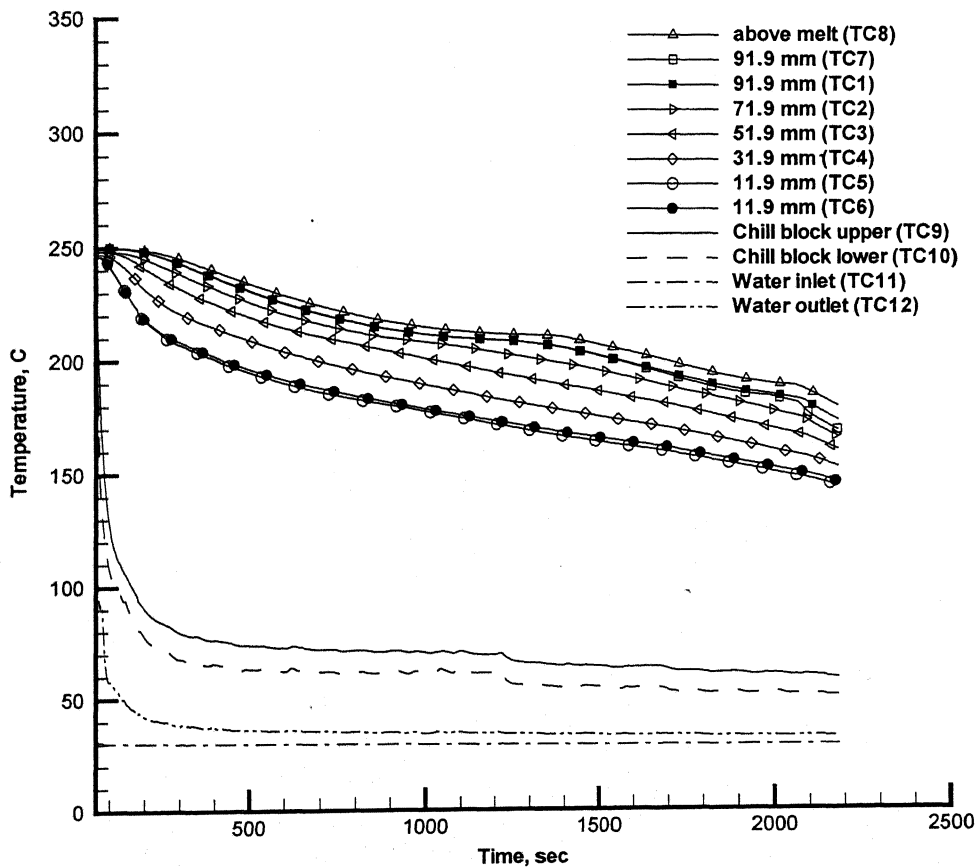


Fig. A1.20: Transient temperature response for E20 in the solidification cell for TC1 to TC12 of Fig. 5.6; vertical distances of thermocouples from the base of the mould are indicated.

APPENDIX II: Macrosegregation experimental data tables

Table AII.1: Composition in wt % Sn
for E1 (Pb - 35 wt % Sn)

Distance from bottom (mm)	Composition Wt % Sn
15.3	33.9
35.3	34.9
55.3	35.1
75.3	34.1
95.3	34.6

Table AII.2: Composition in wt % Sn
for E2 with Pb - 35 wt % Sn

Distance from bottom (mm)	Composition Wt % Sn
15.3	33.6
35.3	34.7
55.3	35.3
75.3	35.6
95.3	35.7

Table AII.3: Composition in wt % Sn
for E3 (Pb - 35 wt % Sn)

Distance from bottom (mm)	Composition Wt % Sn
13.6	35
33.6	35.1
53.6	35.2
73.6	35.4
93.6	35

Table AII.4: Composition in wt % Sn
for E4 (Pb - 35 wt % Sn)

Distance from bottom (mm)	Composition Wt % Sn
13.6	33.6
33.6	33.6
53.6	33.8
73.6	33.7
93.6	34.1

Table AII.5: Composition in wt % Sn
for E5 (Pb - 35 wt % Sn)

Distance from bottom (mm)	Composition Wt % Sn
15.3	33.9
35.3	34.7
55.3	35
75.3	35.6
95.3	35.4

Table AII.6: Composition in wt % Sn
for E6 (Pb - 35 wt % Sn)

Distance from bottom (mm)	Composition Wt % Sn
15.3	34.6
35.3	34.4
55.3	34.7
75.3	34.7
95.3	33.6

Table AII.7: Composition in wt % Sn
for E15 (Pb - 35 wt % Sn)

Distance from bottom (mm)	Composition Wt % Sn
11.9	33.7
31.9	34.1
51.9	34.3
71.9	34.6
91.9	35.8

Table AII.8: Composition in wt % Sn
for E16 (Pb - 35 wt % Sn)

Distance from bottom (mm)	Composition Wt % Sn
11.0	34.2
31.0	34.2
51.0	34
71.0	34.5
91.0	36.3

Table AII.9: Composition in wt % Sn
for E17 (Pb - 35 wt % Sn)

Distance from bottom (mm)	Composition Wt % Sn
7.4	33
27.4	32.7
47.4	33.2
67.4	34
87.4	35.4

Table AII.10: Composition in wt % Sn
for E7 (Pb -19 wt % Sn)

Distance from Bottom (mm)	Composition Wt % Sn
13.6	18.8
33.6	19.1
53.6	19.2
73.6	18.8
93.6	19.2

Table AII.11: Composition in wt % Sn
for E8 (Pb -19 wt % Sn)

Distance from Bottom (mm)	Composition Wt % Sn
15.3	18.2
35.3	18.2
55.3	18
75.3	18.2
95.3	17.9

Table AII.12: Composition in wt % Sn
for E9 (Pb -19 wt % Sn)

Distance from Bottom (mm)	Composition Wt % Sn
15.3	18.2
35.3	18.3
55.3	18.4
75.3	18.6
95.3	17.7

Table AII.13: Composition in wt % Sn
for E10 (Pb -19 wt % Sn)

Distance from Bottom (mm)	Composition Wt % Sn
13.6	18.6
33.6	18.3
53.6	18.4
73.6	18.6
93.6	17.1

Table AII.14: Composition in wt % Sn
for E18 (Pb -19 wt % Sn)

Distance from Bottom (mm)	Composition Wt % Sn
11.9	18.8
31.9	18.9
51.9	18.4
71.9	19.2
91.9	18.8

Table AII.15: Composition in wt % Sn
for E19 (Pb -19 wt % Sn)

Distance from Bottom (mm)	Composition Wt % Sn
7.4	19.4
27.4	19.2
47.4	19.9
67.4	19.7
87.4	19.7

Table AII.16: Composition in wt % Sn
for E11 (Sn -15 wt % Pb)

Distance from bottom (mm)	Composition Wt % Pb
15.3	14.9
35.3	14.8
55.3	14.7
75.3	14.7
95.3	14.3

Table AII.17: Composition in wt % Sn
for E12 (Sn -15 wt % Pb)

Distance from bottom (mm)	Composition Wt % Pb
15.3	15.1
35.3	14.9
55.3	14.7
75.3	14.9
95.3	14.8

Table AII.18: Composition in wt % Sn
for E19 (Sn -15 wt % Pb)

Distance from bottom (mm)	Composition Wt % Pb
13.6	14.5
33.6	14.3
53.6	14.5
73.6	14.5
93.6	14.2

Table AII.19: Composition in wt % Sn
for E19 (Sn -15 wt % Pb)

Distance from bottom (mm)	Composition Wt % Pb
13.6	15
33.6	14.7
53.6	14.9
73.6	14.6
93.6	14.6